Magnetic helicity in astrophysical dynamos

Simon Candelaresi

Stockholm
University

Magnetic helicity in astrophysical dynamos

Simon Candelaresi

Cover image: Volume rendering of the magnetic energy for the 9-foil knot.

ISBN 978-91-7447-593-7

Printed in Sweden by Universitetsservice, US-AB, Stockholm 2012
Distributor: Department of Astronomy, Stockholm University

Abstract

The broad variety of ways in which magnetic helicity affects astrophysical systems, in particular dynamos, is discussed.

The so-called α effect is responsible for the growth of large-scale magnetic fields. The conservation of magnetic helicity, however, quenches the α effect, in particular for high magnetic Reynolds numbers. Predictions from mean-field theories state particular power law behavior of the saturation strength of the mean fields, which we confirm in direct numerical simulations. The loss of magnetic helicity in the form of fluxes can alleviate the quenching effect, which means that large-scale dynamo action is regained. Physically speaking, galactic winds or coronal mass ejections can have fundamental effects on the amplification of galactic and solar magnetic fields.

The gauge dependence of magnetic helicity is shown to play no effect in the steady state where the fluxes are represented in form of gauge-independent quantities. This we demonstrate in the Weyl-, resistive- and pseudo Lorentz-gauge. Magnetic helicity transport, however, is strongly affected by the gauge choice. For instance the advecto-resistive gauge is more efficient in transporting magnetic helicity into small scales, which results in a distinct spectrum compared to the resistive gauge.

The topological interpretation of helicity as linking of field lines is tested with respect to the realizability condition, which imposes a lower bound for the spectral magnetic energy in presence of magnetic helicity. It turns out that the actual linking does not affect the relaxation process, unlike the magnetic helicity content. Since magnetic helicity is not the only topological variable, I conduct a search for possible others, in particular for non-helical structures. From this search I conclude that helicity is most of the time the dominant restriction in field line relaxation. Nevertheless, not all numerical relaxation experiments can be described by the conservation of magnetic helicity alone, which allows for speculations about possible higher order topological invariants.

Acknowledgments

The content of this work has been a collaborative effort with the co-authors on the publications. Their input has been fundamental for the progress of this entire work. Through discussions my overall understanding of the matter presented here has benefited considerably.

Of course I thank my supervisor **Axel Brandenburg**, not only for the supervision, but especially for the encouragements for pursuing my own projects and start collaborations with scientists, even outside this narrowly defined field.

I appreciate the efforts by **Dhrubaditya Mitra** and **Matthias Rheinhardt** for clearly explaining the complex matter we are working with and helping with the Pencil Code, which often works in mysterious ways.

Getting into the world outside my working group has been possible with the help of **Anthony Yeates** and **Nobumitsu Yokoi** who hosted me at their home institutes and with whom we had discussions during my stay. Although the collaborative work has not made it into this thesis it has greatly broadened my perspectives and will surely lead to conclusive work in the near future.

With **Chi-Kwan Chan**, **Alexander Hubbard** and **Gustavo Guerrero** we had various helpful discussions about physics, numerics, computing and the Pencil Code, which helped in progressing this work. Without fellow PhD students **Fabio Del Sordo**, **Jörn Warnecke** and **Koen Kemel**, as well as **Alessandra Cagnazzo** and **Elizabeth Yang** the entire time would have been rather dull. So thanks goes for keeping me away from work and keeping me sane.

Of course thanks goes to **Hans von Zur-Mühlen** for helping with various technical issues and proof reading the Swedish summary of this thesis and **Fabio Del Sordo** for corrections in the thesis.

Special appreciation goes to **Carola Eugster** for her tireless encouragements throughout the whole project and for patiently improve various important texts written during my time as grad student.

Without the professional tools developed by the **open source community** all the research related work would have progressed in a much slower pace. Naming all the contributors would require several phone books, so just a few should be mentioned here: **Linus Torvalds** for developing Linux, **Donald Knuth** and **Leslie Lamport** for developing TeX and LaTeX, **Axel Brandenburg** and **Wolfgang Dobler** for the Pencil Code, **Guido van Rossum** for Python and **John Hunter** for matplotlib.

Even for-profit ventures should be thanked for making this work possible, in particular the **Asus company** for coming up with highly mobile electronics which can be used to do actual work. Without it I couldn't have met all the deadlines while constantly traveling.

Most of the sacrifices for this work were endured by two reliable workhorses who almost never complained: **HP Pavilion Entertainment** and **Asus Eee PC 1015BX**.

Further work horses have been the computers at the **Center for Parallel Computers at the Royal Institute of Technology** in Sweden and Iceland, the **National Supercomputer Centers in Linköping**, the **QMUL HMC facilities** and the **Carnegie Mellon University Supercomputer Center**.

This work has been supported in part by the **European Research Council** under the AstroDyn Research Project 227952 and the **Swedish Research Council** grant 621-2007-4064.

List of Papers

The following papers are included in this thesis. They are referred to in the text by their Roman numerals,

I **Candelaresi, S.** and Brandenburg, A.: 2012, "The kinetic helicity needed to drive large-scale dynamos", *Phys. Rev. E*, submitted, arXiv: 1208.4529

II Brandenburg, A., **Candelaresi, S.** and Chatterjee, P.: 2009, "Small-scale magnetic helicity losses from a mean-field dynamo", *Mon. Not. Roy. Astron. Soc.*, **398**, 1414

III Mitra, D., **Candelaresi, S.**, Chatterjee, P., Tavakol, R. and Brandenburg, A.: 2010, "Equatorial magnetic helicity flux in simulations with different gauges", *Astron. Nachr.*, **331**, 130

IV **Candelaresi, S.**, Hubbard, A., Brandenburg, A. and Mitra, D.: 2011, "Magnetic helicity transport in the advective gauge family", *Phys. Plasmas*, **18**, 012903

V Del Sordo, F., **Candelaresi, S.** and Brandenburg, A.: 2010, "Magnetic-field decay of three interlocked flux rings with zero linking number", *Phys. Rev. E*, **81**, 036401

VI **Candelaresi, S.** and Brandenburg, A.: 2011, "Decay of helical and non-helical magnetic knots", *Phys. Rev. E*, **81**, 016406

My contribution to the papers

I For this work I did most of the simulations and evaluations. I also wrote most of the text.

II I performed a few simulations and contributed in writing and editing the text.

III My contributions for this work were analyzing the results and editing the text.

IV I performed all the simulations and did most of the evaluations. I was also responsible for the text which was mostly written by myself.

V The idea for this work came out of a course on solar physics. I performed some of the simulations and contributed to the evaluation. Writing the text was done jointly with the co-authors.

VI This project came out of my initiative and was completely conducted by myself. I did the simulations for which I modified and extended the used numerical code. The evaluations were done by me as well as writing the text.

Contents

1. Introduction

> *Je n'ai fait celle-ci plus longue*
> *que parce que je n'ai pas eu le loisir*
> *de la faire plus courte.*
>
> *I would have written a shorter letter,*
> *but I did not have the time.*
>
> Blaise Pascal

Asking astronomers about the relevant forces for the dynamics of astrophysical objects the only answer is often "gravity". Gravity is undoubtedly responsible for the structures we see at scales of the Universe. But what is often forgotten is the effect of electromagnetic forces, which often goes beyond radiation pressure. For accretion discs magnetic fields lead to angular momentum transport and ensure quick spin-downs. The presence of magnetic fields in planets and stars provides shielding from charged and energetic particles and suppresses convection. Starspots and sunspots, which are highly magnetized regions, are ares of reduced radiation.

Observations of magnetic fields in the universe date as far back as 364 BCE, when Chinese astronomers observed sunspots for the first time. Of course back then little was known about their magnetic nature. It was thanks to Galileo Galilei that sunspots were recorded more systematically, which has been continued ever since and created an almost complete record spanning four centuries. Their occurrence was explained in 1908 by George Ellery Hale who first obtained Zeeman measurements from the Sun's surface, which revealed strong magnetic fields of ca. 2 kG on sunspots. This strong field suppresses convective motions that would otherwise replenish the surface with hot material. The temperature in those regions drops due to thermal radiation which makes them appear dark. Typical life times are between days and up to 3 months during which proper motion can be observed.

The occurrence of sunspots is not random in time, nor are they randomly distributed on the Sun's surface. Within 11 years the total number observed varies between maximum and minimum during which almost no spots are observed (Fig. 1.1, lower panel). We can trace this behavior back to the first systematic observations in 1610. The only period during which this striking rule does not apply is the so-called Maunder minimum from ca. 1650 to 1700, during which almost no sunspots were observed. At the beginning of each cycle the first sunspots appear at latitudes of around 30 degrees. As time evolves

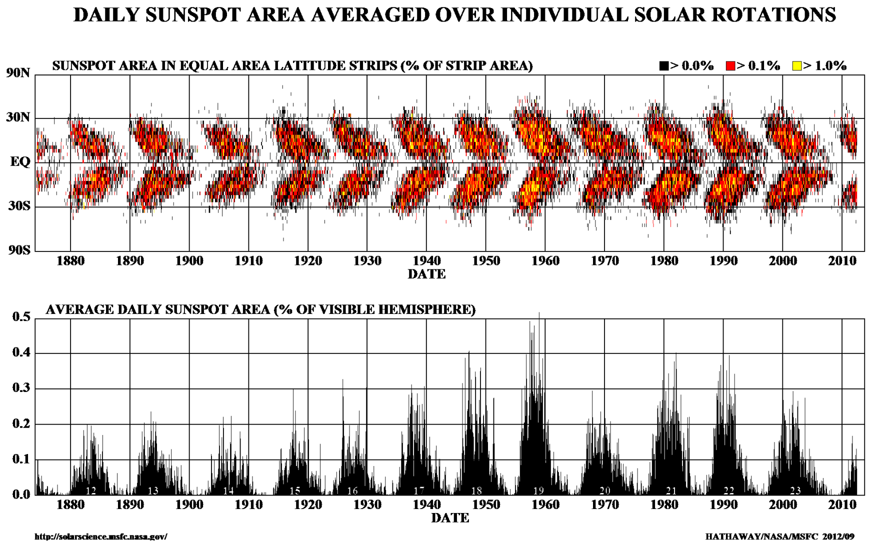

Figure 1.1: Longitudinally averaged area covered by sunspots (upper panel). Percentage of the visible hemisphere covered with sunspots (lower panel). (NASA 2012)

they emerge closer to the equator. Plotting the longitudinal average of the area covered with sunspots gives a butterfly-like diagram (Fig. 1.1, upper panel). Today we can measure all three spatial components of the Sun's magnetic field. One of the most striking revelations from these magnetograms is the reversal of the sign of the magnetic field after every 11 years. This 22 years periodic cycle is the magnetic cycle (Fig. 1.2).

Explaining the occurrence of the Sun's magnetic field first led to the primordial theory, which claims that the creation of the field happened during the Sun's formation from an interstellar gas cloud. Since the hot gas is highly conducting it is plausible that via an induction mechanism potential energy can be partially transformed into magnetic energy. Of course one would need to take into account the full energy balance, which further includes kinetic and thermal energy. Both the large scale and the strength of the field can be explained by this theory. But it falls short in clarifying the cyclic behavior and how it could have outlived 4.5 billions of years of resistive decay.

To address those drawbacks, a mechanism is necessary that constantly regenerates magnetic fields on scales which we observe on the Sun. At the same time it has to explain how the cyclic behavior comes about. The most successful and generally accepted theory is the dynamo theory, which explains how turbulent motions in a conducting medium give rise to magnetic fields of ener-

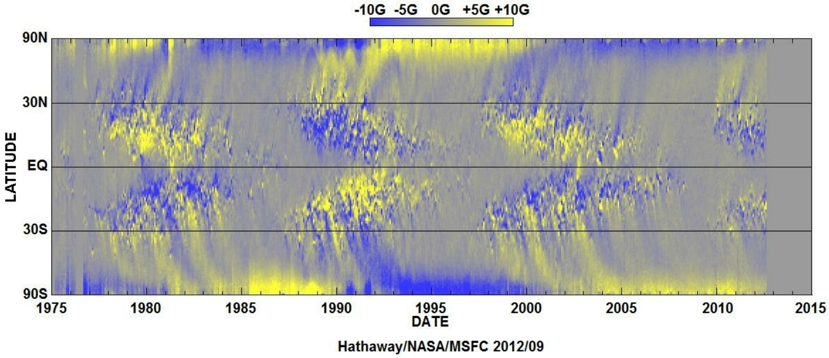

Figure 1.2: Polar magnetic field strength at various latitudes for the Sun. The magnetic active regions coincide with the sunspots. This diagram is often referred to as the magnetic butterfly diagram. (NASA 2012)

gies comparable to the energies of the motions and scales similar to the system size. Turbulent dynamos provide a convincing mechanism for the Sun's magnetic field. Other than the Sun also galactic fields and fields of accretion discs can be explained by this mechanism (Brandenburg et al., 1995).

An important ingredient of turbulent dynamos is kinetic helicity of the turbulent motions, i.e. the scalar product of the velocity with the vorticity. As a result the magnetic field will be helical as well, with helicities of opposite signs in the small and large scales. The presence of small-scale magnetic helicity, however, reduces the production of large-scale magnetic energy, which is produced by small-scale helical motions. For a closed system this means that the field reaches saturation only on time scales determined by the resistivity, which are much longer than the relevant dynamical time scales for astrophysical systems. A quantitative study of the dynamo's behavior for a closed system is presented in **Paper I**, where we investigate conditions under which dynamo action occurs and how the saturation state depends on relevant parameters. This work was motivated by recent findings about the onset of large-scale dynamo action of Pietarila Graham et al. (2012) that did not agree with standard models of Blackman and Brandenburg (2002), confirmed in Käpylä and Brandenburg (2009).

Open systems can reduce the amount of magnetic helicity via fluxes. This reduces the dynamo quenching coming from the presence of small-scale magnetic helicity significantly (**Paper II**). In practical terms it means that astrophysical dynamos must have some mechanism by which helicity is shed. For the Sun one candidate is coronal mass ejections, which frequently occur where

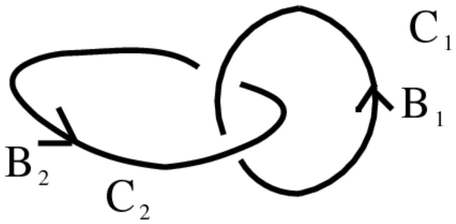

Figure 1.3: Mutually linked magnetic fluxed tube make up one of the simplest helical field configurations.

the field is strongly twisted, i.e. helical.

Magnetic helicity density is the scalar product of the magnetic vector potential $\boldsymbol{A}$ and the magnetic field $\boldsymbol{B}$. Potentials are always defined up to a gauge, which can be chosen freely. That means that magnetic helicity density and its fluxes are dependent on the gauge choice. The conditions under which a dynamo is excited must, however, not depend on the gauge. In **Paper III** and **Paper IV** both magnetic helicity fluxes and transport are investigated. Luckily for the dynamo, the physically relevant quantities, like the time averaged fluxes in the statistically steady state, turn out to be gauge-independent.

To illustrate magnetic helicity, one can think of magnetic flux tubes, which are twisted like a helix, with both ends connected. Helices are not the only helical fields one can think of. Two flux tubes, which are mutually linked, constitute a helical configuration as well (Fig. 1.3). Letting such fields evolve leads to a reduction of magnetic energy through various channels. Resistivity slowly destroys magnetic energy, while reconnection, i.e. braking and connecting magnetic field lines, has a faster effect. Reconnection is, however, a violent process and hence not favored in field relaxation. If we cannot rely on reconnection being effective enough, a helical system of the kind of interlocked flux rings cannot freely evolve due to the conservation of mutual linkage. This restriction is captured in the *realizability condition*, which gives a lower bound for the magnetic energy in presence of magnetic helicity. Unfortunately the overly simple picture of linked field lines can be broken by an idealized non-helical configuration composed of linked field lines. What happens then is part of **Paper V**, where the relaxation of linked, helical and non-helical fields is investigated.

Magnetic helicity is not the only quantity, which quantifies the field's topological structure. There exists an infinite number of topological invariants. Whether or not such invariants could give restrictions on the relaxation is studied in **Paper VI**, in which helical and non-helical knots and links are investigated.

The approach taken in this work is purely theoretical. No observations have been consulted to make quantitative comparisons with the results. Yet, observations provided the impulse for all the investigations. All the setups are investigated within the framework of magnetohydrodynamics, which provides a reasonable description of the physical systems. Solving these non-linear partial differential equations is done numerically using the PENCIL CODE[1], a high-order finite difference PDE solver.

---

[1] http://pencil-code.googlecode.com

2. Framework

> *O studianti, studiate le matematiche,*
> *e non edificate sanza fondamenti.*
>
> *Therefore O students study mathematics*
> *and do not build without foundations.*
>
> Leonardo da Vinci

2.1 Magnetohydrodynamics

Through observations of turbulent motions we know that astrophysical plasma are viscous media. The dynamics of viscous flows is described via the Navier-Stokes equations, which couple the velocity field with the density, the pressure and the viscous forces. Charge separation makes the media highly conducting, which brings the Maxwell equations into play which couple the charges and currents with the electromagnetic field. Combining the Navier-Stokes and Maxwell equations gives the equations of magnetohydrodynamics (MHD) for conducting fluids. The coupling between the velocity and electromagnetic field comes from the Lorentz force.

Differing inertia of electrons and positive ions make plasma sophisticated media to study, in particular in relativistic environments. For those systems studied here the inertia of the charge carrying particles can be neglected. As a consequence any charge separation will be balanced within fractions of the here relevant time scales, which leaves the medium charge neutral. In addition the conductivity of the medium is high enough such that the electric field can be neglected. Further, the maximum velocities of such media are often much less than the speed of light. Hence, the displacement current can be neglected in favor of the electric current density $\boldsymbol{J}$ from Ohm's law.

Under these realistic simplifications the MHD equations for an isothermal medium read:

$$\frac{\partial \boldsymbol{A}}{\partial t} = \boldsymbol{U} \times \boldsymbol{B} - \eta \mu_0 \boldsymbol{J}, \tag{2.1}$$

$$\frac{\mathrm{D}\boldsymbol{U}}{\mathrm{D}t} = -c_\mathrm{s}^2 \boldsymbol{\nabla} \ln\rho + \boldsymbol{J} \times \boldsymbol{B}/\rho + \boldsymbol{F}_\mathrm{visc} + \boldsymbol{f}, \tag{2.2}$$

$$\frac{\mathrm{D}\ln\rho}{\mathrm{D}t} = -\boldsymbol{\nabla} \cdot \boldsymbol{U}, \tag{2.3}$$

with the magnetic vector potential $\boldsymbol{A}$, the velocity $\boldsymbol{U}$, the magnetic field[1] $\boldsymbol{B} = \boldsymbol{\nabla} \times \boldsymbol{A}$, the magnetic diffusivity η, the isothermal speed of sound c_s, the fluid density ρ, the electric current density $\boldsymbol{J} = \boldsymbol{\nabla} \times \boldsymbol{B}/\mu_0$, the external forcing $\boldsymbol{f}$ and the advective time derivative $\frac{\mathrm{D}}{\mathrm{D}t} = \frac{\partial}{\partial t} + \boldsymbol{U} \cdot \boldsymbol{\nabla}$. In the following discussions I will use units for which $\mu_0 = 1$. The viscous force is given by

$$\boldsymbol{F}_\mathrm{visc} = \rho^{-1} \boldsymbol{\nabla} \cdot 2\nu\rho\mathsf{S}, \tag{2.4}$$

with the traceless rate of strain tensor

$$\mathsf{S}_{ij} = \frac{1}{2}\left(U_{i,j} + U_{j,i}\right) - \frac{1}{3}\delta_{ij} \boldsymbol{\nabla} \cdot \boldsymbol{U} \tag{2.5}$$

for a viscous monatomic gas with the viscosity ν. For all the systems in this work isothermality is assumed where the pressure is given as $p = \rho c_\mathrm{s}^2$. Anything else would change the equation of state and lead to an additional equation which involves internal energies in the form of temperature.

2.2 Amplification of Magnetic Fields

Typical strengths of magnetic fields observed in stars and galaxies are of the order of the equipartition value, i.e. their energies are comparable with the kinetic energy of the turbulent motions and scales comparable with the system size. A mechanism is needed to explain the efficient conversion between kinetic and magnetic energies such that the resulting magnetic field has sizes similar to the dimensions of the system. The large scales should be contrasted to the scales of the turbulent eddies. Similar to the electromagnetic dynamo, where mechanical work is transformed into electromagnetic energy, in astrophysical objects there exists a similar mechanism for transforming energies. The relevant induction equation for this case is equation (2.1).

The energy input for the turbulent motions can be easily explained to come from convection where heat provides a source for kinetic energy on large scales through the buoyant rise of material. In a nearly inviscid fluid large-scale motions of sufficient velocities are quickly transformed into small-scale motions via the turbulent cascade, where kinetic energy is dissipated into heat again. Given a weak magnetic seed field, the induction mechanism provides a way of converting motions into magnetic energy by inducing currents. The properties of these motions are crucial in the dynamo mechanism, as well as the environment of the system. The induced currents will lead to a loss of magnetic energy via Joule dissipation. The characteristics of this energy budget (Fig. 2.1)

---

[1] Common usage is to call $\boldsymbol{B}$ the magnetic field. In this work I will do so as well, although strictly speaking the magnetic field is $\boldsymbol{H}$ and $\boldsymbol{B}$ is the magnetic flux density.

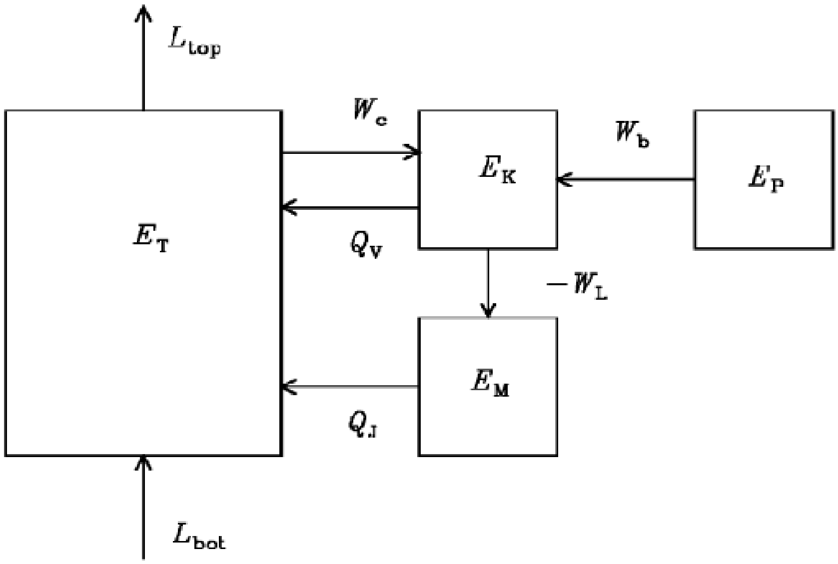

Figure 2.1: Energy budget for e.g. the solar dynamo (Brandenburg and Subramanian, 2005). The thermal energy E_{T} is supplied from the solar interior in form of radiation (L_{bot}), which heats the convection zone. Thermal radiation L_{top} at the Sun's surface provides a sink of energy, which balances L_{bot} in global thermal equilibrium. Buoyancy W_{C} cools the system down by creating motions E_{K}, which are resistively dissipated (Q_{V}). The Lorentz force W_{L} is responsible for transforming kinetic into magnetic energy E_{M}, which decays resistively via Joule heating Q_{J}. In the case of accretion discs also the potential energy E_{P} plays an important role.

strongly depend on various parameters and boundary conditions. Some of the magnetic energy can be in the form of large-scale magnetic fields, and their dynamics is probably best understood in the framework of mean-field theory.

2.2.1 Mean-Field Theory

As there is a clear separation of scales between the observed magnetic fields and the turbulent motions they can be treated as own entities, while any interaction between them might be determining for the dynamo process. In mean-field theory (Steenbeck et al., 1966; Krause and Rädler, 1971; Krause and Rädler, 1980) only the evolution of the mean quantities is considered, where every field $\boldsymbol{B}$ is split into its mean $\overline{\boldsymbol{B}}$ and fluctuating part $\boldsymbol{b}$ like

$$\boldsymbol{B} = \overline{\boldsymbol{B}} + \boldsymbol{b}. \tag{2.6}$$

How the mean $\overline{\boldsymbol{B}}$ is computed is not relevant, as long as it satisfies the Reynolds rules:

$$\overline{\overline{\boldsymbol{B}}_1+\overline{\boldsymbol{B}}_2}=\overline{\boldsymbol{B}}_1+\overline{\boldsymbol{B}}_2, \quad \overline{\overline{\boldsymbol{B}}}=\overline{\boldsymbol{B}}, \quad \overline{\boldsymbol{b}}=0 \tag{2.7}$$

$$\overline{\overline{\boldsymbol{B}}_1\overline{\boldsymbol{B}}_2}=\overline{\boldsymbol{B}}_1\overline{\boldsymbol{B}}_2, \quad \overline{\overline{\boldsymbol{B}}\boldsymbol{b}}=0, \quad \overline{\partial_\mu \boldsymbol{B}}=\partial_\mu \overline{\boldsymbol{B}}, \qquad \mu=0,1,2,3. \tag{2.8}$$

Commonly, averages over one or two spatial coordinates are taken for the mean fields, e.g.

$$\overline{\boldsymbol{B}}(z,t)=\int \boldsymbol{B}(\boldsymbol{x},t)\,\mathrm{d}x\,\mathrm{d}y. \tag{2.9}$$

What happens on scales of the turbulent motions which are not resolved, has to be modeled in a way which strongly depends on the problem. Transport coefficients then incorporate any effects coming from the small-scale fields and affect the mean fields. They directly appear in the evolution equations for the large-scale fields. Any back reaction from the large to the small scales does not need to be excluded. In modern mean-field models such back reactions are modeled by providing evolution equations for the transport coefficients together with the mean-fields.

The mean-field form of the induction equation (2.1) is easily obtained by applying the Reynolds rules:

$$\partial_t \overline{\boldsymbol{B}}=\eta\nabla^2\overline{\boldsymbol{B}}+\boldsymbol{\nabla}\times(\overline{\boldsymbol{U}}\times\overline{\boldsymbol{B}}+\overline{\boldsymbol{\mathcal{E}}}), \quad \boldsymbol{\nabla}\cdot\overline{\boldsymbol{B}}=0, \tag{2.10}$$

with the electromotive force (EMF) $\overline{\boldsymbol{\mathcal{E}}}=\overline{\boldsymbol{u}\times\boldsymbol{b}}$.

In order to dispose of fluctuating quantities in the EMF, it has to be modeled via the mean-fields. Which mean-field quantities are used depends on the relevant physics of the system, e.g. whether it is a rotating system. The from of $\overline{\boldsymbol{\mathcal{E}}}$ also depends on whether or not the system is isotropic. Probably the simplest form is by making $\overline{\boldsymbol{\mathcal{E}}}$ dependent only on the mean magnetic field $\overline{\boldsymbol{B}}$ (Steenbeck et al., 1966):

$$\mathcal{E}_i(\boldsymbol{x},t)=\mathcal{E}_i^{(0)}(\boldsymbol{x},t)+\int\int K_{ij}(\boldsymbol{x},\boldsymbol{x}',t,t')\overline{B}_j(\boldsymbol{x}-\boldsymbol{x}',t-t')\,\mathrm{d}^3x'\,\mathrm{d}t', \tag{2.11}$$

with the Einstein summation convention for double indices and the integration kernel $K_{ij}(\boldsymbol{x},\boldsymbol{x}',t,t')$. A Taylor expansion for $\overline{\boldsymbol{B}}$ simplifies its form to

$$\mathcal{E}_i=\alpha_{ij}\overline{B}_j+b_{ijk}\frac{\partial\overline{B}_j}{\partial x_k}+\ldots, \tag{2.12}$$

where it is also assumed that $\overline{\boldsymbol{B}}$ affects the EMF only instantaneously and locally. The coefficients are then integrals of the kernel:

$$\alpha_{ij} = \int\int K_{ij}(\boldsymbol{x},\boldsymbol{x}',t,t')\,\mathrm{d}^3x'\,\mathrm{d}t', \tag{2.13}$$

$$b_{ijk} = \int\int K_{ij}(\boldsymbol{x},\boldsymbol{x}',t,t')(x_k'-x_k)\,\mathrm{d}^3x'\,\mathrm{d}t'. \tag{2.14}$$

For homogeneous and isotropic systems the EMF attains the often used form

$$\boldsymbol{\mathcal{E}} = \alpha\overline{\boldsymbol{B}} - \eta_{\rm t}\boldsymbol{\nabla}\times\overline{\boldsymbol{B}}, \tag{2.15}$$

$$\alpha_{ij} = \alpha\delta_{ij}, \tag{2.16}$$

$$b_{ijk} = \eta_{\rm t}\varepsilon_{ijk}, \tag{2.17}$$

with the turbulent magnetic diffusivity $\eta_{\rm t} \approx u_{\rm rms}/(3k_{\rm f})$, where $u_{\rm rms}$ is the root mean square of the velocity and $k_{\rm f}$ the inverse length scale of the turbulence. Combining equation (2.15) with the mean-field induction equation (2.10) leads to the induction equation for the mean magnetic field

$$\frac{\partial\overline{\boldsymbol{B}}}{\partial t} = \boldsymbol{\nabla}\times(\alpha\overline{\boldsymbol{B}}) + \eta_{\rm T}\nabla^2\overline{\boldsymbol{B}}, \tag{2.18}$$

where $\eta_{\rm T} = \eta + \eta_{\rm t}$ is the total magnetic diffusivity, which has been assumed to be constant. It is readily clear that, given an initial seed magnetic field of any strength, the presence of α will enhance $\overline{\boldsymbol{B}}$, which leads to its exponential growth. A back reaction of $\overline{\boldsymbol{B}}$ on α is needed in order to stop the growth and make the field saturate. The form of α and its characteristics during saturation is discussed in section 2.2.2.

2.2.2 The α Effect

Modeling the form of α varies depending on the physical system. One of the simplest forms reads (Moffatt, 1978; Krause and Rädler, 1980)

$$\alpha = \alpha_{\rm K} = -\tau\overline{\boldsymbol{\omega}\cdot\boldsymbol{u}}/3, \tag{2.19}$$

with the small-scale vorticity $\boldsymbol{\omega} = \boldsymbol{\nabla}\times\boldsymbol{u}$ and the correlation time of the turbulence $\tau \approx 1/(u_{\rm rms}k_{\rm f})$. This implies that small-scale helical motions $\boldsymbol{u}$ are responsible for the exponential growth of the large-scale magnetic field $\overline{\boldsymbol{B}}$.

Without any quenching mechanism $\overline{\boldsymbol{B}}$ would grow indefinitely. A back reaction of $\overline{\boldsymbol{B}}$ on α when the system is close to equipartition is necessary. The algebraic quenching forms

$$\alpha = \alpha_{\rm K}(1 - \overline{\boldsymbol{B}}^2/B_{\rm eq}^2), \quad (\overline{\boldsymbol{B}}^2 \ll B_{\rm eq}^2), \tag{2.20}$$

with the equipartition field strength $B_{\rm eq}$ and

$$\alpha = \frac{\alpha_{\rm K}}{1 + \overline{\boldsymbol{B}}^2/B_{\rm eq}^2} \tag{2.21}$$

were introduced heuristically by Roberts and Soward (1975) and Ivanova and Ruzmaikin (1977), respectively. The dynamics of magnetized media strongly depends on the magnetic Reynolds number

$$\mathrm{Re}_\mathrm{M} = \frac{u_\mathrm{rms}}{\eta k_\mathrm{f}}. \tag{2.22}$$

Based on simulations, Vaĭnshteĭn and Cattaneo (1992) discovered the importance of the magnetic Reynolds number for the quenching. The resulting quenching is similar to equation (2.21)

$$\alpha = \frac{\alpha_\mathrm{K}}{1 + \mathrm{Re}_\mathrm{M}\overline{\boldsymbol{B}}^2/B_\mathrm{eq}^2} \tag{2.23}$$

and is called catastrophic α quenching, because for the Sun $\mathrm{Re}_\mathrm{M} \approx 10^9$ and galaxies $\mathrm{Re}_\mathrm{M} \approx 10^{15}$, so α would be too small to be meaningful for even $|\overline{\boldsymbol{B}}| \ll B_\mathrm{eq}$.

The construction of α provided by equation (2.19) did not take into account the conservation of magnetic helicity, which is true for astrophysical systems and dynamically relevant times. Under this constraint the total α (Pouquet et al., 1976) is

$$\alpha = \alpha_\mathrm{K} + \alpha_\mathrm{M} = -\tau\overline{\boldsymbol{\omega}\cdot\boldsymbol{u}}/3 + \tau\overline{\boldsymbol{j}\cdot\boldsymbol{b}}/(3\overline{\rho}). \tag{2.24}$$

So it is composed of the kinetic α_K and magnetic α_M. The presence of current helicity α_M will reduce α and provide an efficient quenching mechanism, which proves to be also dependent on the magnetic Reynolds number Re_M (see section 2.2.4). As α_M grows it will balance α_K and the dynamo saturates. For a system in a steady state equation (2.23) can be regained if the mean current density vanishes (Brandenburg and Subramanian, 2005).

2.2.3 α^2 Dynamo

In absence of any mean velocity field $\overline{\boldsymbol{U}}$ the growth of the dynamo is purely powered by the α effect. The induction equation for the mean magnetic field has the simple form of equation (2.18). As long as the mean magnetic field is so small that the Lorentz force does not provide any significant back reaction on the fluid, equation (2.18) can be linearized. One can search for solutions of the form

$$\overline{\boldsymbol{B}}(t) = \Re\left(\hat{\boldsymbol{B}}(k)\exp(\mathrm{i}\boldsymbol{k}\cdot\boldsymbol{x} + \lambda t)\right), \tag{2.25}$$

which results in the eigenvalue problem

$$\lambda\hat{\boldsymbol{B}}(k) = \begin{pmatrix} -\eta_\mathrm{T}k^2 & -\mathrm{i}\alpha k_z & \mathrm{i}\alpha k_y \\ \mathrm{i}\alpha k_z & -\eta_\mathrm{T}k^2 & -\mathrm{i}\alpha k_x \\ -\mathrm{i}\alpha k_y & \mathrm{i}\alpha k_x & -\eta_\mathrm{T}k^2 \end{pmatrix}\hat{\boldsymbol{B}}(k), \tag{2.26}$$

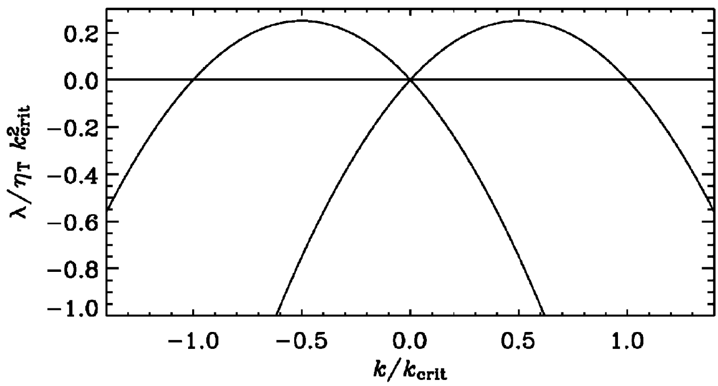

Figure 2.2: Dispersion relation for the mean-field α^2 dynamo, with the growth rate λ in dependence of the wave number. The critical wave number for dynamo action is $k_{\rm crit} = \alpha/\eta_{\rm T}$ (Brandenburg and Subramanian, 2005).

with the eigenvectors $\hat{\boldsymbol{B}}(k)$ and growth rates (roots) λ (Moffatt, 1978)

$$\lambda_0 = -\eta_{\rm T} k^2, \quad \lambda_\pm = -\eta_{\rm T} k^2 \pm |\alpha k|. \tag{2.27}$$

Depending on the value of α different modes get more or less strongly excited. The strongest excited mode is for $k_{\rm max} = \pm\alpha/(2\eta_{\rm T})$ (Fig. 2.2).

Injection of small-scale kinetic helicity leads to the creation of helical small-scale magnetic fields. Since the total magnetic helicity has to be conserved, a helical large-scale field arises with opposite helicity. As time evolves, the scale of the mean field becomes larger (Frisch et al., 1975; Léorat et al., 1975) until it reaches the size of the system. At the end of the saturation the magnetic energy spectrum shows two characteristic humps, one at the forcing scale, i.e. the scale of the turbulent motion, and another at the scale of the system (Brandenburg, 2001).

2.2.4 Magnetic Helicity Conservation

Magnetic helicity conservation is a crucial aspect for the saturation behavior of the large-scale magnetic field in dynamos. Astrophysically relevant cases for which helicity is conserved are closed systems and systems in which fluxes of helicity are so small that they are irrelevant on the time scales of interest. The presence of magnetic helicity not only slows down the saturation of the mean magnetic field, but also determines its saturation amplitude.

For a closed system the evolution equation of the mean magnetic helicity is

$$\frac{\rm d}{{\rm d}t} H_{\rm M}' = \frac{\rm d}{{\rm d}t} \langle \boldsymbol{A} \cdot \boldsymbol{B} \rangle = -2\eta \langle \boldsymbol{J} \cdot \boldsymbol{B} \rangle, \tag{2.28}$$

where $\langle . \rangle$ denote volume averages. In the steady state H'_{M} does not change in time. Splitting the field in mean and fluctuating parts results in the steady state condition

$$\langle \overline{\boldsymbol{J}} \cdot \overline{\boldsymbol{B}} \rangle = -\langle \boldsymbol{j} \cdot \boldsymbol{b} \rangle. \tag{2.29}$$

For a helically driven system the magnetic field and current density are partially helical:

$$\boldsymbol{\nabla} \times \overline{\boldsymbol{B}} = \pm \varepsilon_{\mathrm{m}} k_{\mathrm{m}} \overline{\boldsymbol{B}}, \qquad \boldsymbol{\nabla} \times \boldsymbol{b} = \mp \varepsilon_{\mathrm{f}} k_{\mathrm{f}} \boldsymbol{b}, \tag{2.30}$$

with the wave numbers of the small and large scales, k_{m} and k_{f}, and the fractional helicities ε_{m} and ε_{f}. The different signs in $\overline{\boldsymbol{B}}$ and $\boldsymbol{b}$ come from total current helicity conservation Eq. (2.29), which causes the helically driven dynamo to create helicities of opposite sign in the large and small scales. From equation (2.30) we obtain

$$\langle \overline{\boldsymbol{J}} \cdot \overline{\boldsymbol{B}} \rangle = \pm \varepsilon_{\mathrm{m}} k_{\mathrm{m}} \langle \overline{\boldsymbol{B}}^2 \rangle, \qquad \langle \boldsymbol{j} \cdot \boldsymbol{b} \rangle = \mp \varepsilon_{\mathrm{f}} k_{\mathrm{f}} \langle \boldsymbol{b}^2 \rangle. \tag{2.31}$$

Hence in the steady state we have

$$\langle \overline{\boldsymbol{B}}^2 \rangle = \frac{\varepsilon_{\mathrm{m}} k_{\mathrm{f}}}{\varepsilon_{\mathrm{f}} k_{\mathrm{m}}} \langle \boldsymbol{b}^2 \rangle. \tag{2.32}$$

Or for the fully helical case, i.e. $\varepsilon_{\mathrm{m}} = \varepsilon_{\mathrm{f}} = 1$:

$$\langle \overline{\boldsymbol{B}}^2 \rangle = \frac{k_{\mathrm{f}}}{k_{\mathrm{m}}} \langle \boldsymbol{b}^2 \rangle. \tag{2.33}$$

As the separation of scales $k_{\mathrm{f}}/k_{\mathrm{m}}$ increases, the saturation strength of the mean magnetic field increases with respect to the small-scale field. The conservation of magnetic helicity slows down the saturation of the mean magnetic field. The time which is needed to reach this state is dictated by the magnetic resistivity. Close to saturation the small- and large-scale current helicities cancel (see equation (2.28)). The current helicities can be expressed in terms of the magnetic helicity

$$\begin{aligned} \langle \overline{\boldsymbol{J}} \cdot \overline{\boldsymbol{B}} \rangle &= k_{\mathrm{m}}^2 \langle \overline{\boldsymbol{A}} \cdot \overline{\boldsymbol{B}} \rangle, && (2.34) \\ \langle \boldsymbol{j} \cdot \boldsymbol{b} \rangle &= k_{\mathrm{f}}^2 \langle \boldsymbol{a} \cdot \boldsymbol{b} \rangle. && (2.35) \end{aligned}$$

The small-scale magnetic field saturates with the end of the kinematic phase. This means that $\langle \boldsymbol{j} \cdot \boldsymbol{b} \rangle$ is approximately constant, but $\langle \overline{\boldsymbol{A}} \cdot \overline{\boldsymbol{B}} \rangle$ is not, so one neglects the time derivative of the small-scale magnetic helicity in equation (2.28), which for the steady state means

$$\frac{\mathrm{d}}{\mathrm{d}t} H'_{\mathrm{M}} \approx \frac{\mathrm{d}}{\mathrm{d}t} \langle \overline{\boldsymbol{A}} \cdot \overline{\boldsymbol{B}} \rangle = -2\eta k_{\mathrm{m}}^2 \langle \overline{\boldsymbol{A}} \cdot \overline{\boldsymbol{B}} \rangle - 2\eta k_{\mathrm{f}}^2 \langle \boldsymbol{a} \cdot \boldsymbol{b} \rangle, \tag{2.36}$$

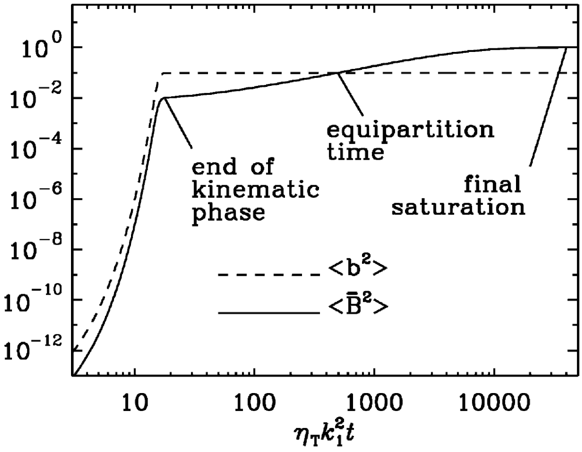

Figure 2.3: Time evolution of the mean magnetic energy $\langle \overline{\boldsymbol{B}}^2 \rangle$ and the energy in the small-scale fields $\langle \boldsymbol{b}^2 \rangle$ for an α^2 dynamo. The small-scale field grows exponentially and saturates within dynamical times. The large-scale field grows exponentially as well, after which its growth is dominated by the magnetic resistivity, which means a long resistive saturation phase (Brandenburg and Dobler, 2002).

which has the solution

$$\langle \overline{\boldsymbol{A}} \cdot \overline{\boldsymbol{B}} \rangle(t) = \langle \boldsymbol{a} \cdot \boldsymbol{b} \rangle(t) \frac{k_\mathrm{f}^2}{k_\mathrm{m}^2} \left(1 - e^{-2\eta k_\mathrm{m}^2 (t - t_\mathrm{sat})}\right). \tag{2.37}$$

As long as the dynamical time scale is much shorter than the resistive time scale, which for physically relevant problems is mostly the case, the small-scale magnetic helicity $\langle \boldsymbol{a} \cdot \boldsymbol{b} \rangle$ can be considered time independent close to saturation. For the mean magnetic field this means

$$\langle \overline{\boldsymbol{B}}^2 \rangle(t) = \langle \boldsymbol{b}^2 \rangle \frac{\varepsilon_\mathrm{f} k_\mathrm{f}}{\varepsilon_\mathrm{m} k_\mathrm{m}} \left(1 - e^{-2\eta k_\mathrm{m}^2 (t - t_\mathrm{sat})}\right). \tag{2.38}$$

The saturation time of the mean magnetic field, therefore, depends on the magnetic resistivity η (Fig. 2.3) as

$$\tau = (2\eta k_\mathrm{m}^2)^{-1}. \tag{2.39}$$

Astrophysical systems have such low values for η that τ exceeds the age of the object or even the age of the Universe. The most promising way to reduce the saturation time is by allowing for magnetic helicity fluxes (Blackman and Field, 2000; Kleeorin et al., 2000) as they are discussed in **Paper II**.

2.3 Gauge Freedom for Magnetic Helicity

Magnetic helicity is defined with the magnetic vector potential $\boldsymbol{A}$. For any potential there exists the freedom of choosing a gauge. The magnetic field $\boldsymbol{B}$ in terms of its vector potential $\boldsymbol{A}$ is $\boldsymbol{B} = \boldsymbol{\nabla} \times \boldsymbol{A}$. Adding the gradient of a scalar field ϕ to $\boldsymbol{A}$ does not change $\boldsymbol{B}$:

$$\boldsymbol{B}' = \boldsymbol{\nabla} \times (\boldsymbol{A} + \boldsymbol{\nabla}\phi) = \boldsymbol{\nabla} \times \boldsymbol{A} = \boldsymbol{B}, \tag{2.40}$$

since $\boldsymbol{\nabla} \times \boldsymbol{\nabla}\phi = 0$. Commonly used gauges include the Coulomb gauge, where $\boldsymbol{\nabla} \cdot \boldsymbol{A} = 0$, and the resistive gauge where the induction equation for $\boldsymbol{A}$ reads

$$\frac{\partial \boldsymbol{A}}{\partial t} = \boldsymbol{U} \times \boldsymbol{B} + \eta \boldsymbol{\nabla}^2 \boldsymbol{A}. \tag{2.41}$$

With the gauge freedom magnetic helicity density can change as well:

$$\boldsymbol{A} \cdot \boldsymbol{B} \to \boldsymbol{A} \cdot \boldsymbol{B} + \boldsymbol{\nabla}\phi \cdot \boldsymbol{B}. \tag{2.42}$$

Total magnetic helicity is in general gauge dependent too:

$$\begin{aligned} \int \boldsymbol{A} \cdot \boldsymbol{B} \, \mathrm{d}V \quad &\to \quad \int \boldsymbol{A}' \cdot \boldsymbol{B} \, \mathrm{d}V + \int \boldsymbol{\nabla}\phi \cdot \boldsymbol{B} \, \mathrm{d}V & (2.43) \\ &= \quad \int \boldsymbol{A}' \cdot \boldsymbol{B} \, \mathrm{d}V + \int_F \phi \boldsymbol{B} \cdot \, \mathrm{d}\boldsymbol{f}, & (2.44) \end{aligned}$$

where at the last step Gauss' theorem was used to transform the volume integral into a surface integral with surface normal $\boldsymbol{f}$. As long as the component of $\boldsymbol{B}$ normal to the bounding surface vanishes the magnetic helicity is gauge independent. Alternatively, periodic boundary conditions have the same result. Fluxes of magnetic helicity are gauge dependent too. From equation (2.1) the magnetic helicity flux can be derived as

$$\boldsymbol{F}_h = \boldsymbol{A} \times (\boldsymbol{U} \times \boldsymbol{B}) + \eta \boldsymbol{\nabla}\phi \times \boldsymbol{J}. \tag{2.45}$$

A gauge-invariant definition of the magnetic helicity is the relative magnetic helicity (Berger and Field, 1984). It is relative to a reference field $\boldsymbol{B}^{\mathrm{ref}} = \boldsymbol{\nabla} \times \boldsymbol{A}^{\mathrm{ref}}$:

$$H_{\mathrm{rel}} = \int (\boldsymbol{A} + \boldsymbol{A}^{\mathrm{ref}}) \cdot (\boldsymbol{B} - \boldsymbol{B}^{\mathrm{ref}}) \, \mathrm{d}V, \tag{2.46}$$

with $\boldsymbol{B}^{\mathrm{ref}} = \boldsymbol{\nabla}\phi$ and the boundary condition $\hat{\mathbf{n}} \cdot \boldsymbol{B}^{\mathrm{ref}} = \hat{\mathbf{n}} \cdot \boldsymbol{B}$, where $\hat{\mathbf{n}}$ is the normal vector at the surface.

Physically the gauge choice has no effect on the dynamics. On the other hand it will be shown that the presence of magnetic helicity fluxes does affect the evolution of the dynamo. In **Paper III** and **Paper IV** this apparent contradiction will be addressed.

2.4 Magnetic Field Relaxation and Stability

2.4.1 Relaxed States

Freely decaying magnetic fields try to develop a state of minimal magnetic energy. The evolution is, however, restricted. The presence of conserved quantities, most notably the magnetic helicity, constitute severe constraints. Finding the minimum of the magnetic energy under the constraint of constant magnetic helicity is a simple variational problem first investigated by Woltjer (1958). The resulting magnetic field obeys

$$\nabla \times \boldsymbol{B} = \alpha \boldsymbol{B}, \tag{2.47}$$

with constant α, thus constitutes a linear force-free field.

A more restrictive constraint was used by Taylor (1974), where the magnetic helicity along each field line has to be conserved. For an ergodic field, where one field line fills the whole space, the two restrictions are equivalent. For laboratory fields confined in tori, however, ergodic field lines may not necessarily exist. Instead one can think of a finite or infinite set of distinct field lines. In that case the minimal energy state is a non-linear force-free state

$$\nabla \times \boldsymbol{B} = \lambda(a,b) \boldsymbol{B}, \tag{2.48}$$

with $\lambda(a,b)$ varying between field lines, which are parameterized by a and b.

2.4.2 Frozen-in Magnetic Fields

For astrophysical objects magnetic resistivity is small enough, such that on dynamically relevant time scales the magnetic field can be considered frozen into the fluid (Batchelor, 1950; Priest and Forbes, 2000). Any magnetic field is transported with the fluid. This implies that the magnetic flux through any surface C does not change, since both fluid and magnetic field move jointly (Fig. 2.4). Flux freezing is a concept used in both, the flux transport dynamos (Choudhuri et al., 1995; Charbonneau et al., 1999) and the enhancements of magnetic energy via the stretch, twist and fold mechanism (Vaǐnshteǐn and Zel'dovich, 1972; Priest and Forbes, 2000).

2.4.3 Realizability Condition

The presence of magnetic helicity has important implications for the stability of the field. For a non-zero helicity spectrum $H_{\mathrm{M}}(k)$, the lowest value of the spectral magnetic energy $E_{\mathrm{M}}(k)$ that can be attained is given by the *realizability condition* (Arnold, 1974; Moffatt, 1978)

$$E_{\mathrm{M}}(k) \geq k|H_{\mathrm{M}}(k)|/2. \tag{2.49}$$

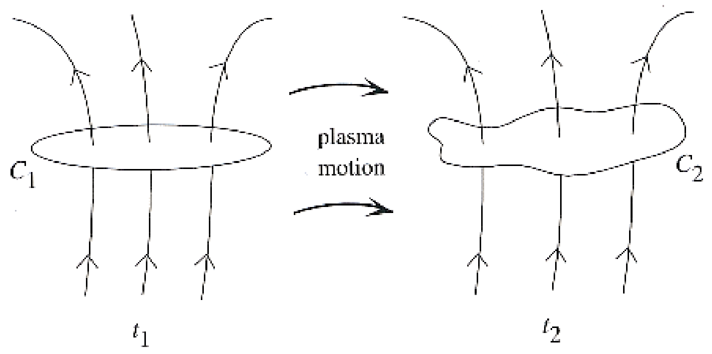

Figure 2.4: As the fluid evolves the surface C_1 gets distorted into the shape C_2. Because the magnetic field is frozen in for low magnetic resistivity the magnetic flux through surface C_2 is unchanged (Priest and Forbes, 2000, p. 24).

Together with the spectral magnetic energy $E_{\mathrm{M}}(k)$ also the total magnetic energy is bound by

$$E_{\mathrm{M}} \geq \int k|H_{\mathrm{M}}(k)|/2 \, \mathrm{d}k. \tag{2.50}$$

In that context the minimum value for the correlation length can be defined as (Tevzadze et al., 2012)

$$l_{\mathrm{corr}}^{\mathrm{min}} = |H_{\mathrm{M}}|/(2E_{\mathrm{M}}). \tag{2.51}$$

2.4.4 Topological Interpretation

A colorful interpretation of magnetic helicity is the mutual linkage of magnetic field lines. For instance two magnetic field lines can be linked into each other once (Fig. 1.3) or several times. The number of mutual linkage, i.e. the number the tubes wind around each other, is directly proportional to the total magnetic helicity (Moffatt, 1969; Moffatt and Ricca, 1992)

$$H_{\mathrm{M}} = \int_V \boldsymbol{A} \cdot \boldsymbol{B} \, \mathrm{d}V = 2n\phi_1\phi_2, \tag{2.52}$$

with the magnetic fluxes ϕ_1 and ϕ_2 through the magnetic field lines and the number of mutual linkage n. The picture also works for flux tubes with finite width but without internal twist or self-linking.

With this picture of magnetic helicity the realizability condition can be interpreted as the reluctance of the field to brake its field lines and change its topology. Hence the magnetic field provides a topological invariant, which not only qualifies the configuration (helical/non-helical), but even gives a quantitative measure for the linking of the field.

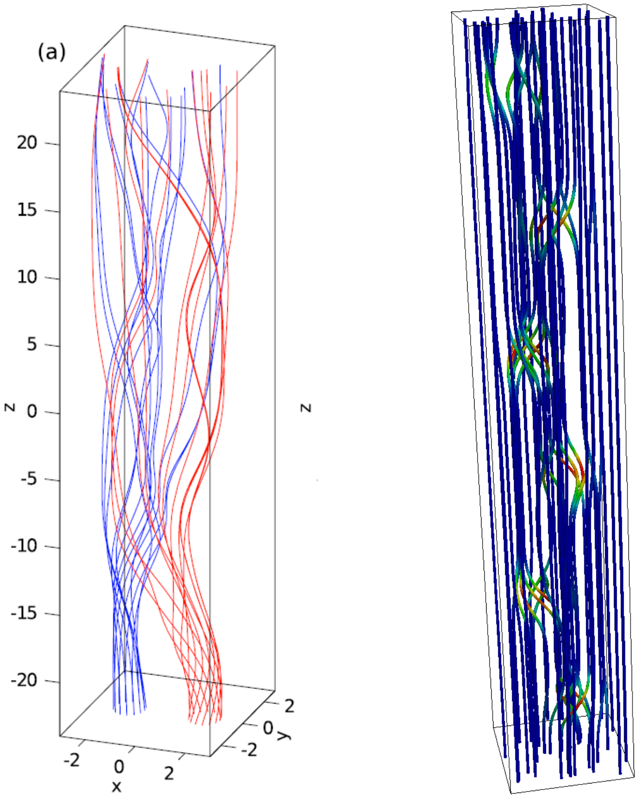

Figure 2.5: Magnetic field lines for the configuration used by Yeates et al. (2010) corresponding to the color mapping in Fig. 2.7.

2.4.5 Topology Beyond Magnetic Helicity

Magnetic helicity is not the only topological quantity which is conserved for low magnetic resistivity. Invariants of order three and four in the magnetic field were suggested by Ruzmaikin and Akhmetiev (1994), which are non-zero for field configurations without magnetic helicity, which makes them intriguing quantities to test decay properties with. The practical usage is, however, limited since they are defined for separate flux tubes and have not been expressed for arbitrary fields, like the linking number for magnetic helicity.

A more practical topological invariant, which is conserved for low magnetic diffusivity, is the fixed points index (see, e.g., Yeates et al. (2010)). It is defined for fields with a preferential direction, like toroidal tokamak fields or fields with a positive component in the z-direction (Fig. 2.5).

For such fields a mapping $(x,y) \rightarrow \boldsymbol{F}(x,y)$ can be defined between two surfaces, where the field lines start and end. Fixed points are those values for

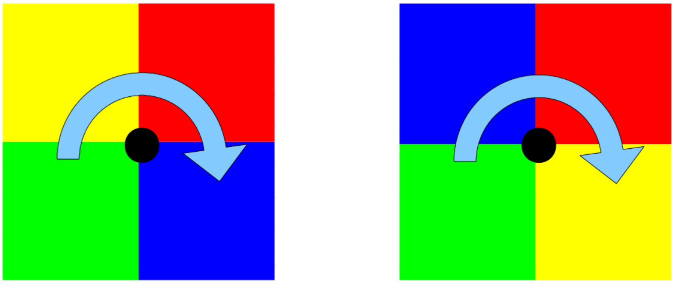

Figure 2.6: Neighborhood of fixed points with different color mappings. The left fixed point has positive sign, while the right has negative sign.

(x,y) for which the mapping is onto itself, i.e. $\boldsymbol{F}(x,y) = (x,y)$. They are signed and can be either $+1$ or -1. For a continuous mapping there is a neighborhood for each fixed point in which it is the only fixed point. Further, there exist points in this neighborhood for which the following inequalities hold:

$$F_x > x, \quad F_y > y, \tag{2.53}$$

$$F_x < x, \quad F_y > y, \tag{2.54}$$

$$F_x < x, \quad F_y < y, \tag{2.55}$$

$$F_x > x, \quad F_y < y. \tag{2.56}$$

Assigning a different color for each case gives the field line mapping of the field. The sign results from the sequence of the colors (Fig. 2.6). The sum over all fixed points gives the fixed point index, which is a conserved quantity in low resistivity MHD (Brown, 1971):

$$T = \sum_i t_i, \tag{2.57}$$

with the sign of the ith fixed point t_i.

Even for simple magnetic fields (Fig. 2.5, right panel) the color mapping can be complex (Fig. 2.7, left panel). The complexity comes about in a similar fashion as in the two-dimensional stirring in fluids (Boyland et al., 2000), where stirring corresponds to braiding of field lines. The number of initial fixed points for the configuration in Fig. 2.5 (right panel) is 26. The fixed points index, however, is 2. After resistive time evolution fixed points of opposite signs merge, while the fixed point index is conserved (Fig. 2.7, right panel).

The conservation of the fixed point index imposes an additional constraint in magnetic field relaxation. In practice it turns out that the field does not reach the Taylor state and retains higher energies.

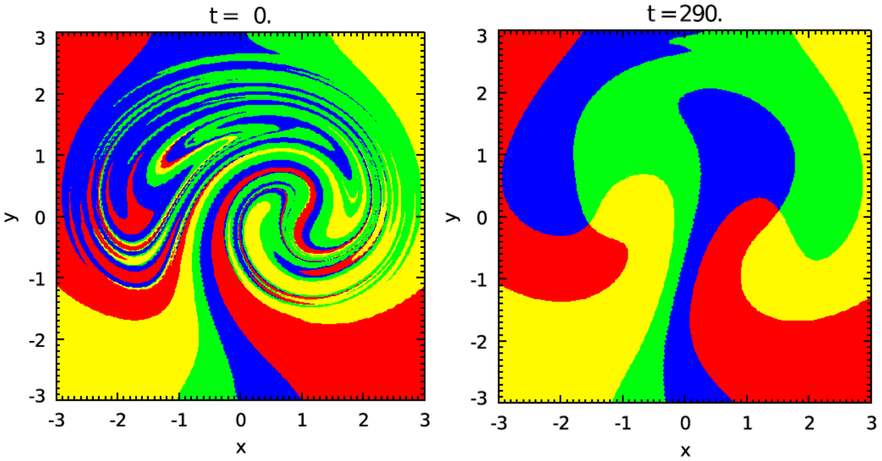

Figure 2.7: Color mapping for the configuration illustrated in Fig. 2.5 at initial time (left) and after some time evolution (right) (Yeates et al., 2010).

2.5 Observing Helical Magnetic Fields

The gauge dependence of magnetic helicity density makes it difficult to measure it directly. As a proxy the current helicity $\boldsymbol{J} \cdot \boldsymbol{B}$ is often used (Yeates et al., 2008). Its measurement is still not easy, since only recently all three components of $\boldsymbol{B}$ could be measured at the solar surface. Prior to that, force-free assumptions were used for field line extrapolation (Gibson et al., 2002).

For helical large-scale structures no direct measurements of $\boldsymbol{B}$ are necessary to infer the helical nature of magnetic fields on, e.g., the Sun's surface. Emerging coronal loops often carry hot plasma with them, which is trapped in the magnetic flux tubes. The plasma can only move along the field lines due to strong Lorentz forces (Fig. 2.8). Often those loops show a pig tail like shape, which suggests large-scale magnetic helicity. Force-free extrapolations support the observation of twisted magnetic loops (Fig. 2.9). The force free assumption is, however, only valid at heights of 400 km and above the photosphere (Metcalf et al., 1995), which casts some doubt on such extrapolations, although they reproduce the loops observed in X-ray observations.

Helical structures have implications for the dynamics of the Sun's plasma. It has been shown that N- and S-shaped helical regions are more likely to result in coronal mass ejections (Canfield et al., 1999). The Sun, therefore, possibly sheds magnetic helicity, which has far reaching implications for the dynamo mechanism.

Figure 2.8: SOHO observations of coronal mass ejections. The image to the right was taken in May 7 2010.

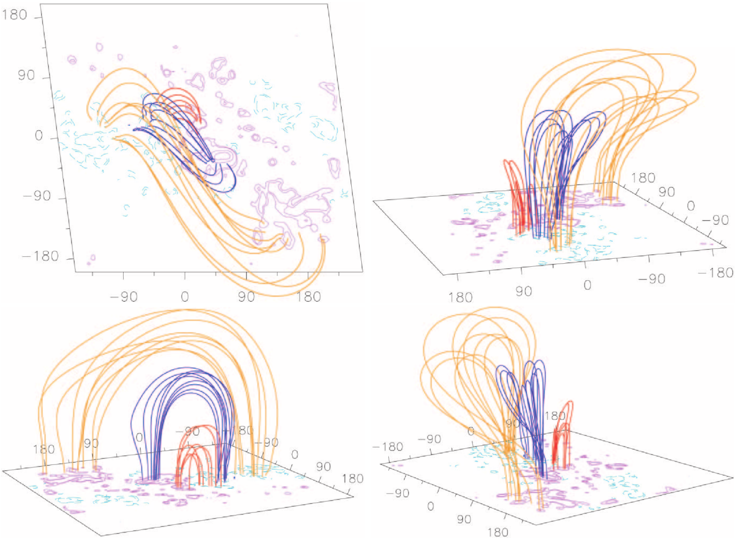

Figure 2.9: Force-free extrapolation of the Sun's surface magnetic field from data taken August 21 1999 (Gibson et al., 2002).

3. Magnetic Helicity Conservation and Fluxes in Turbulent Dynamos

Do you include turbulence?

popular saying

3.1 Magnetic Helicity Conservation in α^2 Dynamos

For the helically driven α^2 dynamo the growth rate of the different modes depends on the forcing α and the wave number k as (Blackman and Brandenburg, 2002)

$$\lambda = \alpha k - \eta_{\mathrm{T}} k^2 = (C_\alpha - 1)\eta_{\mathrm{T}} k^2, \tag{3.1}$$

where $C_\alpha = \alpha_{\mathrm{K}}/(\eta_{\mathrm{T}} k)$ is the dynamo number for the α^2 dynamo. The onset value for dynamo action is obviously at $C_\alpha = 1$. In the limit of high conductivity (Moffatt, 1978; Krause and Rädler, 1980) we have $\alpha_{\mathrm{K}} = -(\tau/3)\langle \boldsymbol{\omega} \cdot \boldsymbol{u} \rangle$ and $\eta_{\mathrm{t}} = (\tau/3)\langle \boldsymbol{u}^2 \rangle$. This allows us to reformulate the expression for the dynamo coefficient C_α such that it reads

$$C_\alpha = -\frac{\langle \boldsymbol{\omega} \cdot \boldsymbol{u} \rangle}{k\langle \boldsymbol{u}^2 \rangle \iota}, \tag{3.2}$$

with the correction factor $\iota = \eta_{\mathrm{T}}/\eta_{\mathrm{t}}$. With the normalized helicity for the small-scale field $\varepsilon_{\mathrm{f}} = \langle \boldsymbol{\omega} \cdot \boldsymbol{u} \rangle / (k_{\mathrm{f}} \langle \boldsymbol{u}^2 \rangle)$ we can write

$$C_\alpha = -\frac{\varepsilon_{\mathrm{f}} k_{\mathrm{f}}}{k_{\mathrm{m}} \iota}. \tag{3.3}$$

The normalized kinetic helicity has to be contrasted with the relative helicity, also called fractional helicity, which is defined in a similar fashion as

$$\tilde{\varepsilon}_{\mathrm{f}} = \frac{\langle \boldsymbol{\omega} \cdot \boldsymbol{u} \rangle}{\omega_{\mathrm{rms}} u_{\mathrm{rms}}}, \tag{3.4}$$

with the root mean square values of the vorticity $\omega_{\mathrm{rms}} = \sqrt{\langle \boldsymbol{\omega}^2 \rangle}$ and velocity $u_{\mathrm{rms}} = \sqrt{\langle \boldsymbol{u}^2 \rangle}$. From equation (3.3) one sees that the critical value of the normalized helicity for dynamo action scales like $\varepsilon_{\mathrm{f}} \propto (k_{\mathrm{f}}/k_{\mathrm{m}})^{-1}$ with the scale separation ratio $k_{\mathrm{f}}/k_{\mathrm{m}}$:

$$\varepsilon_{\mathrm{f}}^{\mathrm{crit}} = \iota \varepsilon_{\mathrm{m}} \left(\frac{k_{\mathrm{f}}}{k_{\mathrm{m}}} \right)^{-1}, \tag{3.5}$$

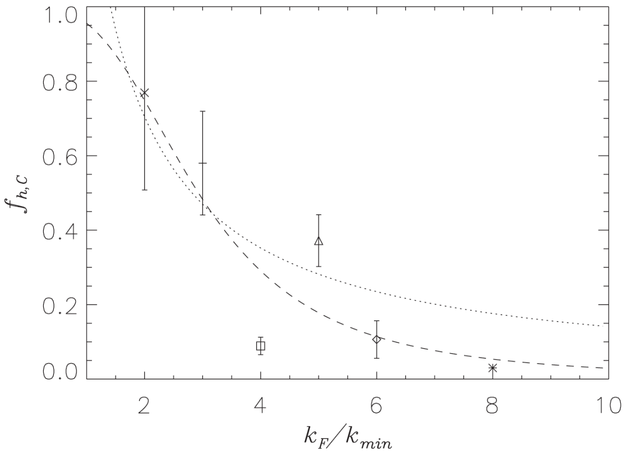

Figure 3.1: Critical values for the fractional helicity f_h in dependence of the scale separation value together with a power law fit (dashed line) and the analytical prediction from mean-field theory given by equation (3.5) (dotted line) (Pietarila Graham et al., 2012).

with the normalized kinetic helicity of the large-scale field

$$\varepsilon_\mathrm{m} = \frac{\langle \overline{\boldsymbol{J}} \cdot \overline{\boldsymbol{B}} \rangle}{k_\mathrm{m} \langle \overline{\boldsymbol{B}}^2 \rangle}. \tag{3.6}$$

Conservation of magnetic helicity still allows for an increase of magnetic helicity at small and large scale if they have opposite signs (Seehafer, 1996; Ji, 1999). In its continuous creation the large scales become even larger (Frisch et al., 1975) until the dynamo saturates with strong magnetic fields in scales of the system size (Blackman and Brandenburg, 2002; Brandenburg et al., 2002). The saturation mean magnetic energy $\overline{B}_\mathrm{sat}$ in dependence of the dynamo number C_α for a closed or periodic system is easily obtained from mean-field theory (Blackman and Brandenburg, 2002):

$$\overline{B}^2_\mathrm{sat}/B^2_\mathrm{eq} = (|C_\alpha| - 1)\,\iota. \tag{3.7}$$

Contrary to this established theory a different scaling was recently found by Pietarila Graham et al. (2012), who predicted a dependence of the form

$$\varepsilon_\mathrm{f}^\mathrm{crit} \propto (k_\mathrm{f}/k_\mathrm{m})^{-3} \tag{3.8}$$

for the critical normalized helicity (Fig. 3.1). The injection of kinetic helicity causes the magnetic field to be helical with magnetic helicity in the small and large scales of opposite sign. As long as the system is closed or periodic, as it is the case in (Pietarila Graham et al., 2012), the build-up of small-scale magnetic helicity reduces the α effect and the growth of the large-scale magnetic field. In practice this means that after a short exponential growth the mean magnetic field continues growing slowly and saturates on a resistive time scale, which can be large compared to the dynamical time scales for astrophysical systems.

The discrepancy in Pietarila Graham et al. (2012) with the semi analytical predictions from equation (3.3) comes from the method used in determining $C_\alpha^{\rm crit}$. As they only looked at the growth rate of the largest mode at $k = 1$ shortly after the exponential phase at a small fraction of the resistive times, the field will be contaminated by small-scale contributions. The large-scale field becomes dominant at later times when nonlinear effects suppress the small-scale field.

To shed light on this issue, we investigate in **Paper I** the saturation characteristics of a large-scale dynamo in the non-linear regime for a helically driven dynamo in a periodic cube shaped domain, similar to Pietarila Graham et al. (2012). The equations to be solved for this problem are the usual resistive, viscous MHD equations for an isothermal medium:

$$\begin{aligned}
\frac{\partial}{\partial t}\boldsymbol{A} &= \boldsymbol{U}\times\boldsymbol{B}-\eta\boldsymbol{J}, && (3.9)\\
\frac{\mathrm{D}}{\mathrm{D}t}\boldsymbol{U} &= -c_{\rm s}^2\boldsymbol{\nabla}\ln\rho+\frac{1}{\rho}\boldsymbol{J}\times\boldsymbol{B}+\boldsymbol{F}_{\rm visc}+\boldsymbol{f}, && (3.10)\\
\frac{\mathrm{D}}{\mathrm{D}t}\ln\rho &= -\boldsymbol{\nabla}\cdot\boldsymbol{U}, && (3.11)
\end{aligned}$$

where the forcing function $\boldsymbol{f}$ is delta correlated in time and provides the energy input. The applied magnetic Reynolds numbers are around 6 in a first set of cases with scale separation values of up to 80. In the latter part we use $\mathrm{Re}_{\rm M}$ values between 80 and 320 at a scale separation value of $k_{\rm f}/k_{\rm m} = 5$. The magnetic Prandtl number $\mathrm{Pr}_{\rm M} = \eta/\nu$ is unity if nothing else is stated.

As kinetic energy is injected the magnetic field in both, small- and large-scales grows exponentially during the kinematic phase. Since the system is isotropic, either the xy, xz or yz averaged magnetic field will be dominant (Fig. 3.2), while the other modes die out. Helicity conservation causes the field to saturate slowly on resistive times, which means the magnetic energy M behaves like (Brandenburg, 2001)

$$M(t) = M_0 - M_1 e^{-t/\tau} \qquad (3.12)$$

in the resistive phase, where M_0 is the saturation energy and M_1 the initial energy of the simulation run. The resistive time for saturation is given as

$$\tau = (2\eta k_{\rm m}^2)^{-1}. \qquad (3.13)$$

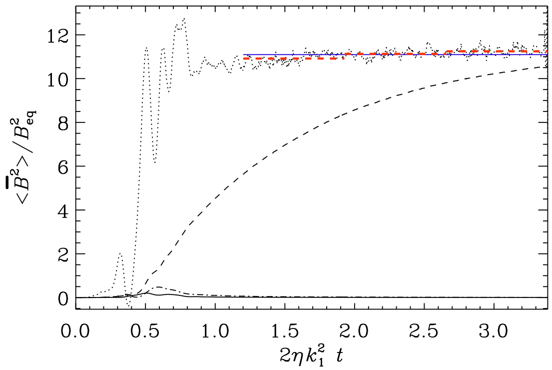

Figure 3.2: Normalized mean magnetic energies in resistive times. The strongest growing mode is the xz average $\langle \boldsymbol{B}\rangle_{xz}$ (dashed line). The xy (solid) and yz (dash-dotted) averages die out. The dotted line represents $\langle \boldsymbol{B}^2\rangle + \tau \mathrm{d}\langle \boldsymbol{B}^2\rangle/\mathrm{d}t$, which was used to compute the saturation magnetic field strength without letting the system saturate.

To speed up the calculation of the saturated magnetic field strength a short cut is taken, where the saturation magnetic energy is computed as the time average of

$$\tilde{M}_0(t) = \langle \overline{\boldsymbol{B}}^2\rangle + \tau \mathrm{d}\langle \overline{\boldsymbol{B}}^2\rangle/\mathrm{d}t, \tag{3.14}$$

which comes from taking the time derivative of equation (3.12).

For different scale separation ratios and normalized magnetic helicities the mean saturation magnetic energy is determined (Fig. 3.3). As predicted by equation (3.7) the saturation magnetic energy behaves linearly with the dynamo number C_α. Further, the critical value for large-scale dynamo action to start ($C_\alpha^{\mathrm{crit}} = 1$) is approximately reproduced. For the critical value we find $C_\alpha^{\mathrm{crit}} \approx 1.2$, which results in a critical value for the normalized helicity

$$\varepsilon_{\mathrm{f}}^{\mathrm{crit}} \approx 1.2\iota(k_{\mathrm{f}}/k_{\mathrm{m}})^{-1} = 1.7(k_{\mathrm{f}}/k_{\mathrm{m}})^{-1}, \tag{3.15}$$

where we use an averaged magnetic Reynolds number that leads to an averaged $\iota \approx 1.41$.

For fixed scale separation ratio, equation (3.7) together with equation (3.3) predict a linear dependence of the saturation energy on the normalized helicity. We plot the normalized magnetic energy for various scale separation ratios in dependence of ε_{f} and make linear fits (Fig. 3.4), from which we can extrapolate the critical values $\varepsilon_{\mathrm{f}}^{\mathrm{crit}} \approx 1.7(k_{\mathrm{f}}/k_{\mathrm{m}})^{-1}$. The extrapolated values for $\varepsilon_{\mathrm{f}}^{\mathrm{crit}}$ agree well with the theory (Fig. 3.5) and the values extracted from Fig. 3.3.

The theoretical predictions for the closed α^2 dynamo are verified in direct numerical simulations. In order to refute the findings by Pietarila Graham et al. (2012), their parameters have to be accommodated in our investigations.

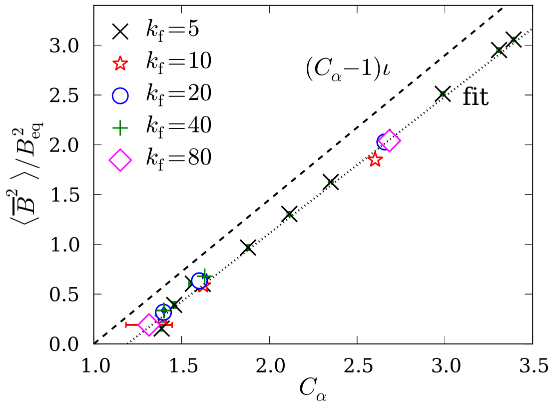

Figure 3.3: Normalized saturation energy of the mean magnetic field in dependence of C_α for various scale separation values. The dashed line is the theoretical prediction given by equation (3.7).

Therefore, high magnetic Reynolds numbers between 80 and 320 are used with magnetic Prandtl numbers 1 and 100. In this case the scale separation ratio is fixed to $k_\mathrm{f}/k_\mathrm{m} = 5$. The dependence of the normalized magnetic energy (Fig. 3.6, for $\mathrm{Pr_M} = 1$) is shown to behave similarly to the case with $\mathrm{Re_M} = 6$. For higher magnetic Prandtl numbers, however, the slope is higher. This behavior can be explained by different values for the equipartition strength B_eq, which is supposed to become smaller for increasing $\mathrm{Pr_M}$, due to the shifted dissipation range. Any different behavior at magnetic Reynolds numbers of 1500, as used by Pietarila Graham et al. (2012), is not to be expected. As a consequence we can refute their findings.

In summary, the theoretical predictions coming from mean-field consideration (equations (3.5) and (3.7)) are well confirmed for the closed α^2 dynamo, which constitutes one of the simplest possible dynamo setups and is often used as reference. The findings by Pietarila Graham et al. (2012) are at variance, most likely because their large-scale dynamo was contaminated by the small-scale dynamo. The present investigation about the non-linear behavior of the large-scale dynamo provides an important confirmation of the general theory.

3.2 Magnetic Helicity Fluxes

The injection of small-scale magnetic helicity causes the small- and large-scale magnetic helicity to grow with opposite sign. The presence of small-scale magnetic helicity $\overline{h}_\mathrm{f} = \overline{\boldsymbol{a}\cdot\boldsymbol{b}}$ causes the total α effect to diminish (Gruzinov and Diamond, 1994), such that the growth of the large-scale magnetic field gets quenched (see **Paper I**). Fluxes of this quantity could alleviate this quenching

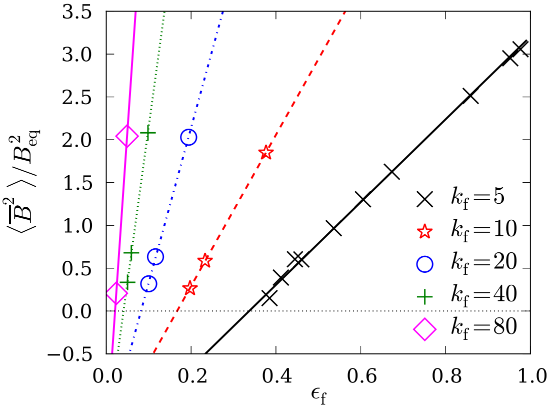

Figure 3.4: Normalized saturation energy of the mean magnetic field in dependence of $\varepsilon_{\rm f}$ for various scale separation values. Equation (3.5) predicts a linear dependence of $\langle\overline{\boldsymbol{B}}^2\rangle/B_{\rm eq}^2$ on $\varepsilon_{\rm f}$, which is shown in the linear fits (lines).

by reducing its value. There are various ways of creating such fluxes (Kleeorin and Rogachevskii, 1999; Vishniac and Cho, 2001; Subramanian and Brandenburg, 2004). Not all of them help in alleviating catastrophic α quenching. In **Paper II** we discuss the most promising type of flux (Blackman and Field, 2000).

Quenching of the α effect becomes more pronounced as the magnetic Reynolds number increases such that for physically relevant values of $\mathrm{Re_M}$ any large-scale dynamo becomes impossible to drive. That is why it is called catastrophic α quenching. To address the question whether magnetic helicity fluxes have any significant effect on the alleviation of the α quenching mechanism high magnetic Reynolds numbers are required of e.g. 10^5. Such simulations require computational resources, which are currently not available. To circumvent this shortcoming we employ the mean-field theory in one dimension and employ magnetic Reynolds numbers in the range of $\mathrm{Re_M} = 2$ to $\mathrm{Re_M} = 10^5$. The mean quantities are spatial averages in x- and y-direction. Any change of variables only occurs in the z-direction, which can be physically interpreted as the vertical distance from the galactic mid-plane or the vertical distance from the equator of the Sun. The domain is limited to the range $0 < z < H$. Because we expect the magnetic field to develop either a symmetric or antisymmetric mode (Krause and Rädler, 1980) the boundaries at $z = 0$ are chosen accordingly such that the field is symmetric or antisymmetric about the mid-plane depending on the type of flux. In physical terms, the x- and y-components can be regarded as poloidal and toroidal components of the fields.

The driving, or energy input, comes from an imposed kinetic α effect, which has a linearly increasing profile switching sign across the equator (Fig. 3.7,

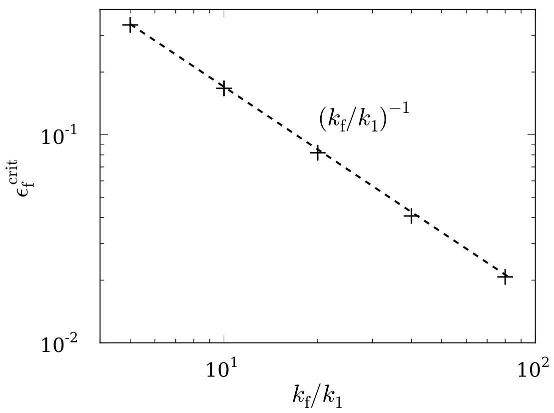

Figure 3.5: Minimal values for the normalized kinetic helicity for which large-scale dynamo action occurs in dependence of the scale separation value.

upper panel):

$$\alpha_K = \alpha_0 z/L, \tag{3.16}$$

with the size of the domain L. The total α effect is the sum of the kinetic and magnetic α effects. The latter is proportional to the current helicity and can be well approximated by the magnetic helicity, since the developing field is expected to be helical:

$$\alpha_M = \frac{\tau}{3}\overline{\boldsymbol{j}\cdot\boldsymbol{b}}/\overline{\rho} \approx \frac{\tau}{3}k_f^2\overline{\boldsymbol{a}\cdot\boldsymbol{b}}/\overline{\rho}, \tag{3.17}$$

with the turbulence correlation time τ, the small-scale current density $\boldsymbol{j}$, magnetic field $\boldsymbol{b}$ and magnetic vector potential $\boldsymbol{a}$ and the average fluid density $\overline{\rho}$.

The evolution equations for the magnetic helicity in the small and large scales are

$$\frac{\partial \overline{h}_m}{\partial t} = 2\overline{\boldsymbol{\mathcal{E}}}\cdot\overline{\boldsymbol{B}} - 2\eta\overline{\boldsymbol{J}}\cdot\overline{\boldsymbol{B}} - \nabla\cdot\overline{\boldsymbol{F}}_m, \tag{3.18}$$

$$\frac{\partial \overline{h}_f}{\partial t} = -2\overline{\boldsymbol{\mathcal{E}}}\cdot\overline{\boldsymbol{B}} - 2\eta\overline{\boldsymbol{j}\cdot\boldsymbol{b}} - \nabla\cdot\overline{\boldsymbol{F}}_f, \tag{3.19}$$

with the magnetic helicity fluxes for the small and large scales $\overline{\boldsymbol{F}}_f$ and $\overline{\boldsymbol{F}}_m$ given as

$$\overline{\boldsymbol{F}}_m = \overline{\boldsymbol{E}}\times\overline{\boldsymbol{A}}, \qquad \overline{\boldsymbol{F}}_f = \overline{\boldsymbol{e}\times\boldsymbol{a}}, \tag{3.20}$$

where $\boldsymbol{E}$ is the electric field. A term of the form $\overline{\boldsymbol{\mathcal{E}}}\cdot\overline{\boldsymbol{B}}$ in equations (3.18) and (3.19) does not occur in the equation for the total magnetic helicity, because this term is only a property of the mean-fields. It makes sure that magnetic helicity is exchanged between the two scales. Equations (3.17) and (3.19)

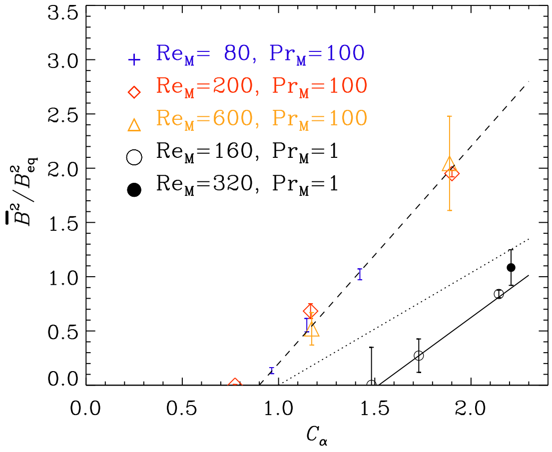

Figure 3.6: Normalized magnetic energy in the steady state in dependence of C_α for various magnetic Reynolds numbers and magnetic Prandtl numbers together with fits (dashed and solid line) and the theoretical prediction from equation (3.7) (dotted line).

give rise to the evolution equation of $\alpha_{\rm M}$, the dynamical quenching formula (Kleeorin and Ruzmaikin, 1982), expressed as

$$\frac{\partial \alpha_{\rm M}}{\partial t} = -2\eta_{\rm t} k_{\rm f}^2 \left(\frac{\overline{\boldsymbol{\mathcal{E}}}\cdot\overline{\boldsymbol{B}}}{B_{\rm eq}^2} + \frac{\alpha_{\rm M}}{\mathrm{Re_M}} \right) - \frac{\partial}{\partial z}\overline{F}_\alpha, \tag{3.21}$$

where $\overline{F}_\alpha$ is the z-component of the flux for $\alpha_{\rm M}$ given as

$$\overline{F}_\alpha = \frac{\mu_0 \overline{\rho} \eta_{\rm t} k_{\rm f}^2}{B_{\rm eq}^2} \overline{\boldsymbol{F}}_{\rm f}^z. \tag{3.22}$$

Apart from equation (3.21) we also solve the induction equation for the mean magnetic field

$$\partial_t \overline{\boldsymbol{B}} = \eta \nabla^2 \overline{\boldsymbol{B}} + \nabla \times (\overline{\boldsymbol{U}} \times \overline{\boldsymbol{B}} + \overline{\boldsymbol{\mathcal{E}}}) \tag{3.23}$$

and the EMF

$$\overline{\boldsymbol{\mathcal{E}}} = \alpha \overline{\boldsymbol{B}} - \eta_{\rm t} \overline{\boldsymbol{J}}. \tag{3.24}$$

It should be pointed out that no momentum or continuity equation are solved, which is chosen for simplicity and to screen off any other non-linear effects.

The form of the fluxes in equation (3.21) is chosen to be either of advective or diffusive nature. For the advective fluxes we impose a mean velocity field, which increases linearly with z (Fig. 3.7, lower panel) of the form $\overline{\boldsymbol{U}}_z = U_0 z/H$, with the scale height H, which is taken from the model used by Shukurov et al. (2006). The motivation comes from observations of galactic outflows

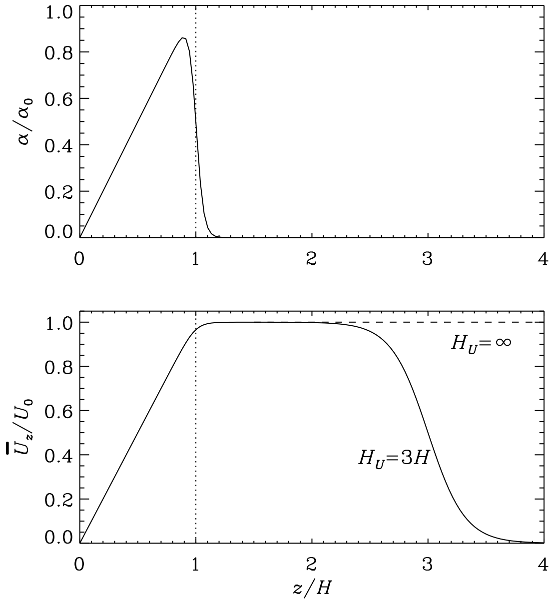

Figure 3.7: Profile of the kinetic α effect (upper panel) and the velocity profile for the case of fluxes through wind (lower panel).

where the outflow speed increases approximately linearly with distance from the galactic center (Shapiro and Field, 1976; Bregman, 1980). The wind drags the magnetic field along with magnetic helicity, which is being shed at the open boundaries. The form of open boundaries condition is $\overline{A}_{x,z} = \overline{A}_{y,z} = \overline{A}_z = 0$. This is frequently called vertical field condition, which becomes clear when writing it in terms of the magnetic field:

$$\overline{\boldsymbol{B}} = \boldsymbol{\nabla} \times \overline{\boldsymbol{A}} = \begin{pmatrix} -\overline{A}_{y,z} \\ \overline{A}_{x,z} \\ 0 \end{pmatrix}. \tag{3.25}$$

For the diffusive fluxes there is no need for open boundaries, which is why they are taken to be closed (perfect conductor), i.e. $\overline{A}_x = \overline{A}_y = 0$. Any fluxes are supposed to occur through the equator and are of the form

$$\overline{F}_\alpha = -\kappa_\alpha \frac{\partial \alpha_{\rm M}}{\partial z}, \tag{3.26}$$

with a diffusion coefficient κ_α. Since the outer boundaries are closed, the only place where diffusive fluxes can occur is at the equator.

The given setup is one of the most simple ones for which dynamo action can be expected. Under the given conditions a mean magnetic field should

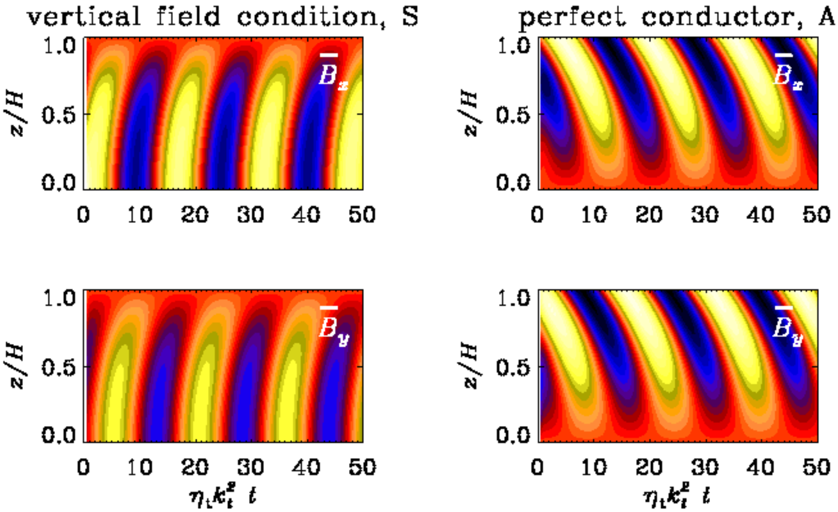

Figure 3.8: x- and y-component of the mean magnetic field for the case of an imposed wind (left panels) and no wind but diffusive fluxes through the equator (right panel) in dependence of time and the distance from the equator.

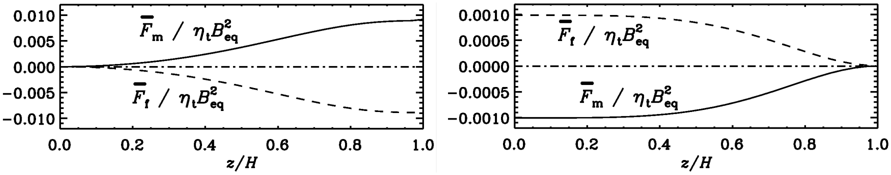

Figure 3.9: Magnetic helicity fluxes of the small- (dashed line) and large-scale fields (solid line) in dependence of the distance from the equator for the case of open boundaries and advective fluxes (left panel) and closed boundaries and diffusive fluxes (right panel).

develop after a time which is well below the resistive time. Indeed, a strong large-scale magnetic field develops and in both cases it shows an oscillatory behavior (Fig. 3.8).

Since the dynamo is working, it is now of interest to know what the effect of the fluxes is, in particular with respect to the dynamical α quenching. The advective fluxes efficiently transport small-scale magnetic helicity out of the domain (Fig. 3.9, left panel). The rate of field transport is chosen low enough not to transport too much magnetic energy out of the dynamo region, which would destroy any amplification effect. It is strong enough to alleviate the catastrophic α quenching and allow the dynamo to work even at high magnetic Reynolds numbers (Fig. 3.10, left panel). Diffusive fluxes through the equator (Fig. 3.9, right panel) allow to alleviate the catastrophic α quenching as well

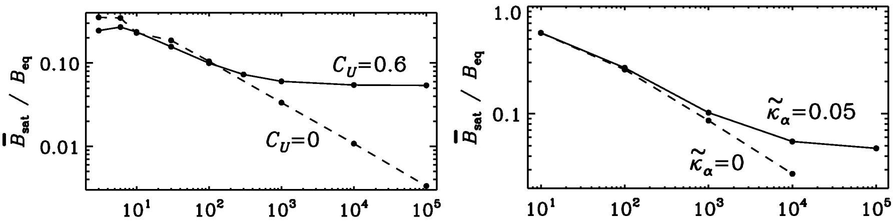

Figure 3.10: Mean magnetic field strength at saturation in dependence of the magnetic Reynolds number Re_M for the case with wind (left panel, solid line) and with diffusive fluxes (right panel, solid line). The cases without any fluxes are represented by dashed lines. Advective an diffusive fluxes efficiently alleviate the catastrophic quenching. Without fluxes catastrophic quenching makes the saturation field drop like $\mathrm{Re}_\mathrm{M}^{-1/2}$.

(Fig. 3.10, right panel). For physical systems like the Sun this implies that as long as it shuffles around magnetic helicity between both hemispheres, such that the small-scale magnetic helicity diminishes, catastrophic α quenching can be alleviated.

Contrary to the algebraic quenching formalisms, where a heuristic formula is proposed for the decrease of α as the mean-field saturates, the dynamical quenching formalism provides a more self-consistent approach. The alleviation of the quenching comes not unexpectedly. As long as the advective wind does not remove too much magnetic energy it merely sheds the magnetic helicity and the α effect does not get quenched. This case is of physical relevance for the galactic dynamo for which small-scale magnetic helicity can be shed through the observed galactic winds. The diffusive fluxes are relevant for systems like our Sun where there exists a sign reversal for the kinetic helicity across the equator. As consequence also the magnetic helicity switches signs (Blackman and Brandenburg, 2003). Fluxes out of the Sun can be mediated by coronal mass ejections, which occur at regions where the magnetic field is helical. For example, Warnecke et al. (2011) found that in a spherical shell dynamo, the flux through the surface from ejections is almost twice as large as the flux through the equator.

4. Gauge Dependencies

> *Take advantage of the ambiguity in the world.*
> *Look at something and think what else it might be.*
>
> Roger von Oech

4.1 Magnetic Helicity Fluxes

The gauge dependence of magnetic helicity fluxes makes the findings in section 3.2 worth revisiting. Since the alleviation of catastrophic α quenching is a physical effect it should not depend on the gauge. By choosing different gauges we investigate which the physically relevant quantities for the large-scale dynamo are. Further, we now consider direct numerical simulations where we can actually measure the diffusive helicity fluxes, which previously were merely imposed, and determine their strength compared to resistive terms and in dependence of the magnetic Reynolds number. The aim of **Paper III** is to first reproduce such diffusive fluxes through the equator (mid-plane) of the domain in direct numerical simulations. By varying the gauge it is observed how that flux changes and how it can retain its physical significance.

Uncurling the induction equation for the magnetic field leaves the freedom to choose a scalar field Ψ, which leaves the physics untouched. The induction equation has then the form

$$\frac{\partial \boldsymbol{A}}{\partial t} = \boldsymbol{U} \times \boldsymbol{B} - \eta \boldsymbol{J} - \boldsymbol{\nabla}\Psi. \tag{4.1}$$

Choosing the form of Ψ fixes the gauge. In the time evolution equation Ψ appears only in the flux term like

$$\boldsymbol{F} = \boldsymbol{E} \times \boldsymbol{A} + \Psi \boldsymbol{B}. \tag{4.2}$$

Here we consider three different gauges. For the Weyl gauge $\Psi = 0$. In the resistive gauge the gauge field Ψ is expressed in terms of the magnetic vector potential as $\Psi = \eta \boldsymbol{\nabla} \cdot \boldsymbol{A}$, which adds a diffusion component to equation (4.1). The pseudo-Lorentz gauge is equivalent to the Lorentz gauge, except that the speed of light c is replaced by the isothermal speed of sound c_{s}:

$$\frac{\partial \Psi}{\partial t} = -c_s^2 \boldsymbol{\nabla} \cdot \boldsymbol{A}. \tag{4.3}$$

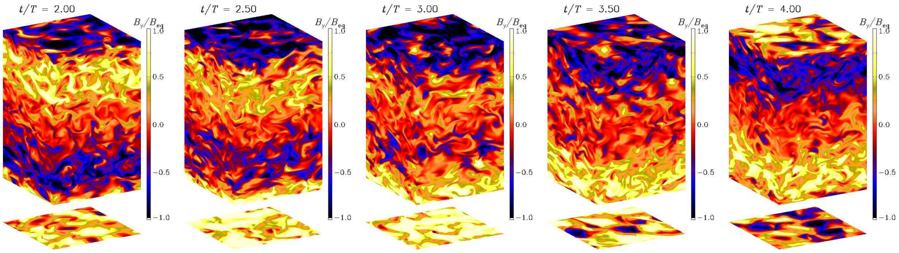

Figure 4.1: Snapshots of the y component of the magnetic field at the domain's periphery for different times. The field reversal occurs at about two resistive times. The time unit is $\tau_{\rm res} = (u_{\rm rms}k_{\rm m}^2/(3k_{\rm f}))^{-1}$.

The equations, which we solve are the same as for the periodic α^2 dynamo in section 3.1, given by equations (3.9)–(3.11), except that the induction equation is enhanced by the gradient of the gauge field Ψ. Similar to the setup used in section 3.2 we impose a forcing function $\boldsymbol{f}$ in the momentum equation, which drives the dynamo. Here, $\boldsymbol{f}$ is again a helical function, which gives rise to turbulent helical motions. The equator, or mid-plane, of the system is defined by the profile of the amplitude of $\boldsymbol{f}$, which is linearly increasing in z and zero at the mid-plane ($z = 0$). This setup resembles somewhat the Sun where kinetic helicity switches sign across the equator. All the boundaries are chosen to be periodic. The domain is a cuboid with sizes $L_x = L_y = L_z/2$, such that both halves are cubes of the same size.

Our setup is motivated by previous work by Mitra et al. (2010) in wedge-shaped domains with helical forcing, which switched sign across the equator. The resulting large-scale magnetic field showed oscillations and equatorward migration. This kind of dynamo produces oscillating magnetic fields of opposite sign in both hemispheres (Fig. 4.1), which is what is seen in Fig. 3.8 in the prefect conductor case.

Unlike in the one-dimensional case, there is no other constraint at the equator, but the vanishing of $\boldsymbol{f}$. The previously imposed diffusive small-scale magnetic helicity fluxes should arise naturally in the three dimensional case. To measure them we need to decompose the field into a small-scale and large-scale part, as it is used in mean-field theory (§ 2.2.1). By fully expanding the terms occurring in the evolution equation for the magnetic helicity for the small and large scales

$$\partial_t \overline{h}_{\rm m} = 2\overline{\boldsymbol{\mathcal{E}}}\cdot\overline{\boldsymbol{B}} - 2\eta\overline{\boldsymbol{J}}\cdot\overline{\boldsymbol{B}} - \boldsymbol{\nabla}\cdot\overline{\boldsymbol{F}}^{\rm H}_{\rm m}, \tag{4.4}$$

$$\partial_t \overline{h}_{\rm f} = -2\overline{\boldsymbol{\mathcal{E}}}\cdot\overline{\boldsymbol{B}} - 2\eta\overline{\boldsymbol{j}\cdot\boldsymbol{b}} - \boldsymbol{\nabla}\cdot\overline{\boldsymbol{F}}^{\rm H}_{\rm f}, \tag{4.5}$$

we can monitor each term of equation (4.5). We are interested in the Fickian diffusion term of the form

$$\overline{\boldsymbol{F}}_{\mathrm{f}}^{\mathrm{H}} = -\kappa_{\mathrm{f}} \boldsymbol{\nabla} \overline{h}_{\mathrm{f}}, \tag{4.6}$$

with the diffusion coefficient κ_{f}. It should be noted that for the fluxes in equation (4.5) not only Fickian diffusion is possible, though the other options need a large-scale velocity field (advective fluxes) or large-scale shear (Vishniac and Cho, 2001). The gradient of the magnetic helicity density $\boldsymbol{\nabla}\overline{h}_{\mathrm{f/m}}$, can be measured from the simulations.

Measuring the small-scale magnetic helicity fluxes $\overline{\boldsymbol{F}}_{\mathrm{f}}^{\mathrm{H}}$ through the equator for the three different gauges at a specific time reveals some significant deviation from each other (Fig. 4.2, upper panel). Instead of fluxes at a given time instance, the physically relevant quantity is the flux at the statistically steady state. For that we need to average over fluctuations which is denote as $\langle . \rangle_t$. Doing so leads to

$$\langle \partial_t \overline{h}_{\mathrm{f}} \rangle_t = 0, \tag{4.7}$$

$$\langle \boldsymbol{\nabla} \cdot \overline{\boldsymbol{F}}_{\mathrm{f}}^{\mathrm{H}} \rangle_t = -2\langle \overline{\boldsymbol{\mathcal{E}}} \cdot \overline{\boldsymbol{B}} \rangle_t - 2\langle \eta \overline{\boldsymbol{J}} \cdot \overline{\boldsymbol{B}} \rangle_t. \tag{4.8}$$

Since the RHS of equation (4.8) is gauge-invariant the LHS has to be so as well. Hence $\overline{\boldsymbol{F}}_{\mathrm{f}}^{\mathrm{H}}$ is gauge-invariant for the statistically steady state. This is reproduced in the lower panel of figure 4.2.

Comparing the terms of the helicity evolution equation of the small-scale field in equation (4.5) (Fig. 4.3, upper panel) reveals that away from the boundaries the time-averaged terms $2\overline{\boldsymbol{\mathcal{E}}} \cdot \overline{\boldsymbol{B}}$ and $2\eta \overline{\boldsymbol{j} \cdot \boldsymbol{b}}$ balance very well. This implies that the fluxes are small and the major part of the magnetic helicity vanishes resistively. This is true for the magnetic Reynolds number $\mathrm{Re}_{\mathrm{M}} = 68$. The reminder of the change in helicity comes through the fluxes (Fig. 4.3, middle panel). The fluxes themselves can be well approximated via Fickian diffusion fluxes, see figure 4.3 lower panel, where we compare the inferred Fickian diffusion with the actual fluxes.

In the present investigation magnetic Reynolds numbers between 2 and 68 are used. In that range the fluxes do not show any clear tendency and can be considered to be independent of Re_{M}, while the terms $2\overline{\boldsymbol{\mathcal{E}}} \cdot \overline{\boldsymbol{B}}$ and $2\eta \overline{\boldsymbol{j} \cdot \boldsymbol{b}}$ scale with Re_{M}. For the fluxes to play any significant role during the dynamo process they need to be comparable to the term $2\overline{\boldsymbol{\mathcal{E}}} \cdot \overline{\boldsymbol{B}}$. Before that no significant alleviation of catastrophic α quenching can be observed (Fig. 4.4, upper panel). For higher magnetic Reynolds numbers it is expected that diffusive fluxes increase such that they become determining and α quenching gets alleviated. This happens for Re_{M} at which $\kappa_{\mathrm{f}} \nabla^2 \overline{\boldsymbol{a} \cdot \boldsymbol{b}} \approx 2\eta \overline{\boldsymbol{j} \cdot \boldsymbol{b}}$. The magnetic Reynolds number for which the terms become comparable is $\mathrm{Re}_{\mathrm{M}} \approx 4600$ (see **Paper III** for details). This result is based on linear extrapolations. Recent findings (Del Sordo et al., 2012) have shown that this breaks down and that the diffusive flux divergence

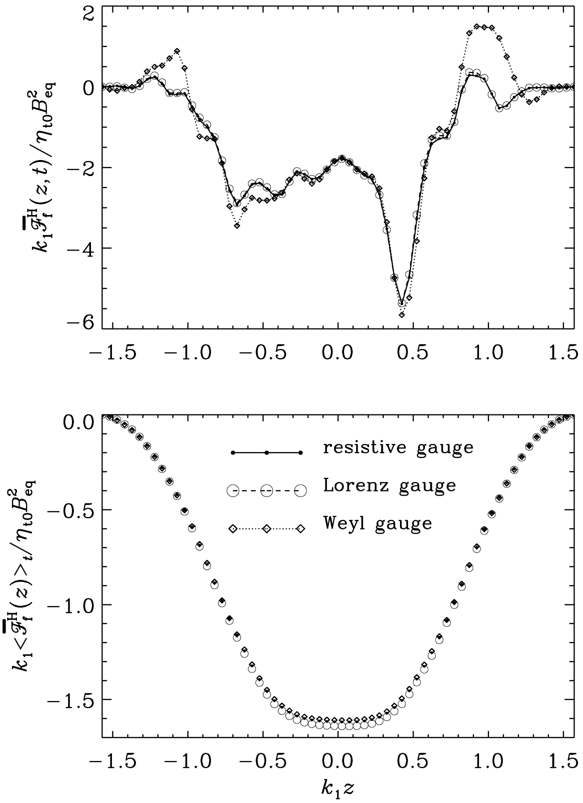

Figure 4.2: Small-scale magnetic helicity fluxes at a random time (upper panel) and their time average (lower panel) for the three gauges. The time averaged quantities are clearly gauge independent.

becomes approximately independent of $\mathrm{Re_M}$ for $\mathrm{Re_M} \approx 100$ and above. For even higher $\mathrm{Re_M}$ the diffusive flux divergence approaches $2\overline{\boldsymbol{\mathcal{E}}} \cdot \overline{\boldsymbol{B}}$.

The gauge dependence of magnetic helicity fluxes is not physically relevant in the statistically steady state, where fluxes are balanced by physical quantities which do not depend on the gauge. Fickian diffusion gives a good proxy for the total magnetic helicity flux. That shows that no other fluxes occur in this particular setup. For low magnetic Reynolds numbers the segregation of magnetic helicity in small- and large-scale parts, expressed in the $2\overline{\boldsymbol{\mathcal{E}}} \cdot \overline{\boldsymbol{B}}$ term, is not balanced by the fluxes. For high, and physically relevant $\mathrm{Re_M}$, we could estimate that it will balance at $\mathrm{Re_M} \approx 4600$. Simulations with such high $\mathrm{Re_M}$ have yet to be realized, but will shed more light on this topic (see Del Sordo et al. (2012)).

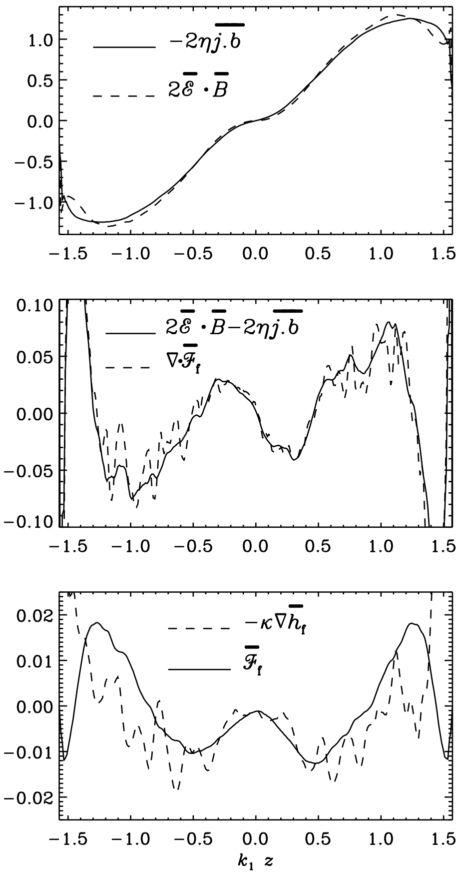

Figure 4.3: z profile of the terms of equation (4.5) (upper two panels) and a comparison between the actual magnetic helicity fluxes and the Fickian diffusion term from equation (4.6).

4.2 The Advecto-Resistive Gauge

In **Paper IV** properties of the magnetic helicity density and its fluxes are examined in a gauge belonging to the advective gauge-families. They are called advective, because velocity shows up as a term which advects the magnetic helicity (Hubbard and Brandenburg, 2011). This should be contrasted to e.g. the resistive gauge, where no such term arises. Gauge-dependent magnetic helicity fluxes mean gauge dependent magnetic helicity transport. The way this physically important quantity is transported in a turbulent environment is part of the present discussion and contrasted with the transport of a passive scalar. Numerical analysis for the advective gauge proves to lead to numerical instabilities, which do not arise in other gauges. To still investigate this gauge a

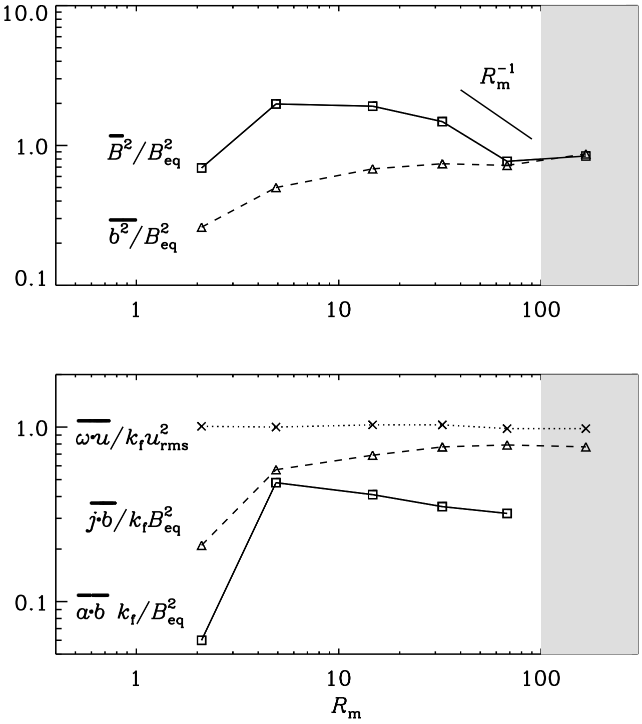

Figure 4.4: Dependence of the normalized magnetic energy in the small and large scale with the magnetic Reynolds number (upper panel). Kinetic, current and magnetic helicity, each appropriately normalized, in dependence of Re_M (lower panel).

universal approach is used for stabilizing the numerical experiment. For that the numerically stable resistive gauge is used for the evolution, while simultaneously solving an evolution equation for the gauge field, which provides the transformation.

In order to distinguish quantities in different gauges a superscript is used, e.g. $\boldsymbol{A}^\mathrm{r}$ for the resistive gauge. The induction equation for the magnetic vector potential in the popular resistive gauge reads

$$\frac{\partial \boldsymbol{A}^\mathrm{r}}{\partial t} = \boldsymbol{U} \times \boldsymbol{B} + \eta \nabla^2 \boldsymbol{A}^\mathrm{r}, \tag{4.9}$$

where the magnetic resistivity η is here assumed to be constant in space. This gauge is numerically stable and commonly used for simulations. Its stability arises form the diffusion term, which reduces any artificial small-scale fluctuations or discontinuities.

In the advective gauge the induction equation reads

$$\frac{\mathrm{D}A_i^{\mathrm{a}}}{\mathrm{D}t} = -U_{j,i}A_j^{\mathrm{a}} - \eta J_i. \tag{4.10}$$

Its form is similar to the gauge, which will be mainly discussed here, which is the advecto-resistive gauge with induction equation

$$\frac{\mathrm{D}A_i^{\mathrm{ar}}}{\mathrm{D}t} = -U_{j,i}A_j^{\mathrm{ar}} + \eta\boldsymbol{\nabla}^2 A_i^{\mathrm{ar}}. \tag{4.11}$$

Any transformation between two gauge-dependent fields can be achieved by adding a gauge field. The transformation between the resistive and advecto-resistive gauge reads

$$\boldsymbol{A}^{\mathrm{ar}} = \boldsymbol{A}^{\mathrm{r}} + \boldsymbol{\nabla}\Lambda^{\mathrm{r:ar}}, \tag{4.12}$$

with the gauge field $\Lambda^{\mathrm{r:ar}}$. The superscript r:ar signifies the original and target gauge. Looking at the induction equation (4.11) it becomes clear why this is called advecto-resistive. It incorporates the advective nature of the advective gauge, as well as the resistive term from the resistive gauge.

Solving the equations in the advecto-resistive gauge leads to numerical instabilities. Therefore we have to make use of the stable resistive gauge and apply the gauge transformation Eq. (4.12) for computing any gauge-dependent quantities in the advecto-resistive gauge. The field $\Lambda^{\mathrm{r:ar}}$ will then have to obey its own evolution equation (see appendix B in **Paper IV** for the derivation):

$$\frac{\mathrm{D}\Lambda^{\mathrm{r:ar}}}{\mathrm{D}t} = -\boldsymbol{U}\cdot\boldsymbol{A}^{\mathrm{r}} + \eta\boldsymbol{\nabla}^2\Lambda^{\mathrm{r:ar}}. \tag{4.13}$$

Applying equation (4.11) together with equation (4.13) is referred to as the Λ method. Although the advecto-resistive gauge is numerically unstable, we will use it in some simulations and discuss where the instability comes from.

Magnetic helicity transport is crucial in dynamo theory (see **Paper I**, **Paper II**, **Paper III** and references therein). In both, the resistive and advecto-resistive gauge, the time evolution of the magnetic helicity density is determined by a resistive term and fluxes given as

$$\begin{aligned} \frac{\partial h^{\mathrm{a}}}{\partial t} &= -2\eta\boldsymbol{J}\cdot\boldsymbol{B} - \boldsymbol{\nabla}\cdot\boldsymbol{F}^{\mathrm{a}}, && (4.14)\\ \frac{\partial h^{\mathrm{r}}}{\partial t} &= -2\eta\boldsymbol{J}\cdot\boldsymbol{B} - \boldsymbol{\nabla}\cdot\boldsymbol{F}^{\mathrm{r}}, && (4.15)\\ \frac{\partial h^{\mathrm{ar}}}{\partial t} &= -2\eta\boldsymbol{J}\cdot\boldsymbol{B} - \boldsymbol{\nabla}\cdot\boldsymbol{F}^{\mathrm{ar}}, && (4.16) \end{aligned}$$

with the magnetic helicity fluxes $\boldsymbol{F}^{\mathrm{a}}$, $\boldsymbol{F}^{\mathrm{r}}$ and $\boldsymbol{F}^{\mathrm{ar}}$ given by

$$\begin{aligned} \boldsymbol{F}^{\mathrm{a}} &= h^{\mathrm{a}}\boldsymbol{U} + \eta\boldsymbol{J}\times\boldsymbol{A}^{\mathrm{a}}, && (4.17)\\ \boldsymbol{F}^{\mathrm{r}} &= h^{\mathrm{r}}\boldsymbol{U} - (\boldsymbol{U}\cdot\boldsymbol{A}^{\mathrm{r}} + \eta\boldsymbol{\nabla}\cdot\boldsymbol{A}^{\mathrm{r}})\boldsymbol{B} + \eta\boldsymbol{J}\times\boldsymbol{A}^{\mathrm{r}}, && (4.18)\\ \boldsymbol{F}^{\mathrm{ar}} &= h^{\mathrm{ar}}\boldsymbol{U} - \eta(\boldsymbol{\nabla}\cdot\boldsymbol{A}^{\mathrm{ar}})\boldsymbol{B} + \eta\boldsymbol{J}\times\boldsymbol{A}^{\mathrm{ar}}. && (4.19) \end{aligned}$$

Fluxes of magnetic helicity in all cases appear as advective fluxes ($h\boldsymbol{U}$) and resistive fluxes ($\eta\boldsymbol{J}\times\boldsymbol{A}$). In the limit of ideal MHD and incompressible fluids, i.e. $\eta = 0$ and $\boldsymbol{\nabla}\cdot\boldsymbol{U} = 0$, equation (4.14) is formally the same as the evolution of a passive scalar:

$$\frac{\mathrm{D}h^{\mathrm{a}}}{\mathrm{D}t} = 0. \tag{4.20}$$

The resistive gauge breaks this analogy, caused by fluxes in the direction of the magnetic field of the form $\boldsymbol{U}\cdot\boldsymbol{A}^{\mathrm{r}}\boldsymbol{B}$, called turbulently diffusive fluxes. The varying nature of the fluxes is one issue addressed in **Paper IV**.

The solved equations are the momentum equation (2.2) with the helical forcing term $\boldsymbol{f}$, the continuity equation (2.3) and the induction equation whose form depends on the method and gauge. The isotropic forcing $\boldsymbol{f}$ provides the energy input and ensures a dynamo is working. For the induction equation we either choose the purely resistive gauge with equation (4.9), the pure advecto-resistive gauge with equation (4.11) or the resistive gauge combined with the evolution equation for the gauge field Λ (Eq. (4.13)), which is used to compute magnetic helicity and its fluxes via the transformation

$$h^{\mathrm{ar}} = h^{\mathrm{r}} + \boldsymbol{\nabla}\Lambda\cdot\boldsymbol{B}. \tag{4.21}$$

Additionally the evolution of a passive scalar C

$$\frac{\mathrm{D}C}{\mathrm{D}t} = \kappa\nabla^2 C, \tag{4.22}$$

is solved to compare its dynamics with the magnetic helicity, where κ is the diffusivity of the passive scalar. The triply periodic boundary conditions imposed lead to a slow saturation of the mean magnetic field.

The helical forcing $\boldsymbol{f}$ injects kinetic energy, which gets transformed into magnetic energy via the α effect. Together with the magnetic field also the magnetic helicity increases (Fig. 4.5). Choosing to directly solve the induction equations in the advecto-resistive gauge causes the simulation to develop high gradients of $\boldsymbol{A}$, which should not affect $\boldsymbol{B}$, but numerically they do. The values grow to such high values that the simulation stops. Changing the simulation's resolution does not have any significant effect on the stability. It is an intrinsic property of the gauge choice.

The instability arises from numerically taking the derivative of $\boldsymbol{A}^{\mathrm{ar}}$ in equation (4.11). The expansion of the Laplacian operator shows that there is a hidden curl operator applied on the gradient of the gauge field $\Lambda^{\mathrm{r:ar}}$ of the form

$$\boldsymbol{\nabla}^2\boldsymbol{A}^{\mathrm{ar}} = \boldsymbol{\nabla}(\boldsymbol{\nabla}\cdot\boldsymbol{A}^{\mathrm{ar}}) - \boldsymbol{\nabla}\times\left(\boldsymbol{\nabla}\times\boldsymbol{A}^{\mathrm{r}} + \boldsymbol{\nabla}\times(\boldsymbol{\nabla}\Lambda^{\mathrm{r:ar}})\right). \tag{4.23}$$

The curl of the gradient should of course vanish. Numerically, however, it does not, which leads to an artificial increase of magnetic field in the small scales.

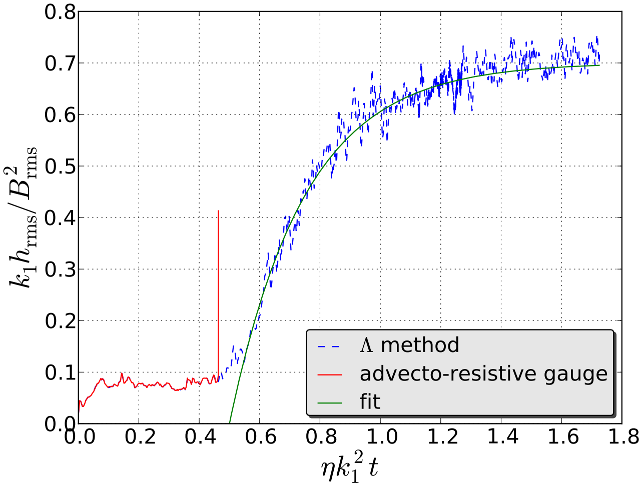

Figure 4.5: Normalized root mean square value of the magnetic helicity for the direct advecto-resistive gauge (solid red line) and the Λ method (dashed line) together with a fit (solid green line).

As consequence also the velocity increases due to the Lorentz force and the simulation crashes. Using the Λ method, this issue is circumvented.

The total magnetic helicity in this setup with periodic boundaries is gauge-invariant. Its density distribution, however, is not. Any difference between the resistive and advecto-resistive gauges on density distribution, in the absence of compressibility effects, can only be caused by the fluxes, which is reflected in the root mean square of the magnetic helicity $h_{\rm rms}$. For the resistive gauge, in contrast to the advecto-resistive gauge, additional flux terms appear in the form of $(\boldsymbol{U} \cdot \boldsymbol{A}^{\rm r})\boldsymbol{B}$, which can diminish the transport. Consequently, magnetic helicity will be transported less efficiently into scales of the turbulent eddies for the resistive, than for the advecto-resistive gauge. This effect increases as the fluid Reynolds number increases. Highly varying concentrations mean an increase of the root mean square value $h_{\rm rms}$. Indeed, we can reproduce this feature for the advecto-resistive gauge (Fig. 4.6, left panel) and provide an approximate law for its quantitative behavior given by

$$\frac{k_1 h^{\rm ar}}{B_{\rm rms}^2} = c{\rm Re}_{\rm M}^{-a}(1 + b{\rm Re}_{\rm M}^{2a}), \tag{4.24}$$

with the fit parameters a and b. This effect is absent for the resistive gauge (Fig. 4.6, right panel).

We compare the dynamics of the passive scalar with the magnetic helicity density by evaluating their spectra (Fig. 4.7). In the kinematic regime, where resistive terms are negligible, the magnetic helicity spectrum shows a drop at

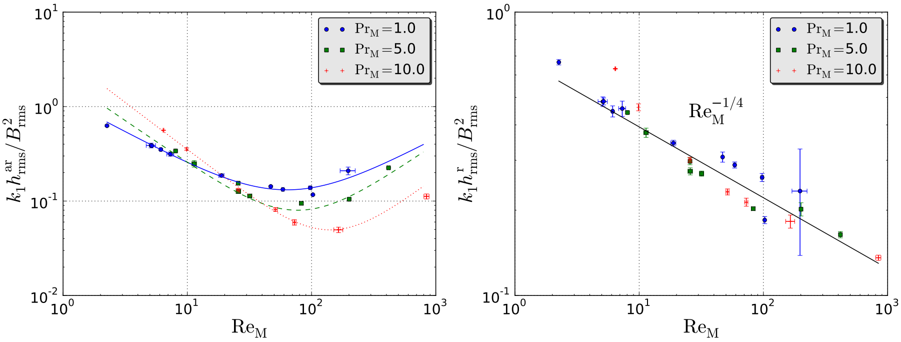

Figure 4.6: Time averaged values of the normalized magnetic helicity for the kinematic phase in dependence of the magnetic Reynolds number for different Prandtl numbers. The advecto-resistive case (left panel) clearly shows a different behavior (model by equation (4.24)) from the resistive case (right panel), which shows a power law dependence.

high wave numbers, which is different from the advecto-resistive gauge. This drop comes from the more effective way of dissipating high spatial variations of $\boldsymbol{A}$, due to the resistive term in the induction equation. This term is of course also present in the advecto-resistive gauge, but due to the efficient transport of helicity into smaller scales, thanks to the advective term, high k components get constantly supplied from low k. This comparison holds true even for the non-linear regime. There it can be seen that $h^{\rm r}$ develops a peak at the forcing scale $k_{\rm f}$, which is to be expected from dynamo theory where the magnetic field peaks there. Of similar reasons is the peak of the passive scalar. The turbulent helical fluid motions trap it into this scale. Since there is no way of transporting C other than advection it retains its peak at the forcing scale $k_{\rm f}$. Because for the advecto-resistive case there is helicity transport into smaller scales the peak vanishes and we see a flatter profile.

In summary we present an effective way to circumvent numerical instabilities arising form the gauge choice, by solving for an evolution equation for the gauge field Λ. In this context one may ask why not solve directly for the physical quantities and applying an inverse curl operator when computing helicities. One reason is the divergence freeness of the magnetic field ($\boldsymbol{\nabla}\cdot\boldsymbol{B}=0$), which is automatically assured when solving for the magnetic vector potential $\boldsymbol{A}$. It makes it also easier to compute the magnetic helicity for which no inverse curling is needed. The differing fluxes result in some interesting consequences for the helicity transport. In the advecto-resistive gauge the co-moving local magnetic helicity density remains closer to its initial value, except at small scales where it leads to a high k tail (Fig. 4.7). The resistive gauge makes the helicity evolve akin a passive scalar. It should be remembered that the only

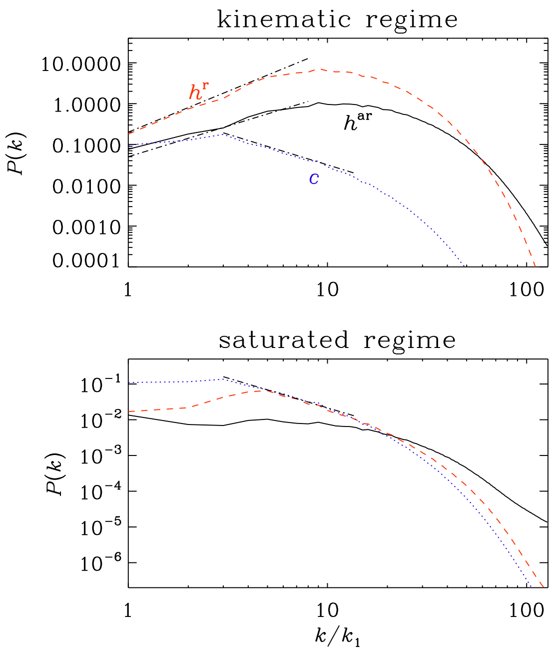

Figure 4.7: Power spectra for the magnetic helicities $h^{\rm r}$, $h^{\rm ar}$ and the passive scalar C for $k_{\rm f}/k_1 = 5$. The additional transport term causes $h^{\rm ar}$ to have a flatter profile and higher values at high k, in contrast to $h^{\rm r}$.

distinction in time evolution between $\boldsymbol{A}^{\rm r}$ and $\boldsymbol{A}^{\rm ar}$ comes from the gauge transformation Eq. (4.13). So the difference in the transport comes solely from the gauge field Λ.

5. Topology

The characters emerge from my rather twisted mind.
That's another enjoyable part of the job making stuff up.

Jonathan Kellerman

Two field configurations are topologically different if they cannot be transformed one into another with a homeomorphic transformation. In other words, without the aid of magnetic reconnection they cannot be converted into each other. This does not mean that reconnection necessarily changes the topology of the field. Even with reconnection the topology can be conserved. Topology is to be contrasted with geometry, which describes the shape of the field.

Field line topology particularly affects relaxation processes (Berger and Field, 1984; Ricca, 2008). Since the field cannot be shaped in any arbitrary way, relaxation does not occur totally freely. This aspect, with connection to magnetic helicity, is discussed in **Paper V**. Magnetic helicity is, however, not the only quantifier for field line topology (Yeates and Hornig, 2012). There exists an infinite number of topological invariants. Whether those can play any role in field line relaxation is discussed in **Paper VI**.

5.1 Flux Linking and Magnetic Helicity

The most common way of quantifying the topology of magnetic fields is the magnetic helicity (Moffatt, 1969), which gives a measure for the mutual linkage of magnetic fields lines. Two mutually liked magnetic flux rings, which do not possess any internal twisting nor are self-interlinked, are an instructive example for the analogy between linkage and magnetic helicity (see Fig. 1.3). It could be shown by Moffatt (1969) that the number of mutual linkage n is related to the total magnetic helicity H_M as

$$H_\mathrm{M} = \int_V \boldsymbol{A} \cdot \boldsymbol{B} \, \mathrm{d}V = 2n\phi_1\phi_2, \tag{5.1}$$

where ϕ_i are the magnetic fluxes through the field lines

$$\phi_i = \int_{S_i} \boldsymbol{B} \cdot \mathrm{d}\boldsymbol{S}. \tag{5.2}$$

Conservation of magnetic helicity for low magnetic resistivity, as it is the case for astrophysical applications, makes it an ideal invariant, even when magnetic reconnection occurs (Taylor, 1974).

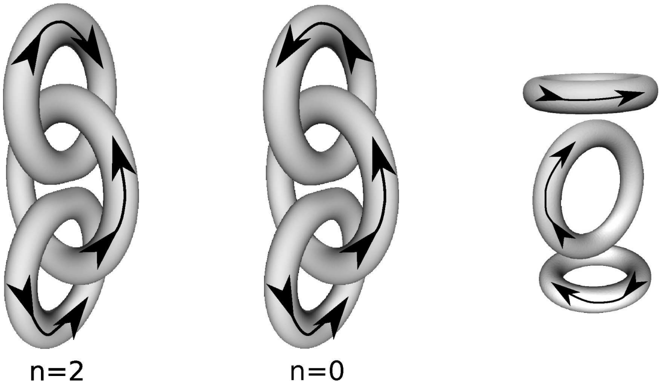

Figure 5.1: Isosurfaces of the magnetic energy for the helical linked (left panel), non-helical linked (central panel) and unlinked (right panel) magnetic field configuration. The direction of the magnetic field is pictured by the arrows.

With this colorful picture of the magnetic helicity it is obvious that with its presence any relaxation must be impeded, as long as the system is not breaking up field lines. This characteristics is captured in the realizability condition Eq. (2.49), which imposes a lower limit on the magnetic energy in presence of magnetic helicity. Of course one can make up non-helical configurations with linked flux tubes. If their topology was conserved that property would need to be captured in a higher order invariant (Ruzmaikin and Akhmetiev, 1994; Komendarczyk, 2010). The question then is what is more important: the actual topology (linking) or the magnetic helicity. This is addressed in **Paper V**.

As a showcase, three field configurations are investigated (Fig. 5.1). Two of them consist of three interlinked magnetic flux rings of finite width and no internal twisting. The reversal of the direction of the field in one of the two outer rings changes the magnetic helicity content from an appreciable value to zero. As reference configuration to compare with, we use the same three rings without any linkage (Fig. 5.1, right panel).

The three magnetic field configurations are used as initial conditions. The cross section and magnetic flux in the tubes is the same for all three rings. The radii of the outer rings are R_0 and for the inner ring is $R = 1.2R_0$. As profile for the magnetic field strength a Gaussian is used, which has the advantage of being a smooth function. The relaxation characteristics is investigated within the framework of resistive MHD. For that we solve the usual MHD equations (2.1)–(2.3) without any forcing $\boldsymbol{f}$. The initial values of velocity and density are $\boldsymbol{U}_0 = 0$ and $\rho_0 = 1$. The initial magnetic flux through the tubes is $\Phi = 0.1c_\mathrm{s}R_0^2\sqrt{\mu_0\rho_0}$, which is small enough to ignore compression effects and consider the density as constant. Magnetic resistivity η is set to a value as small as is numerically admissible for the sake of magnetic helicity conserva-

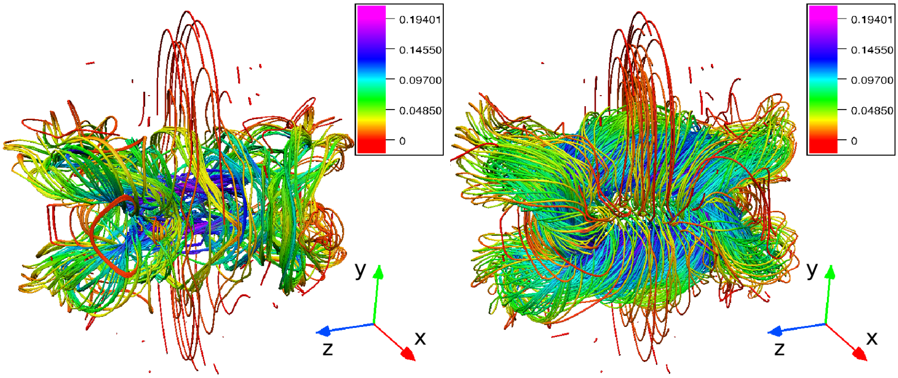

Figure 5.2: Magnetic stream lines after 4 Alfvénic times for the interlocked triple-ring configurations. The non-helical case (left) loses most of its initial structure, while the helical case (right) retains it and distinct tubes can still be observed.

tion. To make sure magnetic helicity cannot escape, the domain boundaries are assumed periodic. Time is measured in Alfvénic times, which in the present cases is only a fraction of the resistive time:

$$T_A = \sqrt{\mu_0 \rho_0} R_0^3 / \Phi. \tag{5.3}$$

As times evolves each outer ring shrinks due to magnetic tension and diffusion. When the field lines touch local reconnection events occur which change the shape of the field. For the non-helical interlocked field the initial structure vanishes after only a few Alfvénic times (Fig. 5.2, left panel), while for the helical configuration the initial topology remains conserved (Fig. 5.2, right panel).

During the relaxation magnetic energy gets lost into heat[1] through reconnection events and resistive effects. The rate of loss depends on how fast the system can attain its equilibrium energy. For the non-helical case it can be seen that energy is dissipated quickly (Fig. 5.3) – in fact as quickly as for the non-interlocked test configuration. The mere linking does apparently not hinder the field to decay almost freely. For the helical case the realizability condition imposes severe restrictions on the relaxation. In practice this means a slow loss of magnetic energy on a resistive time scale on which also the magnetic helicity decays.

In summary we can confirm the importance of the realizability condition for relaxation processes. The naïve interpretation of linked flux tubes whose

---

[1] No energy equation is solved here. So the dissipated energy cannot be reused by any means, like buoyancy.

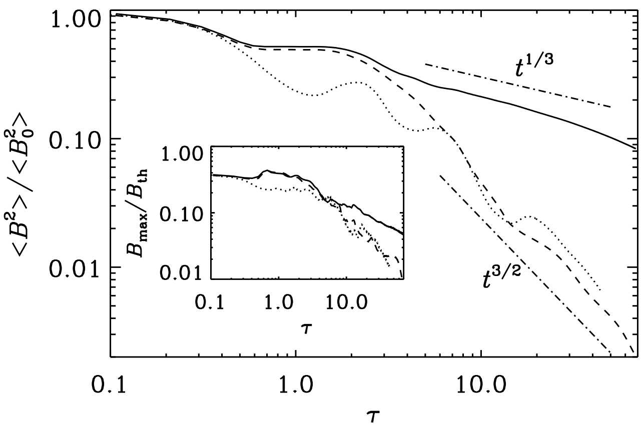

Figure 5.3: Magnetic energy evolution for the three rings configurations normalized by their initial value. The helical interlocked configuration retains its energy content more successfully (solid line), while the linked non-helical one (dashed lines) and the non-linked case (dotted line) lose energy quickly at approximately the same rate.

dynamics is restricted by the linkage does not hold. The only essential quantity is the magnetic helicity.

5.2 Beyond Magnetic Helicity

Since there exists an infinite number of topological invariants it should be investigated if magnetic helicity is always the sole determinant in magnetic field dynamics. To address this question we perform in **Paper VI** similar relaxation experiments as in **Paper V** with field configurations in the shape of knots and links. The investigated magnetic field configurations are the n-foil knots, the Borromean rings and the IUCAA knot (Fig. 5.4). Similar numerical experiments have been carried out for ideal MHD (Maggioni and Ricca, 2009) where no reconnection events could take place.

The family of n-foil knots, of which the trefoil knot is the simplest example, has only helical members. By increasing their complexity with parameter n, their magnetic energy increases, as well as the magnetic helicity. The Borromean rings and IUCAA knot are both non-helical configurations. Yet, they are topologically non-trivial and cannot be undone without braking the field lines. For the Borromean rings there exists a higher order topological invariant, which is conserved in ideal MHD, but gets destroyed during magnetic reconnection (Ruzmaikin and Akhmetiev, 1994).

As in the case of the triple ring configurations of **Paper V** the bound-

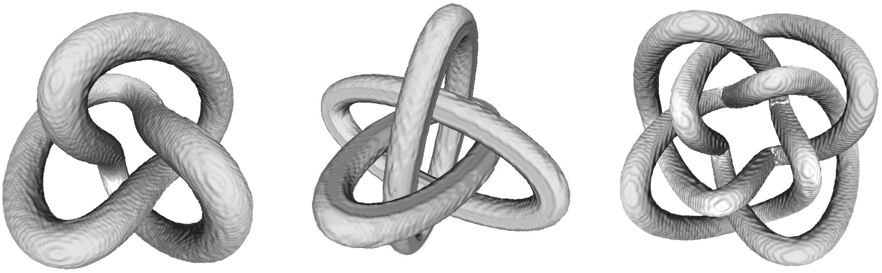

Figure 5.4: Isosurfaces of the magnetic energy for the initial field configurations trefoil knot (left panel), Borromean rings (middle panel) and the IUCAA knot (right panel).

aries are chosen to be periodic in order to conserve magnetic helicity. For the same reason the magnetic resistivity η is chosen as small as computationally possible. The governing equations for this problem are the same as for the triple rings case, which are equations (2.1)–(2.3) without forcing $\boldsymbol{f}$. We use the magnetic field configurations shown in Fig. 5.4 as initial conditions and let the systems relax.

The relaxation of the n-foil knots does not give any surprises. The magnetic helicity imposes restrictions on the field relaxation, which gets more pronounced as the complexity of the configuration is increased. The power laws of $t^{-1/3}$ found in **Paper V** for the energy decay of the helical triple ring configuration could only be found for the most complex member of this family studied here, the 7-foil knot. The least complex, the trefoil knot, shows a $t^{-2/3}$ behavior. This characteristics comes from the increasing ratio of magnetic helicity to magnetic energy as the complexity grows with n. The energy increases linearly with complexity, while the magnetic helicity grows quadratically. Consequently, the realizability condition slows down the energy decay more effectively (see **Paper VI** for details).

The Borromean rings show an intriguing property, which distinguishes this configuration form other non-helical configurations. As the field evolves and tries to relax it undergoes reconnection events. Those events transform the linked rings into two separate rings, which are twisted (Fig. 5.5). The twist is of opposite sign, due to magnetic helicity conservation. The energy decay is not of the form $t^{-3/2}$, but of t^{-1} (Fig. 5.6). This we attribute to the occurrence of separate helical structures, which evolve independently. Similar reconnection steps for this configuration were shown in a theoretical work by Ruzmaikin and Akhmetiev (1994) where it was proposed that the Borromean rings should reconnect into a trefoil knot and three figure eight knots with opposite helicity. After further reconnection the system should end up with two un-knots and six

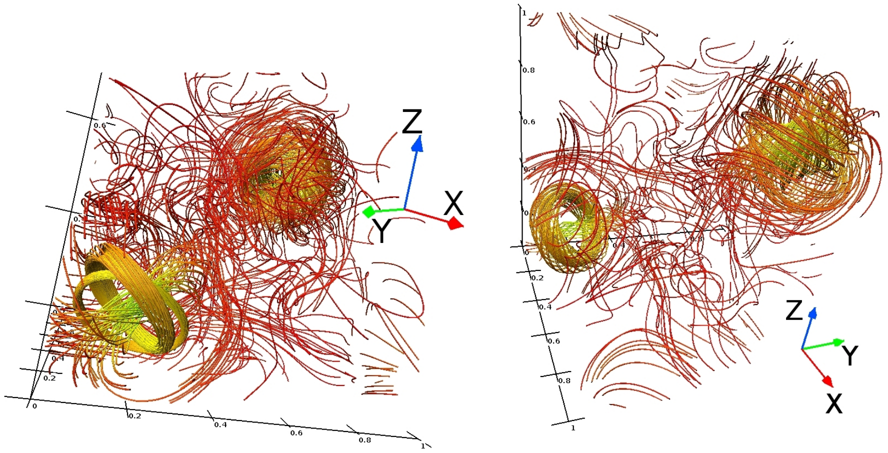

Figure 5.5: Magnetic stream lines for the Borromean field configuration after 70 Alfvénic times (left) and 78 (right). The initial configuration is totally lost and replaced by two twisted fields.

figure eight knots of which three have opposite sign of the other three, in order to conserve helicity. Making the interpretation that those figure eight knots are the internal twist of the final un-knots we can conclude that their findings match with our simulation results. The presence of magnetic helicity in the separate twisted tubes imposes restrictions on the relaxation expressed in the realizability condition Eq. (2.49).

The IUCAA knot also shows a relaxation behavior, which lies in between the decay speed of the helical and non-helical triple-ring configurations (Fig. 5.6). This illustrates that even non-helical fields reveal non-trivial behavior. Since no such helical structures as for the Borromean rings appear, we are tempted to speculate about higher order invariants, which inhibit the field decay.

Once again the importance of the realizability condition is confirmed. For the n-foil knots we see that the higher the magnetic helicity content is compared to the magnetic energy the stronger is the inhibition from the realizability condition to let the field relax into a lower energy state. The surprisingly slow decay of the Borromean rings can be attributed to the emergence of helical structures, which evolve independently and where the realizability condition imposes restrictions on the relaxation. For the IUCAA knot no such explanation could be found and one may again speculate about higher order topological invariants. One way of doing this is by applying the concept of topological flux functions, which can be used to uniquely identify the topology of the magnetic field configuration (Yeates and Hornig, 2012). Defining such a flux function requires a field with a preferential direction as they occur for instance in tokamaks. This, nevertheless, does not restrict one of applying

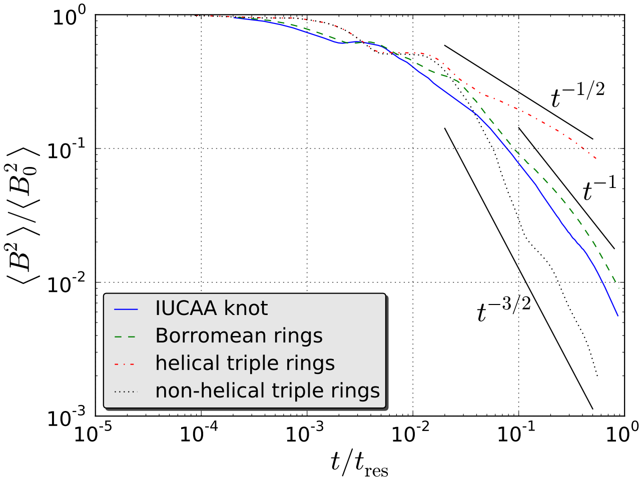

Figure 5.6: Normalized magnetic energy for the linked triple-ring configurations, the Borromean rings and the IUCAA knot together with power laws to guide the eye.

this concept on knots and links, since they can always be represented as braids in a periodic domain.

A potential physical applications of the topologies discussed here is the explanation of magnetic cavities observed in the intergalactic medium (Ruszkowski et al., 2007; Pfrommer and Jonathan Dursi, 2010) which show high resistance against Kelvin-Helmholtz instability. It has been shown by Braithwaite (2010) that tangled fields enhance the stability of bubbles during relaxation. It is yet to be demonstrated that they can reduce the Kelvin-Helmholtz instability.

6. Conclusions

Denn die Menschen glauben an die Wahrheit dessen,
was ersichtlich stark geglaubt wird.

All things are subject to interpretation.
Whichever interpretation prevails at a given time
is a function of power and not truth.

Friedrich Nietzsche

Magnetic helicity is a fundamental quantity in the dynamics of magnetic fields in the Universe. Its importance has been appreciated in several previous works ranging from the implication of its conservation in dynamos (Pouquet et al., 1976) to the constraint it imposes in field relaxation (Moffatt, 1978).

Its conservation causes the turbulent large-scale dynamo to grow on resistive time scales, which, for astrophysical objects like the Sun and galaxies, are much longer than the dynamical time scales we observe. The saturation strength of the large-scale magnetic field is fundamentally affected by magnetic helicity as well and is drastically reduced to values much lower than those observed. In **Paper I** it is discussed how the saturation characteristics change with the relevant parameters, which are the scale separation ratio between the size of the turbulent motion and the system and the relative amount of injected kinetic helicity. As predicted by mean-field estimates (Blackman and Brandenburg, 2002), the saturation magnetic energy of the large-scale field scales proportionally to the scale separation ratio and the injected relative helicity. Further, for the large-scale dynamo to operate, the critical value for the normalized helicity of the small-scale turbulent motions scales inversely proportional to the scale separation ratio. This leads to an excellent confirmation of the mean-field predictions. Previous findings (Pietarila Graham et al., 2012), which suggest different scaling behaviors, arguably lack proper analysis of the magnetic field of the large-scale dynamo.

The form of the forcing function, which drives the dynamo, is usually taken to be of helical nature, which leads to helical magnetic fields. Amongst these different behaviors for the large-scale field is that of **Paper I**, where for most parts a helical forcing random in time is used. There are three different magnetic field averages competing during the resistive saturation, the xy-, xz- and yz-averaged magnetic fields. Only one survives at the end of the saturation phase. For the ABC-flow forcing an intriguing behavior is seen, where the three modes oscillate in time with a phase shift of $2\pi/3$. The nature of this oscillation is not understood yet and has to be investigated further.

A reduction of magnetic helicity in the small scales can be obtained via various kinds of fluxes (Rogachevskii and Kleeorin, 2000; Vishniac and Cho, 2001; Subramanian and Brandenburg, 2004, 2006) of which not all can efficiently reduce its amount such that catastrophic α quenching gets alleviated. Two kinds of fluxes are considered in **Paper II**. Advective fluxes, mediated by a wind, efficiently transport the magnetic field together with small-scale magnetic helicity out of the system. Physically speaking this can be interpreted as coronal mass ejections with helical magnetic fields or as a galactic wind. Diffusive fluxes within closed domains between parts of opposite helicity are also efficient enough to alleviate catastrophic α quenching and allow for high mean magnetic saturation field strengths for high magnetic Reynolds numbers. In practice this means that the mere reshuffling of magnetic helicity within a closed system, through e.g. the equator, reduces sufficiently the amount of "hostile" helicity of small-scale fields.

The gauge dependence of magnetic helicity does not constitute a problem for the physical effect of magnetic helicity fluxes. Choosing different gauges, namely the Weyl, resistive and pseudo Lorentz gauges does not change the time-averaged helicity fluxes through the mid-plane of the domain (**Paper III**). This is shown for equations in the steady state, where fluxes of magnetic helicity appear together with quantities which are gauge-independent, which implies that also the fluxes must be gauge-independent.

Choosing different gauges can be useful to test magnetic helicity transport. It can, however, lead to numerical instabilities arising from large gradient contributions in the magnetic vector potential when computed numerically. This pitfall can be circumvented by solving the evolution equations in a numerically stable gauge and applying a gauge transformation for computing gauge-dependent quantities like the magnetic helicity density or its fluxes (**Paper IV**). Transport and distribution of magnetic helicity in the advecto-resistive gauge is found to differ significantly from the advective gauge. It can transport magnetic helicity more efficiently to smaller length scales, especially in the case of low magnetic resistivity.

Topological constraints coming from field line linkage or knotting is contrasted against the realizability condition, which only holds as long as the configuration is helical. Of course the realizability condition can already be regarded as describing constraints coming from the field's topology. There are, however, non-helical setups, which are topologically non-trivial. For those we find in **Paper V** that their linkage has little effect on the field relaxation. This is compared with non-linked setups, which show the same energy decay characteristics. In **Paper V** the restrictions on the field's dynamics solely arises from the magnetic helicity content, rather than the actual linkage.

The content of magnetic helicity in knotted flux tubes is shown to scale like the number of crossings obtained from an appropriate 2d projection of the configuration (**Paper VI**). The relaxation characteristics of those helical knots is, however, not directly comparable with the previous helical triple-ring configuration. The reason is simply the increasing helicity content with increasing complexity of the knots. Non-helical setups exhibit relaxation speeds, which are found to lie somewhere in between those for helical and non-helical fields. For one configuration, namely the Borromean rings, this departure is attributed to the occurrence of separated helical flux rings for which the realizability condition holds. In the case of the non-helical IUCAA knot no such explanation is possible, which is why one can speculate about higher order topological invariants. Fortunately magnetic helicity is not the only quantifier for the field's topology. There exists an infinite number of such quantities. One of them is the fixed point index, which has been shown to impose another restriction on the field's relaxation (Yeates et al., 2010).

7. Outlook

Dazu gibt er dem Menschen die Hoffnung:
sie ist in Wahrheit das übelste der Übel,
weil sie die Qual der Menschen verlängert.

Hope in reality is the worst of all evils
because it prolongs the torments of man.

Friedrich Nietzsche

Gradually we are extending our grasps on how magnetic helicity is formed and in which ways it affects astrophysical systems. The work presented here is rather abstract, yet fundamental. To make predictions for physical systems more realistic simulations have to be performed.

The helical forcing used in turbulent dynamos leads to a separation of magnetic helicity in the small and large scales. As main consequence the large-scale magnetic field grows to considerable values. In **Paper I** we also use the ABC-flow forcing, which leads to rotating averages for the mean magnetic field. The nature of this rotation and exact characteristics are not known. Further investigations on that would show if the rotation keeps on in time or if the equilibrium solution is stationary or not.

Apart form magnetic helicity, also cross helicity, the correlation of the turbulent velocity with the turbulent magnetic field, takes part in the generation of the magnetic field (Yoshizawa, 1990). Most of the work done so far (Yoshizawa and Yokoi, 1993; Yokoi, 1996, 1999) has been done analytically. Numerical simulations have yet to show the importance of cross helicity for the mean-field dynamo. A setup would consist of a rotating stratified medium where a weak mean magnetic field is imposed. That should lead to the growth of magnetic energy. The mean-field calculations would then be compared to the direct numerical simulations using the test-field method (Schrinner et al., 2005).

In the intergalactic medium X-ray cavities have been observed (Ruszkowski et al., 2007; Pfrommer and Jonathan Dursi, 2010) which are hot under-dense regions. They rise due to buoyancy and are expected to be shred into small pieces due to the Kelvin-Helmholtz instability (von Helmholtz, 1868, Thomson, 1871, Chandrasekhar, 1961). They seem, however, to survive for millions of years, which is a considerably longer time than predicted by simulations. The Kelvin-Helmholtz instability has been shown to be suppressed by helical magnetic fields, which makes the fluid more stable against shredding. Numerical simulations of helical magnetic cavities have to be conducted in order to quantitatively understand their stability in the intergalactic medium. Such configurations could be under-dense regions in a cooler stratified medium with gravity. Inserting a helical magnetic field in those cavities should then show stabilizing effects.

Magnetic helicity is not the only topological invariant. There exists an infinite number of invariants, which can be used to characterize the topology of magnetic field lines. Just a few of them are useful for diffusive fields, which fill the whole volume. Two of them are the magnetic helicity (Moffatt, 1969) and the fixed point index (Yeates et al., 2010). The latter was shown to restrict the relaxation of the magnetic field for particularly braided magnetic fields. As a next step I will use this method for configurations which are topologically equivalent to knots and links. In this context a topological flux function is defined whose change in the fixed points gives a proxy for the magnetic reconnection rate. This will enable us to determine whether magnetic resistivity changes the reconnection rate and if magnetic helicity is conserved during reconnection.

Sammanfattning

Skillnaden mellan geniet och dumheten är
att geniet har sin begränsning.

Torvald Gahlin

Magnetfält spelar en betydande roll inom astrofysiken. De underlättar transporten av rörelsemängdsmoment och kan därför förklara varför solen roterar relativt långsamt. Magnetfälts uppkomst förklaras genom dynamoeffekten där turbulent rörelse ger upphov till magnetisk energi. Sådana magnetfält är helikala, dvs. deras fältlinjer är länkade. Att de är helikala har vidsträckta konsekvenser för deras dynamik.

Att förklara hur sådana fält kommer till stånd är en del av det här avhandlingen. Det visas att det magnetiska heliciteten hindrar det storskaliga fältet att utvecklas. Tiden som fältet behöver att formas blir längre än solens ålder och intensiteten minskas till ett löjligt litet värde. Hur magnetfältet påverkas av turbulensens egenskaper är avhandlingens första del. Det visas hur strömmen av magnetisk helicitet lindrar den dämpade effekten för magnetfältets tillväxt. Fysikaliskt betyder det att koronamassutkastningar stödjer fältets utveckling.

Den magnetiska helicitetens beroende på gaugen leder till frågan om hur den kan vara fysikaliskt relevant. I den andra delen av avhandlingen undersöker jag hur gaugen påverkar transporten av helicitet och hur dess fysikaliska relevans räddas. Det visas att i det stationära tillståndet tidsmedelvärdet av strömmen inte är gaugeberoende. Å andra sidan är spektrumet beroende på gaugen. I den advecto-resistiva gaugen, till exempel, transporteras magnetisk helicitet mer effektivt till små skalor, vilket ger upphov till en flatare profil.

Magnetisk helicitet kan tolkas som länkar av magnetfältlinjer. Därmed blir det tydligt att fältet inte kan relaxera fritt. I den tredje och sista delen undersöker jag hur länkning och heliciteten påverkar fältets dynamik. Det visas att enbart länkning inte är tillräckligt för att inskränka dynamiken; det behövs helicitet. Från ytterligare numeriska experiment visas det att andra topologiska kvantiteter också kan spela en roll i fältets relaxation. Hittills är det inte känt vilka.

References

V. I. Arnold. The asymptotical hopf invariant and its applications. *Sel. Math. Sov.*, 5, 1974. 19

G. K. Batchelor. On the Spontaneous Magnetic Field in a Conducting Liquid in Turbulent Motion. *Roy. Soc. Lond. Proc. Ser. A*, 201:405–416, 1950. 19

M. A. Berger and G. B. Field. The topological properties of magnetic helicity. *J. Fluid Mech.*, 147:133–148, 1984. 18, 49

E. G. Blackman and A. Brandenburg. Dynamic Nonlinearity in Large-Scale Dynamos with Shear. *Astrophys. J.*, 579:359–373, 2002. 5, 25, 26, 57

E. G. Blackman and A. Brandenburg. Doubly Helical Coronal Ejections from Dynamos and Their Role in Sustaining the Solar Cycle. *Astrophys. J.*, 584:L99–L102, 2003. 35

E. G. Blackman and G. B. Field. Constraints on the Magnitude of α in Dynamo Theory. *Astrophys. J.*, 534: 984–988, 2000. 17, 30

P. L. Boyland, H. Aref, and M. A. Stremler. Topological fluid mechanics of stirring. *J. Fluid Mech.*, 403: 277–304, 2000. 22

J. Braithwaite. Magnetohydrodynamic relaxation of AGN ejecta: radio bubbles in the intracluster medium. *Month. Not. Roy. Astron. Soc.*, 406:705–719, 2010. 55

A. Brandenburg. The Inverse Cascade and Nonlinear Alpha-Effect in Simulations of Isotropic Helical Hydromagnetic Turbulence. *Astrophys. J.*, 550:824–840, 2001. 15, 27

A. Brandenburg and W. Dobler. Solar and stellar dynamos - latest developments. *Astron. Nachr.*, 323: 411–416, 2002. 17

A. Brandenburg and K. Subramanian. Astrophysical magnetic fields and nonlinear dynamo theory. *Phys. Rep.*, 417:1–209, 2005. 11, 14, 15

A. Brandenburg, A. Nordlund, R. F. Stein, and U. Torkelsson. Dynamo-generated Turbulence and Large-Scale Magnetic Fields in a Keplerian Shear Flow. *Astrophys. J.*, 446:741, 1995. 5

A. Brandenburg, W. Dobler, and K. Subramanian. Magnetic helicity in stellar dynamos: new numerical experiments. *Astron. Nachr.*, 323:99–122, 2002. 26

J. N. Bregman. The galactic fountain of high-velocity clouds. *Astrophys. J.*, 236:577–591, 1980. 33

R. F. Brown. *The Lefschetz Fixed Point Theorem*. Scott Foresman, London, 1971. 22

R. C. Canfield, H. S. Hudson, and D. E. McKenzie. Sigmoidal morphology and eruptive solar activity. *Geophys. Res. Lett.*, 26:627–630, 1999. 23

S. Chandrasekhar. *Hydrodynamic and hydromagnetic stability*. Oxford Univ. Press, 1961. 61

P. Charbonneau, M. Dikpati, and P. A. Gilman. Stability of the Solar Latitudinal Differential Rotation Inferred from Helioseismic Data. *Astrophys. J.*, 526:523–537, 1999. 19

A. R. Choudhuri, M. Schussler, and M. Dikpati. The solar dynamo with meridional circulation. *Astron. Astrophys.*, 303:L29, 1995. 19

F. Del Sordo, G. Guerrero, and A. Brandenburg. Turbulent dynamo with advective magnetic helicity flux. *arXiv:1205.3502*, 2012. 39, 40

U. Frisch, A. Pouquet, J. Léorat, and A. Mazure. Possibility of an inverse cascade of magnetic helicity in magnetohydrodynamic turbulence. *J. Fluid Mech.*, 68:769–778, 1975. 15, 26

S. E. Gibson, L. Fletcher, G. Del Zanna, C. D. Pike, H. E. Mason, C. H. Mandrini, P. Démoulin, H. Gilbert, J. Burkepile, T. Holzer, D. Alexander, Y. Liu, N. Nitta, J. Qiu, B. Schmieder, and B. J. Thompson. The structure and evolution of a sigmoidal active region. *Astrophys. J.*, 574:1021, 2002. 23, 24

A. V. Gruzinov and P. H. Diamond. Self-consistent theory of mean-field electrodynamics. *Phys. Rev. Lett.*, 72:1651–1653, 1994. 29

A. Hubbard and A. Brandenburg. Magnetic Helicity Flux in the Presence of Shear. *Astrophys. J.*, 727:11, 2011. 41

T. S. Ivanova and A. A. Ruzmaikin. A nonlinear magnetohydrodynamic model of the solar dynamo. *Sov. Astron.*, 21:479–485, 1977. 13

H. Ji. Turbulent Dynamos and Magnetic Helicity. *Phys. Rev. Lett.*, 83:3198–3201, 1999. 26

P. J. Käpylä and A. Brandenburg. Turbulent Dynamos with Shear and Fractional Helicity. *Astrophys. J.*, 699:1059–1066, 2009. 5

N. Kleeorin and I. Rogachevskii. Magnetic helicity tensor for an anisotropic turbulence. *Phys. Rev. E*, 59: 6724–6729, 1999. 30

N. Kleeorin, D. Moss, I. Rogachevskii, and D. Sokoloff. Helicity balance and steady-state strength of the dynamo generated galactic magnetic field. *Astron. Astrophys.*, 361:L5–L8, 2000. 17

N. I. Kleeorin and A. A. Ruzmaikin. Dynamics of the average turbulent helicity in a magnetic field. *Magnetohydrodynamics*, 18:116, 1982. 32

R. Komendarczyk. The third order helicity of magnetic fields via link maps. *J. Math. Phys.*, 51:122702, 2010. 50

F. Krause and K. H. Rädler. Dynamo theory of the suns general magnetic fields on the basis of a mean-field magnetohydrodynamics. In R. Howard, editor, *Solar Magnetic Fields*, volume 43 of *IAU Symposium*, page 770, 1971. 11

F. Krause and K.-H. Rädler. *Mean-field magnetohydrodynamics and dynamo theory*. Oxford, Pergamon Press, 1980. 11, 13, 25, 30

J. Léorat, U. Frisch, and A. Pouquet. Helical magnetohydrodynamic turbulence and the nonlinear dynamo problem. *Ann. N.Y. Acad. Sci.*, 257:173–176, 1975. 15

F. Maggioni and R. L. Ricca. On the groundstate energy of tight knots. *Roy. Soc. Lond. Proc. Ser. A*, 465: 2761–2783, 2009. 52

T. R. Metcalf, L. Jiao, A. N. McClymont, R. C. Canfield, and H. Uitenbroek. Is the solar chromospheric magnetic field force-free? *Astrophys. J.*, 439:474–481, 1995. 23

D. Mitra, R. Tavakol, P. J. Käpylä, and A. Brandenburg. Oscillatory Migrating Magnetic Fields in Helical Turbulence in Spherical Domains. *Astrophys. J.*, 719:L1–L4, 2010. 38

H. K. Moffatt. The degree of knottedness of tangled vortex lines. *J. Fluid Mech.*, 35:117–129, 1969. 20, 49, 62

H. K. Moffatt. *Magnetic field generation in electrically conducting fluids*. Camb. Univ. Press, 1978. 13, 15, 19, 25, 57

H. K. Moffatt and R. L. Ricca. Helicity and the Calugareanu Invariant. *Roy. Soc. Lond. Proc. Ser. A*, 439: 411–429, 1992. 20

C. Pfrommer and L. Jonathan Dursi. Detecting the orientation of magnetic fields in galaxy clusters. *Nature Physics*, 6:520–526, 2010. 55, 61

J. Pietarila Graham, E. G. Blackman, P. D. Mininni, and A. Pouquet. Not much helicity is needed to drive large-scale dynamos. *Physical Review E*, 85:066406, 2012. 5, 26, 27, 28, 29, 57

A. Pouquet, U. Frisch, and J. Léorat. Strong MHD helical turbulence and the nonlinear dynamo effect. *J. Fluid Mech.*, 77:321–354, 1976. 14, 57

E. R. Priest and T. G. Forbes. *Magnetic reconnection: MHD theory and applications*. 2000. 19, 20

R. L. Ricca. Topology bounds energy of knots and links. *Roy. Soc. Lond. Proc. Ser. A*, 464:293–300, 2008. 49

P. H. Roberts and A. M. Soward. A unified approach to mean field electrodynamics. *Astron. Nachr.*, 296: 49–64, 1975. 13

I. Rogachevskii and N. Kleeorin. Electromotive force for an anisotropic turbulence: Intermediate nonlinearity. *Phys. Rev. E*, 61:5202–5210, 2000. 58

M. Ruszkowski, T. A. Enßlin, M. Brüggen, S. Heinz, and C. Pfrommer. Impact of tangled magnetic fields on fossil radio bubbles. *Month. Not. Roy. Astron. Soc.*, 378:662–672, 2007. 55, 61

A. Ruzmaikin and P. Akhmetiev. Topological invariants of magnetic fields, and the effect of reconnections. *Phys. Plasmas*, 1:331–336, 1994. 21, 50, 52, 53

M. Schrinner, K.-H. Rädler, D. Schmitt, M. Rheinhardt, and U. Christensen. Mean-field view on rotating magnetoconvection and a geodynamo model. *Astron. Nachr.*, 326:245–249, 2005. 61

N. Seehafer. Nature of the α effect in magnetohydrodynamics. *Phys. Rev. E*, 53:1283–1286, 1996. 26

P. R. Shapiro and G. B. Field. Consequences of a New Hot Component of the Interstellar Medium. *Astrophys. J.*, 205:762–765, 1976. 33

A. Shukurov, D. Sokoloff, K. Subramanian, and A. Brandenburg. Galactic dynamo and helicity losses through fountain flow. *Astron. Astrophys.*, 448:L33–L36, 2006. 32

M. Steenbeck, F. Krause, and K.-H. Rädler. Berechnung der mittleren Lorentz-Feldstärke $\overline{\mathbf{v}\times\mathbf{B}}$ für ein elektrisch leitendes Medium in turbulenter, durch Coriolis–Kräfte beeinflusster Bewegung. 21a:369–376, 1966. 11, 12

K. Subramanian and A. Brandenburg. Nonlinear Current Helicity Fluxes in Turbulent Dynamos and Alpha Quenching. *Phys. Rev. Lett.*, 93:205001, 2004. 30, 58

K. Subramanian and A. Brandenburg. Magnetic Helicity Density and Its Flux in Weakly Inhomogeneous Turbulence. *Astrophys. J.*, 648:L71–L74, 2006. 58

J. B. Taylor. Relaxation of toroidal plasma and generation of reverse magnetic fields. *Phys. Rev. Lett.*, 33: 1139–1141, 1974. 19, 49

A. G. Tevzadze, L. Kisslinger, A. Brandenburg, and T. Kahniashvili. Magnetic fields from qcd phase transitions. *Astrophys. J.*, 759:54, 2012. 20

W. Thomson. Hydrokinetic solutions and observations. *Philos. Mag.*, 42:362–377, 1871. 61

S. I. Vaĭnshteĭn and F. Cattaneo. Nonlinear restrictions on dynamo action. *ApJ*, 393:165–171, 1992. 14

S. I. Vaǐnshteǐn and Y. B. Zel'dovich. Origin of Magnetic Fields in Astrophysics (Turbulent "Dynamo" Mechanisms). *Sov. Phys. Usp.*, 15:159–172, 1972. 19

E. T. Vishniac and J. Cho. Magnetic Helicity Conservation and Astrophysical Dynamos. *Astrophys. J.*, 550: 752–760, 2001. 30, 39, 58

H. von Helmholtz. Über discontinuierliche Flüssigkeits-Bewegungen. *Monatsberichte der Königlichen Preussische Akademie der Wissenschaften zu Berlin*, 23:215–228, 1868. 61

J. Warnecke, A. Brandenburg, and D. Mitra. Dynamo-driven plasmoid ejections above a spherical surface. *Astron. Astrophys.*, 534:A11, 2011. 35

L. Woltjer. On hydromagnetic equilibrium. *Proceedings of the National Academy of Science*, 44:833–841, 1958. 19

A. R. Yeates and G. Hornig. Unique Topological Characterization of Braided Magnetic Fields. *arXiv:1208.2286*, 2012. 49, 54

A. R. Yeates, D. H. Mackay, and A. A. van Ballegooijen. Evolution and distribution of current helicity in full-sun simulations. *Astrophys. J.*, 680:L165, 2008. 23

A. R. Yeates, G. Hornig, and A. L. Wilmot-Smith. Topological constraints on magnetic relaxation. *Phys. Rev. Lett.*, 105:085002, 2010. 21, 23, 59, 62

N. Yokoi. Large-scale magnetic fields in spiral galaxies viewed from the cross-helicity dynamo. *Astron. Astrophys.*, 311:731–745, 1996. 61

N. Yokoi. Magnetic-field generation and turbulence suppression due to cross-helicity effects. *Physics of Fluids*, 11:2307–2316, 1999. 61

A. Yoshizawa. Self-consistent turbulent dynamo modeling of reversed field pinches and planetary magnetic fields. *Phys. Fluids B*, 2:1589–1600, 1990. 61

A. Yoshizawa and N. Yokoi. Turbulent magnetohydrodynamic dynamo for accretion disks using the cross-helicity effect. *Astrophys. J.*, 407:540–548, 1993. 61

I

NORDITA 2012-62

The kinetic helicity needed to drive large-scale dynamos

Simon Candelaresi^{1,2} and Axel Brandenburg^{1,2}
^{1}*NORDITA, KTH Royal Institute of Technology and Stockholm University, Roslagstullsbacken 23, SE-10691 Stockholm, Sweden*
^{2}*Department of Astronomy, AlbaNova University Center, Stockholm University, SE-10691 Stockholm, Sweden*

(Dated: October 25, 2012, Revision: 1.77)

Magnetic field generation on scales large compared with the scale of the turbulent eddies is known to be possible via the so-called α effect when the turbulence is helical and if the domain is large enough for the α effect to dominate over turbulent diffusion. Using three-dimensional turbulence simulations, we show that the energy of the resulting mean magnetic field of the saturated state increases linearly with the product of normalized helicity and the ratio of domain scale to eddy scale, provided this product exceeds a critical value around unity. This implies that large-scale dynamo action commences when the normalized helicity is larger than the inverse scale ratio. Recent findings by Pietarila Graham et al. (2012, Phys. Rev. E85, 066406) of a smaller minimal helicity may be due to the onset of small-scale dynamo action at large magnetic Reynolds numbers. However, the onset of large-scale dynamo action is difficult to establish when the kinetic helicity is small. Instead of random forcing, they used an ABC-flow with time-dependent phases. We show that such dynamos saturate prematurely in a way that is reminiscent of inhomogeneous dynamos with internal magnetic helicity fluxes. Furthermore, even for very low fractional helicities, such dynamos display large-scale fields that change direction, which is uncharacteristic of turbulent dynamos.

PACS numbers:

I. INTRODUCTION

The origin of magnetic fields in astrophysical bodies like the Earth, the Sun and galaxies is studied in the field of dynamo theory. The temporal variation and strength of those fields rules out a primordial origin, through which the magnetic field would have been created in the early Universe. For magnetic fields with energies of the equipartition value, i.e. the turbulent kinetic energy of the medium, the primordial hypothesis explains their strength after creation, but falls short of explaining how the field outlives billions of years of resistive decay [1].

In dynamo theory, astrophysical plasmas are considered sufficiently well conducting fluids where the inertia of the charge-carrying particles can be neglected. In this approximation the equations of magnetohydrodynamics (MHD) provide an adequate model of the medium. In this framework it has been studied under which conditions magnetic fields of equipartition strength and scales larger than the turbulent motions are created and sustained [2].

A successful theoretical model describing the dynamo's behavior is the mean-field theory. It relates the small-scale turbulent motions to the mean magnetic field via the so-called α effect, which provides the energy input via helical turbulent forcing. During the kinematic phase, i.e. negligible back reaction of the magnetic field on the fluid, the α effect gives a positive feedback on the large-scale magnetic field, which results in its exponential growth. Already the consideration of the kinematic MHD equations with negligible Lorentz force sheds light on the growth rate of the different modes of the magnetic field during the kinematic phase. In the kinematic phase the growth rate λ at wave number k is given by [2]

$$\lambda = \alpha k - \eta_{\rm T} k^2 = (C_\alpha - 1)\eta_{\rm T} k^2, \tag{1}$$

where $C_\alpha = \alpha/\eta_{\rm T} k$ is the relevant dynamo number for the α^2 dynamo, α is the α coefficient which is proportional to the small-scale kinetic helicity, and $\eta_{\rm T} = \eta + \eta_{\rm t}$ is the sum of molecular and turbulent magnetic diffusivity. Clearly, dynamo action occurs when $|C_\alpha| > C_\alpha^{\rm crit}$, where the onset condition is $C_\alpha^{\rm crit} = 1$. Standard estimates for isotropic turbulence in the high conductivity limit [2, 3] yield $\alpha \approx -(\tau/3)\langle\boldsymbol{\omega}\cdot\boldsymbol{u}\rangle$ and $\eta_{\rm t} \approx (\tau/3)\langle\boldsymbol{u}^2\rangle$, where τ is the correlation time of the turbulence, $\boldsymbol{\omega} = \boldsymbol{\nabla}\times\boldsymbol{u}$ is the vorticity and $\boldsymbol{u}$ is the velocity in the small-scale fields. Here, $\langle . \rangle$ denotes a volume average. Using $\eta_{\rm t} \gg \eta$, we have

$$C_\alpha \approx -\langle\boldsymbol{\omega}\cdot\boldsymbol{u}\rangle/k\langle\boldsymbol{u}^2\rangle. \tag{2}$$

It is convenient to define $\langle\boldsymbol{\omega}\cdot\boldsymbol{u}\rangle/k_{\rm f}\langle\boldsymbol{u}^2\rangle$ as the normalized kinetic helicity, $\epsilon_{\rm f}$, so $C_\alpha \approx -\epsilon_{\rm f} k_{\rm f}/k$. This scaling implies that the critical value of the normalized helicity $\epsilon_{\rm f}$ scales inversely proportional to the scale separation ratio, i.e. $\epsilon_{\rm f} \propto (k_{\rm f}/k)^{-1}$, where $k \ll k_{\rm f}$ is the wave number of the resulting large-scale magnetic field. This wave number can be equal to $k = k_1 \equiv 2\pi/L$, which is the smallest wave number in a periodic domain of size L.

In summary, the critical dynamo number $C_\alpha^{\rm crit}$, which decides between growing or decaying solutions of the large-scale dynamo (LSD), is proportional to the product of normalized helicity $\epsilon_{\rm f}$ and scale separation ratio $k_{\rm f}/k$. Therefore, the amount of helicity needed for the LSD is inversely proportional to the scale separation ratio, and not some higher power of it. It should be noted that the *normalized* kinetic helicity $\epsilon_{\rm f}$ used here is not the same as the *relative* kinetic helicity, $\tilde{\epsilon_{\rm f}} = \langle\boldsymbol{\omega}\cdot\boldsymbol{u}\rangle/(\omega_{\rm rms}u_{\rm rms})$. The two are related to each other via the relation

$$\tilde{\epsilon_{\rm f}}/\epsilon_{\rm f} = k_\omega/k_{\rm f}, \tag{3}$$

where $k_\omega \approx \omega_{\rm rms}/u_{\rm rms}$ is inversely proportional to the Taylor microscale. Here, the subscripts rms refer to root-mean-square values. For small Reynolds numbers, k_ω provides a useful estimate of the wave number $k_{\rm f}$ of the energy-carrying eddies. In contrast, for large Reynolds numbers Re, we expect k_ω/k_f to be proportional to $\mathrm{Re}^{1/2}$, so $\tilde{\epsilon}_\mathrm{f}$ decreases correspondingly while ϵ_f remains unchanged. Below we shall present new results suggesting that in the present case of helical turbulence the exponent is not 1/2 but 1/4.

To understand the saturation of a helical dynamo, it is important to understand the relation between the resulting large-scale field and the associated small-scale field. Indeed, the growth of the large-scale field is always accompanied by a growth of small-scale magnetic field. Small-scale here means the scale of the underlying turbulent motions, which drive the dynamo. Conservation of total magnetic helicity causes a build up of magnetic helicity at large scales and of opposite sign at small scales [4, 5]. As the dynamo saturates, the largest scales of the magnetic field become even larger, which finally leads to a field of a scale that is similar to that of the system itself. This can be understood as being the result of an inverse cascade, which was first predicted based on closure calculations [6].

If the domain is closed or periodic, the build up of small-scale magnetic helicity causes the α effect to diminish, which marks the end of the exponential growth and could occur well before final saturation is reached. The dynamo then is said to be catastrophically quenched and, in a closed or periodic system, the subsequent growth to the final state happens not on a dynamical timescale, but on a resistive one. Quenching becomes stronger as the magnetic Reynolds number increases, which, for astrophysically relevant problems, means a total loss of the LSD within the timescales of interest. In the case of open boundaries magnetic helicity fluxes can occur, which can alleviate the quenching and allow for fast saturation of the large-scale magnetic field [7–10].

In a recent publication [11] it was argued that for periodic boundaries the critical value of ϵ_f for LSD action to occur decreases with the scale separation ratio like $\epsilon_\mathrm{f}^\mathrm{crit} \propto (k_\mathrm{f}/k_1)^{-3}$. Their finding, however, is at variance with the predictions made using equation (1), which would rather suggest a dependence of $\epsilon_\mathrm{f}^\mathrm{crit} \propto (k_\mathrm{f}/k_1)^{-1}$ with $C_\alpha^\mathrm{crit} = 1$. This discrepancy could be a consequence of the criterion used in [11] for determining C_α^crit. The authors looked at the growth rate of the magnetic field after the end of the kinematic growth phase, but only at a small fraction of the resistive time. Therefore their results might well be contaminated by magnetic fields resulting from the small-scale dynamo (SSD). Earlier simulations [12] have demonstrated that for $\mathrm{Re}_\mathrm{M} \geq 100$, the growth rate of the helical LSD approaches the well-known scaling of the non-helical SSD with $\lambda \propto \mathrm{Re}^{1/2}$, which corresponds to the turnover rate of the smallest turbulent eddies [13, 14].

Given that the LSD is best seen in the nonlinear regime [15], we decided to determine C_α^crit from a bifurcation diagram by extrapolating to zero. In a bifurcation diagram we plot the energy of the mean or large-scale field versus C_α. Simple considerations using the magnetic helicity equation applied to a homogeneous system in the steady state show that the current helicity must vanish [15]. In a helically driven system, this implies that the current helicity of the large-scale field must then be equal to minus the current helicity of the small-scale field. For a helical magnetic field this yields the value of $\langle\overline{\boldsymbol{B}}^2\rangle/B_\mathrm{eq}^2$ approximately as $\epsilon_\mathrm{f} k_\mathrm{f}/k_1$, i.e., proportional to C_α. Here $B_\mathrm{eq} = (\mu_0\overline{\rho})^{1/2}u_\mathrm{rms}$ is the equipartition value of the magnetic field with the permeability μ_0 and the mean density $\overline{\rho}$. Again, this suggests that the LSD is excited for $\epsilon_\mathrm{f} > (k_\mathrm{f}/k_1)^{-1}$ rather than some higher power of k_f/k_1. This is a basic prediction that has been obtained from nonlinear mean-field dynamo models that incorporate magnetic helicity evolution [16] as well as from direct numerical simulations in the presence of shear [17]. It is important to emphasize that mean field dynamo theory has been criticized on the grounds that no α effect may exist in the highly nonlinear regime at large magnetic Reynolds numbers [18]. This is however in conflict with results of numerical simulations using the test-field method [19] showing that α effect and turbulent diffusivity are both large, and that only the difference between both effects is resistively small. Another possibility is that the usual helical dynamo of α^2 type may not be the fastest growing one [20]. This is related to the fact that, within the framework of the Kazantsev model [21] with helicity, there are new solutions with long-range correlations solutions [22, 23], which could dominate the growth of a large scale field at early times. The purpose of the present paper is therefore to reinvestigate the behavior of solutions in the nonlinear regime over a broader parameter range in the light of recent conflicting findings [11].

II. THE MODEL

A. Basic equations

Following earlier work, we solve the compressible hydromagnetic equations using an isothermal equation of state. Although compressibility is not crucial for the present purpose, it does have the advantage of avoiding the non-locality associated with solving for the pressure, which requires global communication. Thus, we solve the equations

$$\frac{\partial}{\partial t}\boldsymbol{A} = \boldsymbol{U}\times\boldsymbol{B} - \eta\mu_0\boldsymbol{J}, \tag{4}$$

$$\frac{\mathrm{D}}{\mathrm{D}t}\boldsymbol{U} = -c_\mathrm{s}^2\boldsymbol{\nabla}\ln\rho + \frac{1}{\rho}\boldsymbol{J}\times\boldsymbol{B} + \boldsymbol{F}_\mathrm{visc} + \boldsymbol{f}, \tag{5}$$

$$\frac{\mathrm{D}}{\mathrm{D}t}\ln\rho = -\boldsymbol{\nabla}\cdot\boldsymbol{U}, \tag{6}$$

where $\boldsymbol{A}$ is the magnetic vector potential, $\boldsymbol{U}$ the velocity, $\boldsymbol{B}$ the magnetic field, η the molecular magnetic diffusivity, μ_0 the vacuum permeability, $\boldsymbol{J}$ the electric current density, c_s the isothermal sound speed, ρ the density, $\boldsymbol{F}_\mathrm{visc}$ the viscous force, $\boldsymbol{f}$ the helical forcing term, and $\mathrm{D}/\mathrm{D}t = \partial/\partial t + \boldsymbol{U}\cdot\boldsymbol{\nabla}$ the advective time derivative. The viscous force is given as $\boldsymbol{F}_\mathrm{visc} = \rho^{-1}\boldsymbol{\nabla}\cdot 2\nu\rho\boldsymbol{\mathsf{S}}$, where ν is the kinematic viscosity, and $\boldsymbol{\mathsf{S}}$ is the traceless rate of strain tensor with components $\mathsf{S}_{ij} = \frac{1}{2}(u_{i,j} + u_{j,i}) - \frac{1}{3}\delta_{ij}\boldsymbol{\nabla}\cdot\boldsymbol{U}$. Commas denote partial derivatives.

The energy supply for a helically driven dynamo is provided by the forcing function $\boldsymbol{f} = \boldsymbol{f}(\boldsymbol{x}, t)$, which is a helical function that is random in time. It is defined as

$$\boldsymbol{f}(\boldsymbol{x},t)=\mathrm{Re}\{N\boldsymbol{f}_{\boldsymbol{k}(t)}\exp[\mathrm{i}\boldsymbol{k}(t)\cdot\boldsymbol{x}+\mathrm{i}\phi(t)]\}, \tag{7}$$

where $\boldsymbol{x}$ is the position vector. The wave vector $\boldsymbol{k}(t)$ and the random phase $-\pi<\phi(t)\leq\pi$ change at every time step, so $\boldsymbol{f}(\boldsymbol{x},t)$ is δ-correlated in time. For the time-integrated forcing function to be independent of the length of the time step δt, the normalization factor N has to be proportional to $\delta t^{-1/2}$. On dimensional grounds it is chosen to be $N=f_0 c_{\rm s}(|\boldsymbol{k}|c_{\rm s}/\delta t)^{1/2}$, where f_0 is a non-dimensional forcing amplitude. We choose $f_0=0.02$ which results in a maximum Mach number of about 0.3 and an rms value of about 0.085. At each timestep we select randomly one of many possible wave vectors in a certain range around a given forcing wave number. The average wave number is referred to as $k_{\rm f}$. Transverse helical waves are produced via [14]

$$\boldsymbol{f}_{\boldsymbol{k}}=\mathsf{R}\cdot\boldsymbol{f}_{\boldsymbol{k}}^{(\rm nohel)}\quad\text{with}\quad \mathsf{R}_{ij}=\frac{\delta_{ij}-\mathrm{i}\sigma\epsilon_{ijk}\hat{k}_k}{\sqrt{1+\sigma^2}}, \tag{8}$$

where σ is a measure of the helicity of the forcing and $\sigma=1$ for positive maximum helicity of the forcing function. Furthermore,

$$\boldsymbol{f}_{\boldsymbol{k}}^{(\rm nohel)}=(\boldsymbol{k}\times\boldsymbol{e})/\sqrt{\boldsymbol{k}^2-(\boldsymbol{k}\cdot\boldsymbol{e})^2} \tag{9}$$

is a non-helical forcing function, where $\boldsymbol{e}$ is an arbitrary unit vector not aligned with $\boldsymbol{k}$; note that $|\boldsymbol{f}_{\boldsymbol{k}}|^2=1$ and

$$\boldsymbol{f}_{\boldsymbol{k}}\cdot(\mathrm{i}\boldsymbol{k}\times\boldsymbol{f}_{\boldsymbol{k}})^*=2\sigma k/(1+\sigma^2), \tag{10}$$

so the relative helicity of the forcing function in real space is $2\sigma/(1+\sigma^2)$.

For comparison with earlier work, we shall also use in one case an ABC-flow forcing function [24],

$$\boldsymbol{f}(\boldsymbol{x})=\frac{f_0}{\sqrt{\frac{3}{2}(1+\sigma^2)}}\begin{pmatrix}\sin X_3+\sigma\cos X_2\\ \sin X_1+\sigma\cos X_3\\ \sin X_2+\sigma\cos X_1\end{pmatrix}, \tag{11}$$

where $X_i=k_{\rm f}x_i+\theta_i$ and $\theta_i=\theta_0\cos\omega_i t$ are time-dependent phases that vary sinusoidally with frequencies ω_i and amplitude θ_0. This forcing function is easy to implement and serves therefore as a proxy of helical turbulence; see Ref. [11, 25], where the phases changed randomly. We have restricted ourselves to the special case where the coefficients in front of the trigonometric functions are unity, but those could be made time-dependent too; see Ref. [26]. However, as we will see below, ABC-flow driven dynamos do not show some crucial aspects of random plane wave-forced helical turbulence. Most of the results presented below concern the forcing function (7) and only one case with Eq. (11) will be considered at the end.

Our model is governed by several non-dimensional parameters. In addition to the scale separation ratio $k_{\rm f}/k_1$, introduced above, there are the magnetic Reynolds and Prandtl numbers

$$\mathrm{Re}_{\rm M}=u_{\rm rms}/\eta k_{\rm f},\quad \mathrm{Pr}_{\rm M}=\nu/\eta. \tag{12}$$

These two numbers also define the fluid Reynolds number, $\mathrm{Re}=u_{\rm rms}/\nu k_{\rm f}=\mathrm{Re}_{\rm M}/\mathrm{Pr}_{\rm M}$. The maximum values that can be attained are limited by the numerical resolution and become more restrictive at larger scale separation. The calculations have been performed using the PENCIL CODE (see http://pencil-code.googlecode.com) at resolutions of up to 512^3 mesh points.

B. Mean-field interpretation

The induced small-scale motions $\boldsymbol{u}$ are helical and give rise to the usual (kinetic) α effect [3]

$$\alpha_{\rm K}\approx-\frac{\langle\boldsymbol{\omega}\cdot\boldsymbol{u}\rangle}{3u_{\rm rms}k_{\rm f}}. \tag{13}$$

In the nonlinear regime, following the early work of Pouquet, Frisch, and Léorat [27], the relevant α effect for dynamo action is believed to be the sum of the kinetic and a magnetic α, i.e.,

$$\alpha\approx\frac{-\langle\boldsymbol{\omega}\cdot\boldsymbol{u}\rangle+\langle\boldsymbol{j}\cdot\boldsymbol{b}\rangle/\langle\rho\rangle}{3u_{\rm rms}k_{\rm f}}. \tag{14}$$

Simulations have confirmed the basic form of Eq. (14) with equal contributions from $\langle\boldsymbol{\omega}\cdot\boldsymbol{u}\rangle$ and $\langle\boldsymbol{j}\cdot\boldsymbol{b}\rangle/\langle\rho\rangle$, but one may argue that the second term should only exist in the presence of hydromagnetic background turbulence [28], but not if the magnetic fluctuations are a consequence of tangling of a mean field produced by dynamo action as in the simulations in Ref. [15]. However, to explain the resistively slow saturation in those simulations, the only successful explanation [16, 29] comes from considering the magnetic helicity equation, which feeds back onto the α effect via Eq. (14). This is our main argument in support of the applicability of this equation. Another problem with Eq. (14) is the assumption of isotropy [28], which has however been relaxed in subsequent work [30]. Let us also mention that Eq. (14) is usually obtained using the τ approximation. In its simplest form, it yields incorrect results on the low conductivity limit, but this problem can be avoided, too [31].

Equation (14) is used to derive the expression for the resistively slow saturation behavior [29]. We will not reproduce here the derivation, which can be found elsewhere [16]. The resulting large-scale fields can be partially helical, which means one can write

$$\langle\boldsymbol{J}\cdot\boldsymbol{B}\rangle=\epsilon_{\rm m}k_{\rm m}\langle\boldsymbol{B}^2\rangle, \tag{15}$$

with large-scale wave vector $k_{\rm m}$ and corresponding fractional helicity $\epsilon_{\rm m}$, defined through Eq. (15). However, in the cases considered below the domain is triply periodic, so the solutions are Beltrami fields for which $k_{\rm m}\approx k_1$ and $\epsilon_{\rm m}\approx1$ is an excellent approximation, and only $\epsilon_{\rm f}$ will take values less unity. Nevertheless, in some expressions we retain the $\epsilon_{\rm m}$ factor for clarity. For example, the saturation value of the large-scale magnetic field, $B_{\rm sat}$, is given by [16]

$$B_{\rm sat}^2/B_{\rm eq}^2\approx(|C_\alpha|/\epsilon_{\rm m}-1)\,\iota, \tag{16}$$

where $C_\alpha=\alpha_{\rm K}/(\eta_{\rm T}k_1)$ is the relevant dynamo number based on the smallest wavenumber in the domain and $\iota=$

$1+3/\mathrm{Re_M} \equiv \eta_\mathrm{T}/\eta_\mathrm{t}$ is a correction factor resulting from the fact that η_T is slightly bigger than η_t. The factor 3 in the expression for ι results from our definition of $\mathrm{Re_M}$ and the fact that [32]

$$\eta_\mathrm{t} \approx u_\mathrm{rms}/3k_\mathrm{f} = \eta \mathrm{Re_M}/3. \tag{17}$$

Equation (16) shows clearly the onset condition $|C_\alpha| > |\epsilon_\mathrm{m}| \approx 1$. Using Eqs. (13) and (17), we find

$$C_\alpha \approx -\frac{\langle \boldsymbol{\omega}\cdot\boldsymbol{u}\rangle}{\iota k_1 u_\mathrm{rms}^2} = -\frac{\epsilon_\mathrm{f} k_\mathrm{f}}{\iota k_1}. \tag{18}$$

From equation (16) we can derive the critical value of the normalized helicity ϵ_f as a function of the scale separation ratio. Setting C_α to is critical value ($|C_\alpha| = \epsilon_\mathrm{m}$) we obtain

$$\epsilon_\mathrm{f}^\mathrm{crit} \approx \iota\epsilon_\mathrm{m}\left(\frac{k_\mathrm{f}}{k_1}\right)^{-1}, \tag{19}$$

which is at variance with the findings in [11].

Once the dynamo is excited and has reached a steady state, not only α but also η_t will be suppressed. This can be taken into account using a quenching factor $g(\overline{B})$, so $\eta_\mathrm{t}(\overline{B}) = \eta_{\mathrm{t}0} g(\overline{B})$ with $g = (1+\tilde{g}|\overline{\boldsymbol{B}}|/B_\mathrm{eq})^{-1}$ [15, 33, 34]. Equation (16) is then modified and reads $B_\mathrm{sat}^2/B_\mathrm{eq}^2 = (|C_\alpha| - C_{\alpha 0})\iota/\epsilon_\mathrm{m}$ with

$$C_{\alpha 0} = [1-(1-g)/\iota]\epsilon_\mathrm{m}. \tag{20}$$

Note that $C_{\alpha 0} = \epsilon_\mathrm{m}^{-1}$ in the unquenched case, i.e., for $g=1$.

C. Simulation strategy

We recall that our forcing term $\boldsymbol{f}$ in equation (7) is a stochastic forcing centered around the wave number k_f. In contrast to [11] this forcing is δ-correlated in time. The fractional helicity of the helical forcing is a free parameter. The simulation domain is a periodic cube with dimensions 2π. Due to the cubic geometry of the domain the large-scale magnetic field can orient itself in 3 possible directions. Therefore we compute three possible planar averages (xy, xz, and yz averages). From their resistive evolution we infer their saturation values at the end of the resistive phase. The strongest field gives then the relevant mean-field $\overline{\boldsymbol{B}}$.

Since $\overline{\boldsymbol{B}}$ is helical and magnetic helicity can only change on resistive timescales, the temporal evolution of the energy of the mean magnetic field, $M(t)$, is given by [15]

$$M(t) = M_0 - M_1 e^{-t/\tau}, \tag{21}$$

where $\tau^{-1} = 2\eta\epsilon_\mathrm{m}^2 k_1^2$ is known, $M_0 = B_\mathrm{sat}^2$ is the square of the desired saturation field strength, and M_1 is an unknown constant that can be positive or negative, depending on whether the initial magnetic field of a given calculation was smaller or larger than the final value. (Here, an initial field could refer to the last snapshot of another calculation with similar parameters, for example.) The functional behavior given by Eq. (21) allows us to determine B_sat^2 as the time average of $M+\tau\mathrm{d}M/\mathrm{d}t$, which should only fluctuate about a constant value, i.e.,

$$B_\mathrm{sat}^2 \approx \frac{1}{t_2-t_1}\int_{t_1}^{t_2}\left[\langle\overline{\boldsymbol{B}}^2\rangle(t') + \tau\frac{\mathrm{d}}{\mathrm{d}t'}\langle\overline{\boldsymbol{B}}^2\rangle\right]\mathrm{d}t'. \tag{22}$$

This technique has the advantage that we do not need to wait until the field reaches its final saturation field strength. Error bars can be estimated by computing this average for each third of the full time series and taking the largest departure from the average over the full time series. An example is shown in Fig. 1, where we see $\langle\overline{\boldsymbol{B}}^2\rangle$ still growing while $\langle\overline{\boldsymbol{B}}^2\rangle + \tau\mathrm{d}\langle\overline{\boldsymbol{B}}^2\rangle/\mathrm{d}t$ is nearly constant when $\langle\overline{\boldsymbol{B}}^2\rangle$ reaches a value less than half its final one. This figure shows that the growth of $\langle\overline{\boldsymbol{B}}^2\rangle$ follows the theoretical expectation (21) quite closely and that temporal fluctuations about this value are small, as can be seen by the fact that its time derivative fluctuates only little.

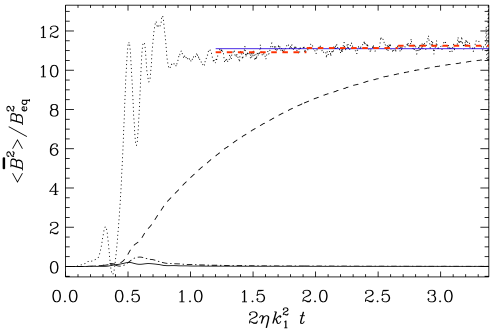

FIG. 1: (Color online) Example showing the evolution of the normalized $\langle\overline{\boldsymbol{B}}^2\rangle$ (dashed) and that of $\langle\overline{\boldsymbol{B}}^2\rangle + \tau\mathrm{d}\langle\overline{\boldsymbol{B}}^2\rangle/\mathrm{d}t$ (dotted), compared with its average in the interval $1.2 \le 2\eta k_1^2 t \le 3.5$ (horizontal blue solid line), as well as averages over 3 subintervals (horizontal red dashed lines). Here, $\overline{\boldsymbol{B}}$ is evaluated as an xz average, $\langle\boldsymbol{B}\rangle_{xz}$. For comparison we also show the other two averages, $\langle\boldsymbol{B}\rangle_{xy}$ (solid) and $\langle\boldsymbol{B}\rangle_{xy}$ (dash-dotted), but their values are very small.

III. RESULTS

A. Dependence of kinetic helicity on σ

We recall that the relative helicity of the forcing function is $\boldsymbol{f}\cdot\boldsymbol{\nabla}\times\boldsymbol{f}/[\boldsymbol{f}_\mathrm{rms}(\boldsymbol{\nabla}\times\boldsymbol{f})_\mathrm{rms}] = 2\sigma/(1+\sigma^2)$. This imposes then a similar variation onto the relative kinetic helicity, $\tilde{\epsilon_\mathrm{f}} = \langle\boldsymbol{\omega}\cdot\boldsymbol{u}\rangle/\omega_\mathrm{rms}u_\mathrm{rms}$; see Fig. 2(a). However, as discussed above, $\tilde{\epsilon_\mathrm{f}}$ is smaller than ϵ_f by a factor k_ω/k_f, which depends on the Reynolds number. It turns out that ϵ_f matches almost exactly the values of $2\sigma/(1+\sigma^2)$; see Fig. 2(b).

The theoretically expected scaling $k_\omega/k_\mathrm{f} \propto \mathrm{Re}^{1/2}$ is a well-known result for non-helical turbulence [35], but for

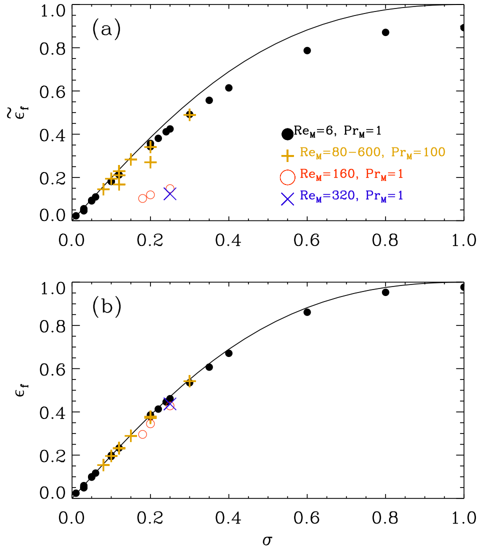

FIG. 2: (Color online) Dependence of relative kinetic helicity $\tilde{\epsilon}_{\rm f}$ (a) and normalized kinetic helicity $\epsilon_{\rm f}$ (b) on the helicity parameter σ of the forcing function Eq. (8) together with the analytical expression $2\sigma/(1+\sigma^2)$ (solid line).

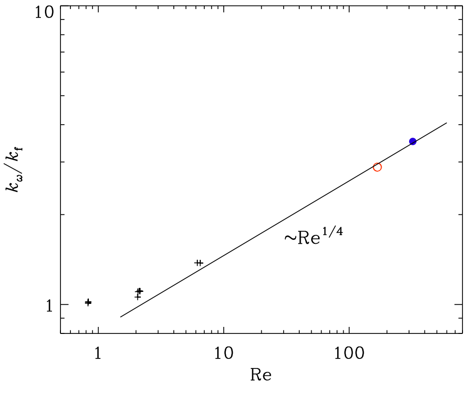

FIG. 3: (Color online) Dependence of $k_\omega/k_{\rm f}$ on Re. The open and closed circles correspond to runs with $\mathrm{Pr_M}=1$, while the + signs correspond to runs with $\mathrm{Pr_M}=100$, so $\mathrm{Re}=\mathrm{Re_M}/\mathrm{Pr_M}$.

helical turbulence those scaling relations are modified; see, e.g., Ref. [36]. For our current data we find that $k_\omega/k_{\rm f}\approx 0.8\,\mathrm{Re}^{1/4}$; see Fig. 3. The reason for this power law behavior is however unclear.

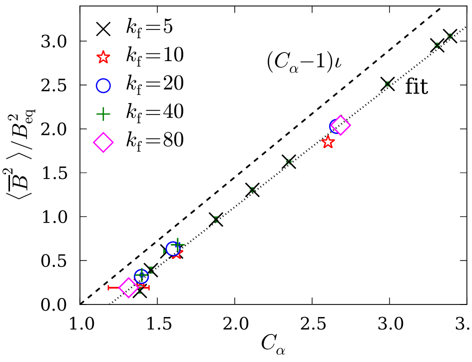

FIG. 4: (Color online) Steady state values of $\langle\overline{\boldsymbol{B}}^2\rangle/B_{\rm eq}^2$ as a function of C_α together with the theoretical prediction from equation (16) (dashed line) and a linear fit (dotted line).

B. Dependence on scale separation

We perform simulations with different forcing wave numbers $k_{\rm f}$ and different values of $\epsilon_{\rm f}$ at approximately constant magnetic Reynolds number, $\mathrm{Re_M}\approx 6$, and fixed magnetic Prandtl number, $\mathrm{Pr_M}=1$. Near the end of the resistive saturation phase we look at the energy of the strongest mode at $k=k_1$, using the method described in § II C. We choose this rather small value of Re because we want to access relatively large scale separation ratios up to $k_{\rm f}/k_1=80$. Given that the Reynolds number based on the scale of the domain is limited by the number of mesh points (500, say), it follows that for $k_{\rm f}/k_1=80$ the Reynolds number defined through Eq. (12) is 6. For comparison, a Reynolds number based on the size of the domain, i.e., $u_{\rm rms}L/\eta$, would be larger by a factor 2π, i.e., 3000.

As seen from Eq. (16), mean-field considerations predict a linear increase of the saturation magnetic energy with C_α and onset at $C_\alpha=1$. This behavior is reproduced in our simulation (Fig. 4), where we compare the theoretical prediction with the simulation results. For different values of $k_{\rm f}/k_1$ and C_α we extrapolate the critical value $C_\alpha^{\rm crit}\approx 1.2$ (Fig. 4), which gives the critical values $\epsilon_{\rm f}^{\rm crit}\approx 1.2\iota\,(k_{\rm f}/k_1)^{-1}=1.7\,(k_{\rm f}/k_1)^{-1}$ for which the LSD is excited. For each scale separation value we plot the dependence of $\langle\overline{\boldsymbol{B}}^2\rangle/B_{\rm eq}^2$ on $\epsilon_{\rm f}$ (Fig. 5) and make linear fits. From these fits we can extrapolate the critical values $\epsilon_{\rm f}^{\rm crit}$, for which the LSD gets excited (Fig. 6), which gives again $\epsilon_{\rm f}^{\rm crit}\approx 1.7\,(k_{\rm f}/k_1)^{-1}$.

It is noteworthy that the graph of $\langle\overline{\boldsymbol{B}}^2\rangle/B_{\rm eq}^2$ versus C_α deviates systematically (although only by a small amount) from the theoretically expected value, $(C_\alpha-1)\iota$. While the slope is rather close to the expected one, the onset of LSD is slightly delayed and occurs at $C_\alpha\approx 1.2$ instead of 1. The reason for this is not clear, although one might speculate that it could be modeled by adopting modified effective values of ι or $\epsilon_{\rm m}$ in

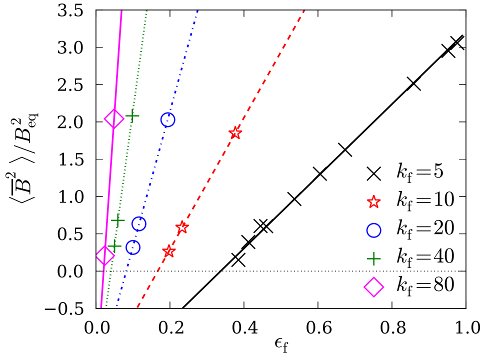

FIG. 5: (Color online) Steady state values of $\langle\overline{\boldsymbol{B}}^2\rangle/B_{\rm eq}^2$ as a function of $\epsilon_{\rm f}$ for various scale separation values $k_{\rm f}/k_1$ together with linear fits.

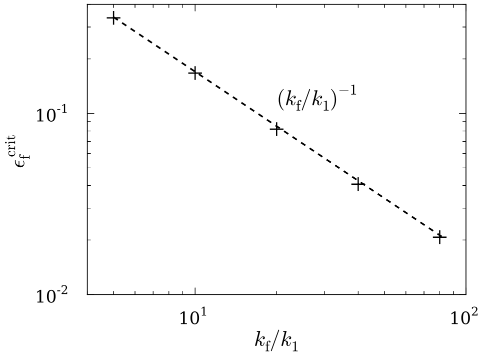

FIG. 6: Critical value for the normalized kinetic helicity $\epsilon_{\rm f}$ for which LSD action occurs for different scale separations.

Eq. (20). Apart from such minor discrepancies with respect to the simple theory, the agreement is quite remarkable. Nevertheless, we must ask ourselves whether this agreement persists for larger values of the magnetic Reynolds number. This will be addressed in § III C.

At this point we should note that there is also a theoretical prediction for the energy in the magnetic fluctuations, namely $\langle\boldsymbol{b}^2\rangle/B_{\rm eq}^2 \approx (C_\alpha - C_\alpha^{\rm crit})/C_\alpha$. Nonetheless, the results shown in Fig. 7 deviate from this relation and are better described by a modified formula

$$\langle\boldsymbol{b}^2\rangle/B_{\rm eq}^2 \propto 1-(C_\alpha^{\rm crit}/C_\alpha)^n \quad \text{(with } n\approx 4). \tag{23}$$

Again, the reason for this departure is currently unclear.

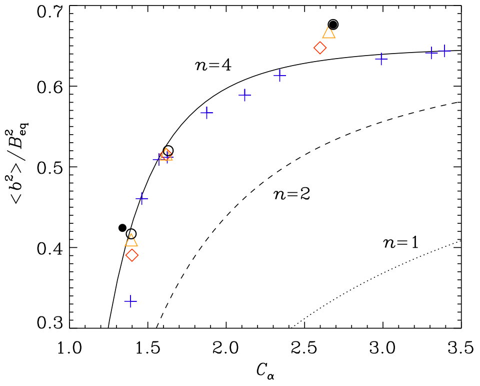

FIG. 7: (Color online) Steady state values of $\langle\boldsymbol{b}^2\rangle/B_{\rm eq}^2$ as a function of C_α together with the fit formula from equation (23) with $n=4$, compared with $n=1$ (dotted) and $n=2$ (dashed).

C. Dependence on $\mathrm{Re}_{\rm M}$

To examine whether there is any unexpected dependence of the onset and the energy of the mean magnetic field on $\mathrm{Re}_{\rm M}$ and to approach the parameters used in [11], who used values up to $\mathrm{Re}_{\rm M}=1500$, we now consider larger values of the magnetic Reynolds number. This widens the inertial range significantly and leads to the excitation of the SSD. Higher values of $\mathrm{Re}_{\rm M}$ can more easily be reached at larger values of $\mathrm{Pr}_{\rm M}$. This is because at large values of $\mathrm{Pr}_{\rm M}$, most of the injected energy is dissipated viscously rather than resistively, leaving less energy to be channeled down the magnetic cascade [37]. This is similar to the case of *small* values of $\mathrm{Pr}_{\rm M}$, where larger *fluid* Reynolds numbers can be reached because then most of the energy is dissipated resistively [12]. Here, however, we shall be concerned with the former case of large values of $\mathrm{Pr}_{\rm M}$.

The results for $\mathrm{Pr}_{\rm M}=100$ are presented in Fig. 8 for different values of $\epsilon_{\rm f}$ and $\mathrm{Re}_{\rm M}$ being either 80, 200, or 600. Most importantly, it turns out that the critical value for the onset of LSD is not much changed. We now find $C_\alpha^{\rm crit}\approx 0.9$ instead of 1. Furthermore, the dependence of $\langle\overline{\boldsymbol{B}}^2\rangle/B_{\rm eq}^2$ on C_α, and thus also the value of $C_\alpha^{\rm crit}$, are the same for all three values of $\mathrm{Re}_{\rm M}$. It is however surprising that it is now even below unity. Furthermore, the slope is different from that of Fig. 4: it is now closer to 2 than to the earlier value of 1. This discrepancy with the theory can be easily explained by arguing that the relevant value of $B_{\rm eq}$ has been underestimated in the large $\mathrm{Pr}_{\rm M}$ cases. Looking at the power spectrum of the high $\mathrm{Pr}_{\rm M}$ simulations in Fig. 10(a), we see that the kinetic energy is indeed subdominant and does not provide a good estimate of the magnetic energy of the small-scale field $\langle\boldsymbol{b}^2\rangle/2\mu_0$. By contrast, for $\mathrm{Pr}_{\rm M}=1$, the magnetic and kinetic energy spectra are similar at all scales except near $k=k_1$; see Fig. 10(b). The slight super-equipartition for $k>k_{\rm f}$ is also typical of

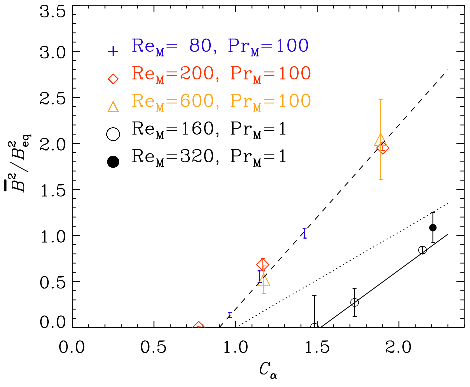

FIG. 8: (Color online) Steady state values of $\langle\overline{\boldsymbol{B}}^2\rangle/B_{\rm eq}^2$ as a function of C_α for $\mathrm{Pr_M}=100$ (dashed line) and $\mathrm{Pr_M}=1$ (solid line) for $k_{\rm f}/k_1=5$ and different values of $\mathrm{Re_M}$ (different symbols), compared with the theoretical prediction (dotted line).

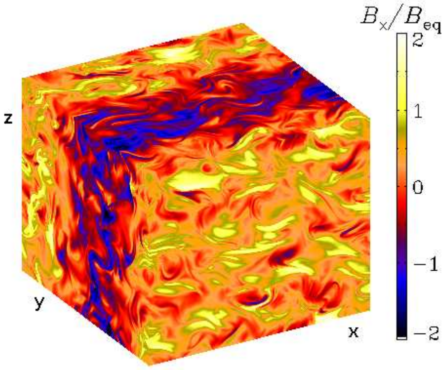

FIG. 9: (Color online) Visualization of B_x on the periphery of the domain for $\mathrm{Pr_M}=100$ after resistive saturation.

small-scale dynamos [14].

A visualization of the magnetic field in this case is given in Fig. 9, where we show B_x on the periphery of the computational domain. The magnetic field has now clearly strong gradients locally, while still being otherwise dominated by a large-scale component at $k=k_1$. In this case the large-scale field shows variations only in the y direction and is of the form

$$\overline{\boldsymbol{B}}=(\sin k_1y,0,\cos k_1y)\,B_{\rm sat}. \tag{24}$$

This field has negative magnetic helicity, so $\overline{\boldsymbol{J}}\cdot\overline{\boldsymbol{B}}=-k_1\overline{\boldsymbol{B}}^2$, as expected for a forcing function with negative helicity.

We have argued that the reason for the larger slope in the graph of $\langle\overline{\boldsymbol{B}}^2\rangle$ versus C_α is related to $B_{\rm eq}$ being underestimated for large values of $\mathrm{Pr_M}$. To confirm this, we now consider calculations with $\mathrm{Pr_M}=1$, two different values of $\epsilon_{\rm f}$, fixed values of $\mathrm{Re_M}$ (either 160 or 320), and fixed scale separation ratio $k_{\rm f}/k_1=5$. We see in Fig. 8 that the slope is indeed smaller. Furthermore, $C_\alpha^{\rm crit}$ is now above 1, and even larger than at low $\mathrm{Re_M}$ (now $C_\alpha^{\rm crit}\approx1.5$ instead of 1.2).

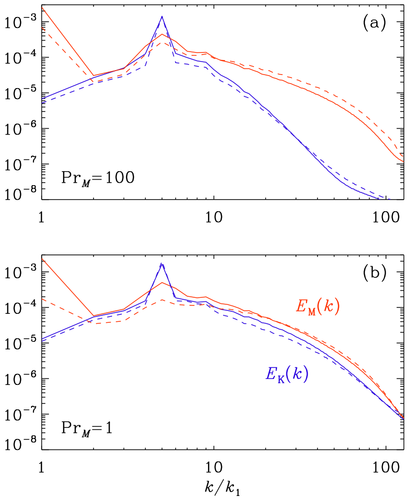

FIG. 10: (Color online) Comparison of kinetic and magnetic energy spectra for $\mathrm{Pr_M}=100$ (upper panel) and $\mathrm{Pr_M}=1$ (lower panel) for $\sigma=0.2$ (solid lines) and 0.12 (dashed lines).

D. ABC-flow forcing

In this paper we have used the fact that the saturation field strength is described by Eq. (16). While this is indeed well obeyed for our randomly driven flows, this does not seem to be the case for turbulence driven by ABC-flow forcing. We demonstrate this by considering a case that is similar to that shown in Fig. 1, where $\mathrm{Re_M}\approx6$ in the saturated state. We thus use Eq. (11) with $\sigma=\theta_0=1$ and $k_{\rm f}/k_1=15$. The *kinematic* flow velocity reaches an equilibrium rms velocity of $U_0=f_0/\nu k_{\rm f}^2$. The magnetic Reynolds number based on this velocity is $U_0/\eta k_{\rm f}$, which is chosen to be 13, so that during *saturation* the resulting value of $\mathrm{Re_M}$ is about 6, just as in Fig. 1. For the x, y, and z components we take different forcing frequencies such that ω_i/k_1U_0 is 10, 11, and 9 for $i=1$, 2, and 3, respectively. These values correspond approximately to the inverse correlation times used in [11]. The result is shown in Fig. 11. It turns out that the magnetic field grows initially as expected, based on Eq. (21), but then the final saturation phase is cut short below $B_{\rm sat}^2/B_{\rm eq}^2\approx3$ rather than the

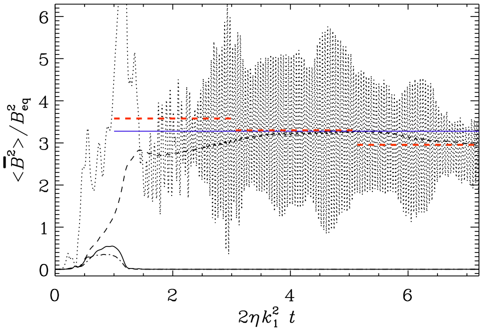

FIG. 11: (Color online) Similar to Fig. 1, but for time-dependent ABC-flow driving. As in Fig. 1, we have here $k_{\rm f}/k_1 = 15$ and $\mathrm{Re_M} \approx 4$.

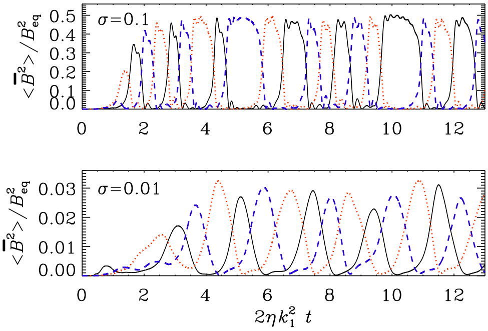

FIG. 12: (Color online) Dependence of the normalized $\langle\overline{\boldsymbol{B}}^2\rangle$ for different planar averages: yz (black), xz (red, dotted), and xy (blue, dashed), for $\sigma = 0.1$ (upper panel) and $\sigma = 0.01$ (lower panel).

value 12 found with random wave forcing. This is reminiscent of inhomogeneous dynamos in which magnetic helicity fluxes operate. In homogeneous systems, however, magnetic helicity flux divergences have only been seen if there is also shear [38]. In any case, the present behavior is unexpected and suggests that the effective value of C_α is reduced. Using the test-field method [39, 40], we have confirmed that the actual value of C_α is not reduced. The dynamo is therefore excited, but the value implied for the effective helicity is reduced.

Another possibility is that, especially for small values of σ, the ABC-flow has non-generic dynamo properties that emulate aspects of large-scale dynamos. An example is shown in Fig. 12 where we plot the time evolution of all three planar averages (yz, xz, and xy). Even for $\sigma = 0.01$, large-scale magnetic fields are still excited, but the field orientation changes periodically on a timescale of 1–2 diffusion times. This is obviously a fascinating topic for further research, but it is unrelated to our main question regarding the minimal helicity of generic turbulent dynamos. It might indeed be an example of so-called incoherent α effect dynamos [41] that have recently attracted increased interest [42–44].

The main point of this section is to emphasize the limited usefulness of ABC-flow dynamos. Another such example are dynamos driven by the Galloway-Proctor flow, which also has a number of peculiar features; see Ref. [45].

IV. CONCLUSIONS

In this paper we have studied the simplest possible LSD and have investigated the dependence of its saturation amplitude on the amount of kinetic helicity in the system. We recall that the case of a periodic domain has already been investigated in some detail [29, 46], and that theoretical predictions in the case with shear [16] have been verified numerically for fractional helicities [17]. Yet the issue has now attracted new interest in view of recent results suggesting that, in the limit of large scale separation, the amount of kinetic helicity needed to drive the LSD might actually be much smaller than what earlier calculations have suggested [11]. This was surprising given the earlier confirmations of the theory. As explained above, the reason for the conflicting earlier results may be the fact that the LSD cannot be safely isolated in the linear regime, because it will be dominated by the SSD or, in the case of the ABC-flow dynamo, by some other kind of dynamo that is not due to the α effect. Furthermore, as already alluded to in the introduction, there can be solutions with long-range correlations that could mimic those that are not due to the α effect. Indeed, within the framework of the Kazantsev model [21], the solutions to resulting Schrödinger-type equations can be described as bound states. The addition of kinetic helicity leads to new solutions with long-range correlations as a result of tunneling from the small-scale dynamo solutions [20, 22, 23]. Indeed, it has been clear for some time that large-scale magnetic fields of the type of an α^2 dynamo become only apparent in the late saturation of the dynamo [15].

While there will always remain some uncertainty regarding the application to the much more extreme astrophysical parameter regime, we can now rule out the possibility of surprising effects within certain limits of $\mathrm{Re_M}$ below 600, Re below 300, and scale separation ratios below 80. In stars and galaxies, the scale separation ratio is difficult to estimate, but it is hardly above the largest value considered here. This ratio is largest in the top layers of the solar convection zone where the correlation length of the turbulence is short ($1\,\mathrm{Mm}$) compared with the spatial extent of the system ($100\,\mathrm{Mm}$).

Of course, the magnetic Reynolds numbers in the Sun and in galaxies are much larger than what will ever be possible to simulate. Nevertheless, the results presented here show very little dependence of the critical value of C_α on $\mathrm{Re_M}$. For $\mathrm{Pr_M} = 1$, for example, we find $C_\alpha^{\rm crit} = 1.2$ for $\mathrm{Re_M} \approx 6$ and $C_\alpha^{\rm crit} = 1.5$ for $\mathrm{Re_M} \approx 600$. On the other hand, for larger values of $\mathrm{Pr_M}$, the value of $C_\alpha^{\rm crit}$ can drop below unity ($C_\alpha^{\rm crit} = 0.9$ for $\mathrm{Pr_M} = 100$). While these changes of $C_\alpha^{\rm crit}$

are theoretically not yet understood, it seems clear that they are small and do not provide support for an entirely different scaling law, as anticipated in recent work [11].

Acknowledgments

The difference between ABC-flows and random plane wave-driven flows was noted during the Nordita Code Comparison Workshop in August 2012, organized by CK Chan, whom we thank for his efforts. We also thank Eric Blackman and Pablo Mininni for useful discussions, and two anonymous referees for their comments and suggestions. This work was supported in part by the European Research Council under the AstroDyn Research Project 227952 and the Swedish Research Council grant 621-2007-4064. Computing resources have been provided by the Swedish National Allocations Committee at the Center for Parallel Computers at the Royal Institute of Technology in Stockholm and Iceland, as well as by the Carnegie Mellon University Supercomputer Center.

[1] E. N. Parker. *Cosmical magnetic fields: Their origin and their activity*. 1979.

[2] H. K. Moffatt. *Magnetic field generation in electrically conducting fluids*. Camb. Univ. Press, 1978.

[3] F. Krause and K.-H. Raedler. *Mean-field magnetohydrodynamics and dynamo theory*. 1980.

[4] N. Seehafer. Nature of the α effect in magnetohydrodynamics. *Phys. Rev. E* , 53:1283–1286, January 1996.

[5] H. Ji. Turbulent dynamos and magnetic helicity. *Phys. Rev. Lett.*, 83:3198–3201, October 1999.

[6] U. Frisch, A. Pouquet, J. Leorat, and A. Mazure. Possibility of an inverse cascade of magnetic helicity in magnetohydrodynamic turbulence. *J. Fluid Mech.*, 68:769–778, 1975.

[7] E. G. Blackman and G. B. Field. Constraints on the magnitude of α in dynamo theory. *ApJ*, 534:984–988, 2000.

[8] E. G. Blackman and G. B. Field. Coronal activity from dynamos in astrophysical rotators. *Mon Not Roy Astron Soc*, 318:724–732, 2000.

[9] N. Kleeorin, D. Moss, I. Rogachevskii, and D. Sokoloff. Helicity balance and steady-state strength of the dynamo generated galactic magnetic field. *Astron. Astrophys.*, 361:L5–L8, September 2000.

[10] A. Brandenburg, S. Candelaresi, and P. Chatterjee. Small-scale magnetic helicity losses from a mean-field dynamo. *Mon Not Roy Astron Soc*, 398:1414–1422, 2009.

[11] J. Pietarila Graham, E. G. Blackman, P. D. Mininni, and A. Pouquet. Not much helicity is needed to drive large-scale dynamos. *Phys. Rev. E* , 85(6):066406, June 2012.

[12] A. Brandenburg. Large-scale dynamos at low magnetic Prandtl numbers. *Astrophys. J.*, 697:1206–1213, June 2009.

[13] A. A. Schekochihin, S. C. Cowley, S. F. Taylor, J. L. Maron, and J. C. McWilliams. Simulations of the small-scale turbulent dynamo. *Astrophys. J.*, 612:276–307, September 2004.

[14] N. E. L. Haugen, A. Brandenburg, and W. Dobler. Simulations of nonhelical hydromagnetic turbulence. *Phys. Rev. E* , 70(1):016308, July 2004.

[15] A. Brandenburg. The Inverse Cascade and Nonlinear Alpha-Effect in Simulations of Isotropic Helical Hydromagnetic Turbulence. *ApJ*, 550:824–840, 2001.

[16] E. G. Blackman and A. Brandenburg. Dynamic nonlinearity in large-scale dynamos with shear. *Astrophys. J.*, 579:359–373, November 2002.

[17] P. J. Käpylä and A. Brandenburg. Turbulent dynamos with shear and fractional helicity. *Astrophys. J.*, 699:1059–1066, July 2009.

[18] F. Cattaneo and D. W. Hughes. Problems with kinematic mean field electrodynamics at high magnetic Reynolds numbers. *Month. Not. Roy. Astron. Soc.*, 395:L48–L51, May 2009.

[19] A. Brandenburg, K.-H. Rädler, M. Rheinhardt, and K. Subramanian. Magnetic Quenching of α and Diffusivity Tensors in Helical Turbulence. *Astrophys. J.*, 687:L49–L52, November 2008.

[20] S. Boldyrev, F. Cattaneo, and R. Rosner. Magnetic-Field Generation in Helical Turbulence. *Physical Review Letters*, 95(25):255001, December 2005.

[21] A. P. Kazantsev. Enhancement of a Magnetic Field by a Conducting Fluid. *Soviet Journal of Experimental and Theoretical Physics*, 26:1031, May 1968.

[22] K. Subramanian. Unified Treatment of Small- and Large-Scale Dynamos in Helical Turbulence. *Physical Review Letters*, 83:2957–2960, October 1999.

[23] A. Brandenburg and K. Subramanian. Large scale dynamos with ambipolar diffusion nonlinearity. *Astron. Astrophys.*, 361:L33–L36, September 2000.

[24] D. Galloway. ABC flows then and now. *Geophysical and Astrophysical Fluid Dynamics*, 106:450–467, August 2012.

[25] B. Galanti, P. L. Sulem, and A. Pouquet. Linear and non-linear dynamos associated with ABC flows. *Geophysical and Astrophysical Fluid Dynamics*, 66:183–208, 1992.

[26] N. Kleeorin, I. Rogachevskii, D. Sokoloff, and D. Tomin. Mean-field dynamos in random Arnold-Beltrami-Childress and Roberts flows. *Phys. Rev. E* , 79(4):046302, 2009.

[27] A. Pouquet, U. Frisch, and J. Léorat. Strong MHD helical turbulence and the nonlinear dynamo effect. *J. Fluid Mech.*, 77:321–354, September 1976.

[28] K.-H. Rädler and M. Rheinhardt. Mean-field electrodynamics: critical analysis of various analytical approaches to the mean electromotive force. *Geophysical and Astrophysical Fluid Dynamics*, 101:117–154, April 2007.

[29] G. B. Field and E. G. Blackman. Dynamical quenching of the α^2 dynamo. *Astrophys. J.*, 572:685–692, June 2002.

[30] A. Brandenburg and K. Subramanian. Simulations of the anisotropic kinetic and magnetic alpha effects. *Astronomische Nachrichten*, 328:507, July 2007.

[31] S. Sur, K. Subramanian, and A. Brandenburg. Kinetic and magnetic α-effects in non-linear dynamo theory. *Month. Not. Roy. Astron. Soc.*, 376:1238–1250, April 2007.

[32] S. Sur, A. Brandenburg, and K. Subramanian. Kinematic α-effect in isotropic turbulence simulations. *Month. Not. Roy. Astron. Soc.*, 385:L15–L19, March 2008.

[33] L. L. Kitchatinov, V. V. Pipin, and G. Ruediger. Turbulent viscosity, magnetic diffusivity, and heat conductivity under the influence of rotation and magnetic field. *Astronomische Nachrichten*, 315:157–170, February 1994.

[34] I. Rogachevskii and N. Kleeorin. Nonlinear turbulent magnetic diffusion and mean-field dynamo. *Phys. Rev. E* , 64(5):056307,

November 2001.
[35] G. K. Batchelor. *The Theory of Homogeneous Turbulence*. 1953.
[36] P. D. Ditlevsen and P. Giuliani. Cascades in helical turbulence. *Phys. Rev. E* , 63(3):036304, March 2001.
[37] A. Brandenburg. Dissipation in dynamos at low and high magnetic Prandtl numbers. *Astron. Nachr.*, 332:51, January 2011.
[38] A. Hubbard and A. Brandenburg. Catastrophic Quenching in $\alpha\Omega$ Dynamos Revisited. *Astrophys. J.*, 748:51, March 2012.
[39] M. Schrinner, K.-H. Rädler, D. Schmitt, M. Rheinhardt, and U. R. Christensen. Mean-field concept and direct numerical simulations of rotating magnetoconvection and the geodynamo. *Geophysical and Astrophysical Fluid Dynamics*, 101:81–116, 2007.
[40] A. Brandenburg, K.-H. Rädler, and M. Schrinner. Scale dependence of alpha effect and turbulent diffusivity. *Astron. Astrophys.*, 482:739–746, 2008.
[41] E. T. Vishniac and A. Brandenburg. An Incoherent alpha - Omega Dynamo in Accretion Disks. *Astrophys. J.*, 475:263, January 1997.
[42] M. R. E. Proctor. Effects of fluctuation on $\alpha\Omega$ dynamo models. *Month. Not. Roy. Astron. Soc.*, 382:L39–L42, November 2007.
[43] T. Heinemann, J. C. McWilliams, and A. A. Schekochihin. Large-Scale Magnetic Field Generation by Randomly Forced Shearing Waves. *Physical Review Letters*, 107(25):255004, December 2011.
[44] D. Mitra and A. Brandenburg. Scaling and intermittency in incoherent α-shear dynamo. *Month. Not. Roy. Astron. Soc.*, 420:2170–2177, March 2012.
[45] K.-H. Rädler and A. Brandenburg. Mean-field effects in the Galloway-Proctor flow. *Month. Not. Roy. Astron. Soc.*, 393:113–125, 2009.
[46] K. Subramanian. Magnetic helicity in galactic dynamos. *Bull. Astron. Soc. India*, 30:715–721, 2002.

II

Mon. Not. R. Astron. Soc. **398,** 1414–1422 (2009) doi:10.1111/j.1365-2966.2009.15188.x

Small-scale magnetic helicity losses from a mean-field dynamo

Axel Brandenburg,[1,2]★ Simon Candelaresi[1,2] and Piyali Chatterjee[3]

[1]*NORDITA, AlbaNova University Center, Roslagstullsbacken 23, SE 10691 Stockholm, Sweden*

[2]*Department of Astronomy, AlbaNova University Center, Stockholm University, SE 10691 Stockholm, Sweden*

[3]*Department of Astronomy and Astrophysics, Tata Institute of Fundamental Research, Colaba, Mumbai 400005, India*

Accepted 2009 June 5. Received 2009 June 5; in original form 2009 May 3

ABSTRACT

Using mean-field models with a dynamical quenching formalism, we show that in finite domains magnetic helicity fluxes associated with small-scale magnetic fields are able to alleviate catastrophic quenching. We consider fluxes that result from advection by a mean flow, the turbulent mixing down the gradient of mean small-scale magnetic helicity density or the explicit removal which may be associated with the effects of coronal mass ejections in the Sun. In the absence of shear, all the small-scale magnetic helicity fluxes are found to be equally strong for both large- and small-scale fields. In the presence of shear, there is also an additional magnetic helicity flux associated with the mean field, but this flux does not alleviate catastrophic quenching. Outside the dynamo-active region, there are neither sources nor sinks of magnetic helicity, so in a steady state this flux must be constant. It is shown that unphysical behaviour emerges if the small-scale magnetic helicity flux is forced to vanish within the computational domain.

Key words: hydrodynamics – magnetic fields – MHD – turbulence.

1 INTRODUCTION

Both mean-field theories and direct simulations of the generation of large-scale magnetic fields in astrophysical bodies, such as the Sun or the Galaxy, invoke the effects of twist. Twist is typically the result of the Coriolis force acting on ascending or descending magnetic field structures in a stratified medium. The net effect of this systematic twisting motion on the magnetic field is called the α effect. In textbooks, the α effect is normally introduced as a result of helical turbulence (Moffatt 1978; Parker 1979; Krause & Rädler 1980), but it could also arise from magnetic buoyancy instabilities (Schmitt 1987; Brandenburg & Schmitt 1998). The latter may also be at the heart of what is known as the Babcock–Leighton mechanism that describes the net effect of the tilt of decaying active regions. Mathematically, this mechanism can also be described by an α effect (Stix 1974). Regardless of all these details, any of these processes face a serious challenge connected with the conservation of magnetic helicity (Pouquet, Frisch & Léorat 1976; Kleeorin & Ruzmaikin 1982; Kleeorin, Rogachevskii & Ruzmaikin 1995). The seriousness of this is not generally appreciated, even though the conservation of magnetic helicity has long been associated with what is called catastrophic α quenching (Gruzinov & Diamond 1994, 1995, 1996). Catastrophic α quenching refers to the fact that the α effect in helical turbulence in a periodic box decreases with increasing magnetic Reynolds number for equipartition strength magnetic fields (Vainshtein & Cattaneo 1992; Cattaneo & Hughes 1996). This would be 'catastrophic' because the magnetic Reynolds number is large (10^9 in the Sun and 10^{15} in the Galaxy).

A promising theory for modelling catastrophic α quenching in a mean-field simulation is the dynamical quenching approach involving an evolution equation for the α effect that follows from magnetic helicity conservation (Kleeorin & Ruzmaikin 1982). Later, Field & Blackman (2002) showed for the first time that this formalism is also able to describe the slow saturation of a helical dynamo in a triply periodic domain (Brandenburg 2001a). As this dynamo evolves towards saturation, a large-scale magnetic field builds up, but this field possesses magnetic helicity. Indeed, the eigenfunction of a homogeneous α^2 dynamo has magnetic and current helicities proportional to α. However, this concerns only the mean field, and since the helicity of the total field is conserved, the small-scale or fluctuating field must have magnetic helicity of the opposite sign (Seehafer 1996). This leads to a reduction of the α effect (Pouquet et al. 1976).

The dynamical quenching formalism is now frequently used to model the non-linear behaviour of mean-field dynamos with and without shear (Blackman & Brandenburg 2002), open or closed boundaries (Brandenburg & Subramanian 2005) and sometimes even without α effect (Yousef, Brandenburg & Rüdiger 2003; Brandenburg & Subramanian 2005). However, it soon became clear that the catastrophic quenching of the α effect can only be alleviated in the presence of magnetic helicity fluxes out of the domain (Blackman & Field 2000a,b; Kleeorin et al. 2000, 2002). There are various contributions to the magnetic helicity flux (Rogachevskii &

★E-mail: brandenb@nordita.org

Kleeorin 2000; Vishniac & Cho 2001; Subramanian & Brandenburg 2004, 2006), but one of the most obvious ones is that associated with advection. Shukurov et al. (2006) have implemented this effect in a mean-field model with dynamical quenching in order to model the effects of outflows on the evolution of the galactic magnetic field. One goal of this paper is to study this effect in more detail. In particular, it is important to clarify the consequences of boundary conditions on the local dynamics away from the boundaries. Indeed, is it really true that a helicity flux has to be maintained all the way to the boundaries, or can the helicity flux be confined to a part of the domain to alleviate catastrophic α quenching at least locally? What happens if this is not the case?

The notion of alleviating catastrophic α quenching only locally is sometimes invoked in models of the solar dynamo that rely on the production of strong magnetic fields at the bottom of the convection zone. By placing the α effect only near the surface, as is done in the interface dynamo of Parker (1993) or dynamos that are controlled by meridional circulation (Choudhuri, Schüssler & Dikpati 1995), one may evade catastrophic quenching more easily. On the other hand, as shown by Yousef et al. (2003), the effects of magnetic helicity conservation can play a role even if there is originally no α effect. It is therefore important to understand in more detail the physics of dynamical α quenching and its dependence on magnetic helicity fluxes.

Our starting point in this paper is the model of Shukurov et al. (2006), where magnetic helicity fluxes were driven by the advection from an outflow. This allows us to study the effects of varying strength of this flux in different parts of the domain. For simplicity, and in order to isolate the main effects, we ignore shear in most parts of this paper. In view of later applications to the Sun and the Galaxy, this is clearly artificial, but it helps significantly in the interpretation of the results. In particular, in the absence of shear, it is possible to have steady solutions, or at least solutions whose magnetic energy density is constant in time.

2 THE MODEL

2.1 Evolution equation of the mean field

In this paper, we consider a simple mean-field dynamo in a local one-dimensional domain. Such a model could be applicable to one hemisphere of a rotating disc or to the region close to the equator of outer stellar convection zones. Denoting the mean magnetic field by $\overline{\boldsymbol{B}} = \overline{\boldsymbol{B}}(z, t)$, the coordinate z would correspond either to the height above the mid-plane in the case of the disc or to the latitudinal distance from the equator in the case of a spherical shell. The x and y components would correspond to poloidal and toroidal fields, although in the absence of shear the two are interchangeable and cannot be distinguished. Using $\nabla \cdot \overline{\boldsymbol{B}} = \partial \overline{B}_z/\partial z = 0$, we have $\overline{B}_z = \text{constant} = 0$, i.e. no $\overline{B}_z$ field is imposed. Such a mean field could be obtained by averaging the actual magnetic field over the x and y directions of a Cartesian domain.

The evolution of $\overline{\boldsymbol{B}}$ is governed by the Faraday equation

$$\frac{\partial \overline{\boldsymbol{B}}}{\partial t} = -\nabla \times \overline{\boldsymbol{E}}, \tag{1}$$

where $\overline{\boldsymbol{E}} = -(\overline{\boldsymbol{U}}_\mathrm{S} + \overline{\boldsymbol{U}}) \times \overline{\boldsymbol{B}} - \overline{\boldsymbol{\mathcal{E}}} + \eta\mu_0\overline{\boldsymbol{J}}$ is the mean electric field, $\overline{\boldsymbol{U}}$ is the mean flow in the z direction, $\overline{\boldsymbol{U}}_\mathrm{S} = (0, Sx, 0)$ is a linear shear flow, $\overline{\boldsymbol{\mathcal{E}}}$ is the mean electromotive force, $\overline{\boldsymbol{J}} = \nabla \times \overline{\boldsymbol{B}}/\mu_0$ is the mean current density and μ_0 is the vacuum permeability. In one case, we adopt a shear parameter S that is different from zero. Since the shear is linear, we can write $\overline{\boldsymbol{U}}_\mathrm{S} \times \overline{\boldsymbol{B}}$ as $-S\overline{A}_y\hat{\boldsymbol{x}}$ plus a gradient term that can be removed by a gauge transformation. Thus, we have

$$-\overline{\boldsymbol{E}} = \nabla(Sx\overline{A}_y) - S\overline{A}_y\hat{\boldsymbol{x}} + \overline{\boldsymbol{U}} \times \overline{\boldsymbol{B}} + \overline{\boldsymbol{\mathcal{E}}} - \eta\mu_0\overline{\boldsymbol{J}}, \tag{2}$$

where $\overline{\boldsymbol{U}}$ is now the flow associated with the outflow only and does not include the shear flow. Next, we express $\overline{\boldsymbol{B}} = \nabla \times \overline{\boldsymbol{A}}$ in terms of the magnetic vector potential $\overline{\boldsymbol{A}}$, and solve equation (1) in its uncurled form, $\partial\overline{\boldsymbol{A}}/\partial t = -\overline{\boldsymbol{E}} - \nabla\overline{\phi}$, where $\overline{\phi}$ is the mean electrostatic potential. We perform a gauge transformation, $\overline{\boldsymbol{A}} \to \overline{\boldsymbol{A}} + \nabla\Lambda$, with the choice $\Lambda = \int(\overline{\phi} - Sx\overline{A}_y)\,\mathrm{d}t$, which removes the gradient term to yield

$$\frac{\partial \overline{\boldsymbol{A}}}{\partial t} = -\overline{\boldsymbol{E}}, \tag{3}$$

which is then the final form of our equation for $\overline{\boldsymbol{A}}$. This form of the equation together with boundary conditions for $\overline{\boldsymbol{A}}$ characterizes the gauge used to calculate magnetic helicity densities and magnetic helicity fluxes for the mean field.

We solve equation (3) in the domain $0 < z < L$ and assume either a vacuum or a perfect conductor boundary condition on $z = L$. This means that on $z = L$ the mean magnetic field either vanishes, i.e. $\overline{B}_x = \overline{B}_y = 0$, or that its z derivatives vanish, i.e. $\overline{B}_{x,z} = \overline{B}_{y,z} = 0$, where a comma denotes partial differentiation. In terms of $\overline{\boldsymbol{A}}$, this means that on $z = L$ we have either

$$\overline{A}_{x,z} = \overline{A}_{y,z} = 0 \quad \text{(vacuum condition)}, \tag{4}$$

or

$$\overline{A}_x = \overline{A}_y = 0 \quad \text{(perfect conductor condition)}. \tag{5}$$

It is well known that the solutions can be in one of the two pure parity states that are either symmetric (S) or antisymmetric (A) about the mid-plane (Krause & Rädler 1980), so we have either $\overline{B}_{x,z} = \overline{B}_{y,z} = 0$ or $\overline{B}_x = \overline{B}_y = 0$ on $z = 0$. In terms of $\overline{\boldsymbol{A}}$,

$$\overline{A}_x = \overline{A}_y = 0 \quad \text{on } z = 0 \quad \text{(S solution)} \tag{6}$$

or

$$\overline{A}_{x,z} = \overline{A}_{y,z} = 0 \quad \text{on } z = 0 \quad \text{(A solution)}. \tag{7}$$

We note that the particular boundary conditions (5) and (6) fix the value of $\overline{\boldsymbol{A}}$ on $z = L$ or 0, respectively. In all other combinations, the value of $\overline{\boldsymbol{A}}$ is not fixed and the magnetic helicity could exhibit an unphysical drift (Brandenburg, Dobler & Subramanian 2002). However, in this paper we study magnetic helicity density and its flux only in situations where either (5) or (6) is used.

We recall that, even though there is no Ω effect, i.e. no mean flow in the y direction, we shall allow for a flow $\overline{\boldsymbol{U}}$ in the z direction. In a disc, this would correspond to a vertical outflow, while in a star this might locally be associated with meridional circulation.

2.2 Magnetic helicity conservation

In this paper, we will study the evolution of magnetic helicity of mean and fluctuating fields. In our gauge, the evolution of the magnetic helicity density of the mean field, $h_\mathrm{m} = \overline{\boldsymbol{A}} \cdot \overline{\boldsymbol{B}}$, is given by

$$\frac{\partial \overline{h}_\mathrm{m}}{\partial t} = 2\overline{\boldsymbol{\mathcal{E}}} \cdot \overline{\boldsymbol{B}} - 2\eta\mu_0\overline{\boldsymbol{J}} \cdot \overline{\boldsymbol{B}} - \nabla \cdot \overline{\boldsymbol{F}}_\mathrm{m}, \tag{8}$$

where $\overline{\boldsymbol{F}}_\mathrm{m} = \overline{\boldsymbol{E}} \times \overline{\boldsymbol{A}}$ is the flux of magnetic helicity of the mean magnetic field. Under the assumption of scale separation, Subramanian & Brandenburg (2006) have defined a magnetic helicity density of the small-scale field in terms of its mutual linkages.

They derived an evolution equation for the magnetic helicity density of the small-scale field,

$$\frac{\partial \overline{h}_\mathrm{f}}{\partial t} = -2\overline{\boldsymbol{\mathcal{E}}}\cdot\overline{\boldsymbol{B}} - 2\eta\mu_0\overline{\boldsymbol{j}\cdot\boldsymbol{b}} - \nabla\cdot\overline{\boldsymbol{F}}_\mathrm{f}, \tag{9}$$

where $\overline{\boldsymbol{F}}_\mathrm{f}$ is the flux of magnetic helicity density of the fluctuating field. Equation (9) is similar to equation (8), except that $\overline{\boldsymbol{\mathcal{E}}}\cdot\overline{\boldsymbol{B}}$ appears with the opposite sign. This implies that turbulent amplification and diffusion of mean magnetic field (characterized by the $\overline{\boldsymbol{\mathcal{E}}}$ term) cannot change the total magnetic helicity density, $\overline{h} = \overline{h}_\mathrm{m} + \overline{h}_\mathrm{f}$, which therefore obeys the equation

$$\frac{\partial \overline{h}}{\partial t} = -2\eta\mu_0\overline{\boldsymbol{J}\cdot\boldsymbol{B}} - \nabla\cdot\overline{\boldsymbol{F}}, \tag{10}$$

where $\overline{\boldsymbol{F}} = \overline{\boldsymbol{F}}_\mathrm{m} + \overline{\boldsymbol{F}}_\mathrm{f}$ is the total magnetic helicity flux, and $\overline{\boldsymbol{J}\cdot\boldsymbol{B}} = \overline{\boldsymbol{J}}\cdot\overline{\boldsymbol{B}} + \overline{\boldsymbol{j}\cdot\boldsymbol{b}}$ is the total current helicity density.

2.3 Dynamical quenching formalism

In order to satisfy the evolution equation for the total magnetic helicity density (10), we have to solve equation (9) along with equation (3), which implies that equations (8) and (10) are automatically obeyed. We assume that $\overline{h}_\mathrm{f}$ is proportional to $\mu_0\overline{\boldsymbol{j}\cdot\boldsymbol{b}}$. This $\overline{\boldsymbol{j}\cdot\boldsymbol{b}}$ term also modifies the mean electromotive force by producing an α effect (Pouquet et al. 1976). This is sometimes referred to as the magnetic α effect,

$$\alpha_\mathrm{M} = \tfrac{1}{3}\tau\overline{\boldsymbol{j}\cdot\boldsymbol{b}}/\overline{\rho}, \tag{11}$$

where τ is the correlation time of the turbulence. In the special case of isotropy of the fluctuating field, the ratio between $\mu_0\overline{\boldsymbol{j}\cdot\boldsymbol{b}}$ and $\overline{h}_\mathrm{f}$ is k_f^2. Direct three-dimensional turbulence simulations (details to be published elsewhere) confirm a proportionality, but the ratio between the two tends to be larger than k_f^2. We should therefore consider k_f^2 as an adjustable parameter. In the following, we ignore compressibility effects and assume that the mean density $\overline{\rho}$ is constant.[1] Next, we assume that the turbulence is helical, so there is also a kinetic α effect proportional to the kinetic helicity,

$$\alpha_\mathrm{K} = -\tfrac{1}{3}\tau\overline{\boldsymbol{\omega}\cdot\boldsymbol{u}}, \tag{12}$$

where $\boldsymbol{\omega} = \nabla\times\boldsymbol{u}$ is the vorticity. The total α effect is then

$$\alpha = \alpha_\mathrm{K} + \alpha_\mathrm{M}, \tag{13}$$

and the resulting mean electromotive force is

$$\overline{\boldsymbol{\mathcal{E}}} = \alpha\overline{\boldsymbol{B}} - \eta_\mathrm{t}\mu_0\overline{\boldsymbol{J}}, \tag{14}$$

where

$$\eta_\mathrm{t} = \tfrac{1}{3}\tau\overline{\boldsymbol{u}^2} \tag{15}$$

is the turbulent magnetic diffusivity. In the following, we consider η_t and η as given and define their ratio as the magnetic Reynolds number, $R_\mathrm{m} = \eta_\mathrm{t}/\eta$. We shall express the strength of the magnetic field in terms of the equipartition value,

$$B_\mathrm{eq} = (\mu_0\overline{\rho}\overline{\boldsymbol{u}^2})^{1/2}, \tag{16}$$

which allows us to determine τ in the mean-field model via $\frac{1}{3}\tau = \mu_0\overline{\rho}\eta_\mathrm{t}/B_\mathrm{eq}^2$. With these preparations, we can write the dynamical quenching formula as

$$\frac{\partial \alpha_\mathrm{M}}{\partial t} = -2\eta_\mathrm{t}k_\mathrm{f}^2\left(\frac{\overline{\boldsymbol{\mathcal{E}}}\cdot\overline{\boldsymbol{B}}}{B_\mathrm{eq}^2} + \frac{\alpha_\mathrm{M}}{R_\mathrm{m}}\right) - \frac{\partial}{\partial z}\overline{\mathcal{F}}_\alpha, \tag{17}$$

where $\overline{\mathcal{F}}_\alpha$ is related to the mean magnetic helicity flux of the fluctuating field via

$$\overline{\mathcal{F}}_\alpha = \frac{\mu_0\overline{\rho}\eta_\mathrm{t}k_\mathrm{f}^2}{B_\mathrm{eq}^2}\overline{\boldsymbol{F}}_\mathrm{f}. \tag{18}$$

In order to compute mean-field models, we have to solve equation (3) together with equation (17) using a closed expression for the flux $\overline{\mathcal{F}}_\alpha$. In this paper, we focus on the advective flux proportional to $\alpha_\mathrm{M}\overline{\boldsymbol{U}}$, but in some cases we consider instead the effects of a turbulent magnetic helicity flux that we model by a Fickian diffusion term proportional to $-\kappa_\alpha\nabla\alpha_\mathrm{M}$, where κ_α is a diffusion term that is either zero or otherwise a small fraction of η_t. A more natural choice might have been $\kappa_\alpha = \eta_\mathrm{t}$, but since the effects of such diffusive magnetic helicity fluxes have never been seen in simulations, we felt that it would be more convincing if even a small fraction of η_t would lead to a notable effect.

In addition, we consider cases where we model magnetic helicity fluxes by an explicit removal of $\overline{h}_\mathrm{f}$ from the domain in regular time intervals Δt. Such an explicit removal of magnetic helicity associated with the fluctuating field may model the effects of coronal mass ejections, although one would expect that in reality such an approach also implies some loss of magnetic helicity associated with the large-scale field. The removal of the fluctuating magnetic field was employed by Brandenburg et al. (2002) in connection with three-dimensional turbulence simulations to demonstrate that it is, at least in principle, possible to alleviate catastrophic quenching by an artificial filtering out of small-scale turbulent magnetic fields. In this paper, we model the occasional removal of $\overline{h}_\mathrm{f}$ by resetting its values

$$\overline{h}_\mathrm{f} \to \overline{h}_\mathrm{f} - \Delta\overline{h}_\mathrm{f} \quad \text{in regular intervals } \Delta t, \tag{19}$$

where $\Delta\overline{h}_\mathrm{f} = \epsilon\overline{h}_\mathrm{f}$ is chosen to be a certain fraction ϵ of the current value of $\overline{h}_\mathrm{f}$. In our one-dimensional model, the corresponding expression for the flux $\Delta\overline{F}_\mathrm{f}$ can be obtained by integration, i.e.

$$\Delta\overline{F}_\mathrm{f}(z,t) = \int_0^z \Delta\overline{h}_\mathrm{f}(z',t)\,\mathrm{d}z'. \tag{20}$$

Since magnetic helicity densities and their fluxes are proportional to each other, we have simply

$$\overline{\mathcal{F}}_\alpha = \alpha_\mathrm{M}\overline{U} - \kappa_\alpha\frac{\partial\alpha_\mathrm{M}}{\partial z} + \Delta\overline{\mathcal{F}}_\alpha, \tag{21}$$

where $\Delta\overline{\mathcal{F}}_\alpha = (\mu_0\overline{\rho}\eta_\mathrm{t}k_\mathrm{f}^2/B_\mathrm{eq}^2)\Delta\overline{F}_\mathrm{f}$ is defined analogously to equation (18).

We note that the α effect will produce magnetic fields that have magnetic helicity with the same sign as that of α, and the rate of magnetic helicity production is proportional to $\alpha\overline{\boldsymbol{B}}^2$. In the Northern hemisphere, we have $\alpha > 0$, so the mean field should have positive magnetic helicity. We recall that shear does not contribute to magnetic helicity production, because the negative electric field associated with the shear flow, $\overline{\boldsymbol{U}}_\mathrm{S}\times\overline{\boldsymbol{B}}$, gives no contribution to magnetic helicity production, which is proportional to $\overline{\boldsymbol{E}}\cdot\overline{\boldsymbol{B}}$, but it can still give a contribution to the flux of magnetic helicity. This is also evident if we write shear using the $-S\overline{A}_y\hat{\boldsymbol{x}}$ term in equation (2): after multiplying with $\overline{\boldsymbol{B}}$ and using $\overline{B}_x = \partial\overline{A}_y/\partial z$, we find that this term can be integrated to give just an additional flux term, $\frac{1}{2}S\overline{A}_y^2$. However, this contribution belongs clearly to the magnetic helicity flux associated with the large-scale field and is therefore unable to alleviate catastrophic quenching.

---

[1] Note that a constant mean density implies that there must exist a small-scale mass flux compensating the losses associated with the mass flux $\overline{\rho}\overline{\boldsymbol{U}}$.

2.4 Model profiles and boundary conditions

We consider a model similar to that of Shukurov et al. (2006) who adopted linear profiles for $\alpha_{\rm K}$ and $\overline{\boldsymbol{U}}$ of the form $\alpha_{\rm K} = \alpha_0 z/H$ and $\overline{U}_z = U_0 z/H$, where the height H was chosen to be equal to the domain size, $H = L$. However, in order to separate boundary effects from effects of the dynamo we also consider the case where we extend the domain in the z direction and choose $L = 4H$ and let $\alpha_{\rm K}$ go smoothly to zero at $z = H$ and $\overline{U}_z$ either goes to a constant for $z > H$ or also goes smoothly to zero. Thus, we choose

$$\alpha = \alpha_0 \frac{z}{H} \Theta(z; H, w_\alpha), \tag{22}$$

where we have defined the profile function

$$\Theta(z; H, w) = \frac{1}{2}\left(1 - \tanh\frac{z - H}{w}\right), \tag{23}$$

which is unity for $z \ll H$ and zero otherwise, and w quantifies the width of this transition. For the outflow, we choose the function

$$\overline{U}_z = U_0 \frac{z}{H}\left[1 + (z/H)^n\right]^{-1/n} \Theta(z; H_U, w_U), \tag{24}$$

with $n = 20$. Both profiles are shown in Fig. 1. The strictly linear profiles of Shukurov et al. (2006) can be recovered by taking $L = H$, $w_\alpha \to 0$ and $n \to \infty$.

As length unit, we take $k_1 = \pi/2H$, and as time unit we take $(\eta_{\rm t} k_1^2)^{-1}$. This deviates from Shukurov et al. (2006), who used π/H as their basic wavenumber. Our motivation for this change is that now the turbulent decay rate is equal to $\eta_{\rm t} k_1^2$, without an extra 1/4 factor. We adopt non-dimensional measures for α_0, U_0 and S, by defining

$$C_\alpha = \frac{\alpha_0}{\eta_{\rm t} k_1}, \quad C_U = \frac{U_0}{\eta_{\rm t} k_1} \quad \text{and} \quad C_S = \frac{S}{\eta_{\rm t} k_1^2}. \tag{25}$$

To match the parameters of Shukurov et al. (2006), we note that $C_U = 0.6$ corresponds to their value of 0.3, and the value $k_{\rm f}/k_1 = 10$ corresponds to their value of 5.

We obtain solutions numerically using two different codes. One code uses an explicit third-order Runge–Kutta time-stepping scheme and the other one is a semi-implicit scheme. Both schemes employ a second-order finite differences. We begin by reporting results for the original profile of Shukurov et al. (2006) with $L = H$.

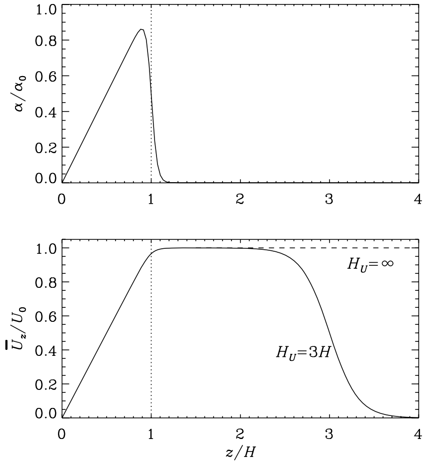

Figure 1. Profiles of α and $\overline{U}$ for $w_\alpha k_1 = 0.2$ and $w_U k_1 = 1$.

3 RESULTS

3.1 Kinematic behaviour of the solutions

When the magnetic field is weak, the back reaction via the Lorentz force and hence the $\alpha_{\rm M}$ term are negligible. The value of $R_{\rm m}$ then does not enter into the theory. The effects of magnetic helicity fluxes are therefore not important, so we begin by neglecting the outflow or other transporters of magnetic helicity. For the linear α profile, we find that the critical value of C_α for dynamo action to occur is about 5.13. These solutions are oscillatory with a dimensionless frequency $\tilde{\omega} \equiv \omega/\eta_{\rm t} k_1^2 = 1.64$. The oscillations are associated with the migration of the dynamo wave in the positive z direction. This is shown in Fig. 2 where we compare with the case of a perfectly conducting boundary condition at $z = H$ for which we find $C_\alpha^{\rm crit} = 7.12$ and $\tilde{\omega} = 2.28$.

The fact that there are oscillatory solutions to the α^2 dynamo is perhaps somewhat unusual, but it is here related to the fact that α changes sign about the equator. Similar solutions were first found by Shukurov, Sokolov & Ruzmaikin (1985) and analysed in detail by Baryshnikova & Shukurov (1987) and Rädler & Bräuer (1987). Oscillations have also been seen in other α^2 dynamos where α changes

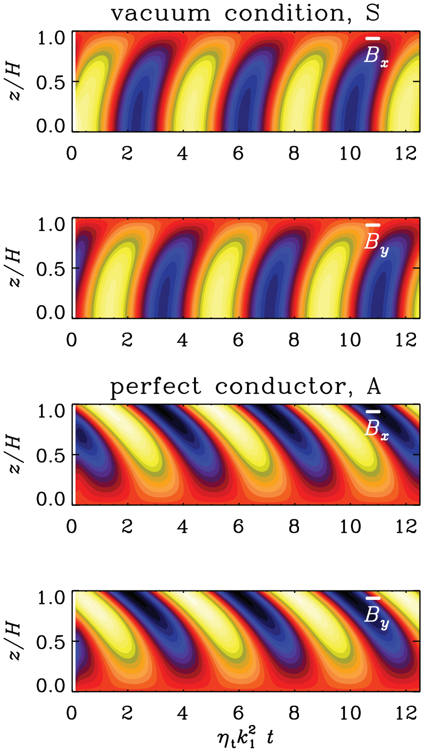

Figure 2. Space–time diagrams for $\overline{B}_x$ and $\overline{B}_y$ for the marginal values of C_α for $L = H$ with $C_U = 0$ and either the symmetric solution (S) with a vacuum boundary condition on $z = H$ or the antisymmetric solution (A) with the perfect conductor boundary condition. In both cases, the critical value $C_\alpha = 5.13$ is applied. Light (yellow) shades indicate positive values and dark (blue) shades indicate negative values.

sign with depth (Stefani & Gerbeth 2003; Rüdiger & Hollerbach 2004; Rüdiger, Elstner & Ossendrijver 2004; Giesecke, Ziegler & Rüdiger 2005) and in simulations of helically forced turbulence with a change of sign about the equator (Mitra et al. 2009). In the latter case, however, the outer boundaries were perfectly conducting. In our mean-field model, such a case is also oscillatory, as will be discussed below.

Note that here we have made the assumption that the solutions are symmetric about the mid-plane, i.e. $\overline{B}_i(z,t) = \overline{B}_i(-z,t)$ for $i = x$ or y. For the application to real systems, such a symmetry condition can only be justified if the symmetric solution is more easily excited than the antisymmetric one for which $\overline{B}_i(z,t) = -\overline{B}_i(-z,t)$ for $i = x$ or y. This is indeed the case when we adopt the vacuum condition at $z = H$, because the antisymmetric solution has $C_\alpha^{\rm crit} = 7.14$ in that case. However, this is not the case for the perfect conductor boundary condition for which the antisymmetric solution has $C_\alpha^{\rm crit} = 5.12$. We remark that there is a striking correspondence in the critical C_α values between the antisymmetric solution with perfect conductor boundary condition and the symmetric solution with vacuum condition on the one hand, and the symmetric solution with perfect conductor condition and the antisymmetric solution with vacuum condition on the other hand.

In the following, we consider both symmetric solutions using the vacuum boundary conditions, as well as antisymmetric ones using the perfect conductor boundary condition, which correspond in each case to the most easily excited mode. In the cases where we use a vacuum condition, we shall sometimes also apply an outflow. This makes the dynamo somewhat harder to excite and raises $C_\alpha^{\rm crit}$ from 5.12 to 5.60 for $C_U = 0.6$, but the associated magnetic helicity flux alleviates catastrophic quenching in the non-linear case. Alternatively, we consider an explicit removal of magnetic helicity to alleviate catastrophic quenching. In cases with perfect conductor boundary conditions, the most easily excited mode is antisymmetric about the equator, which corresponds to a boundary condition that permits a magnetic helicity flux through the equator. This would not be the case for the symmetric solutions.

3.2 Saturation behaviour for different values of $R_{\rm m}$

We now consider the saturated state for a value of C_α that is supercritical for dynamo action. In the following, we choose $C_\alpha = 8$. Throughout this paper, we assume $k_{\rm f}/k_1 = 10$ for the scale separation ratio. This corresponds to the value of 5 in Shukurov et al. (2006), where k_1 was defined differently. The dynamo saturates by building up negative $\alpha_{\rm M}$ when $\alpha_{\rm K}$ is positive. This diminishes the total α in equation (13) and saturates the dynamo. The strength of this quenching can be alleviated by magnetic helicity fluxes that lower the negative value of $\alpha_{\rm M}$.

We plot in Fig. 3 the dependence of the saturation field strength $\overline{B}_{\rm sat}$, defined here as the maximum of $|\overline{\boldsymbol{B}}(z)|$ at the time of saturation. To monitor the degree of quenching, we also plot in Fig. 3 the $R_{\rm m}$ dependence of the maximum of the negative value of $\alpha_{\rm M}$ at the time when the dynamo has saturated and reached a steady state. The maximum value of $-\alpha_{\rm M}$ is lowered by about 5 per cent from 1.8 to 1.7 in units of $\eta_{\rm t}k_1$ (see Fig. 3). Finally, we recall that for the α^2 dynamos considered here both $\overline{B}_x$ and $\overline{B}_y$ oscillate, but their relative phase shift is such that $\overline{\boldsymbol{B}}^2$ is non-oscillatory. The normalized cycle frequency, $\tilde{\omega} \equiv \omega/\eta_{\rm t}k_1$, is also plotted in Fig. 3 as a function of $R_{\rm m}$. It is somewhat surprising that ω does not strongly depend on $R_{\rm m}$. One may have expected that the cycle frequency could scale with the inverse resistive time $\eta\, k_1^2$. On the other hand, for oscillatory $\alpha\Omega$ dynamos the cycle frequency is known to scale with $\eta_{\rm t}k_1^2$ (Blackman & Brandenburg 2002), although that value could decrease if $\eta_{\rm t}(\overline{\boldsymbol{B}})$ is strongly quenched. However, simulations only give evidence for mild quenching (Brandenburg et al. 2008; Käpylä & Brandenburg 2009).

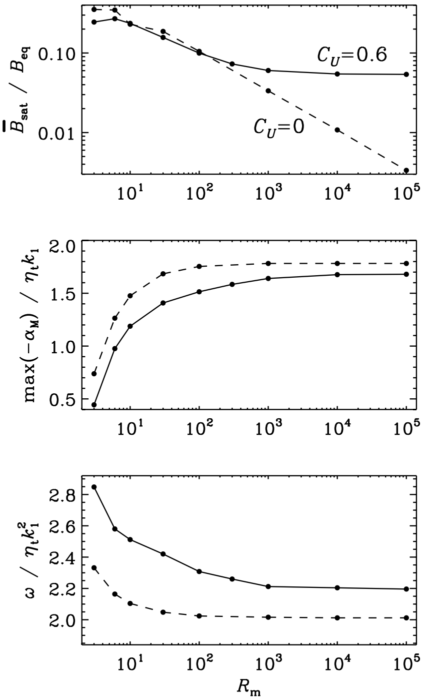

Figure 3. Scaling of the extremal value of $\alpha_{\rm M}$, the saturation field strength $\overline{B}_{\rm sat}$ and the cycle frequency ω with $R_{\rm m}$ and either $C_U = 0.6$ (solid lines) or $C_U = 0$ (dashed lines).

3.3 Helicity fluxes through the equator

We have seen in Section 3.1 that in the perfect conductor case the antisymmetric solutions are the most easily excited ones. The boundary conditions for antisymmetric solutions permit magnetic helicity transfer through the equator. A possible candidate for driving a flux through the equator would be a diffusive flux driven by the $\nabla\alpha_{\rm M}$ term. In Fig. 4, we plot the $R_{\rm m}$ dependence of max$(-\alpha_{\rm M})$, $\overline{B}_{\rm sat}$ and $\tilde{\omega}$ for $\tilde{\kappa}_\alpha = 0.05$ and 0. Again, catastrophic α quenching is alleviated by the action of a magnetic helicity flux, but this time it is through the equator. The maximum value of $-\alpha_{\rm M}$ is lowered by 15 per cent from 2.35 to 2.15 in units of $\eta_{\rm t}k_1$ (see Fig. 4). Again, the cycle frequency is not changed significantly.

In Fig. 5, we compare the profiles of $\overline{h}_{\rm m}$, $\overline{h}_{\rm f}$, $\overline{F}_{\rm m}$ and $\overline{F}_{\rm f}$ for the most easily excited solution with vacuum and perfect conductor boundary conditions on $z = L$. In all cases, we have $\overline{h}_{\rm m} = \overline{h}_{\rm f} = 0$ at the mid-plane due to symmetry, and at $z = L$ we have $\overline{h}_{\rm m} = 0$ and $\overline{h}_{\rm f} \neq 0$. It turns out that the magnetic helicity flux of the small-scale field is balanced nearly exactly by that of the mean field. This agrees with the expectation of Blackman & Brandenburg (2003) who argued that both should be shed at nearly the same rate.

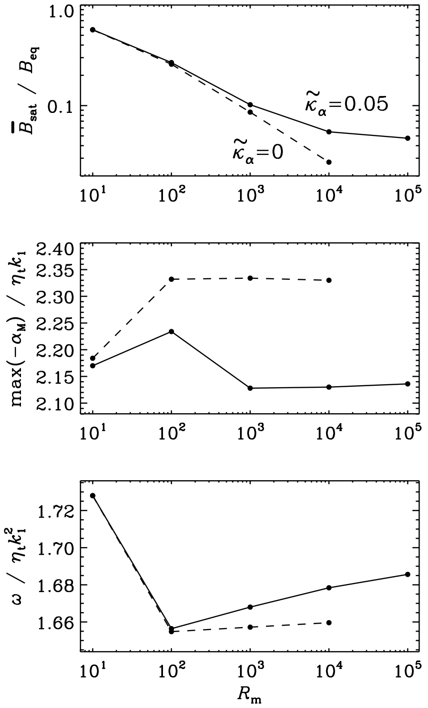

Figure 4. Same as Fig. 3, but for antisymmetric solutions in a model with perfect conductor boundary conditions with $C_U = 0$ and $\tilde{\kappa}_\alpha \equiv \kappa_\alpha/\eta_t = 0.05$ (solid lines) or 0 (dashed lines).

The ad hoc assumption of a turbulent magnetic helicity flux is plausible and has of course been made in the past (Kleeorin et al. 2002), but its effect in alleviating catastrophic quenching has not yet been seen in earlier three-dimensional turbulence simulations (Brandenburg & Dobler 2001; Brandenburg 2001b). However, except for the effects of boundaries, the conditions in those simulation were essentially homogeneous and the gradients of magnetic helicity density may have been just too small. It would therefore be important to reconsider the question of diffusive helicity fluxes in future simulations of inhomogeneous helical turbulence.

3.4 Occasional removal of $\overline{h}_f$

Catastrophic quenching can also be alleviated by the artificial removal of small-scale magnetic fields (see equation 19). We consider the saturation strength of the magnetic field, $\overline{B}_{\rm sat}$, to characterize the alleviating effect of small-scale magnetic helicity losses. It is not surprising that the dynamo becomes stronger ($\overline{B}_{\rm sat}$ increases) when the fraction of small-scale field removal ϵ is increased (upper panel of Fig. 6) or the time interval of field removal is decreased (lower panel of Fig. 6). These dependencies follow approximate power laws,

$$\overline{B}_{\rm sat}/B_{\rm eq} \approx 0.17\,\epsilon^{1/2} \approx 0.024\,\left(\Delta t\eta_{\rm t}k_1^2\right)^{-1/2}, \qquad (26)$$

suggesting that even relatively small amounts of magnetic helicity removal in long intervals can have an effect.

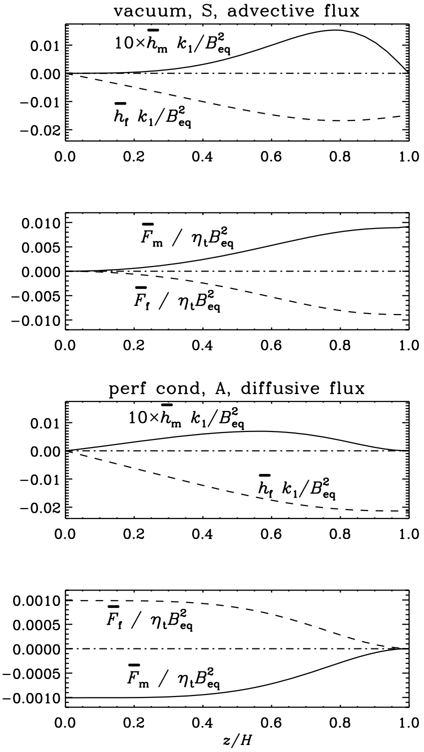

Figure 5. Mean magnetic helicity densities of mean and fluctuating fields as well as mean magnetic helicity fluxes of mean and fluctuating fields as functions of z for the S solution with vacuum boundary condition and advective flux with $C_U = 0.6$ (upper two panels) and for the A solution with perfect conductor boundary condition and diffusive flux with $\tilde{\kappa}_\alpha = 0.05$ (lower two panels). The profiles of $\overline{h}_{\rm f}$ have been scaled by a factor of 10 to make them more clearly visible. In all cases, we used $C_\alpha = 8$ and $R_{\rm m} = 10^5$.

We have also performed some numerical experiments where the magnetic helicity associated with the small-scale field is only removed near the surface layers. However, in those cases the catastrophic quenching was not notably alleviated. This can be explained by noting that, in the absence of additional magnetic helicity fluxes in the interior, there is still a build-up of $\overline{h}_{\rm f}$ in the interior which quenches the α effect catastrophically.

3.5 Magnetic helicity density and flux profiles

In an attempt to understand further the evolution of magnetic helicity we have performed calculations where the magnetic helicity flux of the fluctuating field was forced to vanish at the surface. This was done by choosing a profile for $\overline{U}$ that goes to zero at the surface. However, this invariably led to numerical problems. In order to clarify the origin of these problems we performed calculations with a taller domain, $L = 4H$, using the profiles shown in Fig. 1 and varying the value of H_U. For $H_U \to \infty$, the flux is still able to carry magnetic helicity away from the dynamo-active region into the outer layers $z > H$ (see Fig. 7). The cyclic dynamo in

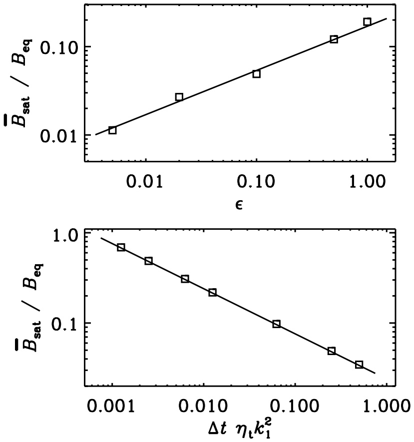

Figure 6. Saturation field strength versus ϵ for $\Delta t\eta_{\rm t}k_1^2 = 0.25$ (upper panel) and versus $\Delta t\eta_{\rm t}k_1^2$ for $\epsilon = 0.1$ (lower panel) in a model with $C_\alpha = 8$, $R_{\rm m} = 10^5$ and $C_U = C_S = \kappa_\alpha = 0$.

$0 \le z \le H$ operates very much like in the case of a smaller domain (Fig. 2), except that the critical value of C_α is now lowered to $C_\alpha^{\rm crit} = 4.32$.

However, for $H_U = 3H$ a problem arises when a parcel of positive magnetic helicity that is shed early on from the dynamo-active region reaches the upper layers at $z \approx 3H$, through which now no magnetic helicity can be transmitted. Positive magnetic helicity piles up into a δ function near $z \approx 3H$ until it cannot be numerically resolved any more. At higher resolution, the evolution can be followed a little longer, but the problem cannot be removed. This demonstrates again that, once a magnetic helicity flux is initiated, there is no way to stop it locally. There is also no tendency for an annihilation between magnetic helicities of mean and fluctuating fields.

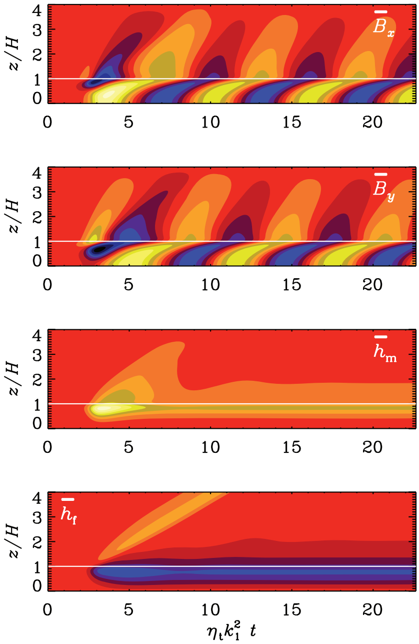

Figure 7. Space–time diagrams for $\overline{B}_x$ and $\overline{B}_y$, as well as the magnetic helicity densities $\overline{h}_{\rm m}$ and $\overline{h}_{\rm f}$ for $L = 4H$, $C_\alpha = 8$, $C_U = 0.6$ and $H_U \to \infty$. The white horizontal line marks the location $z = H$. Light (yellow) shades indicate positive values and dark (blue) shades indicate negative values.

The fact that positive magnetic helicity is produced is somewhat unexpected, because for $\alpha > 0$ the magnetic helicity production is positive definite. However, this can be traced back to the term $\eta_{\rm t}\overline{\boldsymbol{J}}\cdot\overline{\boldsymbol{B}}$, which is part of $\overline{\boldsymbol{\mathcal{E}}}\cdot\overline{\boldsymbol{B}}$ on the right-hand side of equation (9). Since $\overline{\boldsymbol{J}}\cdot\overline{\boldsymbol{B}}$ is positive for positive $\alpha_{\rm K}$, it is clear that this term produces positive $\overline{h}_{\rm f}$ just *outside* the range where $\alpha_{\rm K}$ is finite and where it would produce $\overline{h}_{\rm f}$ of opposite sign.

In another experiment, we adopt a profile for $\overline{\boldsymbol{U}}$ such that H_U is changed from ∞ to $3H$ only after a time $t\eta_{\rm t}k_1^2 = 25$, which is when the parcel of positive $\overline{h}_{\rm f}$ has left the domain. Now it is indeed negative magnetic helicity that the dynamo tries to shed and that begins to pile up near $z = 3H$. However, even though the flux is relatively weak, the blockage at $z = 3H$ leads eventually to a problem and, again, to short-wavelength oscillations indicating that the solution is numerically no longer valid.

These results suggest that the magnetic helicity flux must be allowed to continue through the rest of the domain. Of course, in reality there is the possibility of various fluxes, including diffusive fluxes that have not been included in this particular model. We note, however, that model calculations with finite κ_α in equation (21) then confirm that $\overline{F}_{\rm f}(z, t)$ becomes constant in the outer parts.

3.6 Magnetic helicity with shear

It is remarkable that the magnetic helicity fluxes of the mean and fluctuating fields were always equally strong and of opposite sign. The point of this section is to underline that this is a particular property of the α^2 dynamo, and would not apply to $\alpha\Omega$ dynamos. In Fig. 8, we show the fluxes of the model with $C_\alpha = 8$ and $C_U = 0.6$, where we have varied C_S in the range from -8 to $+8$.

Shear gives rise to an additional magnetic helicity flux (Berger & Ruzmaikin 2000), and the perfect correspondence between magnetic helicity fluxes of opposite sign for mean and fluctuating fields is then broken. This additional flux of magnetic helicity is associated with the mean field and therefore does not, on its own, alleviate

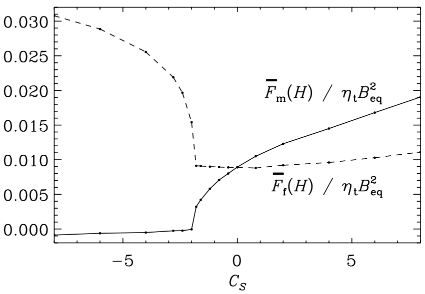

Figure 8. Dependence of $\overline{F}_{\rm m}(H)$ and $\overline{F}_{\rm f}(H)$ on the shear parameter for the S solution in a model with vacuum boundary condition, $C_\alpha = 8$, $C_U = 0.6$ and $R_{\rm m} = 10^5$.

catastrophic quenching. However, in this model we have neglected additional magnetic helicity fluxes arising from the shear that would be associated with the fluctuating field. An example is the Vishniac–Cho flux whose effect in a mean-field model was already studied in an earlier paper (Brandenburg & Subramanian 2005). For $C < -2$, the oscillating solutions are no longer preferred and a new solution branch emerges, where the solutions are now non-oscillatory. Those are also the type of solutions studied by Shukurov et al. (2006), where $C_{\rm S} = -8$ was chosen, corresponding to the value -2 in their normalization.

4 CONCLUSIONS

The present simulations have confirmed that in finite domains magnetic helicity losses through local fluxes are able to alleviate catastrophic quenching. Without such fluxes, the energy of the mean field goes to zero in the limit of large $R_{\rm m}$, while in the presence of such fluxes $|\overline{\boldsymbol{B}}|$ reaches values that are about 5 per cent of the equipartition value. We emphasize at this point that this applies to the case of an α^2 dynamo. For an $\alpha\Omega$ dynamo, the mean field can reach larger values, depending on the amount of shear. For example for the model shown in Fig. 8, the field strength in units of the equipartition value rises from 5 per cent without shear to about 36 per cent with negative shear ($C_{\rm S} = -8$), while for positive shear it stays around 5 per cent. We also emphasize that the difference between the two cases with and without helicity fluxes is rather weak for $R_{\rm m} \le 10^3$, so one really has to reach values around $R_{\rm m} \le 10^4$ or $R_{\rm m} \le 10^5$. Such high values of $R_{\rm m}$ are not currently feasible with three-dimensional turbulence simulations.

The other surprising result is that it is not possible to dissipate magnetic helicity flux locally once it is initiated. If the magnetic helicity flux of the small-scale field has already left the dynamo-active domain, it has to stay constant in the steady state. By adding a diffusive flux, the boundary layer in the magnetic helicity of the small-scale field could be smoothed out, but this contribution would then carry the same amount of energy as before, although now by other means.

In the presence of shear, there are additional contributions to the magnetic helicity flux associated with the mean magnetic field. There are first of all the fluxes associated with the mean field itself, but those fluxes cannot contribute to alleviating catastrophic quenching on their own. However, earlier work has shown that in the presence of shear there are also additional contributions associated with the fluctuating field (Vishniac & Cho 2001; Subramanian & Brandenburg 2004, 2006). Those terms have not been included in the present work, because they have already been studied in an earlier paper (Brandenburg & Subramanian 2005).

Several new issues have emerged from the present study. The fact that diffusive magnetic helicity fluxes through the equator can alleviate catastrophic quenching is not surprising as such, but its effects in alleviating catastrophic saturation behaviour in three-dimensional turbulence simulations have not yet been reported (Brandenburg & Dobler 2001; Brandenburg 2001b). On the other hand, simulations of forced turbulence in spherical shells with an equator did show near-equipartition strength saturation fields (Mitra et al. 2009), although the values of $R_{\rm m}$ were typically below 20, so it was not possible to draw conclusions about catastrophic quenching. A new dedicated attempt in that direction would be worthwhile using driven turbulence, but now with a linear gradient of its intensity and in the Cartesian geometry.

In view of applications to the Sun and other stars, another important development would be to extend the present work to spherical domains. Again, some work in that direction was already reported in Brandenburg et al. (2007), but none of these models used diffusive fluxes, nor has any attempt been made to model the Sun. This would now be an important target for future research.

ACKNOWLEDGMENTS

We thank Anvar Shukurov for detailed comments and suggestions regarding an earlier version of the manuscript. We acknowledge the use of computing time at the Center for Parallel Computers at the Royal Institute of Technology in Sweden. This work was supported in part by the European Research Council under the AstroDyn Research Project 227952 and the Swedish Research Council grant 621-2007-4064.

REFERENCES

Baryshnikova Y., Shukurov A. M., 1987, Astron. Nachr., 308, 89
Berger M. A., Ruzmaikin A., 2000, J. Geophys. Res., 105, 10481
Blackman E. G., Brandenburg A., 2002, ApJ, 579, 359
Blackman E. G., Brandenburg A., 2003, ApJ, 584, L99
Blackman E. G., Field G. B., 2000a, ApJ, 534, 984
Blackman E. G., Field G. B., 2000b, MNRAS, 318, 724
Brandenburg A., 2001a, ApJ, 550, 824
Brandenburg A., 2001b, in Chossat P., Armbruster D., Iuliana O., eds, Nato ASI Series 26, Dynamo and Dynamics, a Mathematical Challenge. Kluwer, Dordrecht, p. 125
Brandenburg A., Dobler W., 2001, A&A, 369, 329
Brandenburg A., Schmitt D., 1998, A&A, 338, L55
Brandenburg A., Subramanian K., 2005, Astron. Nachr., 326, 400
Brandenburg A., Dobler W., Subramanian K., 2002, Astron. Nachr., 323, 99
Brandenburg A., Käpylä P. J., Mitra D., Moss D., Tavakol R., 2007, Astron. Nachr., 328, 1118
Brandenburg A., Rädler K.-H., Rheinhardt M., Subramanian K., 2008, ApJ, 687, L49
Cattaneo F., Hughes D. W., 1996, Phys. Rev. E, 54, R4532
Choudhuri A. R., Schüssler M., Dikpati M., 1995, A&A, 303, L29
Field G. B., Blackman E. G., 2002, ApJ, 572, 685
Giesecke A., Ziegler U., Rüdiger G., 2005, Phys. Earth Planet. Inter., 152, 90
Gruzinov A. V., Diamond P. H., 1994, Phys. Rev. Lett., 72, 1651
Gruzinov A. V., Diamond P. H., 1995, Phys. Plasmas, 2, 1941
Gruzinov A. V., Diamond P. H., 1996, Phys. Plasmas, 3, 1853
Käpylä P. J., Brandenburg A., 2009, ApJ, 699, 1059
Kleeorin N. I., Ruzmaikin A. A., 1982, Magnetohydrodynamics, 18, 116
Kleeorin N., Rogachevskii I., Ruzmaikin A., 1995, A&A, 297, 159
Kleeorin N., Moss D., Rogachevskii I., Sokoloff D., 2000, A&A, 361, L5
Kleeorin N., Moss D., Rogachevskii I., Sokoloff D., 2002, A&A, 387, 453
Kleeorin N., Moss D., Rogachevskii I., Sokoloff D., 2003, A&A, 400, 9
Krause F., Rädler K.-H., 1980, Mean-field Magnetohydrodynamics and Dynamo Theory. Pergamon Press, Oxford
Mitra M., Tavakol R., Käpylä P. J., Brandenburg A., 2009, Phys. Rev. Lett., submitted
Moffatt H. K., 1978, Magnetic Field Generation in Electrically Conducting Fluids. Cambridge Univ. Press, Cambridge
Parker E. N., 1979, Cosmical Magnetic Fields. Clarendon Press, Oxford
Parker E. N., 1993, ApJ, 408, 707
Pouquet A., Frisch U., Léorat J., 1976, J. Fluid Mech., 77, 321
Rädler K.-H., Bräuer H.-J., 1987, Astron. Nachr., 308, 101
Rogachevskii I., Kleeorin N., 2000, Phys. Rev. E, 61, 5202
Rüdiger G., Hollerbach R., 2004, The Magnetic Universe. Wiley-VCH, Weinheim
Rüdiger G., Elstner D., Ossendrijver M., 2003, A&A, 406, 15
Schmitt D., 1987, A&A, 174, 281
Seehafer N., 1996, Phys. Rev. E, 53, 1283

Shukurov, A. M., Sokolov, D. D., Ruzmaikin, A. A., 1985, Magn. Gidrodin., 3, 9
Shukurov A., Sokoloff D., Subramanian K., Brandenburg A., 2006, A&A, 448, L33
Stefani F., Gerbeth G., 2003, Phys. Rev. E, 67, 027302
Stix M., 1974, A&A, 37, 121
Subramanian K., Brandenburg A., 2004, Phys. Rev. Lett., 93, 205001
Subramanian K., Brandenburg A., 2006, ApJ, 648, L71
Vainshtein S. I., Cattaneo F., 1992, ApJ, 393, 165
Vishniac E. T., Cho J., 2001, ApJ, 550, 752
Yousef T. A., Brandenburg A., Rüdiger G., 2003, A&A, 411, 321

This paper has been typeset from a TEX/LATEX file prepared by the author.

III

Astron. Nachr. / AN **331**, No. 1, 130 – 135 (2010) / **DOI** 10.1002/asna.200911308

Equatorial magnetic helicity flux in simulations with different gauges

D. Mitra^{1,*}, **S. Candelaresi**^{2,3}, **P. Chatterjee**^{2}, **R. Tavakol**^{1}, and **A. Brandenburg**^{2,3}

[1] Astronomy Unit, School of Mathematical Sciences, Queen Mary University of London, Mile End Road, London E1 4NS, United Kingdom
[2] NORDITA, AlbaNova University Center, Roslagstullsbacken 23, SE-10691 Stockholm, Sweden
[3] Department of Astronomy, AlbaNova University Center, Stockholm University, SE-10691 Stockholm, Sweden

Received 2009 Nov 4, accepted Nov 16

Key words Sun: magnetic fields – magnetohydrodynamics (MHD)

We use direct numerical simulations of forced MHD turbulence with a forcing function that produces two different signs of kinetic helicity in the upper and lower parts of the domain. We show that the mean flux of magnetic helicity from the small-scale field between the two parts of the domain can be described by a Fickian diffusion law with a diffusion coefficient that is approximately independent of the magnetic Reynolds number and about one third of the estimated turbulent magnetic diffusivity. The data suggest that the turbulent diffusive magnetic helicity flux can only be expected to alleviate catastrophic quenching at Reynolds numbers of more than several thousands. We further calculate the magnetic helicity density and its flux in the domain for three different gauges. We consider the Weyl gauge, in which the electrostatic potential vanishes, the pseudo-Lorenz gauge, where the speed of light is replaced by the sound speed, and the 'resistive gauge' in which the Laplacian of the magnetic vector potential acts as a resistive term. We find that, in the statistically steady state, the time-averaged magnetic helicity density and the magnetic helicity flux are the same in all three gauges.

1 Introduction

The generation of magnetic fields on scales larger than the eddy scale of the underlying turbulence in astrophysical bodies has posed a major problem. Magnetic helicity is believed to play an important role in this process (Brandenburg & Subramanian 2005a). The magnetic helicity density, defined by $\boldsymbol{A}\cdot\boldsymbol{B}$, where $\boldsymbol{B}=\boldsymbol{\nabla}\times\boldsymbol{A}$ is the magnetic field and $\boldsymbol{A}$ is the corresponding magnetic vector potential, is important because at large scales it is produced in many dynamos. This has been demonstrated for dynamos based on the α effect (Shukurov et al. 2006; Brandenburg et al. 2009), the shear-current effect (Brandenburg & Subramanian 2005b), and the incoherent α-shear effect (Brandenburg et al. 2008). The volume integral of the magnetic helicity density over periodic domains (as well as domains with perfect-conductor boundary conditions or infinite domains where the magnetic field and the vector potential decays fast enough at infinity) is a conserved quantity in ideal MHD. This conservation is also believed to be recovered in the limit of infinite magnetic Reynolds number in non-ideal MHD (Berger 1984). This implies that for finite (but large) magnetic Reynolds numbers magnetic helicity can decay only through microscopic resistivity. This would in turn control the saturation time and cycle periods of large-scale *helical* magnetic field which would be too slow to explain the observed variations of magnetic fields in astrophysical settings, such as for example the 11 year variation of the large-scale fields during the solar cycle.

A possible way out of this deadlock is provided by fluxes of magnetic helicity out of the domain (Blackman & Field 2000; Kleeorin et al. 2000). In the case of the solar dynamo, such a flux could be out of the domain, mediated by coronal mass ejections, or it could be across the equator, mediated by internal gradients within the domain. Several possible candidates for magnetic helicity fluxes have been proposed (Kleeorin & Rogachevskii 1999; Vishniac & Cho 2001; Subramanian & Brandenburg 2004).

In this paper we measure the diffusive flux across the domain with two different signs of magnetic helicity. This measurement, however, poses an additional difficulty due to the fact that neither the flux nor the magnetic helicity density remain invariant under the gauge transformation $\boldsymbol{A}\to\boldsymbol{A}+\boldsymbol{\nabla}\Lambda$, up to which the vector potential is defined. This constitutes a gauge problem. This problem, however, does not arise in homogeneous (or nearly homogeneous) domains with periodic or perfect-conductor boundary conditions, or in infinitely large domains where both the magnetic field and the vector potential decay fast enough at infinity. In these cases the volume integral of magnetic helicity is *gauge-invariant*, because surface terms vanish and $\boldsymbol{\nabla}\cdot\boldsymbol{B}=0$, so that $\int\boldsymbol{B}\cdot\boldsymbol{\nabla}\Lambda\,\mathrm{d}V=-\int\Lambda\boldsymbol{\nabla}\cdot\boldsymbol{B}\,\mathrm{d}V=0$. However, in practice we are often interested in finite or open domains with more realistic boundary conditions. Also, if we are to talk meaningfully about the exchange of magnetic helicity between two parts of the domain we need to evaluate changes in magnetic helicity densities locally even if the

---

* Corresponding author: dhruba.mitra@gmail.com integral of the magnetic helicity density over the whole domain is gauge-invariant. An important question then is how to calculate this quantity across arbitrary surfaces in numerical simulations. Ideally one would like to have a gauge-invariant description of magnetic helicity. A number of suggestions have been put forward in the literature (Berger & Field 1984; Subramanian & Brandenburg 2006). In practice, however, calculating the gauge-invariant volume integral of magnetic helicity poses an awkward complication and may not be the quantity relevant for dynamo quenching (Subramanian & Brandenburg 2006). In this paper, to partially address this question, we take an alternative view and try to compare and contrast the magnetic helicity and its flux across the domain in three different gauges that are often used in numerical simulations.

2 Model and background

The setup in this paper is inspired by the recent work of Mitra et al. (2009), who considered a wedge-shaped domain encompassing parts of both the southern and northern hemispheres. Direct numerical simulations (DNS) of the compressible MHD equations with an external force which injected negative (positive) helicity in the northern (southern) hemisphere shows a dynamo with polarity reversals, oscillations and equatorward migration of magnetic activity. It was further shown, using mean-field models, that such a dynamo is well described by an α^2 dynamo, where α has positive (negative) sign in the northern (southern) hemisphere. However, the mean-field dynamo showed catastrophic quenching, i.e., the ratio of magnetic energy to the equipartition magnetic energy decreases as R_m^{-1}, where R_m is the magnetic Reynolds number. Such catastrophic quenching could potentially be alleviated by a mean flux of small-scale magnetic helicity across the equator (Brandenburg et al. 2009). Diffusive flux of this kind has previously been employed in mean-field models on empirical grounds (Covas et al. 1998; Kleeorin et al. 2000). Using a one-dimensional mean-field model of an α^2 dynamo with positive α in the north and negative in the south, it was possible to show that for large enough values of R_m catastrophic quenching is indeed alleviated (Brandenburg et al. 2009). However, three questions still remained:

1. Can such a diffusive flux result from DNS?
2. Is it strong enough to alleviate catastrophic quenching?
3. When is it independent of the gauge chosen?

In this paper we provide partial answers to these questions.

We proceed by simplifying our problem further, both conceptually and numerically, by considering simulations performed in a rectangular Cartesian box with dimensions $L_x \times L_y \times L_z$. The box is divided into two equal cubes along the z direction, with sides $L_x = L_y = L_z/2$. We shall refer to the xy plane at $z = 0$ as the 'equator' and the regions with positive (negative) z as 'north' and 'south' respectively. We shall choose the helicity of the external force such that it has negative (positive) helicity in the northern (southern) part of the domain. All the sides of the simulation domain are chosen to have periodic boundary conditions. The slowest resistive decay rate of the mean magnetic field is ηk_1^2, where η is the microscopic magnetic diffusivity and $k_1 = \pi/L_z$ is the lowest wavenumber of the domain.

We employ two different random forcing functions: one where the helicity of the forcing function varies sinusoidally with z (Model A) and one where it varies linearly with z (Model B). This also leads to a corresponding variation of the kinetic and small-scale current helicities in the domain. Model A minimizes the possibility of boundary effects, while Model B employs the same profile as that used in an earlier mean-field model (Brandenburg et al. 2009). The typical wavenumber of the forcing function is chosen to be $k_\mathrm{f} = 20k_1$ in Model A and $k_\mathrm{f} = 16k_1$ in Model B. An important control parameter of our simulations is the magnetic Reynolds number, $R_\mathrm{m} = u_\mathrm{rms}/\eta k_\mathrm{f}$, which is varied between 2 and 68, although we also present a result with a larger value of R_m. This last simulation may not have run long enough and will therefore not be analyzed in detailed.

We perform DNS of the equations of compressible MHD for an isothermal gas with constant sound speed c_s,

$$\mathrm{D}_t\boldsymbol{U} = -c_\mathrm{s}^2\boldsymbol{\nabla}\ln\rho + \frac{1}{\rho}\boldsymbol{J}\times\boldsymbol{B} + \boldsymbol{F}_\mathrm{visc} + \boldsymbol{f}, \tag{1}$$

$$\mathrm{D}_t\ln\rho = -\boldsymbol{\nabla}\cdot\boldsymbol{U}, \tag{2}$$

$$\partial_t\boldsymbol{A} = \boldsymbol{U}\times\boldsymbol{B} - \eta\mu_0\boldsymbol{J} - \boldsymbol{\nabla}\Psi, \tag{3}$$

where $\boldsymbol{F}_\mathrm{visc} = (\mu/\rho)(\nabla^2\boldsymbol{U} + \frac{1}{3}\boldsymbol{\nabla\nabla}\cdot\boldsymbol{U})$ is the viscous force when the dynamic viscosity μ is constant (Model A), and $\boldsymbol{F}_\mathrm{visc} = \nu(\nabla^2\boldsymbol{U} + \frac{1}{3}\boldsymbol{\nabla\nabla}\cdot\boldsymbol{U} + 2\mathsf{S}\ln\rho)$ is the viscous force when the kinematic viscosity ν is constant (Model B), $\boldsymbol{U}$ is the velocity, $\boldsymbol{J} = \boldsymbol{\nabla}\times\boldsymbol{B}/\mu_0$ is the current density, μ_0 is the vacuum permeability (in the following we measure the magnetic field in Alfvén units by setting $\mu_0 = 1$ everywhere), ρ is the density, Ψ is the electrostatic potential, and $\mathrm{D}_t \equiv \partial_t + \boldsymbol{U}\cdot\boldsymbol{\nabla}$ is the advective derivative. Here, $\boldsymbol{f}(\boldsymbol{x}, t)$ is an external random white-in-time helical function of space and time. The simulations were performed with the PENCIL CODE[1], which uses sixth-order explicit finite differences in space and third order accurate time stepping method. We use a numerical resolution of $128 \times 128 \times 256$ meshpoints.

These simulations in a Cartesian box capture the essential aspects of the simulations of Mitra et al. (2009) in spherical wedge-shaped domains. In particular, in this case we also observe the generation of large-scale magnetic fields which show oscillations on dynamical time scales, reversals of polarity and equatorward migration, as can be seen from the sequence of snapshots in Fig. 1 for a run with $R_\mathrm{m} = 68$. Here we express time in units of the expected turbulent diffusion time, $T = (\eta_{t0}k_1^2)^{-1}$, where $\eta_{t0} = u_\mathrm{rms}/3k_\mathrm{f}$ is used as the reference value (Sur et al. 2008).

Below we shall employ this setup to study the magnetic helicity and its flux. We shall discuss the issue of gauge-dependence in Sect. 5.

---

[1] http://www.nordita.org/software/pencil-code/

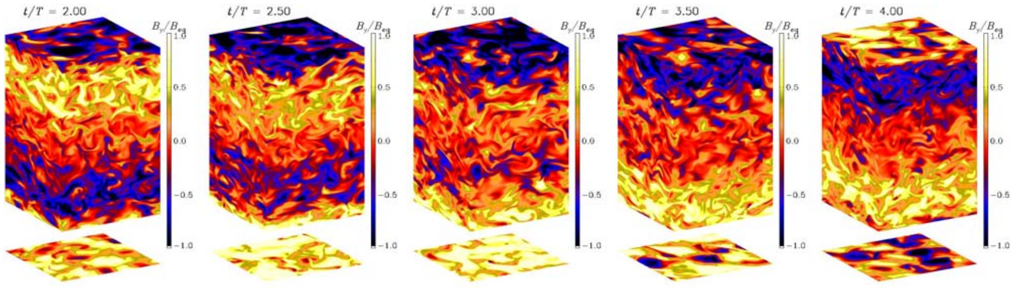

Fig. 1 (online colour at: www.an-journal.org) Visualization of the B_y component of the magnetic field on the periphery of the domain at different times showing the migration of magnetic patterns from the top and bottom boundaries toward the equator. Yellow (light) shades denote positive values and blue (dark) shades denote negative values. Time is measured in turbulent diffusion times, $T = (\eta_{\rm t0}k_1^2)^{-1}$, where $\eta_{\rm t0} = u_{\rm rms}/3k_{\rm f}$ is used as reference.

3 Magnetic helicity fluxes

Let us first summarize the role played by magnetic helicity and its fluxes in large-scale helical dynamos. In the spirit of mean-field theory, we define large-scale (or mean) quantities, denoted by an overbar, as a horizontal average taken over the x and y directions. In addition, we denote a volume average by angular brackets, $\langle\cdot\rangle$. The magnetic helicity density is denoted by

$$h^{\rm M} \equiv \boldsymbol{A}\cdot\boldsymbol{B}. \tag{4}$$

In general the evolution equation of $h^{\rm M}$ can be written down using the MHD equations, which yields

$$\partial_t h^{\rm M} = -2\boldsymbol{E}\cdot\boldsymbol{B} - \boldsymbol{\nabla}\cdot\boldsymbol{\mathcal{F}}^{\rm H}, \tag{5}$$

where

$$\boldsymbol{\mathcal{F}}^{\rm H} = \boldsymbol{E}\times\boldsymbol{A} + \Psi\boldsymbol{B} \tag{6}$$

is the magnetic helicity flux and $\boldsymbol{E}$ is the electric field, which is given by

$$\boldsymbol{E} = -\boldsymbol{U}\times\boldsymbol{B} + \eta\boldsymbol{J}. \tag{7}$$

Given that our system is statistically homogeneous in the horizontal directions, we consider the evolution equation for the horizontally averaged magnetic helicity density,

$$\partial_t\overline{h}^{\rm M} = -2\eta\overline{\boldsymbol{J}\cdot\boldsymbol{B}} - \boldsymbol{\nabla}\cdot\overline{\boldsymbol{\mathcal{F}}}^{\rm H}, \tag{8}$$

where the contribution from the full electromotive force, $\boldsymbol{U}\times\boldsymbol{B}$, has dropped out after taking the dot product with $\boldsymbol{B}$. However, the mean electromotive force from the fluctuating fields, $\overline{\boldsymbol{\mathcal{E}}} = \overline{\boldsymbol{u}\times\boldsymbol{b}}$, enters the evolution of the mean fields, so this contribution does not vanish if we consider separately the contributions to $\overline{h}^{\rm M}$ that result from mean and fluctuating fields, i.e.

$$\partial_t\overline{h}^{\rm M}_{\rm m} = 2\overline{\boldsymbol{\mathcal{E}}}\cdot\overline{\boldsymbol{B}} - 2\eta\overline{\boldsymbol{J}}\cdot\overline{\boldsymbol{B}} - \boldsymbol{\nabla}\cdot\overline{\boldsymbol{\mathcal{F}}}^{\rm H}_{\rm m}, \tag{9}$$

$$\partial_t\overline{h}^{\rm M}_{\rm f} = -2\overline{\boldsymbol{\mathcal{E}}}\cdot\overline{\boldsymbol{B}} - 2\eta\overline{\boldsymbol{j}\cdot\boldsymbol{b}} - \boldsymbol{\nabla}\cdot\overline{\boldsymbol{\mathcal{F}}}^{\rm H}_{\rm f}, \tag{10}$$

where

$$\overline{\boldsymbol{\mathcal{F}}}^{\rm H}_{\rm m} = \overline{\boldsymbol{E}}\times\overline{\boldsymbol{A}} + \overline{\Psi}\,\overline{\boldsymbol{B}}, \tag{11}$$

$$\overline{\boldsymbol{\mathcal{F}}}^{\rm H}_{\rm f} = \overline{\boldsymbol{e}\times\boldsymbol{a}} + \overline{\psi\boldsymbol{b}}, \tag{12}$$

and $\Psi = \overline{\Psi} + \psi$.

In mean-field dynamo theory one solves the evolution equation for $\overline{\boldsymbol{B}}$, so $\overline{\boldsymbol{\mathcal{F}}}^{\rm H}_{\rm m}$ is known explicitly from the actual mean fields. However, the evolution equation for $\overline{h}^{\rm M}_{\rm f}$ is not automatically obeyed in the usual mean-field treatment. This is the reason why in the dynamical quenching formalism this equation is added as an additional constraint equation. The terms $\overline{h}^{\rm M}_{\rm f}$ and $\overline{\boldsymbol{j}\cdot\boldsymbol{b}} \approx k_{\rm f}^2\overline{h}^{\rm M}_{\rm f}$ are coupled to the mean-field equations through an additional contribution to the α effect with a term proportional to $k_{\rm f}^2\overline{h}^{\rm M}_{\rm f}$. However, the coupling of the flux term $\overline{\boldsymbol{\mathcal{F}}}^{\rm H}_{\rm f}$ is less clear, because there are several possibilities and their relative importance is not well established.

In this paper we are primarily interested in $\overline{\boldsymbol{\mathcal{F}}}^{\rm H}_{\rm f}$ across the equator. We assume that this flux can be written in terms of the gradient of the magnetic helicity density via a Fickian diffusion law, i.e.,

$$\overline{\boldsymbol{\mathcal{F}}}^{\rm H}_{\rm f} = -\kappa_{\rm f}\boldsymbol{\nabla}\overline{h}^{\rm M}_{\rm f}, \tag{13}$$

where $\kappa_{\rm f}$ is an effective diffusion coefficient for the magnetic helicity density.

There are several points to note regarding Eq. (13). Firstly, both the magnetic helicity and its flux are *gauge-dependent*. Hence this expression should in principle depend on the gauge we choose. On the other hand, catastrophic quenching is a physically observable phenomenon that should not depend on the particular gauge chosen. Secondly, we recall that Eq. (13) is purely a conjecture at this stage, and it is the aim of this paper to test this conjecture. Thirdly, Eq. (13) is not the only form of flux of magnetic helicity possible. Two other obvious candidates are the advective flux and the Vishniac-Cho flux (Vishniac & Cho 2001).

Table 1 Dependence of $\overline{\boldsymbol{B}}^2$, normalized by $B_{\rm eq}^2$, the slopes of the three terms on the RHS of Eq. (10), normalized by $\eta_{\rm t0}B_{\rm eq}^2$, as well as the value of $\kappa_{\rm f}/\eta_{\rm t0}$.

Run	$R_{\rm m}$	$\overline{\boldsymbol{B}}^2$	$2\overline{\boldsymbol{\mathcal{E}}}\cdot\overline{\boldsymbol{B}}$	$2\eta\overline{\boldsymbol{j}\cdot\boldsymbol{b}}$	$\boldsymbol{\nabla}\cdot\overline{\boldsymbol{\mathcal{F}}}_{\rm f}^{\rm H}$	$\kappa_{\rm f}/\eta_{\rm t0}$
B1	2	1.1	9.42	−9.38	−0.04	0.41
B2	5	2.2	11.18	−11.14	−0.04	0.34
B3	15	2.0	4.54	−4.52	−0.02	0.27
B4	33	1.7	2.28	−2.27	−0.01	0.31
B5	68	0.8	1.15	−1.12	−0.03	0.34

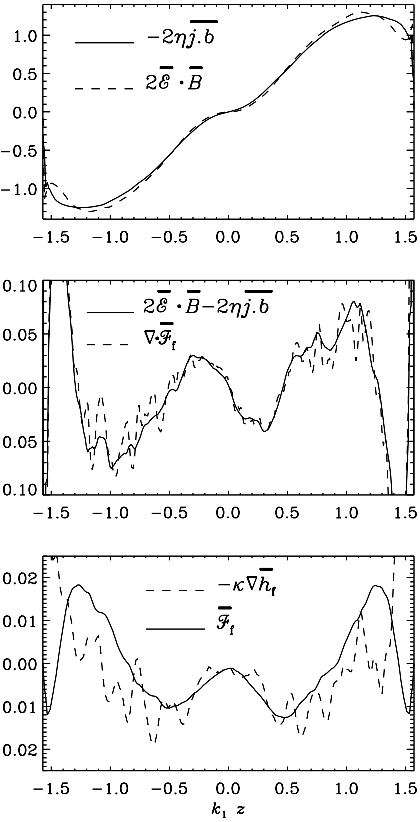

Fig. 2 z dependence of the terms on the RHS of Eq. (10) in the first two panels and in Eq. (13) for Run B5.

However, none of them can be of importance to the problem at hand, because we have neither a large-scale velocity (thus ruling out advective flux) nor a large-scale shear (thus ruling out Vishniac-Cho flux).

4 Diffusive flux and $R_{\rm m}$ dependence

Let us postpone the discussion of the complications arising from the choice of gauge until Sect. 5 and use the *resistive gauge* for the results reported in this section, i.e. we set

$$\Psi = \eta\boldsymbol{\nabla}\cdot\boldsymbol{A}. \tag{14}$$

We then calculate $\overline{\mathcal{F}}_{\rm f}^{\rm H}$ and $\overline{h}_{\rm f}^{\rm M}$ as functions of z from our simulations, time-average both of them and use Eq. (13) to calculate $\kappa_{\rm f}$ from a least-square fit of $\overline{\mathcal{F}}_{\rm f}^{\rm H}$ versus $-\boldsymbol{\nabla}\overline{h}_{\rm f}^{\rm M}$ within the range $-1.3 \leq k_1 z \leq 1.3$. The values of $\kappa_{\rm f}$ as a function of $R_{\rm m}$ is given in the last column of Table 1.

In order to determine the relative importance of equatorial magnetic helicity fluxes, we now consider individually the three terms on the RHS of Eq. (10). Within the range $-1.3 \leq k_1 z \leq 1.3$, all three terms vary roughly linearly with z. We therefore determine the slope of this dependence. In Table 1 we compare these three terms at $k_1 z = -1$, evaluated in units of $\eta_{\rm t0}k_1 B_{\rm eq}^2$, as well as the value of $\kappa_{\rm f}/\eta_{\rm t0}$. In Fig. 2 we show the z dependence of these three terms for Run B5, where $R_{\rm m} = 68$. The values of $\kappa_{\rm f}$ as a function of $R_{\rm m}$ is given in the last column of Table 1. The z dependence of $\overline{\mathcal{F}}_{\rm f}^{\rm H}$ and $\overline{h}_{\rm f}^{\rm M}$ is shown in the last panel of Fig. 2. Note that the two profiles agree quite well.

We point out that, near $z = 0$, all simulations show either a local reduction in the gradients of the terms on the RHS of Eq. (10) or even a local reversal of the gradient. This is likely to be associated with a local reduction in dynamo activity near $z = 0$, where kinetic helicity is zero. The non-uniformity of the turbulent magnetic field also leads to transport effects (Brandenburg & Subramanian 2005a) that may modify the gradient. However, we shall not pursue this question further here.

Looking at Table 1, we see that the terms $2\overline{\boldsymbol{\mathcal{E}}}\cdot\overline{\boldsymbol{B}}$ and $2\eta\overline{\boldsymbol{j}\cdot\boldsymbol{b}}$ balance each other nearly perfectly, and that only a small residual is then balanced by the diffusive flux divergence, $\boldsymbol{\nabla}\cdot\overline{\boldsymbol{\mathcal{F}}}_{\rm f}^{\rm H}$. For the values of $R_{\rm m}$ considered here, the terms $2\overline{\boldsymbol{\mathcal{E}}}\cdot\overline{\boldsymbol{B}}$ and $2\eta\overline{\boldsymbol{j}\cdot\boldsymbol{b}}$ scale with $R_{\rm m}$, while the dependence of $\boldsymbol{\nabla}\cdot\overline{\boldsymbol{\mathcal{F}}}_{\rm f}^{\rm H}$ on $R_{\rm m}$ is comparatively weak. If catastrophic quenching is to be alleviated by the magnetic helicity flux, one would expect that at large values of $R_{\rm m}$ the terms $2\overline{\boldsymbol{\mathcal{E}}}\cdot\overline{\boldsymbol{B}}$ and $\boldsymbol{\nabla}\cdot\overline{\boldsymbol{\mathcal{F}}}_{\rm f}^{\rm H}$ should balance. At the moment our values of $R_{\rm m}$ are still too small by about a factor of 30–60 (assuming that the same scaling with $R_{\rm m}$ persists). This result is compatible with that of earlier mean field models (Brandenburg et al. 2009). Consequently, we see that the energy of the mean magnetic field decreases with increasing $R_{\rm m}$ from 33 to 68; see Fig. 3. For larger values of $R_{\rm m}$ the situation is still unclear.

In Table 1, we also give the approximate values of $\kappa_{\rm f}/\eta_{\rm t0}$. Note that this ratio is always around 0.3 and independent of $R_{\rm m}$. This is the first time that an estimate for the diffusion coefficient of the diffusive flux has been obtained. There exists no theoretical prediction for the value of $\kappa_{\rm f}$ other than the naive expectation that such a term should be expected and that its value should be of the order of $\eta_{\rm t0}$.

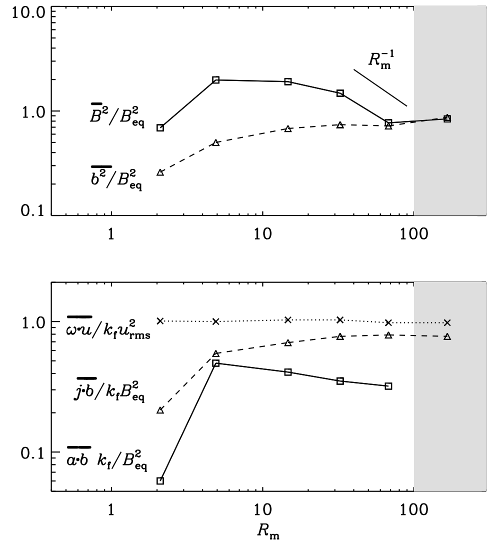

Fig. 3 R_m dependence of the normalized magnetic energy of the mean field, $\langle\overline{\boldsymbol{B}}^2\rangle/B_\mathrm{eq}^2$, and the fluctuating field, $\langle\boldsymbol{b}^2\rangle/B_\mathrm{eq}^2$, in the *upper panel* together with the normalized helicities of the small-scale magnetic field, $\overline{\boldsymbol{a}\cdot\boldsymbol{b}}\,k_\mathrm{f}/B_\mathrm{eq}^2$, the small-scale current density, $\overline{\boldsymbol{j}\cdot\boldsymbol{b}}/k_\mathrm{f}B_\mathrm{eq}^2$, and the small-scale velocity, $\overline{\boldsymbol{\omega}\cdot\boldsymbol{u}}/k_\mathrm{f}u_\mathrm{rms}^2$, at $k_1 z=-1$ (i.e. in the south) in the *lower panel*. (All three helicities are negative in the north and positive in the south.) The shaded areas indicate that the solutions are different in nature, and that the simulations may not have run for long enough.

This now allows us to state more precisely the point where the turbulent diffusive helicity flux becomes comparable with the resistive term, i.e. we assume $\kappa_\mathrm{f}\nabla^2\overline{\boldsymbol{a}\cdot\boldsymbol{b}}$ to become comparable with $2\eta\overline{\boldsymbol{j}\cdot\boldsymbol{b}}$. Using the relation $\overline{\boldsymbol{j}\cdot\boldsymbol{b}}\approx k_\mathrm{f}^2\overline{\boldsymbol{a}\cdot\boldsymbol{b}}$ (Blackman & Brandenburg 2002), which is confirmed by the current simulations within a factor of about 2 (see the second panel of Fig. 3), we find that

$$\kappa_\mathrm{f}/2\eta > (k_\mathrm{f}/k_1)^2, \tag{15}$$

where we have assumed that the Laplacian of $\overline{\boldsymbol{a}\cdot\boldsymbol{b}}$ can be replaced by a k_1^2 factor. Using our empirical finding, $\kappa_\mathrm{f}\approx\eta_{\mathrm{t}0}/3$, together with the definition $\eta_{\mathrm{t}0}/\eta\approx u_\mathrm{rms}/3\eta k_\mathrm{f}=R_\mathrm{m}/3$, we arrive at the condition

$$R_\mathrm{m} > 18(k_\mathrm{f}/k_1)^2\approx 4600 \quad (\text{for } \kappa_\mathrm{f} \text{ to be important}), \tag{16}$$

where we have inserted the value $k_\mathrm{f}/k_1=16$ for the present simulations. Similarly, large values of R_m for alleviating catastrophic quenching by turbulent diffusive helicity fluxes were also found using mean-field modelling (Brandenburg et al. 2009). Unfortunately, the computing resources are still not sufficient to verify this in the immediate future.

5 Gauge-dependence of helicity flux

Let us now consider the question of gauge-dependence of the helicity flux. Equation (10) is obviously gauge-dependent. However, if, in the statistically steady state, $\overline{h}_\mathrm{f}^\mathrm{M}$ becomes independent of time, we can average this equation and obtain

$$\frac{\partial\overline{\mathcal{F}}_\mathrm{f}^\mathrm{H}}{\partial z} = -2\overline{\boldsymbol{\mathcal{E}}}\cdot\overline{\boldsymbol{B}} - 2\eta\overline{\boldsymbol{j}\cdot\boldsymbol{b}}, \tag{17}$$

where $\overline{\mathcal{F}}_\mathrm{f}^\mathrm{H}$ refers to the z component of $\overline{\boldsymbol{\mathcal{F}}}_\mathrm{f}^\mathrm{H}$. On the RHS of this equation the two terms are gauge-independent. Therefore $\boldsymbol{\nabla}\cdot\overline{\boldsymbol{\mathcal{F}}}_\mathrm{f}^\mathrm{H}$ must also be gauge-independent. The same applies also to $\overline{\boldsymbol{\mathcal{F}}}_\mathrm{m}^\mathrm{H}$ and $\overline{\boldsymbol{\mathcal{F}}}^\mathrm{H}$; see Eq. (8). We have confirmed that, in the steady state, $\overline{h}_\mathrm{f}^\mathrm{M}$ is statistically steady and does not show a long-term trend; cf. Fig. 4 for the three gauges. We note that the fluctuations of $\overline{h}_\mathrm{f}^\mathrm{M}$ are typically much larger for the Weyl gauge than for the other two.

We now verify the expected gauge-independence explicitly for three different gauges: the *Weyl gauge*,

$$\Psi = 0, \tag{18}$$

the *Lorenz gauge* (or pseudo-Lorenz gauge)[2], defined by

$$\partial_t\Psi = -c_\Psi^2\boldsymbol{\nabla}\cdot\boldsymbol{A}, \tag{19}$$

and the resistive gauge, defined by (14) above. We calculate the normalized magnetic helicity for both the mean and fluctuating parts and the respective fluxes for all the three gauges. These simulations are done for Model A with low R_m ($R_\mathrm{m}\approx 1.9$).

We find the transport coefficient κ_f in the way described in the previous section. A snapshot of the mean flux $\overline{\mathcal{F}}_\mathrm{f}^\mathrm{H}$ is plotted in the top panel of Fig. 5. The flux is different in all the three gauges. However, when averaged over the horizontal directions as well as time the fluxes in the three different gauges agree with one another as shown in the bottom panel of Fig. 5. We find the transport coefficient κ_f as described in the previous section and obtain the same value in all the three gauges.

6 Conclusion

In this paper we use a setup in which the two parts of the domain have different signs of kinetic and magnetic helicities. Using DNS we show that the flux of magnetic helicity due to small-scale fields can be described by Fickian diffusion down the gradient of this quantity. The corresponding diffusion coefficient is approximately independent of R_m. However, in the range of R_m values considered here, the flux is not big enough to alleviate catastrophic quenching. The critical value of R_m for the flux to become important is proportional to the square of the scale separation ratio. In the present case, where this ratio is 16, the critical value of R_m is estimated to be 4600. We have also calculated the flux and the diffusion coefficient in the three gauges discussed above and have found the fluxes to be independent

---

[2] In fact, this is not the true Lorenz gauge because we use velocity of sound (Brandenburg & Käpylä 2007) instead of the velocity of light which appears in the original Lorenz gauge

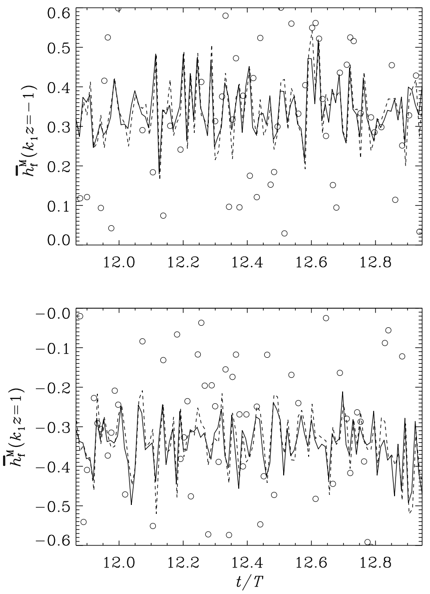

Fig. 4 Plot of $\overline{h}_\mathrm{f}^\mathrm{M}$ as a function of time in the statistically stationary state for $k_1z = -1$ (south, *top panel*) and $k_1z = 1$ (north, *bottom panel*) for the three different gauges, Weyl gauge (open circle), Lorenz gauge (line) and resistive gauge (broken line).

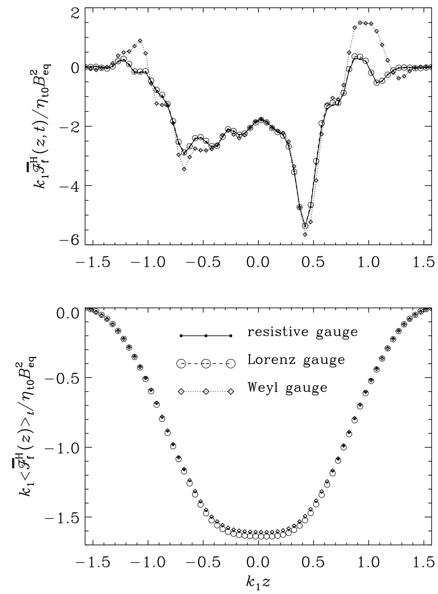

Fig. 5 Comparison of the flux $\overline{\mathcal{F}}_\mathrm{f}^\mathrm{H}(z,t)$ at a randomly chosen instant (*upper panel*) and its time average $\overline{\mathcal{F}}_\mathrm{f}^\mathrm{H}(z)$ for the three different gauges. Lorenz gauge (○), Weyl gauge (◇) and the resistive gauge (·). The instantaneous flux is plotted in the top panel and the time-averaged flux is plotted in the *bottom panel*.

of the choice of these gauges. This is explained by the fact that in the steady state the divergence of magnetic helicity flux is balanced by terms that are gauge-independent.

Several immediate improvements on this study spring to mind. One is to compare our results with the gauge-independent magnetic helicity of Berger & Field (1984) and the corresponding magnetic helicity flux. The second is to extend the present study to higher values of R_m to understand the asymptotic behavior of the flux. Finally, it may be useful to compare the results for different profiles of kinetic helicity to see whether or not our results depend on such details.

Acknowledgements. We thank the referee for a careful assessment of the paper and for pointing out an error in the original notation. The simulations were performed with the computers hosted by QMUL HMC facilities purchased under the SRIF initiative. We also acknowledge the allocation of computing resources provided by the Swedish National Allocations Committee at the Center for Parallel Computers at the Royal Institute of Technology in Stockholm and the National Supercomputer Centers in Linköping. This work was supported in part by the European Research Council under the AstroDyn Research Project 227952 and the Swedish Research Council grant 621-2007-4064. DM is supported by the Leverhulme Trust.

References

Berger, M.: 1984, GApFD 30, 79
Berger, M., Field, G.B.: 1984, JFM 147, 133
Blackman, E.G., Field, G.B.: 2000, ApJ 534, 984
Blackman, E.G., Brandenburg, A.: 2002, ApJ 579, 359
Brandenburg, A., Käpylä, P.J.: 2007, NJPh 9, 305
Brandenburg, A., Subramanian, K.: 2005a, PhR 417, 1
Brandenburg, A. & Subramanian, K.: 2005b, AN 326, 400
Brandenburg, A., Candelaresi, S., Chatterjee, P.: 2009, MNRAS 398, 1414
Brandenburg, A., Rädler, K.-H., Rheinhardt, M., Käpylä, P.J.: 2008, ApJ 676, 740
Covas, E., Tavakol, R., Tworkowski, A., Brandenburg, A.: 1998, A&A 329, 350
Kleeorin, N., Rogachevskii, I.: 1999, Phys Rev E 59, 6724
Kleeorin, N., Moss, D., Rogachevskii, I., Sokoloff, D.: 2000, A&A 361, L5
Mitra, D., Tavakol, R., Käpylä, P.J., Brandenburg, A.: 2009, astro-ph/0901.2364
Shukurov, A., Sokoloff, D., Subramanian, K., Brandenburg, A.: 2006, A&A 448, L33
Subramanian, K., Brandenburg, A.: 2004, Phys Rev Lett 93, 205001
Subramanian, K., Brandenburg, A.: 2006, ApJ 648, L71
Sur, S., Brandenburg, A., Subramanian, K.: 2008, MNRAS 385, L15
Vishniac, E.T., Cho, J.: 2001, ApJ 550, 752

IV

PHYSICS OF PLASMAS **18**, 012903 (2011)

Magnetic helicity transport in the advective gauge family

Simon Candelaresi,[1,2] Alexander Hubbard,[1] Axel Brandenburg,[1,2]
and Dhrubaditya Mitra[1]
[1]*NORDITA, AlbaNova University Center, Roslagstullsbacken 23, SE-10691 Stockholm, Sweden*
[2]*Department of Astronomy, Stockholm University, SE 10691 Stockholm, Sweden*

(Received 29 October 2010; accepted 14 December 2010; published online 10 January 2011)

Magnetic helicity fluxes are investigated in a family of gauges in which the contribution from ideal magnetohydrodynamics takes the form of a purely advective flux. Numerical simulations of magnetohydrodynamic turbulence in this advective gauge family exhibit instabilities triggered by the build-up of unphysical irrotational contributions to the magnetic vector potential. As a remedy, the vector potential is evolved in a numerically well behaved gauge, from which the advective vector potential is obtained by a gauge transformation. In the kinematic regime, the magnetic helicity density evolves similarly to a passive scalar when resistivity is small and turbulent mixing is mild, i.e., when the fluid Reynolds number is not too large. In the dynamical regime, resistive contributions to the magnetic helicity flux in the advective gauge are found to be significant owing to the development of small length scales in the irrotational part of the magnetic vector potential. © *2011 American Institute of Physics*. [doi:10.1063/1.3533656]

I. INTRODUCTION

Most astrophysical and laboratory plasmas are good conductors. This, together with high-speed flows and large length scales, nearly universal in the astrophysical context, makes for large magnetic Reynolds numbers. In the limit of infinitely large magnetic Reynolds number, and for domains with closed boundaries, total magnetic helicity is a conserved quantity. Here, an analogy can be drawn with mass conservation in domains whose boundaries are closed to mass flux. Furthermore, in open domains, the change in total mass is governed by the mass flux across open surfaces. In ideal magnetohydrodynamics (MHD), a similar property holds for the total magnetic helicity. But unlike mass, magnetic helicity depends on the choice of gauge. In the special case of the advective gauge, the magnetic helicity flux is given by the velocity times the magnetic helicity density,[1] making this gauge particularly interesting for studying pointwise properties of magnetic helicity. This is an important goal of this paper.

Magnetic helicity plays an important role in many fields of plasma physics and astrophysics, and has applications ranging from tokamaks and other plasma confinement machines, to dynamo action in the Sun and the galaxy. Our physical understanding of the role of magnetic helicity in MHD is greatly aided by concepts such as Taylor relaxation,[2] selective decay,[3] and the inverse cascade of magnetic helicity.[4]

Furthermore, magnetic helicity is a crucial ingredient of the turbulent dynamos which are believed to be the source of the equipartition magnetic fields in astrophysical bodies such as stars and galaxies.[5] In all such cases the characteristic length scales of the dynamo generated magnetic field exceed those of the fluid's energy carrying scale. In dynamo theory, the formation of such a large-scale magnetic field is typically possible through the α effect, which is nonzero for helical turbulent flows. In periodic boxes with helical turbulence, the α effect becomes strongly quenched when the (appropriately normalized) magnetic helicity in the small-scale field (i.e., scales that are smaller than the energy-carrying scale of turbulent fluid) is comparable to the helicity in the small-scale velocity. Conservation of magnetic helicity implies that the helicity in small- and large-scale fields will have comparable magnitudes, so the quenching of the large-scale dynamo will occur for weak large-scale fields. This α quenching[6,7] increases with scale separation and endures for as long as magnetic helicity is nearly conserved, a resistive time that scales with the magnetic Reynolds number $\mathrm{Re}_M \equiv UL/\eta$. The quenching is called "catastrophic" because for the Sun $\mathrm{Re}_M \sim 10^9$ and the galaxy $\mathrm{Re}_M \sim 10^{15}$, and their resistive timescales are problematically long. This rapid pre-resistive saturation of the dynamo generated field poses clear difficulties in applying theory to astronomical systems, but it may be possible to alleviate the problem through magnetic helicity fluxes.[8,9] It should also be pointed out that problems with catastrophic quenching are often not clearly seen in present-day simulations.[10–12] While trend lines suggest that catastrophic quenching will occur, simulations at currently achievable, low to intermediate Re_M and scale separation have shown significant large-scale fields.

There exists reasonable observational evidence is support of such fluxes of magnetic helicity. The Sun's surface magnetic field shows helical structures.[13,14] Further, it was shown[15] that the S-shaped (helical) regions which are active in the corona are precursors of coronal mass ejections (CMEs) and later[16] that those regions are more likely to erupt. This suggests that the Sun sheds magnetic helicity via CMEs. Since the Sun's large-scale magnetic field is believed to be generated by a helical dynamo[17,18] this shedding of magnetic helicity could play an important role in the 11 year solar cycle. Physically, magnetic helicity fluxes out of the domain can be mediated in many ways, such as the aforementioned CMEs for the Sun[19] or fountain flows in the case of galaxies.[17] In direct simulations magnetic helicity fluxes are permitted by adjusting the boundary conditions, e.g., to vertical field boundaries, but their actual presence can be difficult to ascertain. Internal helicity fluxes have also been found to alleviate α quenching[18] in systems with internal boundaries that separate zones of oppositely signed kinetic and magnetic helicities.

A difficulty in addressing the generation and transport of magnetic helicity is its gauge dependence. We denote the magnetic vector potential as $\boldsymbol{A}$ such that $\boldsymbol{B}\equiv\boldsymbol{\nabla}\times\boldsymbol{A}$ is the magnetic field. Magnetic helicity $H\equiv\int_V \boldsymbol{A}\cdot\boldsymbol{B}dV$ is independent of the gauge for perfectly conducting boundaries, as well as periodic boundaries so long as $\boldsymbol{A}$ is also required to be periodic. However, if one wishes to study the transport of magnetic helicity for physically motivated systems a nonvolume integral formulation will be needed. Magnetic helicity *density*, $h\equiv\boldsymbol{A}\cdot\boldsymbol{B}$, the quantity we will be working with, clearly depends on the gauge choice for $\boldsymbol{A}$. The gauge dependence of fluxes of mean magnetic helicity contained in the fluctuating fields was examined via direct numerical simulations (DNS) for three different gauges,[20] and it was found that, averaged over time, they do not depend on the gauge choice. This is a result of the fact that, for sufficient scale separation, the magnetic helicity of the fluctuating field can be expressed as the density of linkages, which in turn is gauge-invariant.[21] This result implies that the study of specific but useful gauge choices is a meaningful task.

In this work we examine the properties of magnetic helicity density in a particularly interesting gauge-family which we call "advective" because in this gauge the effect of velocity on the evolution equation of magnetic helicity takes the form of a purely advective term. In previous work[1] this gauge choice was shown to be crucial to understanding magnetic helicity fluxes in the presence of shear, including the Vishniac–Cho flux.[22] Unfortunately, evolving $\boldsymbol{A}$ in this gauge proves numerically unstable. This may be related to earlier findings in smoothed particle MHD calculations.[23,24] There, the problem was identified as the result of an unconstrained evolution of vector potential components, which were argued to be connected with "poor accuracy with respect to "reverse-advection"-type terms."[23] Our present work clarifies that this instability is related to the excessive build-up of irrotational contributions to the magnetic vector potential. These contributions have no physical meaning, but discretization errors at small length scales can spoil the solution dramatically.

We shall therefore describe a novel method for obtaining $\boldsymbol{A}$ in this gauge by evolving it first in a numerically robust gauge and then applying a gauge transformation with a simultaneously evolved gauge potential. This will be referred to as the Λ method throughout the text. Next, we show that the magnetic helicity density in the advective gauge tends to be small even pointwise, provided turbulent effects are still weak, and discuss the analogy with passive scalar transport. We conclude by pointing out that resistive terms break the analogy with passive scalar advection through the emergence of a turbulently diffusive magnetic helicity flux.

II. MAGNETIC EVOLUTION EQUATIONS

A. Weyl and advective gauges

In this work we remain within nonrelativistic MHD and hence neglect the Faraday displacement current. So the current density is given by $\boldsymbol{J}=\boldsymbol{\nabla}\times\boldsymbol{B}$, where $\boldsymbol{B}$ is the magnetic field and we use units where the vacuum permeability is unity. At the core of MHD is the induction equation

$$\frac{\partial \boldsymbol{B}}{\partial t}=\boldsymbol{\nabla}\times(\boldsymbol{U}\times\boldsymbol{B}-\eta\boldsymbol{J}), \quad (1)$$

where $\boldsymbol{U}$ is the velocity and η is the molecular magnetic diffusivity. Equation (1) can be uncurled to give an evolution equation for the magnetic vector potential $\boldsymbol{A}$, but only up to a gauge choice. In the Weyl gauge, indicated by a superscript W on the magnetic vector potential, we just have

$$\frac{\partial \boldsymbol{A}^W}{\partial t}=\boldsymbol{U}\times\boldsymbol{B}-\eta\boldsymbol{J} \quad (2)$$

but by adding the gradient of a scalar field, the vector potential can be obtained in any other gauge. Of particular interest to this paper is the advective gauge

$$\boldsymbol{A}^a=\boldsymbol{A}^W+\boldsymbol{\nabla}\Lambda^{W:a}, \quad (3)$$

where $\Lambda^{W:a}$ is the gauge potential that transforms from $\boldsymbol{A}^W$ to $\boldsymbol{A}^a$. We demand that[25]

$$\frac{DA_i^a}{Dt}=-U_{j,i}A_j^a-\eta J_i. \quad (4)$$

Here, $D/Dt=\partial/\partial t+\boldsymbol{U}\cdot\boldsymbol{\nabla}$ is the advective derivative. Consequently one can show that $\Lambda^{W:a}$ obeys the evolution equation (see Appendix A)

$$\frac{D\Lambda^{W:a}}{Dt}=-\boldsymbol{U}\cdot\boldsymbol{A}^W. \quad (5)$$

Thus, to obtain $\boldsymbol{A}^a$, one can either solve Eq. (4) directly or, alternatively, solve Eq. (2) together with Eq. (5) and use Eq. (3) to obtain $\boldsymbol{A}^a$. A possible initial condition for $\Lambda^{W:a}$ would be $\Lambda^{W:a}=0$, in which case $\boldsymbol{A}^a=\boldsymbol{A}^W$ initially. For numerical reasons that will be discussed in more detail below, we shall consider the indirect method of obtaining the magnetic vector potential in the advective gauge, but starting from more numerically stable gauge which will be discussed in Sec. II B.

Variants on the advective gauge have seen significant use, particularly in DNS with constant imposed shear. Although the magnetic field in such simulations must obey shearing-periodic boundary condition the vector potential need not. In particular, the evolution Eq. (2) does not impose shearing-periodicity on the vector potential, while Eq. (4) does, enabling shearing-periodic numerical simulations[26] in terms of $\boldsymbol{A}$.

For our purposes, the importance of Eq. (4) lies in the form of the magnetic helicity density evolution equation. By writing the induction equation in the form

$$\frac{DB_i}{Dt} = + U_{i,j}B_j - (\boldsymbol{\nabla}\cdot\boldsymbol{U})B_i - (\boldsymbol{\nabla}\times\eta\boldsymbol{J})_i \tag{6}$$

computing $D(\boldsymbol{A}^a\cdot\boldsymbol{B})/Dt=\boldsymbol{A}^a\cdot D\boldsymbol{B}/Dt+\boldsymbol{B}\cdot D\boldsymbol{A}^a/Dt$, and noting that the $A_iU_{i,j}B_j$ terms from both equations cancel, we find that

$$\frac{Dh^a}{Dt} = -h^a\boldsymbol{\nabla}\cdot\boldsymbol{U} - \boldsymbol{\nabla}\cdot(\eta\boldsymbol{J}\times\boldsymbol{A}^a) - 2\eta\boldsymbol{J}\cdot\boldsymbol{B} \tag{7}$$

which shows that in ideal MHD ($\eta=0$) under the assumption of incompressibility ($\boldsymbol{\nabla}\cdot\boldsymbol{U}=0$) the magnetic helicity density in the advective gauge, $h^a=\boldsymbol{A}^a\cdot\boldsymbol{B}$ is just advected with the flow like a passive scalar, i.e.,

$$\frac{Dh^a}{Dt} = 0 \quad (\text{for} \quad \eta=0 \quad \text{and} \quad \boldsymbol{\nabla}\cdot\boldsymbol{U}=0). \tag{8}$$

In the general case with $\boldsymbol{\nabla}\cdot\boldsymbol{U}\neq 0$, the rate of change of the local value of h^a is given by $-\boldsymbol{\nabla}\cdot(h^a\boldsymbol{U})$, which is analogous to the continuity equation for the fluid density. However, for $\eta\neq 0$, there is also a source term

$$\frac{\partial h^a}{\partial t} = -2\eta\boldsymbol{J}\cdot\boldsymbol{B} - \boldsymbol{\nabla}\cdot\boldsymbol{F}^a, \tag{9}$$

as well as a resistive contribution to the magnetic helicity flux

$$\boldsymbol{F}^a = h^a\boldsymbol{U} + \eta\boldsymbol{J}\times\boldsymbol{A}^a. \tag{10}$$

In this paper we address the question how the $\eta\boldsymbol{J}\times\boldsymbol{A}^a$ contribution scales in the limit $\eta\to 0$, i.e., for large values of Re_M. It could either stay finite, just like the resistive energy dissipation $\eta\boldsymbol{J}^2$, which tends to a finite limit[5] as $\eta\to 0$, or it could go to zero like the source term $\eta\boldsymbol{J}\cdot\boldsymbol{B}$.[27,28]

B. Resistive and advecto-resistive gauges

There are two important issues to be noted about the equations discussed above. First, for numerical reasons, Eq. (2) is often replaced by

$$\frac{\partial\boldsymbol{A}^r}{\partial t} = \boldsymbol{U}\times\boldsymbol{B} + \eta\nabla^2\boldsymbol{A}^r, \tag{11}$$

where $\boldsymbol{A}^r$ is the magnetic vector potential in the resistive gauge and we have assumed that $\eta=$const; otherwise there would be an additional gradient term of the magnetic diffusivity that results from[29]

$$-\eta\boldsymbol{J} + \boldsymbol{\nabla}(\eta\boldsymbol{\nabla}\cdot\boldsymbol{A}) = \eta\nabla^2\boldsymbol{A} + (\boldsymbol{\nabla}\cdot\boldsymbol{A})\boldsymbol{\nabla}\eta. \tag{12}$$

This "resistive" gauge introduces an explicit, numerically stabilizing diffusion term for each component of $\boldsymbol{A}$. Second, and again for numerical reasons, Eq. (5) should be solved with a small diffusion term proportional to $\nabla^2\Lambda^{W:a}$. These two issues are actually connected and can be resolved by considering the gauge transformation

$$\boldsymbol{A}^{\mathrm{ar}} = \boldsymbol{A}^r + \boldsymbol{\nabla}\Lambda^{r:\mathrm{ar}} \tag{13}$$

which allows us to obtain the magnetic vector potential $\boldsymbol{A}^{\mathrm{ar}}$ in the advecto-resistive gauge obeying

$$\frac{DA_i^{\mathrm{ar}}}{Dt} = -U_{j,i}A_j^{\mathrm{ar}} + \eta\nabla^2A_i^{\mathrm{ar}}, \tag{14}$$

by solving Eq. (11) for $\boldsymbol{A}^r$ together with

$$\frac{D\Lambda^{r:\mathrm{ar}}}{Dt} = -\boldsymbol{U}\cdot\boldsymbol{A}^r + \eta\nabla^2\Lambda^{r:\mathrm{ar}} \tag{15}$$

and finally using the gauge transformation Eq. (13). For a full derivation of this equation we refer to Appendix B. Note that the microscopic magnetic diffusivity automatically enters the $\Lambda^{r:\mathrm{ar}}$ equation as a diffusion term, which implies that the $\Lambda^{r:\mathrm{ar}}$ equation is numerically well behaved.

The magnetic helicity density $h^{\mathrm{ar}}=\boldsymbol{A}^{\mathrm{ar}}\cdot\boldsymbol{B}$ in the advecto-resistive gauge can be calculated from the magnetic helicity in the resistive gauge through $h^{\mathrm{ar}}=h^r+\boldsymbol{\nabla}\Lambda^{r:\mathrm{ar}}\cdot\boldsymbol{B}$, and it obeys

$$\frac{\partial h^{\mathrm{ar}}}{\partial t} = -2\eta\boldsymbol{J}\cdot\boldsymbol{B} - \boldsymbol{\nabla}\cdot\boldsymbol{F}^{\mathrm{ar}} \tag{16}$$

with

$$\boldsymbol{F}^{\mathrm{ar}} = h^{\mathrm{ar}}\boldsymbol{U} - \eta(\boldsymbol{\nabla}\cdot\boldsymbol{A}^{\mathrm{ar}})\boldsymbol{B} + \eta\boldsymbol{J}\times\boldsymbol{A}^{\mathrm{ar}}. \tag{17}$$

For comparison, the evolution equation of the magnetic helicity density in the resistive gauge is given by an equation similar to Eq. (16), but with h^{ar} being replaced by h^r and $\boldsymbol{F}^{\mathrm{ar}}$ being replaced by

$$\boldsymbol{F}^r = h^r\boldsymbol{U} - (\boldsymbol{U}\cdot\boldsymbol{A}^r + \eta\boldsymbol{\nabla}\cdot\boldsymbol{A}^r)\boldsymbol{B} + \eta\boldsymbol{J}\times\boldsymbol{A}^r \tag{18}$$

which contains a nonadvective velocity driven flux of the form $(\boldsymbol{U}\cdot\boldsymbol{A}^r)\boldsymbol{B}$—even in the ideal case.

C. Numerical details

We perform simulations for isotropically forced, triply periodic cubic domains with sides of length 2π, as was done in earlier work.[28] The $\eta\boldsymbol{J}\cdot\boldsymbol{B}$ term in Eq. (9) implies (and past simulations have shown) that such a system will experience a slow, but steady production of magnetic helicity. This is the price to pay for a system which is both helical, providing us with a signal, and homogeneous, so avoiding extraneous magnetic helicity fluxes. In addition to the uncurled induction Eq. (11) and the gauge transformation evolution Eq. (15), we solve

$$\frac{D\boldsymbol{U}}{Dt} = -c_s^2\boldsymbol{\nabla}\ln\rho + \frac{c_L}{\rho}\boldsymbol{J}\times\boldsymbol{B} + \boldsymbol{F}_{\mathrm{visc}} + \boldsymbol{f}, \tag{19}$$

$$\frac{D\ln\rho}{Dt} = -\boldsymbol{\nabla}\cdot\boldsymbol{U}, \tag{20}$$

where c_s(=const) is the isothermal sound speed, ρ is the density, $\boldsymbol{F}_{\mathrm{visc}}=\rho^{-1}\boldsymbol{\nabla}\cdot(2\rho\nu\mathsf{S})$ is the viscous force, $\mathsf{S}_{ij}=\frac{1}{2}(U_{i,j}+U_{j,i})-\frac{1}{3}\delta_{ij}\boldsymbol{\nabla}\cdot\boldsymbol{U}$ is the rate of strain tensor, ν is the kinematic viscosity, $\boldsymbol{f}$ the forcing term, and $c_L=1$ is a prefactor that can be put to 0 to turn off the Lorentz force in kinematic calculations. As in earlier work[28] the forcing function consists of plane polarized waves whose direction and phase change randomly from one time step to the next. The modulus of its wavevectors is taken from a band of wavenumbers around a given average wavenumber k_f. The magnetic vector potential is initialized with a weak nonhelical sine wave along one direction. In some cases we shall also consider solutions to the passive scalar equation in the incompressible case

$$\frac{DC}{Dt} = \kappa \nabla^2 C, \tag{21}$$

where κ is the passive scalar diffusivity. Following earlier work,[30] we impose a linear gradient in C, i.e., $C=Gz+c$, and solve for the departure from this gradient G, i.e.,

$$\frac{Dc}{Dt} = \kappa \nabla^2 c - GU_z, \tag{22}$$

where GU_z acts essentially as a forcing term.

We use the PENCIL CODE (http://pencil-code.googlecode.com)[31] to solve the equations for $\boldsymbol{A}^r$, $\boldsymbol{U}$, $\Lambda^{r:\mathrm{ar}}$, ρ, and in some cases also c. The calculations involving $\Lambda^{r:\mathrm{ar}}$ have been carried out with the publicly available revision r15211 (or similar) of the module special/advective_gauge.f90.

The control parameters we use are the magnetic Reynolds number Re_M, the magnetic Prandtl number Pr_M, and the Schmidt number

$$\mathrm{Re}_M \equiv \frac{u_{\mathrm{rms}}}{\eta k_f}, \quad \mathrm{Pr}_M \equiv \frac{\nu}{\eta}, \quad \mathrm{Sc} \equiv \frac{\nu}{\kappa}, \tag{23}$$

where u_{rms} is the root mean square velocity. We use $k_f=3k_1$ where k_1, the box wavenumber, is unity. The numerical resolution is varied between 32^3 and 256^3 meshpoints for values of Re and Re_M between 3 and 300. In one case we used $\mathrm{Re}_M \approx 800$, which was only possible because in that case we used $\mathrm{Pr}_M=10$, so that most of the energy gets dissipated viscously, leaving relatively little magnetic energy at high wavenumbers.[32]

III. IMPORTANCE OF MAGNETIC HELICITY DENSITY

A. Implications of Eq. (7) for dynamo theory

Magnetic helicity is not only of interest by being a conserved quantity in ideal MHD, but also by being the basis of a methodology to treat nonlinear helical MHD dynamos, namely, dynamical α quenching.[33] This methodology relates the current helicity in small scale fields with the magnetic helicity in small-scale fields, $\boldsymbol{j}\cdot\boldsymbol{b} \simeq k_f^2 \boldsymbol{a}\cdot\boldsymbol{b}$, and invokes the magnetic α effect.[4] The evolution equation of the magnetic helicity density then becomes the evolution equation of the magnetic part of the α effect and the nonlinear evolution of the dynamo can be modeled. This methodology has been used successfully in systems where no net helicity flux is possible, and initial work invoking the methodology has captured the behavior of at least one system with finite helicity fluxes.[34] A major prediction of the theory is that in the absence of preferential helicity fluxes of small-scale fields, dynamo action is quenched to subequipartition mean field strengths. This phenomenon is sometimes referred to as "catastrophic quenching."

B. Magnetic helicity as passive scalar

In the advective and advecto-resistive gauges, the velocity appears in the evolution equations of the magnetic helicity density, Eqs. (7) and (16), only as advection terms in the fluxes, Eqs. (10) and (17). In the limit of ideal, incompressible, kinematic MHD, Eq. (7) is the evolution equation for a passive scalar. Even in nonideal MHD, if the fluctuations of h^{ar} due to the velocity field $\boldsymbol{U}$ were purely advective in nature (i.e., passive), magnetic helicity transport would only be resistive, large-scale advective, and/or turbulently diffusive. This would forbid the preferential export of small-scale magnetic helicity and might call for alternate solutions to the catastrophic quenching problem than helicity fluxes.[18]

While in ideal MHD ($\eta=0$) the resistive terms in Eq. (7) vanish, resistive terms need not vanish in the limit of $\eta \to 0$ (high Re_M). For example, in a turbulent flow, Ohmic dissipation $\eta \boldsymbol{J}^2$ tends to a finite value as η decreases. The need for nonresistive solutions to the build-up of magnetic helicity is therefore not a given. We will examine this by performing kinematic simulations where the Lorentz force is turned off, i.e., $c_L=0$.

If the Lorentz force is significant, the fluctuations of h^{ar} and $\boldsymbol{U}$ might be correlated beyond simple turbulent diffusion concerns (i.e., the fluctuations of h^{ar} could drive flow patterns). In the limit of incompressible flows, if the helicity is uniform, then the only source terms for helicity patterns of finite k are the resistive terms. The terms are small compared to dimensional estimates for the velocity terms when $\mathrm{Re}_M \gg 1$. We will look for signals of magnetic helicity transport by examining spectra of h^r and h^{ar} as (pseudo) scalars, together with spectra of a true passive scalar. As we will show, the advecto-resistive gauge is adequately efficient at turbulently diffusing magnetic helicity that no inertial range for the magnetic helicity density can be identified. However, the spectra of h^r help elucidate previous results[34] which found diffusive fluxes, but at values well below turbulent diffusivities. Instead, our spectra show clear diffusive behavior in the inertial range, but the mere existence of the inertial range implies nondiffusive behavior.

We emphasize that our spectra of h^r and h^{ar} have nothing to do with the usual magnetic helicity spectrum that obeys a realizability condition and whose integral gives the volume-averaged magnetic helicity. Here we are looking instead at the power of the magnetic helicity density as a (pseudo) scalar field. Our h_k measures the spatial variation of h. In order to avoid confusion, we shall refer to these spectra as scalar spectra.

IV. RESULTS

The results reported below for the magnetic helicity density h refer to the advecto-resistive gauge and have been obtained by the Λ method, unless indicated otherwise. The results from the direct method agree (Sec. IV A), but this method develops an instability when nonlinear effects become important (Sec. IV B).

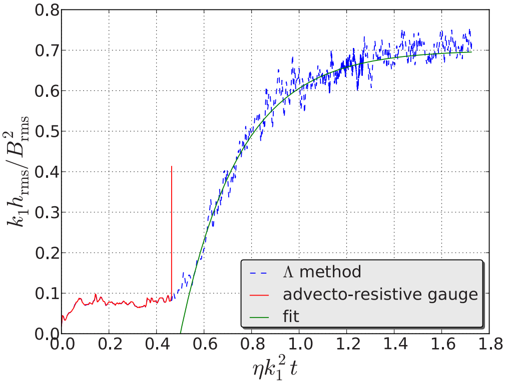

FIG. 1. (Color online) Time dependence of the normalized helicity for the advecto-resistive gauge with the direct method and the Λ method. Both curves agree perfectly just until the moment when the code develops an instability in the direct calculation. Time is normalized in terms of the magnetic diffusion time. The fit is an exponential relaxation to a constant value proportional to $1-\exp(-2\eta k_m^2\Delta t)$, where $\Delta t = t - t_{\rm sat}$ is the time after the small-scale magnetic field has saturated (Ref. 28) and $k_m = 1.4k_1$ has been chosen for a good fit.

A. Agreement between Λ and direct methods

To test the agreement between the Λ method and directly solving the induction equation in the advecto-resistive gauge, we plot the normalized rms magnetic helicity $h_{\rm rms}^{\rm ar}$ with respect to time (Fig. 1). Note that the nondimensional ratio $k_1 h_{\rm rms}^{\rm ar}/B_{\rm rms}^2$ has a well-defined plateau during the kinematic stage. Below we shall study the average value of this plateau as a function of magnetic Reynolds and Prandtl numbers. At the end of the kinematic phase, there is a slow saturation phase on a resistive time scale during which the large-scale field of the dynamo develops.[28] The results of the two calculations agree just until the moment when the direct calculation develops a numerical instability, whose nature will be discussed in more detail below. The perfect agreement until this moment can be taken as confirmation that the Λ method works and is correctly implemented in the code.

B. Nature of the instability

In Fig. 2 we show time series for a range of modest values of Re_M and two resolutions, 32^3 and 64^3. Reducing the magnetic Reynolds number may stabilize the system somewhat, but changing the resolution has no clear effect. In Fig. 3 we present data from equivalent runs that solve either Eq. (14) or alternatively Eqs. (11) and (15). We can see that the solutions match up until time $t=220/c_s k_f$, where the run that solves Eq. (14) becomes unstable.

The key point is that when we evolve Eqs. (11) and (15), Λ never enters the equations for physical quantities. However, when we evolve Eq. (14), the magnetic field includes a term $\nabla\times(\nabla\Lambda)$, which, when computed numerically, is not zero. The first panel in Fig. 3 shows the power spectra of the vector potential. Comparing the advecto-resistive gauge (dashed/red) with resistive gauge (dotted/blue) we see that $\boldsymbol{A}^{\rm ar}=\boldsymbol{A}^{r}+\nabla\Lambda$ has significantly more power at high k than $\boldsymbol{A}^{r}$. Numerics cannot adequately handle the requirement that $\nabla\times\nabla\Lambda=0$ at high k in the direct method, introducing errors in $\boldsymbol{B}$, as can be seen in the second panel. This fictitious increase in magnetic power at high k (and the attendant increase in current) result in a fictitious high k increase in the velocity field (third panel) that produces the numerical instability. The results of Fig. 2 suggest that the power of Λ (remembering that $\boldsymbol{J}$ includes that the third derivative of Λ) drops slowly enough at high k that numerical stability can only be achieved by enforcing an adequate resistivity η to damp Λ for only modest wavenumbers. Indeed, any gauge with large power in $\boldsymbol{A}$ for high k is expected to be numerically unstable, and the method sketched in Appendix A orAppendix B may be used to make the connection between analytical results in such a numerically unstable gauge and numerical results produced in a stable gauge.

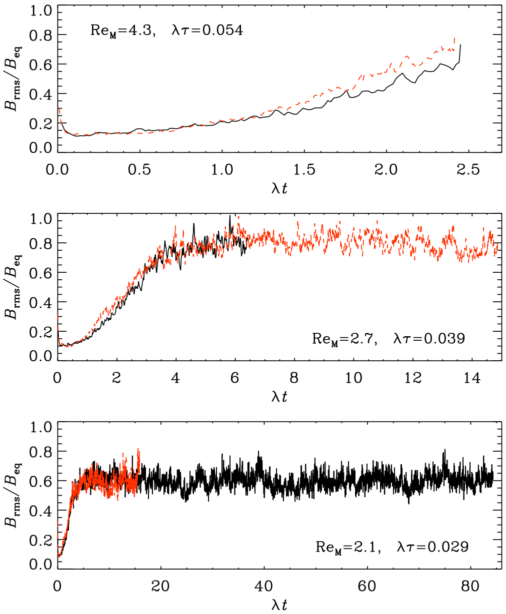

FIG. 2. (Color online) Evolution of $B_{\rm rms}/B_{\rm eq}$ for small values of Re_M between 4.3 (top) and 2.1 (bottom), using 32^3 (solid lines) and 64^3 (dashed, red lines). In each case, time on the abscissa is normalized by the growth rate λ, whose value is given in each panel in units of the inverse turnover time, $\tau^{-1}=u_{\rm rms}k_f$. The ends of each line mark the point when the solution became unstable.

C. Evolution of rms helicity density

In Fig. 4 we present a time series of the normalized rms magnetic helicity density in the kinematic regime (Lorentz force turned off, i.e., $c_L=0$). In both the advecto-resistive and resistive gauges, there is an initial adjustment of the nondimensional ratio $k_1 h_{\rm rms}/B_{\rm rms}^2$ to a certain value, followed by a plateau. In the kinematic regime the magnetic helicity

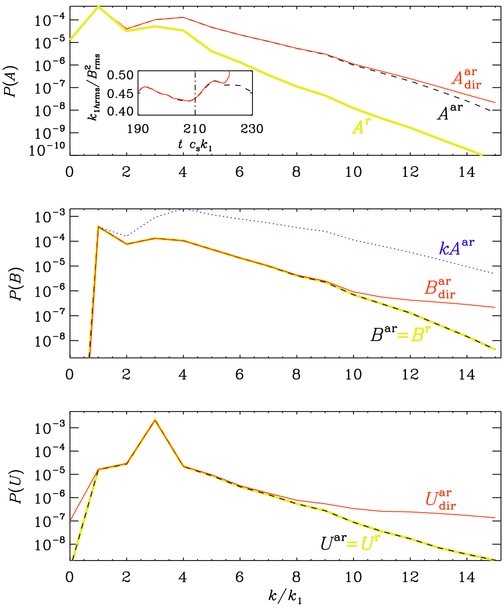

FIG. 3. (Color online) Power spectra of $\boldsymbol{A}$, $\boldsymbol{B}$, and $\boldsymbol{U}$ for two runs that are identical except that the first run solves for $\boldsymbol{A}^{\rm ar}$ directly while the second solves for $\boldsymbol{A}^r$ and Λ. In the top panel we plot the spectrum of $\boldsymbol{A}$ obtained either via $\boldsymbol{A}^{\rm ar}=\boldsymbol{A}^r+\boldsymbol{\nabla}\Lambda$ (dashed) or directly, $\boldsymbol{A}_{\rm dir}^{\rm ar}$ (solid/red), and compare with $\boldsymbol{A}^r$ (thick gray/yellow), showing that the vector potential in the advecto-resistive gauge has much more power at high k. The inset shows the time evolution of the normalized $h_{\rm rms}$ shortly before the time of the numerical instability. The dash-dotted line indicates the time for which the power spectra is taken. In the second panel we present magnetic energy spectra obtained in the direct gauge (solid/red), with the Λ method (dashed/black) as well as $k\boldsymbol{A}^{\rm ar}$ (dotted/blue), showing that there is significant power in the irrotational part of $\boldsymbol{A}$. We see that in the direct calculation of $\boldsymbol{A}^{\rm ar}$ the numerics are unable to adequately handle the high wavenumber power of $\boldsymbol{A}^{\rm ar}$ with consequences for the velocity seen in the last panel (solid/red line). The spectra of $\boldsymbol{B}$ and $\boldsymbol{U}$ agree for resistive and advecto-resistive gauges (thick gray/yellow line underneath the dashed black line) because the evaluation of the curl of a gradient has been avoided (last two panels). The three spectra are all taken for $t=210/c_s k_1$.

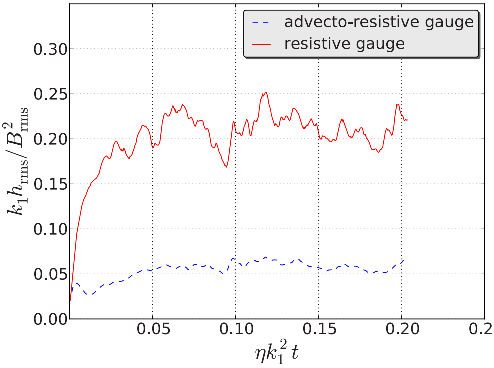

FIG. 4. (Color online) Time dependence of the rms values for the helicity in the advecto-resistive (solid/red) and resistive (dashed/blue) gauges with the Lorentz force switched off, i.e., $c_L=0$ in both cases.

density is passive and the advection term in the advecto-resistive gauge merely serves to turbulently diffuse any local concentrations of $h^{\rm ar}$. Therefore there cannot be any spontaneous growth of $h^{\rm ar}$, except for effects from the resistive terms in the early adjustment phase. Turbulent diffusion itself, on the other hand, cannot generate variance of $h^{\rm ar}$.

In Figs. 5 and 6 we plot the height of the rms-magnetic helicity density plateau as a function of Re_M for several values of the magnetic Prandtl number and constant forcing amplitude. The differences between the evolution equations for h^r and $h^{\rm ar}$ are contained entirely in the flux terms so the volume integral of h is the same in the two gauges. Any difference between the rms values of h therefore is due to spatial fluctuations generated by the flux terms.

We fit the data points in Fig. 5 with functions of the form

$$\frac{k_1 h^{\rm ar}}{B_{\rm rms}^2} = c\,\mathrm{Re}_M^{-a}(1+b\,\mathrm{Re}_M^{2a}). \tag{24}$$

The fit results for the parameters are presented in Table I. Of interest is c, which increases with Pr_M and scales approximately with $\mathrm{Pr}_M^{1/2}$. A more general, although less accurate fit is given by

$$\frac{k_1 h^{\rm ar}}{B_{\rm rms}^2} \approx 3\,\mathrm{Re}_M^{-1}\left[1+\left(\frac{\mathrm{Re}_M/\mathrm{Pr}_M^{1/3}}{50}\right)^2\right] \tag{25}$$

see Fig. 7.

It is clear that high wavenumber fluid eddies (which are damped for small Re, i.e., large Pr_M, contribute significantly to $h_{\rm rms}^{\rm ar}$ for $\mathrm{Re}_M>100$, while from Fig. 6 we see that they do not contribute to $h_{\rm rms}^r$. That these eddies could contribute in the advecto-resistive gauge is to be expected as the advective

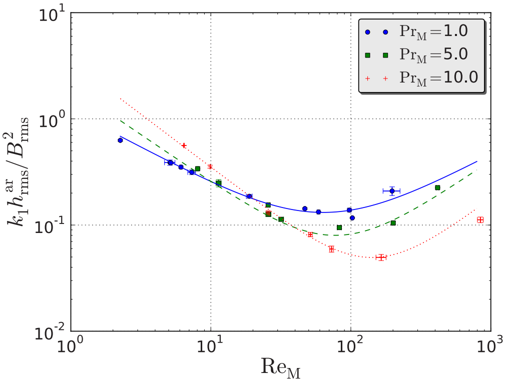

FIG. 5. (Color online) Re_M dependence of $k_1 h_{\rm rms}^{\rm ar}/B_{\rm rms}^2$ for the kinematic phase. Values are averages over times where they reach a stationary state. The curves represent fits according to Eq. (24).

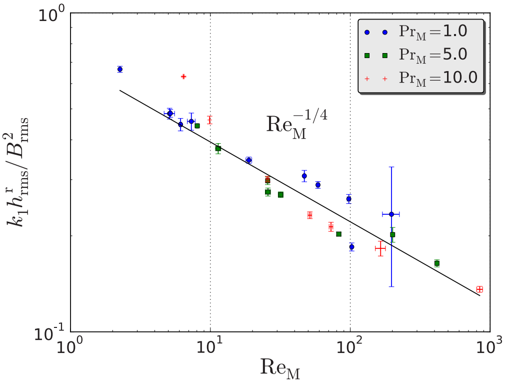

FIG. 6. (Color online) Re_M dependence of $k_1 h^r_{\mathrm{rms}}/B^2_{\mathrm{rms}}$ for the kinematic phase. Values are averages over times where they reach a stationary state. A $-1/4$ power law can be seen.

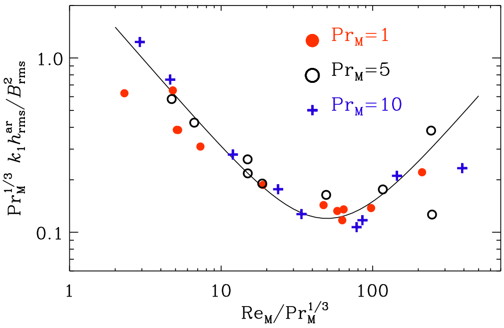

FIG. 7. (Color online) Dependence of $k_1 h^{\mathrm{ar}}_{\mathrm{rms}}/B^2_{\mathrm{rms}}$, scaled by $\mathrm{Pr}_M^{1/3}$ on $\mathrm{Re}_M/\mathrm{Pr}_M^{1/3}$ for the kinematic phase and $\mathrm{Pr}_M=1$ (filled circles), 5 (open circles), and 10 (plus signs). The solid line represents the fit of Eq. (25).

nature of that gauge implies the existence of an efficient turbulent cascade; the fact that they do contribute there and that the $\eta \boldsymbol{J}\times\boldsymbol{A}^{\mathrm{ar}}$ and $\eta(\boldsymbol{\nabla}\cdot\boldsymbol{A}^{\mathrm{ar}})\boldsymbol{B}$ terms remain important implies that resistive terms both become important at small length scales and have nondissipative effects. This is explained by the fact that $\boldsymbol{A}^{\mathrm{ar}}$ develops a strong high-k tail; see also Fig. 3. This is confirmed in Fig. 8, which shows that the resistive magnetic helicity fluxes in the advecto-resistive gauge are proportional to Re_M. In this gauge the rms resistive helicity fluxes are therefore independent of the actual value of the resistivity, staying finite even in the high Re_M limit. This is quite different from the resistive magnetic helicity fluxes in the resistive gauge, and the global magnetic helicity dissipation (which is gauge-independent): both terms are only proportional to $\mathrm{Re}_M^{1/2}$ and, after multiplying with η these terms tend to zero for $\mathrm{Re}_M\to\infty$.

D. Comparison with passive scalar

In Fig. 9 we present scalar spectra of the magnetic helicity density for both the resistive and advecto-resistive gauges and for the passive scalar concentration c, in the kinematic (arbitrary units) and saturated regimes. The passive scalar spectrum shows a peak at the forcing scale, $k_f/k_1=3$, followed by an approximate $k^{-5/3}$ subrange and an exponential diffusive subrange. As long as the magnetic energy density is still small compared with the kinetic energy density, the field exhibits exponential growth and a Kazantsev $k^{3/2}$ energy spectrum, which is well seen in simulations even at magnetic Prandtl numbers of unity both with and without kinetic helicity in the velocity field.[35] This $k^{3/2}$ spectrum is also reflected in the scalar spectrum of h^{ar}. The scalar spectrum of h^r is somewhat steeper and closer to k^2, indicating that h^r is dominated by white noise in space at large scales.

The saturated regime exhibits some interesting properties. The pronounced peak of the power of the passive scalar at the driving scale is easily understood as being due to the source of c. However, the magnetic helicity density in the resistive gauge shows a significant peak there as well, while it does not in the advecto-resistive gauge. This implies that the velocity term in Eq. (18) generates significant spatial variations in the magnetic helicity density—even in the absence of external modulations. As in dynamical α quenching, h influences the α effect, this suggests a way to quantify the appropriateness of different gauge choices: systems where spatial and temporal fluctuations in α can be adequately constrained would allow one to determine whether spatial fluctuations in h, as seen in Fig. 9, are fictitious as suggested by the advecto-resistive gauge or not.

TABLE I. Fit parameters for Eq. (24) and Fig. 5.

Pr_M	a	b	c	Line type
1	0.7	3×10^{-3}	1.2	Solid/blue
5	0.9	4×10^{-4}	2.0	Dashed/green
10	1.0	5×10^{-5}	3.5	Dotted/red

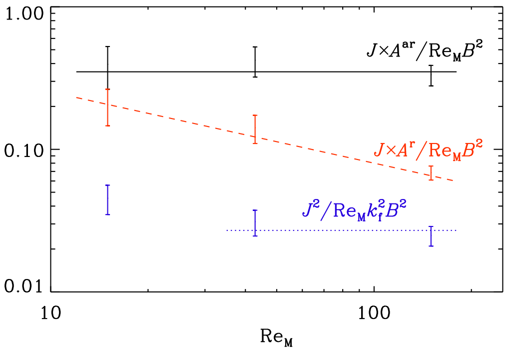

FIG. 8. (Color online) Re_M scaling of the rms value of $\boldsymbol{J}\times\boldsymbol{A}$, normalized by $\mathrm{Re}_M B^2_{\mathrm{rms}}$, for the advecto-resistive and resistive gauges. The solid line represents constant scaling, i.e., $\eta\boldsymbol{J}\times\boldsymbol{A}^{\mathrm{ar}}\approx\mathrm{const}$, while the dashed line represents inverse square root scaling, i.e., $\eta\boldsymbol{J}\times\boldsymbol{A}^{r}\propto\mathrm{Re}_M^{-1/2}$, for three runs with $\mathrm{Pr}_M=1$ in the saturated regime. The dotted/blue line shows that ηJ^2, properly normalized, is approximately constant.

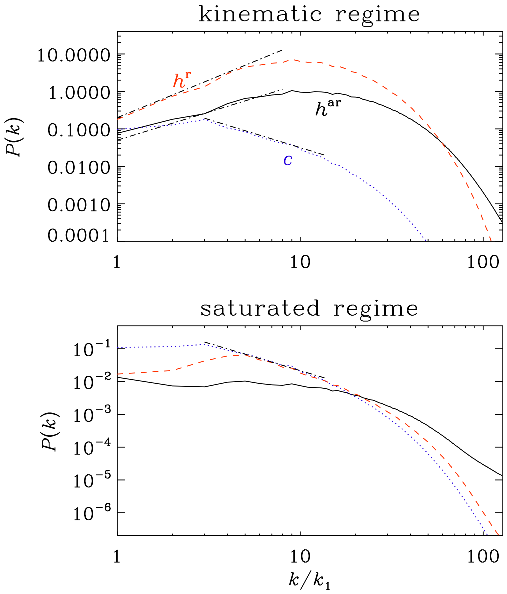

FIG. 9. (Color online) Power spectra of h^r, $h^{\rm ar}$, and the passive scalar c, both in the kinematic regime (top) and the nonlinear saturated regime (bottom) for Re=80 with $\mathrm{Pr}_M=\mathrm{Sc}=1$. In the kinematic regime, the dash-dotted lines have slopes +2 for h^r, +3/2 for $h^{\rm ar}$, −3/2 for c (top), and −5/3 for c in the saturated regime.

The spectra of $h^{\rm ar}$ in the saturated regime do not present a clear inertial range, so we cannot draw strong conclusions as to possible nondiffusive turbulent fluxes. However, h^r follows the same cascade as the passive scalar. Previous studies in that gauge[1] found that magnetic helicity fluxes were best treated as diffusive, although the fits were imperfect. The diffusive nature is clearly seen in the spectrum while the imperfections of the diffusive fit can be seen in the generation of a peak at the driving scale. This evidence in support of diffusive magnetic helicity fluxes gives us the confidence to predict at what Re_M diffusive magnetic helicity fluxes will play a dominant role in dynamo saturation, i.e., when the diffusive fluxes have a greater effect on magnetic helicity evolution than the resistive terms. This will be done in Sec. V where we reanalyze simulation data from earlier work.[34]

V. REVISITING EARLIER WORK

Earlier work[20,34] on magnetic helicity fluxes in inhomogeneous open systems confirmed that the magnetic helicity density of the small-scale field is gauge-invariant —even if that of the large-scale field is not. The divergence of the mean magnetic helicity flux of the small-scale field is then also gauge-invariant, but its value is small compared with resistive magnetic helicity dissipation. We return to this work to estimate at what Re_M diffusive magnetic helicity fluxes will begin to play a dominant role in dynamo saturation.

We emphasize that we are now discussing helicity properties of what we call the small-scale field. Such a field is defined by introducing an averaged magnetic field, $\overline{\boldsymbol{B}}$, indicated by an overbar. Following earlier work[20,34] we restrict ourselves here to planar (or horizontal) averaging. The small-scale field is then given by $\boldsymbol{b}=\boldsymbol{B}-\overline{\boldsymbol{B}}$, and the mean magnetic and current helicity densities of the fluctuating fields are then $\overline{h}_f \equiv \overline{\boldsymbol{a}\cdot\boldsymbol{b}}$ and $\overline{\boldsymbol{j}\cdot\boldsymbol{b}}$, respectively, where $\nabla\times\boldsymbol{a}=\boldsymbol{b}$ and $\boldsymbol{j}=\nabla\times\boldsymbol{b}$. Turbulent diffusion and the α effect imply helicity transfer between scales[36,37] through the mean electromotive force of the fluctuating field, $\overline{\mathcal{E}}=\overline{\boldsymbol{u}\times\boldsymbol{b}}$, so that the evolution equation for $\overline{h}_f$ takes the form

$$\frac{\partial \overline{h}_f}{\partial t} = -2\overline{\mathcal{E}}\cdot\overline{\boldsymbol{B}} - 2\eta\overline{\boldsymbol{j}\cdot\boldsymbol{b}} - \nabla\cdot\overline{\boldsymbol{F}}_f. \tag{26}$$

Here, both $\overline{h}_f$ and $\nabla\cdot\overline{\boldsymbol{F}}_f$ are a gauge-dependent, but if there is a steady state, and if $\overline{h}_f$ is constant, then $\partial\overline{h}_f/\partial t=0$, and since both $\overline{\mathcal{E}}\cdot\overline{\boldsymbol{B}}$ and $\overline{\boldsymbol{j}\cdot\boldsymbol{b}}$ are gauge-invariant, $\nabla\cdot\overline{\boldsymbol{F}}_f$ must also be gauge-invariant. Numerical values for $\overline{\mathcal{E}}\cdot\overline{\boldsymbol{B}}$, $\overline{\boldsymbol{j}\cdot\boldsymbol{b}}$, and $\nabla\cdot\overline{\boldsymbol{F}}_f$ were given earlier[34] for a particular simulation of a slab of helically driven turbulence embedded in a poorly conducting nonhelically driven turbulent halo. In Fig. 10 we show the scaling of all three terms versus Re_M. Note that $-\overline{\mathcal{E}}\cdot\overline{\boldsymbol{B}}$ is balanced mainly by $\overline{\boldsymbol{j}\cdot\boldsymbol{b}}$. However, if the current trend, $\overline{\boldsymbol{j}\cdot\boldsymbol{b}} \sim \mathrm{Re}_M^{-1}$ and $\nabla\cdot\overline{\boldsymbol{F}}_f \sim \mathrm{Re}_M^{-1/2}$ were to continue, one might expect a cross-over at $\mathrm{Re}_M \approx 3\times10^4$. If so, the scaling of $\overline{\mathcal{E}}\cdot\overline{\boldsymbol{B}}$ is expected to become shallower, following that of $\nabla\cdot\overline{\boldsymbol{F}}_f$. Given that the largest Re_M accessible today is of order 10^3, we may conclude that an alleviation of quenching through diffusive magnetic helicity fluxes will not be prominent in simulations for the near future. Nevertheless, astrophysical systems such as the Sun are orders of magnitude beyond the estimated critical point of $\mathrm{Re}_M \sim 3\times10^4$; and we expect their dynamo dynamics to behave accordingly.

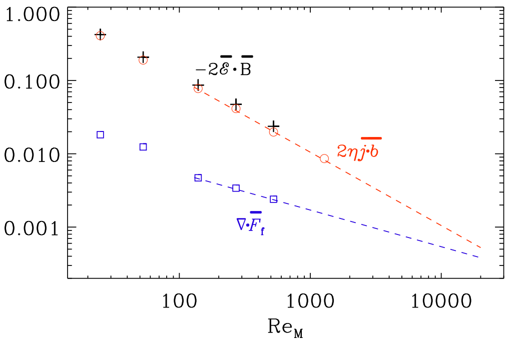

FIG. 10. (Color online) Scaling of $\overline{\mathcal{E}}\cdot\overline{\boldsymbol{B}}$, $\overline{\boldsymbol{j}\cdot\boldsymbol{b}}$, and $\nabla\cdot\overline{\boldsymbol{F}}_f$ vs Re_M for the data of an earlier simulation (Ref. 34) of helically driven turbulence embedded in a poorly conducting nonhelically driven turbulent halo. The symbols show actual data obtained from simulations, the dashed lines are the extrapolation to high Re_M.

VI. CONCLUSIONS

In view of the fact that the time averaged magnetic helicity of the fluctuating fields is gauge-invariant in systems with sufficient scale separation, the gauge-freedom can be exploited to gain insights using gauges that are particularly revealing. Here we have examined an interesting gauge: the advecto-resistive gauge. As the advecto-resistive gauge is inherently numerically unstable, we had to implement a possibly universal technique to run numerical simulations in such unstable gauges by running in a stable gauge while also solving a further equation for the gauge transformation.

The advecto-resistive gauge has allowed us to examine both the consequences of finite resistivity for magnetic helicity density as well as the possibilities of turbulent transport. The magnetic helicity flux, and in particular the contribution from $\eta \boldsymbol{J} \times \boldsymbol{A}^{\mathrm{ar}}$ (properly normalized) reaches a constant value as $\eta \rightarrow 0$. This behavior is similar to the behavior of energy dissipation in turbulence, known as the law of finite energy dissipation.[38] This is interesting as the source term for the volume integrated magnetic helicity H does in fact tend to zero as η does. In this sense, the high Re_M behavior of magnetic helicity is richer than previously anticipated. Indeed, the generation of spatial magnetic helicity fluctuations *ex nihilo* in nonadvecto-resistive gauges is interesting, with potentially testable implications. We expect that the magnetic helicity fluxes resulting from terms of the form $\eta \boldsymbol{J} \times \boldsymbol{A}^{\mathrm{ar}}$ can be modeled as turbulent Fickian diffusion-type fluxes down the gradient of mean magnetic helicity. However, it is clear that fluxes from turbulent diffusion provide only a poor escape from catastrophic α quenching, partly because they cannot distinguish between large- and small-scale fields. Furthermore, in simulations with such turbulent diffusion fluxes, their contribution is still much smaller than the local resistive magnetic helicity dissipation.[20,34] However, the latter decreases faster ($\sim \mathrm{Re}_M^{-1}$) with magnetic Reynolds number than the former ($\sim \mathrm{Re}_M^{-1/2}$), so one may estimate that only for magnetic Reynolds numbers of around 10^4 one has a chance to see the effects of turbulent diffusion. If true, however, such fluxes would definitely be important for the magnetic Reynolds numbers relevant to stars and galaxies—even though such values cannot be reached with present day computer power.

ACKNOWLEDGMENTS

National Supercomputer Centre in Linköping and the Center for Parallel Computers at the Royal Institute of Technology in Sweden. This work was supported in part by the Swedish Research Council (Grant No. 621-2007-4064), and the European Research Council under the AstroDyn Research Project 227952.

APPENDIX A: DERIVATION OF EQ. (5)

We begin by expressing $\boldsymbol{U} \times \boldsymbol{B}$ in terms of $\boldsymbol{A}$

$$(\boldsymbol{U} \times \boldsymbol{B})_i = U_j A_{j,i} - U_j A_{i,j}. \tag{A1}$$

The last term can be subsumed into an advective derivative term for $\boldsymbol{A}$. Using furthermore $U_j A_{j,i} = (U_j A_j)_{,i} - U_{j,i} A_j$, we can write Eq. (2) as

$$\frac{DA_i^W}{Dt} = -U_{j,i} A_j^W + (\boldsymbol{U} \cdot \boldsymbol{A}^W)_{,i} - \eta J_i. \tag{A2}$$

We now insert Eq. (3) for $\boldsymbol{A}^W = \boldsymbol{A}^a - \boldsymbol{\nabla} \Lambda^{W:a}$, so

$$\frac{DA_i^a}{Dt} - \frac{D\Lambda_{,i}^{W:a}}{Dt} = -U_{j,i} A_j^a + U_{j,i} \Lambda_{,j}^{W:a} + (\boldsymbol{U} \cdot \boldsymbol{A}^W)_{,i} - \eta J_i. \tag{A3}$$

and note that

$$-\frac{D\Lambda_{,i}^{W:a}}{Dt} = -\nabla_i \left(\frac{D\Lambda^{W:a}}{Dt} \right) + U_{j,i} \Lambda_{,j}^{W:a}. \tag{A4}$$

The last term cancels and we are left with

$$\frac{DA_i^a}{Dt} + U_{j,i} A_j^a + \eta J_i = \nabla_i \left(\frac{D\Lambda^{W:a}}{Dt} + \boldsymbol{U} \cdot \boldsymbol{A}^W \right), \tag{A5}$$

so we recover the evolution equation for the advective gauge provided Eq. (5) is obeyed.

APPENDIX B: DERIVATION OF EQ. (15)

We present here the derivation of the transformation from the resistive gauge to the advecto-resistive gauge, proceeding analogously to the derivation presented in Appendix A. However, instead of Eq. (A2) we now have

$$\frac{DA_i^r}{Dt} = -U_{j,i} A_j^r + (\boldsymbol{U} \cdot \boldsymbol{A}^r)_{,i} + \eta \nabla^2 A_i^r. \tag{B1}$$

Inserting Eq. (13) for $\boldsymbol{A}^r = \boldsymbol{A}^{\mathrm{ar}} - \boldsymbol{\nabla} \Lambda^{r:\mathrm{ar}}$, we obtain an Equation similar to Eq. (A3)

$$\frac{DA_i^{\mathrm{ar}}}{Dt} - \frac{D\Lambda_{,i}^{r:\mathrm{ar}}}{Dt} = -U_{j,i} A_j^{\mathrm{ar}} + U_{j,i} \Lambda_{,j}^{r:\mathrm{ar}} + (\boldsymbol{U} \cdot \boldsymbol{A}^r)_{,i} + \eta \nabla^2 A_i^{\mathrm{ar}} - \eta \nabla^2 \Lambda_{,i}^{r:\mathrm{ar}} \tag{B2}$$

which leads to

$$\frac{DA_i^{\mathrm{ar}}}{Dt} + U_{j,i} A_j^{\mathrm{ar}} - \eta \nabla^2 A_i^{\mathrm{ar}} = \nabla_i \left(\frac{D\Lambda_i^{r:\mathrm{ar}}}{Dt} + \boldsymbol{U} \cdot \boldsymbol{A}^r - \eta \nabla^2 \Lambda^{r:\mathrm{ar}} \right) \tag{B3}$$

so we recover the evolution equation for the advecto-resistive gauge provided Eq. (15) is obeyed.

[1] A. Hubbard and A. Brandenburg, Astrophys. J. **727**, 11 (2010).
[2] J. B. Taylor, Rev. Mod. Phys. **58**, 741 (1986).
[3] W. H. Matthaeus and D. Montgomery, Ann. N.Y. Acad. Sci. **357**, 203 (1980).
[4] A. Pouquet, U. Frisch, and J. Leorat, J. Fluid Mech. **77**, 321 (1976).
[5] A. Brandenburg and K. Subramanian, Phys. Rep. **417**, 1 (2005).
[6] S. I. Vainshtein and F. Cattaneo, Astrophys. J. **393**, 165 (1992).
[7] F. Cattaneo and D. W. Hughes, Phys. Rev. E **54**, R4532 (1996).

[8] E. G. Blackman and G. B. Field, Mon. Not. R. Astron. Soc. **318**, 724 (2000).
[9] E. G. Blackman and G. B. Field, Astrophys. J. **534**, 984 (2000).
[10] B. P. Brown, M. K. Browning, A. S. Brun, M. S. Miesch, and J. Toomre, Astrophys. J. **711**, 424 (2010).
[11] P. J. Käpylä, M. J. Korpi, A. Brandenburg, D. Mitra, and R. Tavakol, Astron. Nachr. **331**, 73 (2010).
[12] P. Charbonneau, Living Reviews in Solar Physics **7**, 3 (2010), http://livingreviews.org/lrsp-2010-3.
[13] S. E. Gibson, L. Fletcher, G. D. Zanna, C. D. Pike, H. E. Mason, C. H. Mandrini, P. Dmoulin, H. Gilbert, J. Burkepile, T. Holzer, D. Alexander, Y. Liu, N. Nitta, J. Qiu, B. Schmieder, and B. J. Thompson, Astrophys. J. **574**, 1021 (2002).
[14] K. D. Leka, R. C. Canfield, A. N. McClymont, and L. van Driel-Gesztelyi, Astrophys. J. **462**, 547 (1996).
[15] P. K. Manoharan, L. van Driel-Gesztelyi, M. Pick, and P. Demoulin, Astrophys. J. **468**, L73+ (1996).
[16] R. C. Canfield, H. S. Hudson, and D. E. McKenzie, Geophys. Res. Lett. **26**, 627, doi:10.1029/1999GL900105 (1999).
[17] A. Shukurov, D. Sokoloff, K. Subramanian, and A. Brandenburg, Astron. Astrophys. **448**, L33 (2006).
[18] A. Brandenburg, S. Candelaresi, and P. Chatterjee, Mon. Not. R. Astron. Soc. **398**, 1414 (2009).
[19] E. G. Blackman and A. Brandenburg, Astrophys. J. **584**, L99 (2003).
[20] D. Mitra, S. Candelaresi, P. Chatterjee, R. Tavakol, and A. Brandenburg, Astron. Nachr. **331**, 130 (2010).
[21] K. Subramanian and A. Brandenburg, Astrophys. J. Lett. **648**, L71 (2006).
[22] E. T. Vishniac and J. Cho, Astrophys. J. **550**, 752 (2001).
[23] D. J. Price and C. Federrath, Astron. Soc. Pac. Conf. Ser. **429**, 274 (2010).
[24] D. J. Price, Mon. Not. R. Astron. Soc. **401**, 1475 (2010).
[25] A. Brandenburg, Mon. Not. R. Astron. Soc. **401**, 347 (2010).
[26] A. Brandenburg, A. Nordlund, R. F. Stein, and U. Torkelsson, Astrophys. J. **446**, 741 (1995).
[27] M. A. Berger, Geophys. Astrophys. Fluid Dyn. **30**, 79 (1984).
[28] A. Brandenburg, Astrophys. J. **550**, 824 (2001).
[29] W. Dobler, A. Shukurov, and A. Brandenburg, Phys. Rev. E **65**, 036311 (2002).
[30] A. Brandenburg, P. J. Käpylä, and A. Mohammed, Phys. Fluids **16**, 1020 (2004).
[31] A. Brandenburg and W. Dobler, Comput. Phys. Commun. **147**, 471 (2002).
[32] A. Brandenburg, Astron. Nachr. **332**, 51 (2010).
[33] N. I. Kleeorin and A. A. Ruzmaikin, Magnetohydrodynamics **2**, 17 (1982).
[34] A. Hubbard and A. Brandenburg, Geophys. Astrophys. Fluid Dyn. **104**, 577 (2010).
[35] N. E. L. Haugen, A. Brandenburg, and W. Dobler, Phys. Rev. E **70**, 016308 (2004).
[36] N. Seehafer, Phys. Rev. E **53**, 1283 (1996).
[37] H. Ji, Phys. Rev. Lett. **83**, 3198 (1999).
[38] U. Frisch, *Turbulence. The Legacy of A. N. Kolmogorov* (Cambridge University Press, Cambridge, 1995).

V

PHYSICAL REVIEW E **81**, 036401 (2010)

Magnetic-field decay of three interlocked flux rings with zero linking number

Fabio Del Sordo, Simon Candelaresi, and Axel Brandenburg
NORDITA, AlbaNova University Center, Roslagstullsbacken 23, SE-10691 Stockholm, Sweden and Department of Astronomy, Stockholm University, SE 10691 Stockholm, Sweden

(Received 22 October 2009; revised manuscript received 27 January 2010; published 3 March 2010)

The resistive decay of chains of three interlocked magnetic flux rings is considered. Depending on the relative orientation of the magnetic field in the three rings, the late-time decay can be either fast or slow. Thus, the qualitative degree of tangledness is less important than the actual value of the linking number or, equivalently, the net magnetic helicity. Our results do not suggest that invariants of higher order than that of the magnetic helicity need to be considered to characterize the decay of the field.

DOI: 10.1103/PhysRevE.81.036401 PACS number(s): 52.65.Kj, 52.30.Cv, 52.35.Vd

I. INTRODUCTION

Magnetic helicity plays an important role in plasma physics [1–3], solar physics [4–6], cosmology [7–9], and dynamo theory [10,11]. This is connected with the fact that magnetic helicity is a conserved quantity in ideal magnetohydrodynamics [12]. The conservation law of magnetic helicity is ultimately responsible for inverse cascade behavior that can be relevant for spreading primordial magnetic field over large length scales. It is also likely the reason why the magnetic fields of many astrophysical bodies have length scales that are larger than those of the turbulent motions responsible for driving these fields. In the presence of finite magnetic diffusivity, the magnetic helicity can only change on a resistive time scale. Of course, astrophysical bodies are open, so magnetic helicity can change by magnetic helicity fluxes out of or into the domain of interest. However, such cases will not be considered in the present paper.

In a closed or periodic domain without external energy supply, the decay of a magnetic field depends critically on the value of the magnetic helicity. This is best seen by considering spectra of magnetic energy and magnetic helicity. The magnetic energy spectrum $M(k)$ is normalized such that

$$\int M(k)dk = \langle \boldsymbol{B}^2\rangle/2\mu_0, \tag{1}$$

where $\boldsymbol{B}$ is the magnetic field, μ_0 is the magnetic permeability, and k is the wave number (ranging from 0 to ∞). The magnetic helicity spectrum $H(k)$ is normalized such that

$$\int H(k)dk = \langle \boldsymbol{A}\cdot\boldsymbol{B}\rangle, \tag{2}$$

where $\boldsymbol{A}$ is the magnetic vector potential with $\boldsymbol{B}=\boldsymbol{\nabla}\times\boldsymbol{A}$. In a closed or periodic domain, $H(k)$ is gauge invariant, i.e., it does not change after adding a gradient term to $\boldsymbol{A}$. For finite magnetic helicity, the magnetic energy spectrum is bound from below [12] such that

$$M(k) \geq k|H(k)|/2\mu_0. \tag{3}$$

This relation is also known as the realizability condition [13]. Thus, the decay of a magnetic field is subject to a corresponding decay of its associated magnetic helicity. Given that in a closed or periodic domain the magnetic helicity changes only on resistive time scales [14], the decay of magnetic energy is slowed down correspondingly. More detailed statements can be made about the decay of turbulent magnetic fields, where the energy decays in a power-law fashion proportional to $t^{-\sigma}$. In the absence of magnetic helicity, $\langle\boldsymbol{A}\cdot\boldsymbol{B}\rangle=0$, we have a relatively rapid decay with $\sigma\approx 1.3$ [15], while with $\langle\boldsymbol{A}\cdot\boldsymbol{B}\rangle\neq 0$, the decay is slower with σ between 1/2 [9] and 2/3 [16].

The fact that the decay is slowed down in the helical case is easily explained in terms of the topological interpretation of magnetic helicity. It is well known that the magnetic helicity can be expressed in terms of the linking number n of discrete magnetic flux ropes via [13]

$$\int \boldsymbol{A}\cdot\boldsymbol{B}dV = 2n\Phi_1\Phi_2, \tag{4}$$

where

$$\Phi_i = \int_{S_i} \boldsymbol{B}\cdot d\boldsymbol{S} \quad (\text{for } i=1 \text{ and } 2) \tag{5}$$

are the magnetic fluxes of the two ropes with cross-sectional areas S_1 and S_2. The slowing down of the decay is then plausibly explained by the fact that a decay of magnetic energy is connected with a decay of magnetic helicity via the realizability condition (3). Thus, a decay of magnetic helicity can be achieved either by a decay of the magnetic flux or by magnetic reconnection. Magnetic flux can decay through annihilation with oppositely oriented flux. Reconnection on the other hand reflects a change in the topological connectivity, as demonstrated in detail in Ref. [17], p. 28.

The situation becomes more interesting when we consider a flux configuration that is interlocked, but with zero linking number. This can be realized quite easily by considering a configuration of two interlocked flux rings where a third flux ring is connected with one of the other two rings such that the total linking number becomes either 0 or 2, depending on the relative orientation of the additional ring, as is illustrated in Fig. 1. Topologically, the configuration with linking numbers of 0 and 2 are the same except that the orientation of the field lines in the upper ring is reversed. Nevertheless, the simple topological interpretation becomes problematic in the case of zero linking number, because then also the magnetic helicity is zero, so the bound of M from below disappears,

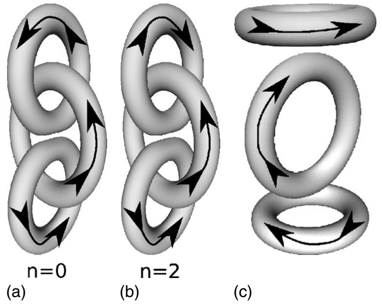

FIG. 1. Visualization of the triple ring configuration at the initial time. Arrows indicate the direction of the field lines in the rings, corresponding to a configuration with $n=0$ (left) and $n=2$ (center). On the right the noninterlocked configuration with $n=0$ is shown.

and M can now in principle freely decay to zero. One might expect that the topology should then still be preserved and that the linking number as defined above, which is a quadratic invariant, should be replaced with a higher-order invariant [18–20]. It is also possible that in a topologically interlocked configuration with zero linking number the magnetic helicity spectrum $H(k)$ is still finite and that bound (3) may still be meaningful. In order to address these questions we perform numerical simulations of the resistive magnetohydrodynamic equations using simple interlocked flux configurations as initial conditions. We also perform a control run with a noninterlocked configuration and zero helicity in order to compare the magnetic energy decay with the interlocked case.

Magnetic helicity evolution is independent of the equation of state and applies hence to both compressible and incompressible cases. In agreement with earlier work [21] we assume an isothermal gas, where pressure is proportional to density and the sound speed is constant. However, in all cases the bulk motions stay subsonic, so for all practical purposes our calculations can be considered nearly incompressible, which would be an alternative assumption that is commonly made [22].

II. MODEL

We perform simulations of the resistive magnetohydrodynamic equations for a compressible isothermal gas where the pressure is given by $p=\rho c_s^2$, with ρ being the density and c_s being the isothermal sound speed. We solve the equations for $\boldsymbol{A}$, the velocity $\boldsymbol{U}$, and the logarithmic density $\ln\rho$ in the form

$$\frac{\partial \boldsymbol{A}}{\partial t} = \boldsymbol{U}\times\boldsymbol{B} + \eta\nabla^2\boldsymbol{A}, \tag{6}$$

$$\frac{\mathrm{D}\boldsymbol{U}}{\mathrm{D}t} = -c_s^2\boldsymbol{\nabla}\ \ln\rho + \boldsymbol{J}\times\boldsymbol{B}/\rho + \boldsymbol{F}_{\mathrm{visc}}, \tag{7}$$

$$\frac{\mathrm{D}\ln\rho}{\mathrm{D}t} = -\boldsymbol{\nabla}\cdot\boldsymbol{U}, \tag{8}$$

where $\boldsymbol{F}_{\mathrm{visc}}=\rho^{-1}\boldsymbol{\nabla}\cdot 2\nu\rho\mathsf{S}$ is the viscous force; S is the traceless rate of strain tensor, with components $\mathsf{S}_{ij}=\frac{1}{2}(U_{i,j}+U_{j,i})-\frac{1}{3}\delta_{ij}\boldsymbol{\nabla}\cdot\boldsymbol{U}$; $\boldsymbol{J}=\boldsymbol{\nabla}\times\boldsymbol{B}/\mu_0$ is the current density; ν is the kinematic viscosity; and η is the magnetic diffusivity.

The initial magnetic field is given by a suitable arrangement of magnetic flux ropes, as already illustrated in Fig. 1. These ropes have a smooth Gaussian cross-sectional profile that can easily be implemented in terms of the magnetic vector potential. We use the PENCIL code [23], where this initial condition for $\boldsymbol{A}$ is already prepared, except that now we adopt a configuration consisting of three interlocked flux rings (Fig. 1) where the linking number can be chosen to be either 0 or 2, depending only on the field orientation in the last (or the first) of the three rings. Here, the two outer rings have radii R_o, while the inner ring is slightly bigger and has the radius $R_i=1.2R_o$, but with the same flux. We use R_o as our unit of length. The sound travel time is given by $T_s=R_o/c_s$.

In the initial state we have $\boldsymbol{U}=\boldsymbol{0}$ and $\rho=\rho_0=1$. Our initial flux, $\Phi=\int\boldsymbol{B}\cdot d\boldsymbol{S}$, is the same for all tubes with $\Phi=0.1c_sR_o^2\sqrt{\mu_0\rho_0}$. This is small enough for compressibility effects to be unimportant, so the subsequent time evolution is not strongly affected by this choice. For this reason, the Alfvén time, $T_A=\sqrt{\mu_0\rho_0R_o^3}/\Phi$, will be used as our time unit. In all our cases we have $T_A=10T_s$ and denote the dimensionless time as $\tau=t/T_A$. In all cases we assume that the magnetic Prandtl number ν/η is unity, and we choose $\nu=\eta=10^{-4}R_oc_s=10^{-3}R_o^2/T_A$. We use 256^3 mesh points.

We have chosen a fully compressible code, because it is readily available to us. Alternatively, as discussed at the end of Sec. I, one could have chosen an incompressible code by ignoring the continuity equation and computing the pressure such that $\boldsymbol{\nabla}\cdot\boldsymbol{U}=0$ at all times. Such an operation breaks the locality of the physics and is computationally more intensive, because it requires global communication.

III. RESULTS

Let us first discuss the visual appearance of the three interlocked flux rings at different times. In Fig. 2 we compare the three rings for the zero and finite magnetic helicity cases at the initial time and at $\tau=0.5$. Note that each ring shrinks as a result of the tension force. This effect is strongest in the core of each ring, causing the rings to show a characteristic indentation that was also seen in earlier inviscid and nonresistive simulations of two interlocked flux rings [21].

At early times, visualizations of the field show little difference, but at time $\tau=0.5$ some differences emerge in that the configuration with zero linking number develops an outer ring encompassing the two rings that are connected via the inner ring; see Fig. 2. This outer ring is absent in the configuration with finite linking number.

The change in topology becomes somewhat clearer if we plot the magnetic-field lines (see Fig. 3). For the $n=2$ configuration, at time $\tau=4$ one can still see a structure of three interlocked rings, while for the $n=0$ case no clear structure

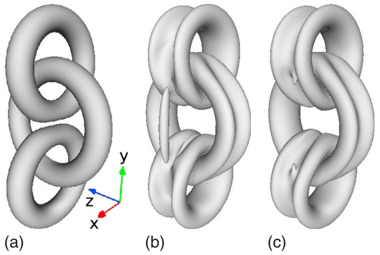

FIG. 2. (Color online) Visualization of the triple ring configuration at $\tau=0$ (left), as well as at $\tau=0.5$ with zero linking number (center) and finite linking number (right). The three images are in the same scale. The change in the direction of the field in the upper ring gives rise to a corresponding change in the value of the magnetic helicity. In the center we can see the emergence of a new flux ring encompassing the two outer rings. Such a ring is not seen on the right.

can be recognized. Note that the magnitude of the magnetic field has diminished more strongly for $n=0$ than for $n=2$. This is in accordance with our initial expectations.

The differences between the two configurations become harder to interpret at later times. Therefore, we compare in Fig. 4 cross sections of the magnetic field for the two cases. The xy cross sections show clearly the development of the new outer ring in the zero linking number configuration. From this figure it is also evident that the zero linking number case suffers more rapid decay because of the now *anti-aligned* magnetic fields (in the upper panel B_x is of opposite sign about the plane $y=0$ while it is negative in the lower panel).

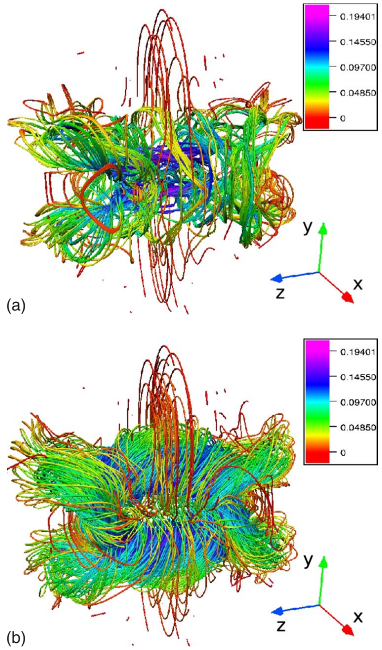

FIG. 3. (Color online) Magnetic flux tubes at time $\tau=4$ for the case of zero linking number (upper picture) and finite linking number (lower picture). The colors represent the magnitude of the magnetic field, where the scale goes from red (lowest) over green to blue (highest).

The evolution of magnetic energy is shown in Fig. 5 for the cases with zero and finite linking numbers. Even at the time $\tau\approx0.6$, when the rings have just come into mutual contact, there is no clear difference in the decay for the two cases. Indeed, until the time $\tau\approx2$ the magnetic energy evolves still similarly in the two cases, but then there is a pronounced difference where the energy in the zero linking number case shows a rapid decline (approximately like $t^{-3/2}$), while in the case with finite linking number it declines much more slowly (approximately like $t^{-1/3}$). However, power-law behavior is only expected under turbulent conditions and not for the relatively structured field configurations considered here. The energy decay in the zero linking number case is roughly the same as in a case of three flux rings that are not interlocked. The result of a corresponding control run is shown as a dotted line in Fig. 5. At intermediate times, $0.5<\tau<5$, the magnetic energy of the control run has diminished somewhat faster than in the interlocked case with $n=0$. It is possible that this is connected with the interlocked nature of the flux rings in one of the cases. Alternatively, this might reflect the presence of rather different dynamics in the noninterlocked case, which seems to be strongly controlled by oscillations on the Alfvén time scale. Nevertheless, at later times the decay laws are roughly the same for noninterlocked and interlocked nonhelical cases.

The time when the rings come into mutual contact is marked by a maximum in the kinetic energy at $\tau\approx0.6$. This can be seen from Fig. 6, where we compare kinetic and magnetic energies separately for the cases with finite and zero linking numbers. Note also that in the zero linking number case magnetic and kinetic energies are nearly equal and decay in the same fashion.

Next we consider the evolution of magnetic helicity in Fig. 7. Until the time $\tau\approx0.6$ the value of the magnetic helicity has hardly changed at all. After that time there is a gradual decline, but it is slower than the decline of magnetic energy. Indeed, the ratio $\langle \boldsymbol{A}\cdot\boldsymbol{B}\rangle/\langle \boldsymbol{B}^2\rangle$, which corresponds to a length scale, shows a gradual increase from $0.1R_{\mathrm{o}}$ to nearly $0.6R_{\mathrm{o}}$ at the end of the simulation. This reflects the fact that the field has become smoother and more space filling with time.

Given that the magnetic helicity decays only rather slowly, one must expect that the fluxes Φ_i of the three rings also only change very little. Except for simple configurations where flux tubes are embedded in field-free regions, it is in general difficult to measure the actual fluxes, as defined in Eq. (5). On the other hand, especially in observational solar physics, one often uses the so-called *unsigned* flux [24,25], which is defined as

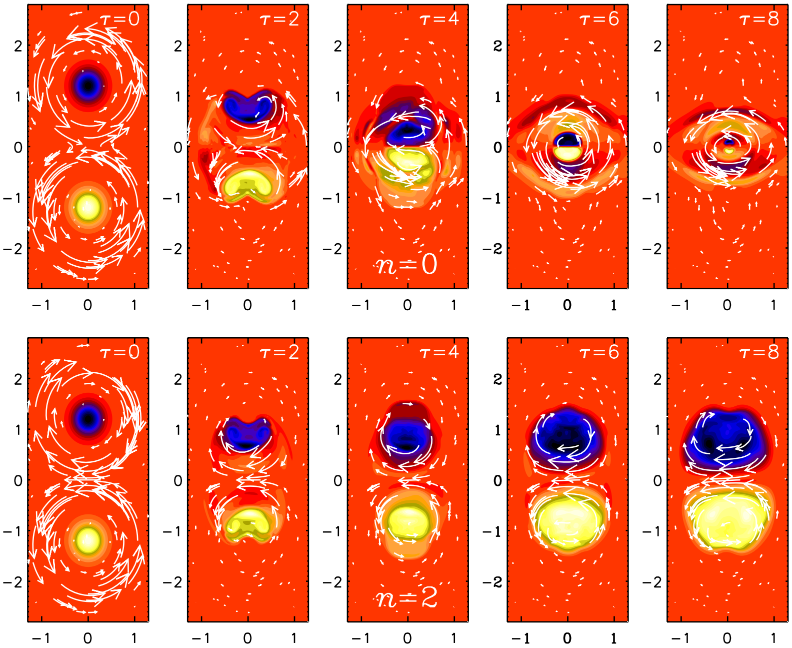

FIG. 4. (Color online) Cross sections in the *xy* plane of the magnetic field with zero linking number (upper row) and finite linking number (lower row). The *z* component (pointing out of the plane) is shown together with vectors of the field in the plane. Light (yellow) shades indicate positive values and dark (blue) shades indicate negative values. Intermediate (red) shades indicate zero value.

$$P_{2D} = \int_S |\boldsymbol{B}| dS. \tag{9}$$

For a ring of flux Φ that intersects the surface in the middle at right angles the net flux cancels to zero, but the unsigned flux gets contributions from both intersections, so $P_{2D}=2|\Phi|$. In three-dimensional simulations it is convenient to determine

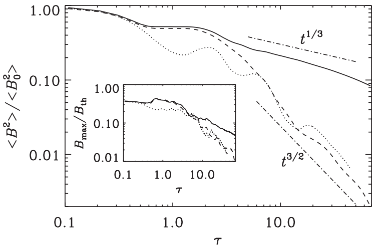

FIG. 5. Decay of magnetic energy (normalized to the initial value) for linking numbers of 2 (solid line) and 0 (dashed line). The dotted line gives the decay for a control run with noninterlocked rings. The dashed-dotted lines indicate $t^{1/3}$ and $t^{3/2}$ scalings for comparison. The inset shows the evolution of the maximum field strength in units of the thermal equipartition value, $B_{\rm th}=c_s(\rho_0\mu_0)^{1/2}$.

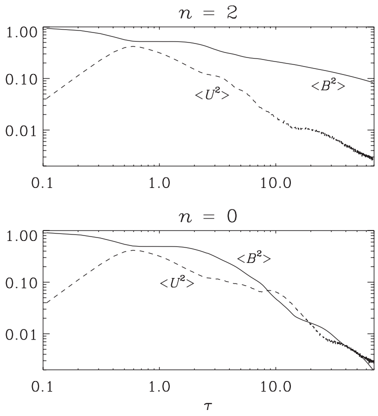

FIG. 6. Comparison of the evolution of kinetic and magnetic energies in the cases with finite and with vanishing linking numbers. Note that in both cases the maximum kinetic energy is reached at the time $\tau \approx 0.6$. The two cases begin to depart from each other after $\tau \approx 2$. In the nonhelical case the magnetic energy shows a sharp drop and reaches equipartition with the kinetic energy, while in the helical case the magnetic energy stays always above the equipartition value.

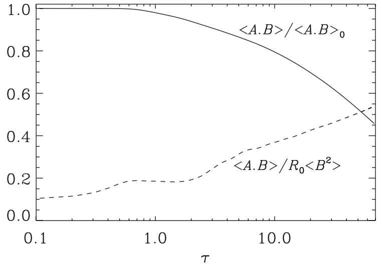

FIG. 7. Evolution of magnetic helicity in the case with finite linking number. In the upper panel, $\langle \boldsymbol{A}\cdot\boldsymbol{B}\rangle$ is normalized to its initial value (indicated by subscript 0) while in the lower panel it is normalized to the magnetic energy divided by R_0.

$$P = \int_V |\boldsymbol{B}| dV. \qquad (10)$$

For several rings, all with radius R, we have

$$P = 2\pi R \sum_{i=1}^{N} |\Phi_i| = \pi N R P_{2D}, \qquad (11)$$

where N is the number of rings. In Fig. 8 we compare the evolution of P (normalized to the initial value P_0) for the cases with $n=0$ and 2. It turns out that after $\tau=1$ the value of p is nearly constant for $n=2$, but not for $n=0$.

Let us now return to the earlier question of whether a flux configuration with zero linking number can have finite spectral magnetic helicity, i.e., whether $H(k)$ is finite but of opposite sign at different values of k. The spectra $M(k)$ and $H(k)$ are shown in Fig. 9 for the two cases at time $\tau=5$. This figure shows that in the configuration with zero linking number $H(k)$ is essentially zero for all values of k. This is not the case and, in hindsight, is hardly expected; see Fig. 9 for the spectra of $M(k)$ and $k|H(k)|/2\mu_0$ in the two cases at $\tau=5$. What might have been expected is a segregation of helicity not in the wave-number space, but in the physical space for positive and negative values of y. It is then possible that magnetic helicity has been destroyed by locally generated magnetic helicity fluxes between the two domains in $y>0$ and $y<0$. However, this is not pursued further in this paper.

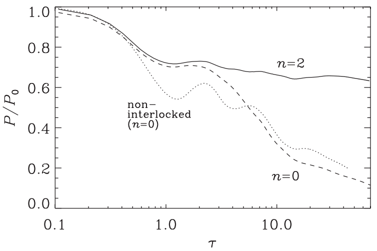

FIG. 8. Decay of the unsigned magnetic flux P (normalized to the initial value P_0) for the cases with $n=0$ and 2. The dotted line gives the decay for a control run with noninterlocked rings.

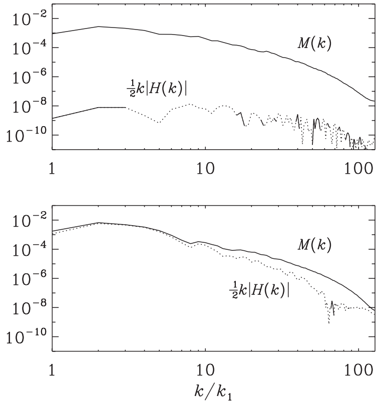

FIG. 9. Comparison of spectra of magnetic energy and magnetic helicity in the case with zero linking number (upper panel) and finite linking number (lower panel) at $\tau=5$. Stretches with negative values of $H(k)$ are shown as dotted lines.

In order to understand in more detail the way the energy is dissipated, we plot in Fig. 10 the evolution of the time derivative of the magnetic energy $E_M=(1/2\mu_0)\int \boldsymbol{B}^2 dV$ (upper panel) and the kinetic energy $E_K=\frac{1}{2}\int \rho \boldsymbol{U}^2 dV$ (lower panel). In the lower panel we also show the rate of work done by the Lorentz force, $W_L=\int \boldsymbol{U}\cdot(\boldsymbol{J}\times\boldsymbol{B})dV$, and in the upper panel we show the rate of work done against the Lorentz force, $-W_L$.

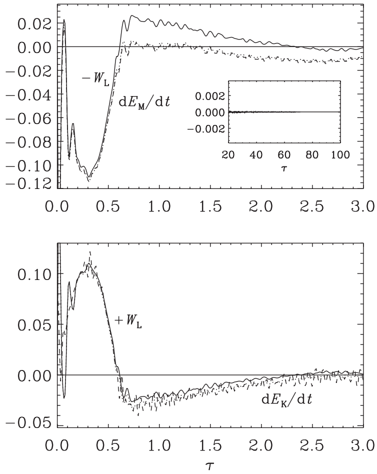

FIG. 10. Evolution of the rate of work done against the Lorentz force, $-W_L$, together with dE_M/dt (upper panel), as well as the rate of work done by the Lorentz force, $+W_L$, together with dE_K/dt (lower panel), all normalized in units of E_M/T_s, for the case with finite linking number. The inset shows $-W_L$ at late times for the case with $n=0$ (solid line) and $n=2$ (dashed line).

All values are normalized by E_{M0}/T_s, where E_{M0} is the value of E_M at $\tau=0$.

The rates of magnetic and kinetic energy dissipations, ϵ_M and ϵ_K, respectively, can be read off as the difference between the two curves in each of the two panels in Fig. 10. Indeed, we have

$$-W_L - dE_M/dt = \epsilon_M, \tag{12}$$

$$W_L + W_C - dE_K/dt = \epsilon_K, \tag{13}$$

where the compressional work term $W_C=\int p\boldsymbol{\nabla}\cdot\boldsymbol{U}dV$ is found to be negligible in all cases. Looking at Fig. 10 we can say that at early times $(0<\tau<0.7)$ the magnetic field contributes to driving fluid motions $(W_L>0)$ while at later times some of the magnetic energy is replenished by kinetic energy $(W_L<0)$, but since magnetic energy dissipation still dominates, the magnetic energy is still decaying $(dE_M/dt<0)$. The maximum dissipation occurs around the time $\tau=0.7$. The magnetic energy dissipation is then about twice as large as the kinetic energy dissipation. We note that the ratio between magnetic and kinetic energy dissipations should also depend on the value of the magnetic Prandtl number $\mathrm{Pr}_M=\nu/\eta$, which we have chosen here to be unity. In this connection it may be interesting to recall that one finds similar ratios of ϵ_K and ϵ_M both for helical and nonhelical turbulence [26]. At smaller values of Pr_M the ratio of ϵ_K to $\epsilon_K+\epsilon_M$ diminishes like $\mathrm{Pr}_M^{-1/2}$ for helical turbulence [27]. In the present case the difference between $n=0$ and 2 is, again, small. Only at later times there is a small difference in W_L, as is shown in the inset of Fig. 10. It turns out that, for $n=2$, W_L is positive while for $n=0$ its value fluctuates around zero. This suggests that the $n=2$ configuration is able to sustain fluid motions for longer times than the $n=0$ configuration. This is perhaps somewhat unexpected, because the helical configuration $(n=2)$ should be more nearly force free than the nonhelical configuration. However, this apparent puzzle is simply explained by the fact that the $n=2$ configuration has not yet decayed as much as the $n=0$ configuration has.

IV. CONCLUSIONS

The present work has shown that the rate of magnetic energy dissipation is strongly constrained by the presence of magnetic helicity and not by the qualitative degree of knottedness. In our example of three interlocked flux rings we considered two flux chains, where the topology is the same except that the relative orientation of the magnetic field is reversed in one case. This means that the linking number switches from 2 to 0, just depending on the sign of the field in one of the rings. The resulting decay rates are dramatically different in the two cases, and the decay is strongly constrained in the case with finite magnetic helicity.

The present investigations reinforce the importance of considering magnetic helicity in studies of reconnection. Reconnection is a subject that was originally considered in two-dimensional studies of *X*-point reconnection [28,29]. Three-dimensional reconnection was mainly considered in the last 20 years. An important aspect is the production of current sheets in the course of field line braiding [30]. Such current sheets are an important contributor to coronal heating [31]. The crucial role of magnetic helicity has also been recognized in several papers [32,33]. However, it remained unclear whether the decay of interlocked flux configurations with zero helicity might be affected by the degree of tangledness. Our present work suggests that a significant amount of dissipation should only be expected from tangled magnetic fields that have zero or small magnetic helicity, while tangled regions with finite magnetic helicity should survive longer and are expected to dissipate less efficiently.

ACKNOWLEDGMENTS

We acknowledge the allocation of computing resources provided by the Swedish National Allocations Committee at the Center for Parallel Computers at the Royal Institute of Technology in Stockholm and the National Supercomputer Centers in Linköping. This work was supported in part by the European Research Council under the AstroDyn Research Project No. 227952 and the Swedish Research Council Grant No. 621-2007-4064.

[1] J. B. Taylor, Phys. Rev. Lett. **33**, 1139 (1974).
[2] T. H. Jensen and M. S. Chu, Phys. Fluids **27**, 2881 (1984).
[3] M. Berger and G. B. Field, J. Fluid Mech. **147**, 133 (1984).
[4] D. M. Rust and A. Kumar, Sol. Phys. **155**, 69 (1994).
[5] D. M. Rust and A. Kumar, Astrophys. J. **464**, L199 (1996).
[6] B. C. Low, Sol. Phys. **167**, 217 (1996).
[7] A. Brandenburg, K. Enqvist, and P. Olesen, Phys. Rev. D **54**, 1291 (1996).
[8] G. B. Field and S. M. Carroll, Phys. Rev. D **62**, 103008 (2000).
[9] M. Christensson, M. Hindmarsh, and A. Brandenburg, Astron. Nachr. **326**, 393 (2005).
[10] A. Pouquet, U. Frisch, and J. Léorat, J. Fluid Mech. **77**, 321 (1976).
[11] A. Brandenburg and K. Subramanian, Phys. Rep. **417**, 1 (2005).
[12] L. Woltjer, Proc. Natl. Acad. Sci. U.S.A. **44**, 489 (1958).
[13] H. K. Moffatt, J. Fluid Mech. **35**, 117 (1969).
[14] M. Berger, Geophys. Astrophys. Fluid Dyn. **30**, 79 (1984).
[15] M.-M. Mac Low, R. S. Klessen, and A. Burkert, Phys. Rev. Lett. **80**, 2754 (1998).
[16] D. Biskamp and W.-C. Müller, Phys. Rev. Lett. **83**, 2195 (1999).
[17] E. Priest and T. Forbes, *Magnetic Reconnection* (Cambridge University Press, Cambridge, England, 2000).
[18] A. Ruzmaikin and P. Akhmetiev, Phys. Plasmas **1**, 331 (1994).
[19] G. Hornig and C. Mayer, J. Phys. A **35**, 3945 (2002).
[20] R. Komendarczyk, Commun. Math. Phys. **292**, 431 (2009).
[21] R. M. Kerr and A. Brandenburg, Phys. Rev. Lett. **83**, 1155 (1999).

[22] R. Grauer and C. Marliani, Phys. Rev. Lett. **84**, 4850 (2000).
[23] http://pencil-code.googlecode.com
[24] C. Zwaan, Sol. Phys. **100**, 397 (1985).
[25] C. J. Schrijver and K. L. Harvey, Sol. Phys. **150**, 1 (1994).
[26] N. E. L. Haugen, A. Brandenburg, and W. Dobler, Astrophys. J. **597**, L141 (2003).
[27] A. Brandenburg, Astrophys. J. **697**, 1206 (2009).
[28] E. N. Parker, J. Geophys. Res. **62**, 509 (1957).
[29] D. Biskamp, Phys. Fluids **29**, 1520 (1986).
[30] M. A. Berger, Phys. Rev. Lett. **70**, 705 (1993).
[31] K. Galsgaard and Å. Nordlund, J. Geophys. Res. **101**, 13445 (1996).
[32] Y. Q. Hu, L. D. Xia, X. Li, J. X. Wang, and G. X. Ai, Sol. Phys. **170**, 283 (1997).
[33] Y. Liu, H. Kurokawa, C. Liu, D. H. Brooks, J. Dun, T. T. Ishii, and H. Zhang, Sol. Phys. **240**, 253 (2007).

VI

PHYSICAL REVIEW E **84**, 016406 (2011)

Decay of helical and nonhelical magnetic knots

Simon Candelaresi and Axel Brandenburg
NORDITA, AlbaNova University Center, Roslagstullsbacken 23, SE-10691 Stockholm, Sweden and
Department of Astronomy, Stockholm University, SE-10691 Stockholm, Sweden

(Received 17 March 2011; revised manuscript received 8 May 2011; published 25 July 2011)

We present calculations of the relaxation of magnetic field structures that have the shape of particular knots and links. A set of helical magnetic flux configurations is considered, which we call n-foil knots of which the trefoil knot is the most primitive member. We also consider two nonhelical knots; namely, the Borromean rings as well as a single interlocked flux rope that also serves as the logo of the Inter-University Centre for Astronomy and Astrophysics in Pune, India. The field decay characteristics of both configurations is investigated and compared with previous calculations of helical and nonhelical triple-ring configurations. Unlike earlier nonhelical configurations, the present ones cannot trivially be reduced via flux annihilation to a single ring. For the n-foil knots the decay is described by power laws that range form $t^{-2/3}$ to $t^{-1/3}$, which can be as slow as the $t^{-1/3}$ behavior for helical triple-ring structures that were seen in earlier work. The two nonhelical configurations decay like t^{-1}, which is somewhat slower than the previously obtained $t^{-3/2}$ behavior in the decay of interlocked rings with zero magnetic helicity. We attribute the difference to the creation of local structures that contain magnetic helicity which inhibits the field decay due to the existence of a lower bound imposed by the realizability condition. We show that net magnetic helicity can be produced resistively as a result of a slight imbalance between mutually canceling helical pieces as they are being driven apart. We speculate that higher order topological invariants beyond magnetic helicity may also be responsible for slowing down the decay of the two more complicated nonhelical structures mentioned above.

DOI: 10.1103/PhysRevE.84.016406 PACS number(s): 52.65.Kj, 52.30.Cv, 52.35.Vd

I. INTRODUCTION

Magnetic helicity is an important quantity in dynamo theory [1,2], astrophysics [3,4] and plasma physics [5–8]. In the limit of high magnetic Reynolds numbers it is a conserved quantity [9]. This conservation is responsible for an inverse cascade which can be the cause for large-scale magnetic fields as we observe them in astrophysical objects. The small-scale component of magnetic helicity is responsible for the quenching of dynamo action [10] and has to be shed in order to obtain magnetic fields of equipartition strength and sizes larger then the underlying turbulent eddies [11].

Helical magnetic fields are observed on the Sun's surface [12,13]. Such fields are also produced in tokamak experiments for nuclear fusion to contain the plasma [14]. It could be shown that the helical structures on the Sun's surface are more likely to erupt in coronal mass ejections [15], which could imply that the Sun sheds magnetic helicity [16]. In [17] it was shown that, for a force-free magnetic field configuration, there exists an upper limit of the magnetic helicity below which the system is in equilibrium. Exceeding this limit leads to coronal mass ejections which drag magnetic helicity from the Sun.

Magnetic helicity is connected with the linking of magnetic field lines. For two separate magnetic flux rings with magnetic flux ϕ_1 and ϕ_2 it can be shown that magnetic helicity is equal to twice the number of mutual linking n times the product of the two fluxes [18]:

$$H_{\rm M} = \int_V \boldsymbol{A} \cdot \boldsymbol{B} dV = 2n\phi_1\phi_2, \qquad (1)$$

where $\boldsymbol{B}$ is the magnetic flux density, expressed in terms of the magnetic vector potential $\boldsymbol{A}$ via $\boldsymbol{B} = \nabla \times \boldsymbol{A}$ and the integral is taken over the whole volume. As we emphasize in this paper, however, that this formula does not apply to the case of a single interlocked flux tube.

The presence of magnetic helicity constrains the decay of magnetic energy [5,9] due to the the realizability condition [19] which imposes a lower bound on the spectral magnetic energy if magnetic helicity is finite; that is,

$$M(k) \geqslant k|H(k)|/(2\mu_0), \qquad (2)$$

where $M(k)$ and $H(k)$ are magnetic energy and helicity at wave number k and μ_0 is the vacuum permeability. These spectra are normalized such that $\int M(k)dk = \langle \boldsymbol{B}^2\rangle/(2\mu_0)$ and $\int H(k)dk = \langle \boldsymbol{A} \cdot \boldsymbol{B}\rangle$, where angular brackets denote volume averages. Note that the energy at each scale is bound separately, which constrains conversions from large to small scales and vice versa. For most of our calculations we assume a periodic domain with zero net flux. Otherwise, in the presence of a net flux, magnetic helicity would not be conserved [20,21], but it would be produced at a constant rate by the α effect [22].

The connection with the topology of the magnetic field makes the magnetic helicity a particularly interesting quantity for studying relaxation processes. One could imagine that the topological structure imposes limits on how magnetic field lines can evolve during magnetic relaxation. To test this it has been studied whether the field topology alone can have an effect on the decay process or if the presence of magnetic helicity is needed [23]. The outcome was that, even for topologically nontrivial configurations, the decay is only effected by the magnetic helicity content. This was, however, questioned [24] and a topological invariant was introduced via field line mapping which adds another constraint even in absence of magnetic helicity. Further evidence for the importance of extra constraints came from numerical simulations of braided magnetic field with zero magnetic helicity [25] where, at the end of a complex cascade-like process, the system relaxed into an approximately force-free field state consisting of two flux tubes of oppositely signed twist. Since the net

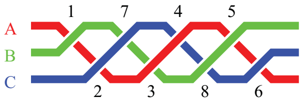

FIG. 1. (Color online) Braid representation of the 4-foil knot. The letters denote the starting position and the numbers denote the crossings.

magnetic helicity is zero, the evolution of the field would not be governed by Taylor relaxation [5] but by extra constraints.

A serious shortcoming of some of the earlier work is that the nonhelical field configurations considered so far were still too simple. For example, in the triple ring of [23] it would have been possible to rearrange freely one of the outer rings on top of the other one without crossing any other field lines. The magnetic flux of these rings would annihilate to zero, making this configuration trivially nonhelical. Therefore, we construct in the present paper more complex nonhelical magnetic field configurations and study the decay of the magnetic field in a similar fashion as in our earlier work. Candidates for suitable field configurations are the IUCAA logo[1] (which is a single nonhelically interlocked flux rope that will be referred to below as the IUCAA knot) and the Borromean rings for which $H_M = 0$. The IUCAA knot is commonly named 8_{18} in knot theory. Furthermore, we test if Eq. (1) is applicable for configurations where there are no separated flux tubes while magnetic helicity is finite. Therefore we investigate setups where the magnetic field has the shape of a particular knot which we call n-foil knot.

II. MODEL

A. Representation of *n*-foil knots

In topology a knot or link can be described via the braid notation [26], where the crossings are plotted sequentially, which results in a diagram that resembles a braid. Some convenient starting points have to be chosen from where the lines are drawn in the direction according to the sense of the knot (Figs. 1 and 2).

For each crossing either a capital or small letter is assigned depending on whether it is a positive or negative crossing.

For the trefoil knot the braid representation is simply AAA. For each new foil a new starting point is needed; at the same time the number of crossings for each line increases by one. This means that, for the 4-foil knot, the braid representation is ABABABAB, for the 5-foil ABCABCABCABCABC, etc.

We construct an initial magnetic field configuration in the form of an n-foil knot with n_f foils or leaves. First, we construct its spine or backbone as a parametrized curve in three-dimensional space. In analogy to [27] we apply the convenient parametrization

$$\boldsymbol{x}(s) = \begin{pmatrix} (C + \sin s n_f) \sin[s(n_f - 1)] \\ (C + \sin s n_f) \cos[s(n_f - 1)] \\ D \cos s n_f \end{pmatrix}, \qquad (3)$$

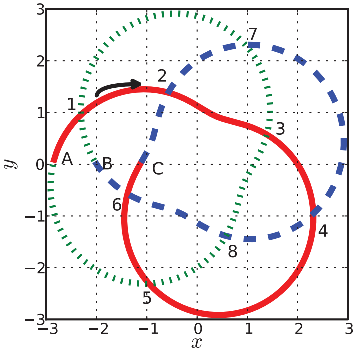

FIG. 2. (Color online) xy projection of the 4-foil knot. The numbers denote the crossings while the colors (line styles) separate different parts of the curve. The letters denote the different starting positions for the braid representation in Fig. 1. The arrow shows the sense of the knot.

where $(C - 1)$ is some minimum distance from the origin, D is a stretch factor in the z direction and s is the curve parameter (see Fig. 3).

The strength of the magnetic field across the tube's cross section is constant and equal to B_0. In the following we shall use B_0 as the unit of the magnetic field. Since we do not want the knot to touch itself we set $C = 1.6$ and $D = 2$. The full three-dimensional magnetic field is constructed radially around this curve (Fig. 4), where the thickness of the cross section is set to 0.48.

B. The IUCAA knot

A prominent example of a single nonhelically interlocked flux rope is the IUCAA knot. For the IUCAA knot we apply

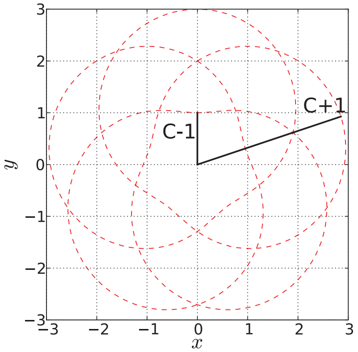

FIG. 3. (Color online) Projection of the 5-foil on the xy plane. The lines show the meaning of the distance C, which has to be larger than 1 to make sense.

---

[1] The Inter-University Centre for Astronomy and Astrophysics in Pune, India.

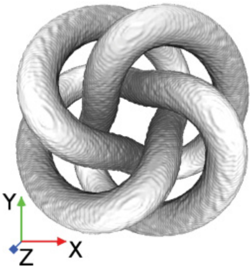

FIG. 4. (Color online) Isosurface of the initial magnetic field energy for the 4-foil configuration.

a very similar parametrization as for the n-foil knots. We have to consider the faster variation in z direction, which yields

$$\boldsymbol{x}(s)=\begin{pmatrix}(C+\sin 4s)\sin 3s\\(C+\sin 4s)\cos 3s\\D\cos(8s-\varphi)\end{pmatrix}, \tag{4}$$

where C and D have the same meaning as for the n-foil knots and φ is a phase shift of the z variation. The full three-dimensional magnetic field is constructed radially around this curve (Fig. 5), where the thickness of the cross section is set to 0.48.

C. Borromean rings

The Borromean rings are constructed with three ellipses whose surface normals point in the direction of the unit vectors (Fig. 6).

The major and minor axes are set to 2.5 and 1, respectively, and the thickness of the cross section is set to 0.6. If any one of the three rings were removed, the remaining 2 rings would no longer be interlocked. This means that there is no mutual linking and hence no magnetic helicity. One should, however, not consider this configuration as topologically trivial, since the rings cannot be separated, which is reflected in a nonvanishing third-order topological invariant [28].

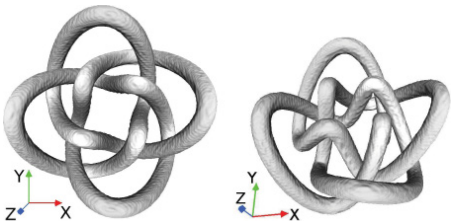

FIG. 5. (Color online) Isosurface of the initial magnetic field energy for the IUCAA knot seen from the top (left panel) and slightly from the side (right panel).

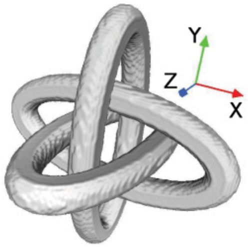

FIG. 6. (Color online) Isosurface of the initial magnetic field energy for the Borromean rings configuration.

D. Numerical setup

We solve the resistive magnetohydrodynamical (MHD) equations for an isothermal compressible gas, where the gas pressure is given by $p=\rho c_S^2$, with the density ρ and isothermal sound speed c_S. Instead of solving for the magnetic field $\boldsymbol{B}$ we solve for its vector potential $\boldsymbol{A}$ and choose the resistive gauge, since it is numerically well behaved [29]. The equations we solve are

$$\frac{\partial \boldsymbol{A}}{\partial t}=\boldsymbol{U}\times\boldsymbol{B}+\eta\nabla^2\boldsymbol{A}, \tag{5}$$

$$\frac{\mathrm{D}\boldsymbol{U}}{\mathrm{D}t}=-c_{\mathrm{S}}^2\boldsymbol{\nabla}\ln\rho+\boldsymbol{J}\times\boldsymbol{B}/\rho+\boldsymbol{F}_{\mathrm{visc}}, \tag{6}$$

$$\frac{\mathrm{D}\ln\rho}{\mathrm{D}t}=-\boldsymbol{\nabla}\cdot\boldsymbol{U}, \tag{7}$$

where $\boldsymbol{U}$ is the velocity field, η is the magnetic diffusivity, $\boldsymbol{J}=\boldsymbol{\nabla}\times\boldsymbol{B}/\mu_0$ is the current density, $\boldsymbol{F}_{\mathrm{visc}}=\rho^{-1}\boldsymbol{\nabla}\cdot 2\nu\rho\mathsf{S}$ is the viscous force with the traceless rate of strain tensor S with components $\mathsf{S}_{ij}=\frac{1}{2}(u_{i,j}+u_{j,i})-\frac{1}{3}\delta_{ij}\boldsymbol{\nabla}\cdot\boldsymbol{U}$, ν is the kinematic viscosity, and $\mathrm{D}/\mathrm{D}t=\partial/\partial t+\boldsymbol{U}\cdot\boldsymbol{\nabla}$ is the advective time derivative. We perform simulations in a box of size $(2\pi)^3$ with fully periodic boundary conditions for all quantities. To test how boundary effects play a role we also perform simulations with perfect conductor boundary conditions (i.e., the component of the magnetic field perpendicular to the surface vanishes). In both choices of boundary conditions, magnetic helicity is gauge invariant and is a conserved quantity in ideal MHD (i.e., $\eta=0$). As a convenient parameter we use the Lundquist number $\mathrm{Lu}=U_{\mathrm{A}}L/\eta$, where U_{A} is the Alfvén velocity and L is a typical length scale of the system. The value of the viscosity is characterized by the magnetic Prandtl number $\mathrm{Pr}_{\mathrm{M}}=\nu/\eta$. However, in all cases discussed below we use $\mathrm{Pr}_{\mathrm{M}}=1$. To facilitate comparison of different setups it is convenient to normalize time by the resistive time $t_{\mathrm{res}}=r^2\pi/\eta$, where r is the radius of the cross section of the flux tube.

We solve Eqs. (5)–(7) with the PENCIL CODE [30,31], which employs sixth-order finite differences in space and a third-order time stepping scheme. As in our earlier work [23], we use 256^3 meshpoints for all our calculations. We recall that we use explicit viscosity and magnetic diffusivity. Their values are dominant over numerical contributions associated with discretization errors of the scheme.[2]

---

[2] The discretization error of the temporal scheme scheme implies a small diffusive contribution proportional to ∇^4, but even at the Nyquist frequency this is subdominant.

III. RESULTS

A. Helicity of *n*-foil knots

We test equation (1) for the n-foil knots in order to see how the number of foils n_f relates to the number of mutual linking n for the separated flux tubes. From our simulations we know the magnetic helicity H_M and the magnetic flux ϕ through the tube. Solving (1) for n will lead to an apparent self-linking number which we call n_app. It turns out that n_app is much larger then n_f and increases faster (Fig. 7).

We note that (1) does not apply to this setup of flux tubes and propose therefore a different formula for the magnetic helicity:

$$H_\mathrm{M} = (n_\mathrm{f} - 2)n_\mathrm{f}\phi^2/2. \tag{8}$$

In Fig. 7 we plot the apparent linking number together with a fit which uses Eq. (8).

Equation (8) can be motivated via the number of crossings. The flux tube is projected onto the xy plane such that the number of crossings is minimal. The linking number can be determined by adding all positive crossings and subtracting all negative crossings according to Fig. 8.

The linking number is then simply given as [32]

$$n_\mathrm{linking} = (n_+ - n_-)/2, \tag{9}$$

where n_+ and n_- correspond to positive and negative crossings, respectively. If we set $n_\mathrm{linking} = n_\mathrm{app}$ then we easily see the validation of (8). Each new foil creates a new ring of crossings and adds up one crossing in each ring (see Fig. 9), which explains the quadratic increase.

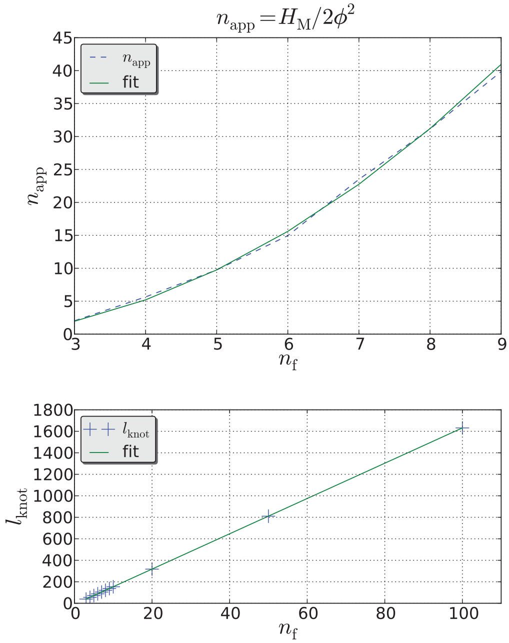

FIG. 7. (Color online) The apparent self-linking number for n-foil knots with respect to n_f (upper panel). The fit is obtained by equating (1) and (8). The length of a n-foil knot is plotted with respect to n_f (lower panel), which can be fit almost perfectly by a linear function.

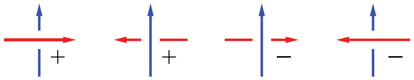

FIG. 8. (Color online) Schematic representation illustrating the sign of a crossing. Each crossing has a handedness which can be either positive or negative. The sum of the crossings gives the number of linking and eventually the magnetic helicity content via equation (8).

B. Magnetic energy decay for *n*-foil knots

Next, we plot in Fig. 10 the magnetic energy decay for n-foil knots with $n_\mathrm{f} = 3$ up to $n_\mathrm{f} = 7$ for periodic boundary conditions. It turns out that, at later times, the decay slows down as n_f increases. The decay of the magnetic energy obeys an approximate $t^{-2/3}$ law for $n_\mathrm{f} = 3$ and a $t^{-1/3}$ law for $n_\mathrm{f} = 7$. The rather slow decay is surprising in view of earlier results that, for turbulent magnetic fields, the magnetic energy decays like t^{-1} in the absence of magnetic helicity and like $t^{-1/2}$ with magnetic helicity [33]. Whether or not the decay seen in Fig. 10 really does follow a power law with such an exponent remains therefore open.

The different power laws for a given number of foils n_f are unexpected because the setups differ only in their magnetic helicity and magnetic energy content and not in the qualitative nature of the knot. Indeed, one might have speculated that the faster $t^{-2/3}$ decay applies to the case with larger n_f, because this structure is more complex and involves sharper gradients. On the other hand, a larger value of n_f increases the total helicity, making the resulting knot more strongly packed. This can be verified by noting that the magnetic helicity increases quadratically with n_f while the magnetic energy increases only linearly. This is because the energy is proportional to the length of the tube which, in turn, is proportional to n_f

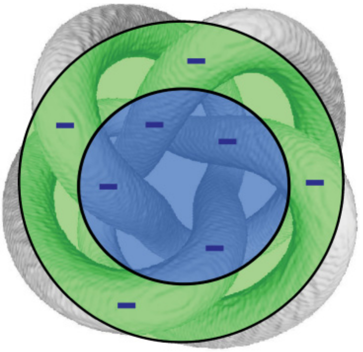

FIG. 9. (Color online) The isosurface for the 4-foil knot field configuration. The sign of the crossing is always negative. The rings show the different areas where crossings occur.

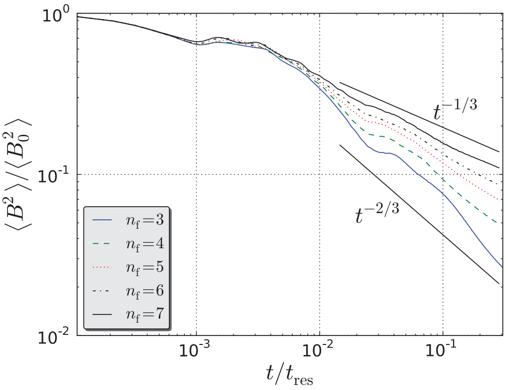

FIG. 10. (Color online) Time dependence of the normalized magnetic energy for a given number of foils with periodic boundary conditions. The power law for the energy decay varies between $-2/3$ for $n_{\rm f} = 3$ [solid (blue) line] and $-1/3$ for $n_{\rm f} = 7$ [solid (black)].

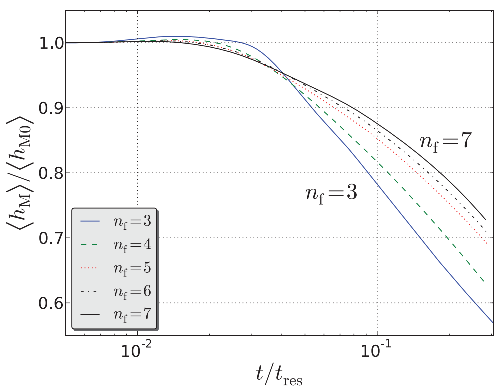

FIG. 12. (Color online) Time dependence of the normalized magnetic helicity for a given number of foils with periodic boundary conditions.

(Fig. 7). Therefore we expect that, for the higher $n_{\rm f}$ cases, the realizability condition should play a more significant role at early times. This can be seen in Fig. 11, where we plot the ratio $2M(k)/[k|H(k)|]$ for $n_{\rm f} = 3$ to $n_{\rm f} = 7$ for $k = 2$. Since the magnetic helicity relative to the magnetic energy is higher for larger values of $n_{\rm f}$, it plays a more significant role for high $n_{\rm f}$. This would explain a different onset of the power law decay, although it would not explain a change in the exponent. Indeed the decay of $H_{\rm M}$ shows approximately the same behavior for all $n_{\rm f}$ (Fig. 12). We must therefore expect that the different decay laws are described only approximately by power laws.

For periodic boundary conditions it is possible that the flux tube reconnects over the domain boundaries which could lead to additional magnetic field destruction. To exclude such complications we compare simulations with perfectly conducting or closed boundaries with periodic boundary conditions (Fig. 13). Since there is no difference in the two cases we can exclude the significance of boundary effects for the magnetic energy decay.

In all cases the magnetic helicity can only decay on a resistive time scale (Fig. 12). This means that, during faster dynamical processes like magnetic reconnection, magnetic helicity is approximately conserved. To show this we plot the magnetic field lines for the trefoil knot at different times (Fig. 14). Since magnetic helicity does not change significantly, the self-linking is transformed into a twisting of the flux tube which is topologically equivalent to linking. Such a process has also been mentioned in connection with Fig. 1 of Ref. [34], while the opposite process of the conversion of twist into linkage has been seen in Ref. [35]. We can also see that the reconnection process, which transforms the trefoil knot into a twisted ring, does not aid the decay of magnetic helicity.

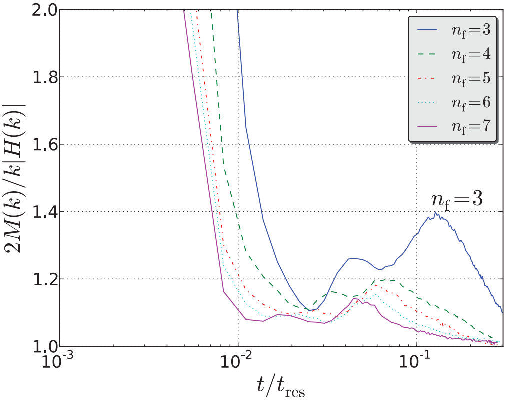

FIG. 11. (Color online) Time dependence of the quotient from the realizability condition (2) for $k = 2$. It is clear that, for larger $n_{\rm f}$, the energy approaches its minimum faster.

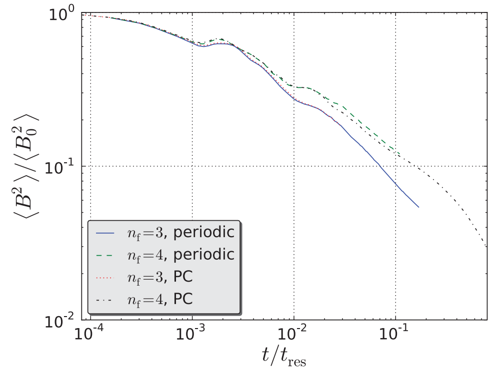

FIG. 13. (Color online) Time dependence of the normalized magnetic energy for the trefoil and 4-foil knot with periodic and perfect conductor (PC) boundary conditions. There is no significant difference in the energy decay for the different boundary conditions.

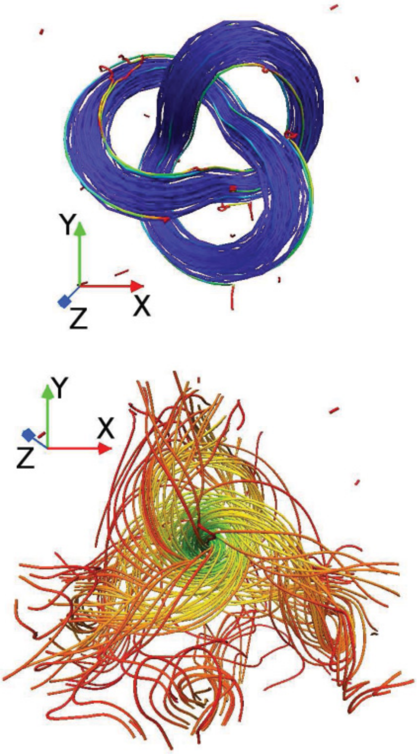

FIG. 14. (Color online) Magnetic field lines for the trefoil knot at time $t = 0$ (upper panel) and $t = 7.76 \times 10^{-2} t_{\mathrm{res}}$ (lower panel). Both images were taken from the same viewing position to make comparisons easier. The Lundquist number was chosen to be 1000. The colors indicate the field strength.

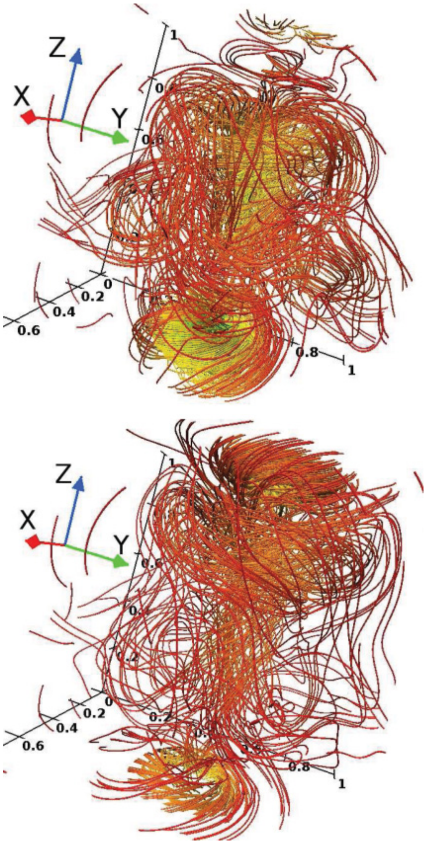

FIG. 15. (Color online) Magnetic field lines for the IUCAA knot at $t = 0.108 t_{\mathrm{res}}$ (upper panel) and at $t = 0.216 t_{\mathrm{res}}$ (lower panel) for $\mathrm{Lu} = 1000$ and $\varphi = (4/3)\pi$.

C. Decay of the IUCAA knot

For the nonhelical triple-ring configuration of Ref. [23] it was found that the topological structure gets destroyed after only 10 Alfvén times. The destruction was attributed to the absence of magnetic helicity whose conservation would pose constraints on the relaxation process. Looking at the magnetic field lines of the IUCAA knot at different times (Fig. 15), we see that the field remains structured and that some helical features emerge above and below the $z = 0$ plane. These localized helical patches could then locally impose constraints on the magnetic field decay.

The asymmetry of the IUCAA knot in the z direction leads to different signs of magnetic helicity above and below the $z = 0$ plane. This is shown in Figs. 16 and 17 where we plot the magnetic helicity for the upper and lower parts for two different values of φ; see Eq. (4). In the plot, we refer to the upper and lower parts as north and south, respectively. These plots show that there is a tendency of magnetic helicity of opposite sign to emerge above and below the $z = 0$ plane. Given that the magnetic helicity was initially zero, one may speculate that higher order topological invariants could provide an appropriate tool to characterize the emergence of such a "bihelical" structure from an initially nonhelical one.

Note that there is a net increase of magnetic helicity over the full volume. Furthermore, the initial magnetic helicity is not exactly zero either, but this is probably a consequence of discretization errors associated with the initialization. The subsequent increase of magnetic helicity can only occur on the longer resistive time scales, since magnetic helicity is conserved on dynamical time scales. Note, however, that the increase of magnetic helicity is exaggerated because we divide by the mean magnetic energy density which is decreasing with time.

In Fig. 18 we plot the xy-averaged magnetic helicity as a function of z and t. This shows that the asymmetry between upper and lower parts increases with time, which we attribute to the Lorentz forces through which the knot shrinks and compresses its interior. This is followed by the ejection of magnetic field.

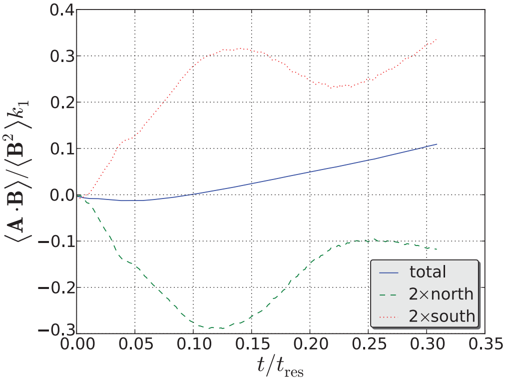

FIG. 16. (Color online) Normalized magnetic helicity in the northern [green (dashed) line] and southern [red (dotted) line] domain half together with the total magnetic helicity [blue (solid) line] for the IUCAA knot with $\mathrm{Lu} = 2000$ and $\varphi = (4/3)\pi$.

To clarify this we plot slices of the magnetic energy density in the xz plane for different times (Fig. 19). The slices are set in the center of the domain.

Due to the rose-like shape, our representation of the IUCAA knot is not quite symmetric and turns out to be narrower in the lower half (negative z) than in the upper half (positive z), which is shown in Fig. 5 (right panel). When the knot contracts due to the Lorentz force, it begins to touch the inner parts, which creates motions in the positive z direction which, in turn, drag the magnetic field away from the center (Fig. 19). The pushing of material can, however, be decreased when the phase φ is changed. For $\varphi = (4/3 + 0.2)\pi$ there is no such upward motion visible and the configuration stays nearly symmetric (Fig. 20).

In Fig. 21 the decay behavior of the magnetic energy is compared with previous work [23]. We note in passing that the power law of t^{-1} is expected for nonhelical turbulence [33], but it is different from the helical ($t^{-1/2}$) and nonhelical ($t^{-3/2}$) triple-ring configurations studied earlier. A possible explanation is the conservation of magnetic structures for the IUCAA knot, whereas the nonhelical triple-ring configuration loses its structure.

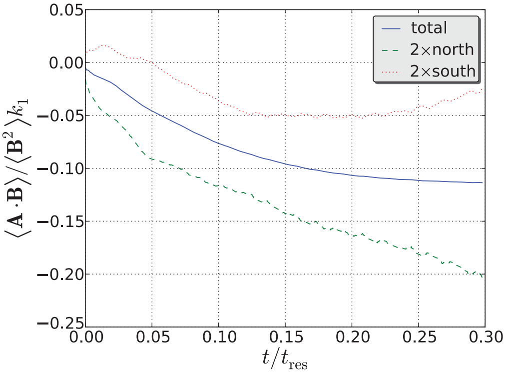

FIG. 17. (Color online) Normalized magnetic helicity in the northern [green (dashed) line] and southern [red (dotted) line] domain half together with the total magnetic helicity [blue (solid) line] for the IUCAA knot with $\mathrm{Lu} = 2000$ and $\varphi = (4/3 + 0.2)\pi$.

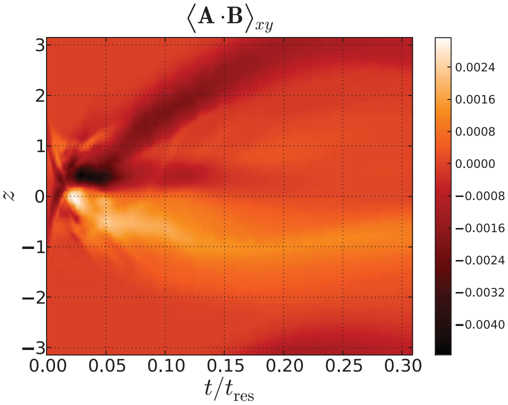

FIG. 18. (Color online) xy-averaged magnetic helicity density profile in z direction for the IUCAA knot with $\mathrm{Lu} = 2000$ and $\varphi = (4/3)\pi$. There is an apparent asymmetry in the distribution amongst the hemispheres.

D. Borromean rings

Previous calculations showed a significant difference in the decay process of three interlocked flux rings in the helical and nonhelical case [23]. In Fig. 21 we compare the magnetic energy decay found from previous calculations using triple-ring configurations with the IUCAA knot and the Borromean rings.

The Borromean rings show a similar behavior as the IUCAA knot where the magnetic energy decays like t^{-1}. Similarly to the IUCAA knot we expect some structure, which is conserved during the relaxation process and causes the relatively slow energy decay compared to other nonhelical configurations. We plot the magnetic field lines at times $t = 0.248t_{\rm res}$ and $t = 0.276t_{\rm res}$; see Figs. 22 and 23, respectively. At $t = 0.248t_{\rm res}$ there are two interlocked flux rings in the lower left corner, while in the opposite half of the simulation domain a clearly twisted flux ring becomes visible. The interlocked rings reconnect at $t = 0.276t_{\rm res}$ and merge into one flux tube with a twist opposite to the other flux ring. The magnetic helicity stays zero during the reconnection, but changes locally, which then imposes a constraint on the magnetic energy decay and could explain the power law that we see in Fig. 21. This finding is similar to that of Ruzmaikin and Akhmetiev [28] who propose that, after reconnection, the Borromean ring configuration transforms first into a trefoil knot and three 8-form flux tubes and after subsequent reconnection into two untwisted flux rings (so-called unknots) and six 8-form flux tubes. We can partly reproduce this behavior, but instead of a trefoil knot we obtain two interlocked flux rings and, instead of the 8-form flux tubes, we obtain internal twist in the flux rings.

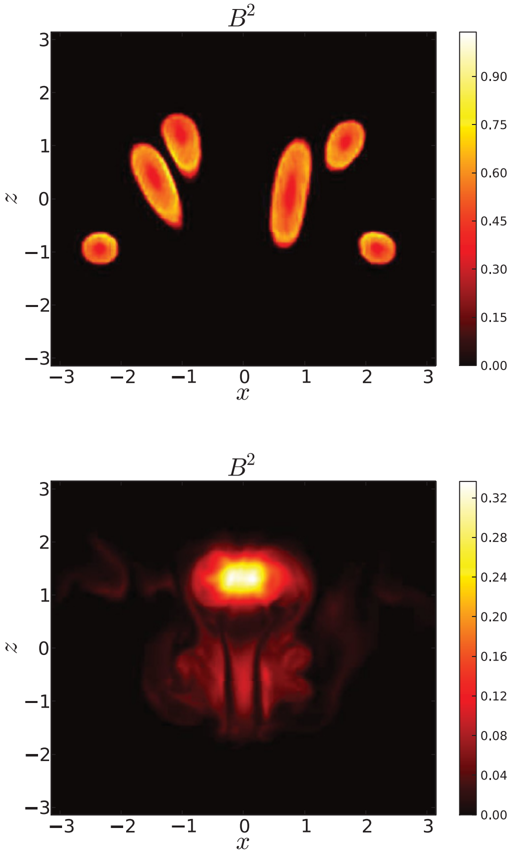

FIG. 19. (Color online) Magnetic energy density in the xz plane for $y = 0$ at $t = 0$ (upper panel) and $t = 5.58 \times 10^{-2} t_{\text{res}}$ (lower panel) for the IUCAA knot with Lu = 2000 and $\varphi = (4/3)\pi$.

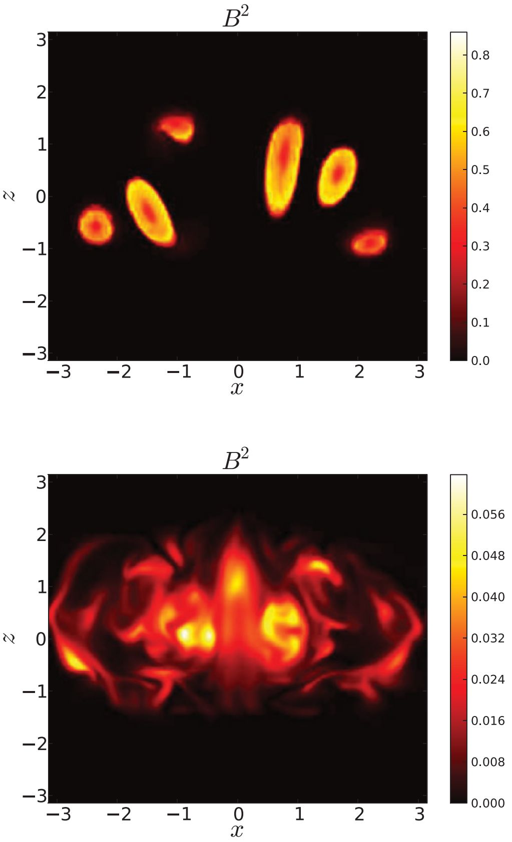

FIG. 20. (Color online) Magnetic energy density in the xz plane for $y = 0$ at $t = 0$ (upper panel) and $t = 5.58 \times 10^{-2} t_{\text{res}}$ (lower panel) for the IUCAA knot with Lu = 2000 and $\varphi = (4/3 + 0.2)\pi$. The magnetic field stays centered.

IV. CONCLUSIONS

In this paper we have analyzed for the first time the decay of complex helical and nonhelical magnetic flux configurations. A particularly remarkable one is the IUCAA knot for which the linking number is zero, and nevertheless, some finite magnetic helicity is gradually emerging from the system on a resistive time scale. It turns out that both the IUCAA knot and the Borromean rings develop regions of opposite magnetic helicity above and below the midplane, so the net magnetic helicity remains approximately zero. In that process, any slight imbalance can then lead to the amplification of the ratio of magnetic helicity to magnetic energy—even though the magnetic field on the whole is decaying. This clearly illustrates the potential of nonhelical configurations to exhibit nontrivial behavior, and thus the need for studying the evolution of higher order invariants that might capture such processes.

The role of resistivity in producing magnetic helicity from a nonhelical initial state has recently been emphasized [36], but it remained puzzling how a resistive decay can increase the topological complexity of the field, as measured by the magnetic helicity. Our results now shed some light on this. Indeed, the initial field in our examples has topological complexity that is not captured by the magnetic helicity as a quadratic invariant. This is because of mutual cancellations that can gradually undo themselves during the resistive decay process, leading thus to finite magnetic helicity of opposite sign in spatially separated locations. We recall in this context that the magnetic helicity over the periodic domains considered here is gauge invariant and should thus agree with any other definition, including the absolute helicity defined in Ref. [36].

Contrary to our own work on a nonhelical interlocked flux configuration [23], which was reducible to a single flux ring after mutual annihilation of two rings, the configurations studied here are nonreducible even when mutual annihilation is taken into account.

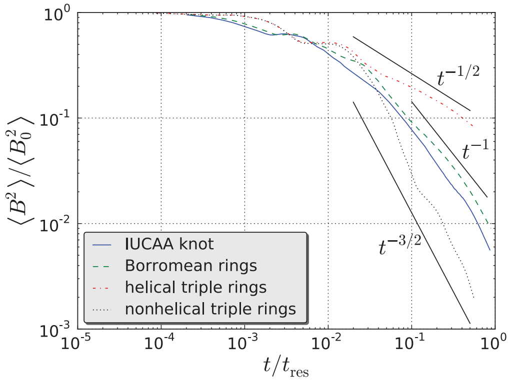

FIG. 21. (Color online) Magnetic energy versus time for the different initial field configurations together with power laws which serve as a guide. The decay speed of the IUCAA knot and Borromean rings lies well in between the helical and nonhelical triple-ring configuration.

For the helical n-foil knot, we have shown that the magnetic helicity increases quadratically with n. Furthermore, their decay exhibits different power laws of magnetic energy which lie between $t^{-2/3}$ for the 3-foil knot and $t^{-1/3}$ for the 7-foil knot. The latter case corresponds well with the previously discussed case of three interlocked flux rings that are interlocked in a helical fashion. The appearance of different power laws seems surprising since we first expected a uniform power law in all helical cases in the regime where the magnetic helicity is so large that the realizability condition plays a role. This makes us speculate whether there are other quantities that are different for the various knots and constrain magnetic energy decay. Such quantities would be higher order topological invariants [28], which are so far only defined for spatially separated flux tubes. In order to investigate their role they need to be generalized such that they can be computed for any magnetic field configuration, similar to the integral for the magnetic helicity.

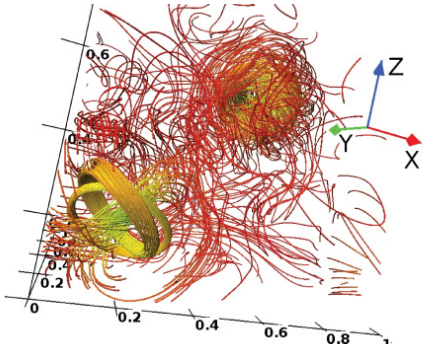

FIG. 22. (Color online) Magnetic field lines at $t = 0.248 t_{\mathrm{res}}$ for the Borromean rings configuration for Lu $= 1000$. In the lower-left corner the interlocked flux rings are clearly visible which differs from the proposed trefoil knot [28]. The flux ring in the opposite corner has an internal twist which makes it helical. The colors denote the strength of the field, where the scale goes from red over green to blue.

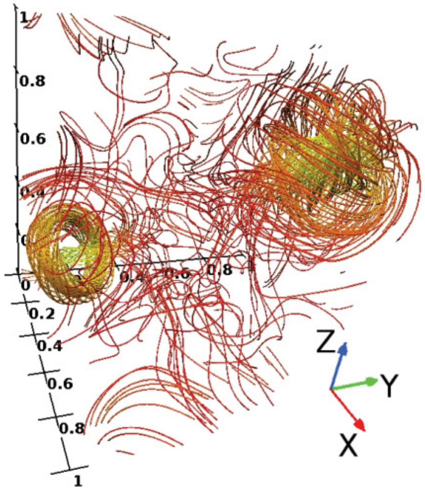

FIG. 23. (Color online) Magnetic field lines at $t = 0.276 t_{\mathrm{res}}$ for the Borromean rings configuration for Lu $= 1000$. The two flux rings in the corners both have an internal twist which makes them helical. The twist is, however, of opposite sign which means that the whole configuration does not contain magnetic helicity. The colors denote the strength of the field, where the scale goes from red over green to blue.

The power law of t^{-1} in the decay of the magnetic energy for the IUCAA knot and the Borromean rings is different from the $t^{-3/2}$ behavior found earlier for the nonhelical triple-ring configuration. The observed decay rate can be attributed to the creation of local helical structures that constrain the decay of the local magnetic field. But we cannot exclude higher order invariants [28] whose conservation would then constrain the energy decay.

The Borromean rings showed clearly that local helical structures can be generated without forcing the system. These can then impose constraints on the field decay. We suggest that spatial variations should be taken into account to reformulate the realizability condition (2), which would increase the lower bound for the magnetic energy. For astrophysical systems local magnetic helicity variations have to be considered to give a more precise description of both relaxation and reconnection processes.

Both the IUCAA logo and the Borromean rings do not stay stable during the simulation time and split up into two separated helical magnetic structures. On the other hand we see that the helical n-foil knots stay stable. A similar behavior was seen in [37], where magnetic fields in bubbles inside galaxy clusters were simulated. In the case of a helical initial magnetic field the field decays into a confined structure, while for sufficiently low initial magnetic helicity, separated structures of opposite magnetic helicity seem more preferable.

ACKNOWLEDGMENTS

We thank the anonymous referee for making useful suggestions, and the Swedish National Allocations Committee for providing computational resources at the National Supercomputer Centre in Linköping and the Center for Parallel Computers at the Royal Institute of Technology in Sweden. This work was supported in part by the Swedish Research Council, Grant 621-2007-4064, the European Research Council under the AstroDyn Research Project 227952, and the National Science Foundation under Grant No. NSF PHY05-51164.

---

[1] U. Frisch, A. Pouquet, J. Leorat, and A. Mazure, J. Fluid Mech. **68**, 769 (1975).
[2] A. Brandenburg and K. Subramanian, Phys. Rep. **417**, 1 (2005).
[3] D. M. Rust and A. Kumar, Astrophys. J. Lett. **464**, L199 (1996).
[4] B. C. Low, Sol. Phys. **167**, 217 (1996).
[5] J. B. Taylor, Phys. Rev. Lett. **33**, 1139 (1974).
[6] J. B. Taylor, Rev. Mod. Phys. **58**, 741 (1986).
[7] T. H. Jensen and M. S. Chu, Phys. Fluids **27**, 2881 (1984).
[8] M. A. Berger and G. B. Field, J. Fluid Mech. **147**, 133 (1984).
[9] L. Woltjer, Proc. Nat. Acad. Sci. USA **44**, 489 (1958).
[10] A. V. Gruzinov and P. H. Diamond, Phys. Rev. Lett. **72**, 1651 (1994).
[11] E. G. Blackman and A. Brandenburg, Astrophys. J. Lett. **584**, L99 (2003).
[12] N. Seehafer, Sol. Phys. **125**, 219 (1990).
[13] A. A. Pevtsov, R. C. Canfield, and T. R. Metcalf, Astrophys. J. Lett. **440**, L109 (1995).
[14] B. A. Nelson, T. R. Jarboe, A. K. Martin, D. J. Orvis, J. Xie, C. Zhang, and L. Zhou, Phys. Plasmas **2**, 2337 (1995).
[15] R. C. Canfield, H. S. Hudson, and D. E. McKenzie, Geophys. Res. Lett. **26**, 627 (1999).
[16] M. Zhang and B. C. Low, Annu. Rev. Astron. Astrophys. **43**, 103 (2005).
[17] M. Zhang, N. Flyer, and B. C. Low, Astrophys. J. **644**, 575 (2006).
[18] H. K. Moffatt, J. Fluid Mech. **35**, 117 (1969).
[19] H. K. Moffatt, *Magnetic Field Generation in Electrically Conducting Fluids* (Cambridge University Press, Cambridge, 1978).
[20] T. Stribling, W. H. Matthaeus, and S. Ghosh, J. Geophys. Res. **99**, 2567 (1994).
[21] M. A. Berger, J. Geophys. Res. **102**, 2637 (1997).
[22] A. Brandenburg and W. H. Matthaeus, Phys. Rev. E **69**, 056407 (2004).
[23] F. Del Sordo, S. Candelaresi, and A. Brandenburg, Phys. Rev. E **81**, 036401 (2010).
[24] A. R. Yeates, G. Hornig, and A. L. Wilmot-Smith, Phys. Rev. Lett. **105**, 085002 (2010).
[25] D. I. Pontin, A. L. Wilmot-Smith, G. Hornig, and K. Galsgaard, Astron. Astrophys. **525**, A57 (2011).
[26] E. Artin, Ann. Math. **48**, 101 (1947).
[27] P. Pieranski and S. Przybyl, Phys. Rev. E **64**, 031801 (2001).
[28] A. Ruzmaikin and P. Akhmetiev, Phys. Plasmas **1**, 331 (1994).
[29] S. Candelaresi, A. Hubbard, A. Brandenburg, and D. Mitra, Phys. Plasmas **18**, 012903 (2011).
[30] A. Brandenburg and W. Dobler, Comput. Phys. Commun. **147**, 471 (2002).
[31] [http://pencil-code.googlecode.com].
[32] R. G. Scharein, Ph.D. thesis, University of British Columbia (1998) (unpublished).
[33] M. Christensson, M. Hindmarsh, and A. Brandenburg, Astron. Nachr. **326**, 393 (2005).
[34] R. M. Kerr and A. Brandenburg, Phys. Rev. Lett. **83**, 1155 (1999).
[35] M. G. Linton, R. B. Dahlburg, and S. K. Antiochos, Astrophys. J. **553**, 905 (2001).
[36] B. C. Low, Phys. Plasmas **18**, 052901 (2011).
[37] J. Braithwaite, Mon. Not. R. Astron. Soc. **406**, 705 (2010).